JAERI-Research
97-047

REVIEW OF JT-60U EXPERIMENTAL RESULTS FROM FEBRUARY TO NOVEMBER, 1996

July 1997

JT-60 Team

日本原子力研究所
Japan Atomic Energy Research Institute

本レポートは，日本原子力研究所が不定期に公刊している研究報告書です。
入手の問合わせは，日本原子力研究所研究情報部研究情報課（〒319-11 茨城県那珂郡東海村）あて，お申し越しください。なお，このほかに財団法人原子力弘済会資料センター（〒319-11 茨城県那珂郡東海村日本原子力研究所内）で複写による実費頒布をおこなっております。

This report is issued irregularly.
Inquiries about availability of the reports should be addressed to Research Information Division, Department of Intellectual Resources, Japan Atomic Energy Research Institute, Tokai-mura, Naka-gun, Ibaraki-ken 319-11, Japan.

編集兼発行　日本原子力研究所
印　　刷　㈱原子力資料サービス

Review of JT-60U Experimental Results from February to November, 1996

JT-60 Team※

Department of Fusion Plasma Research
and
Department of Fusion Facility
Naka Fusion Research Establishment
Japan Atomic Energy Research Institute
Naka-machi, Naka-gun, Ibaraki-ken

(Received June 6, 1997)

In 1996, the plasma performance has been significantly enhanced in the high confinement regimes of reversed shear discharges, high-β_p H-mode discharges and high triangularity discharges with increasing the plasma current under the maximum utilization of plasma shape and profile controls in JT-60U. In the reversed shear discharges with an L-mode edge, the equivalent conditions of plasmas for break-even was achieved with the equivalent D-T fusion amplification factor, Q_{DT}^{eq}, of 1.05 in a thermonuclear dominant regime. In ICRF heating experiments with reversed shear plasmas, second harmonic ICRF minority heating into the deuterium discharges were found to be effective for bulk plasmas inside the internal transport barrier. In the high-β_p H-mode discharges with intense NBI up to 40 MW, the world record of fusion triple product was renewed to be $n_D(0)\tau_E T_i(0)=1.5\times10^{21}$ m^{-3}•s•keV with the world record of ion temperature of 45 keV. The high triangularity plasma shaping for the high-β_p H-mode discharges was effective for improving the stability, so that the the high performance plasma relevant to ITER was sustained with Q_{DT}^{eq}=0.25-0.3 during a couple of the energy confinement times. The negative-ion based neutral beam experiments has started from March 1996 as planned. Current drive and heating characteristics of N-NBI were intensively investigated with the beam energy and power up to 400 keV and 2.3 MW, respectively, in support of ITER. A full non-inductive current drive has been demonstrated at 1 MA with the N-NBI in combination with conventional NBI. Current profile control with LHCD for the reversed shear discharges has shown the controllability for internal transport barriers in the reversed shear discharges. The radiative divertor compatible with high performance plasmas was achieved using neon gas puffing into the reversed shear discharges.

Keywords: JT-60U, Confinement, Current drive, Divertor, Plasma control, Break-even, N-NBI, Reversed shear, High- β_p H-mode, High triangularity discharges

※ The JT-60 Team

V. Afnassiev[1], H. Akasaka, K. Akiba[2], N. Akino, K. Annou, T. Aoyagi, T. Arai, K. Arakawa, N. Asakura, M. Azumi, B.M. Bernholz[24], J. Cao[3], C.Z. Chen[6], Z. Chang[6], S. Chiba, O. Da Costa[4], N. Ebisawa, Y. Fang[5], G.Y. Fu[6], T. Fujii, T. Fujita, H. Fukuda[2], T. Fukuda, A. Funahashi, L. Grisham[6], S. Gunji, H. Haginoya[2], K. Hamamatsu, Y. Hasegawa, T. Hatae, S. Higashijima, H. Hiratsuka, S. Hirauchi, T. Hirayama, A. Hirose[22], A. Honda, M. Honda, B.G. Hong[7], R.M. Hong[17], N. Hosogane, C.K. Hwang[7], H. Ichige, S. Ide, Y. Ikeda, M. Isaka, A. Isayama, N. Isei, S. Ishida, Y. Ishii, M. Isobe[8], N. Isozaki, K. Itami, T. Itoh, T. Iwahashi, R. Jimbou[2],K. Lackner[20], Y. Kamada, A. Kaminaga, T. Kashiwabara, M. Kawai, Y. Kawamata, Y. Kawano, M. Kawanobe[2], D. Kazama, M. Kazawa, M. Kikuchi, J.Y. Kim[9], H. Kimura, T. Kimura, H. Kishimoto, Y. Kishimoto, S. Kitamura, K. Kiyono, K. Kodama, J. Koga[10], Y. Koide, S. Kokusen, K. Komuro[2], T. Kondoh, S. Konoshima, J. Koog[8], G.J. Kramer[11], A.V. Krasilnikov[12], H. Kubo, A. Kumagai[13], K. Kurihara, G. Kurita, M. Kuriyama, M. Kusaka[2], Y. Kusama, L. Lao[17], C. Liu[3], K. Masaki, T. Matsuda, T. Matsumoto, M. Matukawa, V.G. Merezhkin[14], B.E. Mills[21],T. Miura, N. Miya, K. Miyachi, H. Miyata, Y. Miyo, K. Mogaki, M. Mori, M. Morimoto, A. Morioka, S. Moriyama, M. Nagami, A. Nagashima, K. Nagashima, S. Nagaya, O. Naito, Y. Nakamura, R. Nazikian[6], M. Nemoto, S.V. Neudatchin[14], Y. Neyatani, T. Nishitani, H. Nobuska[2], N. Ogiwara, T. Ohga, M. Ohsawa[15], K. Ohshima[2], T. Ohshima, T. Oikawa, T. Okabe, J. Okano, K. Omori, S. Omori, Y. Omori, Y. Onose, T. Ooba[2], H. Oohara, T. Ozeki, R. Ramakrishnan[6], G. Rewoldt[6], M. Saidoh, M. Saigusa, N. Saito, A. Sakasai, S. Sakata, S. Sakurai, T. Sasajima, N. Sasaki[2], M. Sato, T. Sato[2], G. Schilling[6], S.D. Scott[6],M. Seimiya, H. Seki, M. Seki, M. Shibayama[2], M. Shimada, K. Shimizu, K. Shimizu[2], M. Shimizu, M. Shimono, S. Shinozaki, H. Shirai, M. Shitomi, F.X Sodner[18], K. Suganuma, T. Sugie, H. Sunaoshi, M. Takahashi, S. Takahashi, S. Takahashi[2], S. Takeji, H. Takenaga, T. Takenouchi[2], T. Takizuka, H. Tamai, T.S. Taylor1[7], F.V. Tchernychev[16], M. Terakado, T. Terakado, K. Tobita, S. Tokuda, T. Totsuka, Y. Toyokawa, N. Toyoshima, K. Tsuchiya, T. Tsugita, Y. Tsukahara, S. Tsurumi[2], T. Tsuruoka[2], T. Tuda, Y. Uramoto, H. Usami[2], K. Ushigusa, K. Usui, J. Van Dam[19], K.A. Vladimirovich[16], J. Von Seggern[23], T.F. Vsevolodovich[16], M. Vitali[14], J. Yagyu, M. Yamagiwa, M. Yamamoto, T. Yamamoto, O. Yamashita, K. Yokokura, H. Yoshida, M. Yoshida, R. Yoshino

1)STA fellow, Ioffe Inst., RF,

2)Staff on loan,
3)STA scientist exchange program, SWIP, China,
4)STA fellow, Ecole Polytech., France,
5)JAERI fellow, ASIPP, China,
6)PPPL, USA,
7)KAERI, Korea,
8)NIFS, Japan,
9)STA fellow, Univ. Texas, USA,
10)JAERI fellow, Univ. Texas, USA,
11)STA fellow, Netherlands,
12)TRINITI, RF,
13)Tsukuba Univ., Japan,
14)Kurchatov Inst., RF,
15)Kyushu Univ., Japan,
16)Ioffe Inst., RF,
17)GA, USA,
18)JET Joint Undertaking, UK,
19)Univ. Texas, USA,
20)IPP, Germany,
21)SNL, USA,
22)Univ. Saskatchewan, Canada,
23)ISSVP, Germany,
24)ENSGI, France

JT-60U1996年2月－11月期実験結果のレビュー

日本原子力研究所那珂研究所炉心プラズマ研究部・核融合装置試験部
JT-60チーム※

（1997年6月6日受理）

1996年，JT-60Uのプラズマ性能は，プラズマ形状および分布制御を最大限に活用し，負磁気シア放電，高β_pHモード放電および高三角度放電という高閉じ込め領域において格段に改善した。Lモード境界をもつ負磁気シア放電において，熱核融合領域において$Q_{DT}^{eq}=1.05$という等価核融合増倍率を得て，臨界プラズマ条件を達成した。負磁気シア放電へのICRF加熱実験では，第2高調波ICRFマイノリティー加熱によって，内部輸送障壁内部のバルクプラズマへの効率的な加熱が観測された。高β_pHモード放電では，核融合積およびイオン温度の世界記録を更新し，$n_D(0)\,\tau_E T_i(0)=1.5\times10^{21}\,m^{-3}\cdot s\cdot keV$と45keVを達成した。高三角度配位の高$\beta_p$Hモード放電では安定性が改善し，ITERを模擬した高性能プラズマ（$Q_{DT}^{ep}=0.25$-0.3）を2倍の閉じ込め時間にわたって維持することに成功した。負イオン中性粒子入射（N-NBI）実験は，1996年3月より計画通り開始された。400keVおよび2.3MWに及ぶN-NB入射によって，加熱・電流駆動特性の取得がITERを支援して実施され，負イオンと正イオンビームを組み合わせて，1MAの完全非誘導電流駆動を実現した。低域混成波入射による電流分布制御によって，負磁気シア放電における内部輸送障壁の制御性が検証された。そして，負磁気シア放電へのネオンガス入射によって，高性能プラズマと両立する放射冷却ダイバータの形成に成功した。

那珂研究所：〒311-01 茨城県那珂郡那珂町向山801-1

※ JT-60チーム

青柳 哲雄 . 赤坂 博美 . 秋野 昇 . 秋葉 賢一[2] . 朝倉 伸幸 .
安積 正史 . 新井 貴 . 荒川喜代次 . 安納 勝人 . 池田 幸治 .
井坂 正義 . 諫山 明彦 . 石井 康友 . 石田 真一 . 伊世井宣明 .
礒崎 信光 . 磯部 光孝[8] . 伊丹 潔 . 市毛 尚志 . 井手 俊介 .
伊藤 孝雄 . 岩橋 孝明 . 宇佐美広次[2] . 牛草 健吉 . 薄井 勝富 .
浦本 保幸 . 海老沢 昇 . 及川 聡洋 . 大賀 徳道 . 大澤 正哉 .
大島 克己[2] . 大島 貴幸 . 大場 俊夫[2] . 大原比呂志 . 大森 憲一郎 .
大森 俊造 . 大森 栄和 . 岡野 潤 . 岡部 友和 . 荻原 徳男 .
小関 隆久 . 小野瀬義秋 . 風間 大介 . 梶沢 稔 . 柏原 庸央 .
鎌田 裕 . 神永 敦嗣 . 河合視己人 . 河野 康則 . 川野辺 満[2] .
川俣 陽一 . 菊池 満 . 岸本 浩 . 岸本 泰明 . 北村 繁 .
木村 豊秋 . 木村 晴行 . 清野 公広 . 日下 誠[2] . 草間 義紀 .
久保 博孝 . 熊谷 晃 . 栗田 源一 . 栗原 研一 . 栗山 正明 .
軍司 操一 . 小出 芳彦 . 石仙 茂晴 . 児玉 幸三 . 木島 滋 .
小室 健一[2] . 近藤 貴 . 三枝 幹雄 . 斎藤 直之 . 西堂 雅博 .
逆井 章 . 坂田 信也 . 櫻井 真治 . 佐々木 昇[2] . 笹島 唯之 .
佐藤 稔 . 佐藤 正泰 . 佐藤 臣夫[2] . 薗 守正 . 篠崎 信一 .
柴山 実[2] . 嶋田 道也 . 清水 和彦[2] . 清水 勝宏 . 清水 正亜 .
下野 貢 . 白井 浩 . 神保龍太郎[2] . 菅沼 和明 . 杉江 達夫 .
砂押 秀則 . 清宮 宗孝 . 関 宏 . 関 正美 . 高橋 春次 .
高橋 昇竜[2] . 高橋 実 . 滝塚 知典 . 竹治 智 . 竹永 秀信 .
竹之内 忠[2] . 玉井 広史 . 千葉 真一 . 塚原 美光 . 次田 友宣 .
津田 孝 . 土屋 勝彦 . 鶴岡 卓哉[2] . 鶴見 聡[2] . 寺門 恒久 .
寺門 正之 . 徳田 伸二 . 戸塚 俊之 . 飛田 健次 . 豊川 良治 .
豊島 昇 . 内藤 麿 . 長島 章 . 永島 圭介 . 永見 正幸 .
中村 幸治 . 永谷 進 . 西谷 健夫 . 根本 正博 . 閨谷 譲 .
信坂 裕通[2] . 萩野谷裕文[2] . 長谷川幸弘 . 波多江仰紀 . 濱松 清隆 .
東島 智 . 平内 慎一 . 平塚 一 . 平山 俊雄 . 福田 武司 .
福田 裕実[2] . 藤井 常幸 . 藤田 隆明 . 船橋 昭昌 . 細金 延幸 .
本田 敦 . 本田 正男 . 正木 圭 . 松川 誠 . 松田 俊明 .
松本 太郎 . 三浦 友史 . 宮 直之 . 宮田 寛 . 宮地 謙吾 .
三代 康彦 . 藻垣 和彦 . 森 雅博 . 森岡 篤彦 . 森本 将明 .
森山 伸一 . 柳生 純一 . 山極 満 . 山下 修 . 山本 巧 .
山本 正弘 . 横倉 賢治 . 吉田 通治 . 吉田 英俊 . 芳野 隆治

V.I. Afanassiev[1] . B.M. Bernholz[24] . J. Cao[3] .

C.Z. Chen[6] ．　C.Z. Chang[6] ．　O. Da Costa[4] ．
Y. Fang[5] ．　G. Y. Fu[6] ．　L. Grisham[6] ．
A. Hirose[22] ・　B. G. Hong[17] ．　R. M. Hong[17] ．
C. K. Hwang[7] ．　K. Lacker[20] ．　J. Y. Kim[9] ．
J. Koga[10] ．　J. Koog[8] ．　G. J. Kramer[11] ．
A. V. Krasilnikov[12] ．　L. Lao[17] ．　C. Liu[3] ．
V. G. Merezhkin[14] ．　B. E. Mills[21] ．　R. Nazikian[6] ．
S. V. Neudatchin[14] ．　R. Ramakrishnan[6] ．　G. Rewoldt[6] ．
G. Schilling[6] ．　S. D. Scott[6] ．　F. X. Soldner[18]．
T. S. Taylor[17] ．　F. V. Tchernychev[16] ．　J. Van. Dam[19] ．
K. A. Vladimirovich[16] ．　J. Von Seggern[23] ．　T. F. Vsevolodovich[16] ．
M. Vitali[14] ．

1）ロシア、ＳＴＡフェローシップヨッフェ研究所
2）業務協力員
3）原研フェローシップ、現在、オランダ、FOMプラズマ物理研究所
4）フランス、ＳＴＡフェローシップエコールポリテーク
5）中国、科学院プラズマ物理研究所
6）米国、プリンストンプラズマ物理研究所
7）韓国、韓国原子力研究所
8）核融合科学研究所
9）米国、ＳＴＡフェローテキサス大学
10）米国、ＪＡＥＲＩフェローテキサス大学
11）オランダ、ＳＴＡフェロー
12）ロシア、トリニティ研究所
13）筑波大学
14）ロシア、クルチャトフ原子力研究所
15）九州大学
16）ロシア、ヨッフェ研究所
17）米国、ゼネラル・アトミクス社
18）イギリス、共同欧州トカマク
19）米国、テキサス大学
20）ドイツ、マックスプランク・プラズマ物理研究所
21）米国、サンディア国立研究所
22）カナダ、サスカチュワン大学
23）ドイツ、ユーリッヒ研究機構
24）フランス、エオール・ナシオナーレ・スペリオール・デ・ジニ・インダストリアル

Contents

目　　次

1. Overview of the Experiments in 1996

1. 1 Plasma Control

(1) Negative-ion-based neutral beam

A negative-ion-based neutral beam (N-NB) was successfully injected into plasmas at March 1996 for the first time. The initial injection power was about 100 kW with the energy of 200 keV and the D- beam current of 3.2 A. The pulse duration of the beam reached 0.47 s. The neutron yield was slightly increased in response to the NNB injection. The NNB injected ions were measured with the tangentially viewing charge-exchange neutral particle analyzer, which was developed under the collaboration between the Ioffe Institute in Russia and JAERI. The decay time of neutron emission produced by the NNB injection is consistent with that evaluated from the classical slowing-down time, suggesting the NNB injected ions could be confined well as expected.

After the first injection, beam conditioning of the N-NB has been continued to increase the beam power and acceleration voltage. Using Cs in the two ion sources, the total neutral beam power was increased up to 2 MW at a beam acceleration voltage of 350 keV. The beam pulse duration was up to 0.7 s and the re-ionization losses were lower than 10%. Beam profile inside the N-NB beam line was estimated from the D-alpha emission profile. The thermal image on the target first wall was measured by IRTV. The beam dissipation angle was ~ 10 mrad, which is two times as large as the design value. Preliminary, data of density dependence of the shine-through of N-NB was obtained with 350 kV beam energy. The shine-through fractions were ~25% at n_e-line (line averaged electron density) ~0.5×10^{19} m^{-3} and ~5% at ne-line ~3×10^{19} m^{-3}.

(2) Plasma operation

Boronization by a glow discharge was carried out at June. Decaborane ($B_{10}H_{14}$) of 75 g was consumed by the glow discharge. Mixed gas of helium (60%) and deuterium (40%) was used as working gas of the glow discharge. Deuterium gas was used to reduce hydrogen-deuterium dilution in NB heated discharges after the boronization. As a result, the hydrogen/deuterium ratio was rapidly reduced less than 0.1 after one day NB heated operation. Oxygen concentration was decreased to below 0.02% and 1-1.5% during OH and NB phases, respectively.

Vertical position (Z_j) control has been demonstrated to avoid VDE during I_p-quench phase. The coefficients of the statistical method using real-time calculation of plasma position were modified based on both steady state and I_p-quench databases to improve the accuracy of Z_j calculation during I_p-quench. After the modification, the Z_j was successfully controlled and VDE was avoided during I_p-quench at density limit disruptions. No halo current was observed as a result of VDE avoidance. The operation regime was extended toward a ITER-like low-q regime. The Z_j was successfully controlled and VDE was avoided during I_p-quench at q_{95}~2.9

(I_p=1.7 MA, density limit disruption), too.

Control of Runaway Electrons (REs) have been investigated for killer pellet shut down scenario. A neon-ice pellet with 4mm diameter x 4mm length was injected with a velocity of 600~950 m/s. The REs tails were usually generated at the killer pellet injection. Burst-like MHD activities produced by DCW (Disruption Control Winding), where the DCW mainly produced 3/2 and 2/1 modes during the current quench, were effective to suppress the generation of REs. The amplitude of the error field by DCW more than 0.12-0.14% of toroidal field at the plasma center was necessary to suppress REs.

The properties of plasma position control have been investigated. The difference of ADCs bit error between for ZENKEI and PF-coil power supplies was reduced by using common data. The voltage control was used instead of current control to reduce the fluctuation of PF-coil power supply voltage. As a results, the fluctuation of plasma radial position was suppressed by a factor of 8~10.

The deuterium pellet (4 mm diameter x 4 mm length, injection speed = 1.2~1.6 km/s) was injected into reversed shear plasmas to produce an H-mode edge by increasing edge beam deposition power. While the edge density was increased from 1x1019m-3 to 3x1019m-3 by the pellet., the electron density and temperature inside ITB was not changed even after the pellet injection. After all, the n=1 modes became unstable just after the pellet injection and no H-mode was produced.

The formation of the internal transport barrier (ITB) in reversed shear discharges was investigated in optimizing the reversed shear discharges. The role of tangential neutral beams is found to be very important for the formation of internal transport barrier. Co- and counter-tangential beams into core region and a counter-tangential beam into edge region were necessary for the ITB formation with good reproducibility. This suggests that the toroidal rotation and the heating power deposition are the key aspects of the ITB formation.

1.2 High Performance

High performance experiments have been most highlighted in 1996 using high power neutral beam injection up to 40 MW. During the year, reversed shear discharges, high-β_p H-mode discharges, high triangularity discharges have made significant progress in performance improvement by increasing the plasma current with maximizing the utilization of profile and shape controls.

Plasma performance of the reversed shear plasmas has been progressively enhanced with the plasma current up to 2.8 MA. Discharge optimization was attempted in the high current region with tuning the beam injection, plasma density, current ramp-up rate, beam deposition profile and plasma configuration etc, where the pressure and current profile optimization was so important to achieve stable discharges with persistent internal transport barriers at the high current. The fusion performance has been significantly enhanced with the

plasma current. As a result of the high performance campaigns, equivalent conditions for break-even in thermonuclear fusion regime were achieved with the JT-60U record of stored energy, 10.9 MJ, in October; the calculated fusion amplification factor Q_{DT}^{eq} reached 1.05 in an assumed deuterium-tritium fuel.

High performance experiments in high-β_p H-mode regime have been conducted at high currents above 2.1MA under the maximum utilization of neural beam power up to 41 MW. High-current high-β_p H-mode discharges were established up to 2.7 MA in which the stored energy reached 9.4 MJ at 2.6 MA. The world record of fusion triple product has been renewed to be $n_D(0)\tau_E T_i(0)=1.5\times10^{21}$ m^{-3}•s•keV with the world record of ion temperature, 45 keV. A high performance high-β_p H-mode discharge was sustained for ~1.5 times energy confinement times at 2.5 MA with ELMy H-mode where high neutron rate of 4-5x10^{16} /s and large stored energy of 8-9 MJ were maintained. Systematic scan of plasma current up to 2.7 MA at a maximum toroidal field of 4.3 T have shown that the fusion performance can be maximized around q_{95}~3 in support of ITER.

In high triangularity discharges, enhanced performance on both confinement and stability has been successfully demonstrated at I_p=0.9-2 MA with high power NB injection up to 28 MW. The high triangularity plasma shaping for the high-β_p H-mode discharges were found to be so effective for improving the stability and confinement and sustaining the high performance conditions. The ITER-like ELMy discharges at I_p=1.8MA has been sustained in quasi-steady state by high triangularity operation (δ~0.3, q_{95} ~ 3.4) for 0.7 s two times longer than the energy confinement time with high fusion performance of Q_{DT}^{eq}=0.25-0.3 at the normalized beta of 2.7-2.9 and the H-factor of ~2.5. For ITER physics R&D, β-limit and non-dimensional transport experiments were also carried out with an ITER-like triangular configuration.

In terms of high energy particle physics, the following results were highlighted. The triton loss due to the toroidal field ripple have been systematically investigated for reversed field discharges. In the triton burn-up experiments, the enhanced loss of a half of MeV tritons dependent on the substantial ripple rate have been observed from the plasma with the reversed field configuration. In ICRF heating experiments with reversed shear plasmas, second harmonic ICRF minority heating into the deuterium discharges were found to be effective for bulk plasmas inside the transport barrier. TAE modes were also studied in detail for both normal and reversed shear discharges using ICRF heating.

1.3 Steady State

(1) Current drive study

Main objectives are to study NB heating and NBCD by the negative-ion based NBI (N-NBI), and to apply LHCD to control current profiles in reversed shear plasmas.

Current drive by N-NBI (350 keV, 2.5 MW) was examined by injecting N-NBI into

partially current-driven discharges by positive-ion based NB. During the N-NBI pulse, the surface loop voltage became negative, indicating a fully non-inductive current drive. The neutron emission increased by a factor of 2. The NB driven current of 0.28 MA was predicted by ACCOME code. It was found that the CD efficiency of ~0.8×10^{19} $m^{-2}A/W$ with 73% of the injected N-NB power (the shine through was 27%). These results indicates an effectiveness of N-NBI as a core heating and current drive method in reactor relevant plasma.

The N-NB power of 2.3 MW (350 keV) with the pulse length of 1.0 sec was injected into a OH discharge at the line averaged electron density of $\bar{n}_e=1.5\times10^{19}$ m^{-3}. The central electron temperature was increased from $T_e(0)$~1.4 keV before the N-NB injection to $T_e(0)$~2.2 keV and a peaked electron temperature profile was formed. The behavior of the injected ions was studied by analyzing the neutron signal. Both the neutron emission rate and the decay time agreed with the classical theory, indicating the classical behavior of the injected beam ions in the experimental parameter regiem ($\bar{n}_e=(0.5\text{-}2.8)\times10^{19}$ m^{-3}, E_B=200-300 keV).

Using hydrogen N-NBI with EB=350 keV, the shine-through power was measured with two thermo-couple arrays. The shine-through rate of the N-NBI decreased exponentially with increasing the electron density. The enhancement factor of the multi-step ionization cross section to the single-step one for the high energy neutral beam was evaluated about 0.8 at $\bar{n}_e=1.6\times10^{19}$ m^{-3}.

LHCD was applied to reversed shear plasmas. A reversed shear configuration could be sustained by LHCD for about 7.5 s. The area of better confinement could be changed in coincidence with the reversed shear control by LHCD. The formation of a reversed shear configuration by an LHW injection alone was successfully demonstrated. The strongly reversed shear with large area of shear reversal was formed by LHW alone, which was even stronger than one formed by a normal scenario (NBI heating at current ramp-up).

(2) Divertor study

Main objectives are to sustain radiative divertor and detached plasma, to measure SOL profiles for SOL database of ITER, to study helium transport and exhaust and to estimate the particle confinement time of deuterium and helium.

Radiative divertor plasmas were obtained in reversed shear discharges (I_p=1.8 MA and B_T=4 T) with high ion temperature by neon and D2 gas puffing. Radiation loss from the divertor increased by 20% of the input power (P_{NB}=10 MW) after the neon and deuterium gas puff. The central ion temperature of $T_i(0)$=10 keV was sustained during the gas puff. While the neutron emission rate decreased by 30%, the H-factor=1.8 was sustained until the collapse of the reversed shear discharge.

Radial profiles of electron density $n_{e,mid}$, electron temperature $T_{e,mid}$, and ion temperature $T_{i,mid}$ in the scrape-off layer (SOL) plasmas at the midplane were investigated under radiative and detached divertor conditions in L-mode discharges. The ratio of $T_{e,mid}/T_{i,mid}$ was about 3 over a wide range of the electron density in the main plasma. The measured value of

$T_{e,mid}/\ T_{i,mid}$ ~3 at the separatrix was consist with $T_{e,mid}/\ T_{i,mid} = (m_i/m_e)^{1/9}$~2.5, which is predicted by the SOL/divertor two-point model assuming cross-field heat conductivity and the power into the SOL. During the X-point MARFE, the decay lengths of $T_{e,mid}$, $n_{e,mid}$, and $T_{i,mid}$ increased substantially with a reduction in $T_{e,mid}$ and $T_{i,mid}$ at the plasma edge and the first SOL.

The SOL currents $J_{//}$ have been investigated in high density plasmas with the ion grad-B drift towards the divertor. Under the detached divertor condition, the direction of $J_{//}$ was reversed as compared with the attached case, accompanied by the reversal of the in-out asymmetry in Tediv. The direction of $J_{//}$ corresponded to the direction of the thermoelectric current.

Helium transport characteristics of reversed shear plasmas has been studied using a ^{4}He beam (central fueling) and a short pulse He gas puff (edge fueling). $n_e(r)$, $T_e(r)$ and $T_i(r)$ profiles inside the internal transport barrier (ITB) are peaked. He particle confinement is enhanced due to an ITB formation. The He transport in reversed shear plasmas was found to be characterized by a large inward velocity near the ITB. Helium accumulation was observed inside the ITB. However, the profile of He concentration in reversed shear plasma is almost flat because the shape of $n_e(r)$ profile is almost the same as the He density profile. When a partial collapse occurred, He particles inside the ITB was expelled at the same time of the disappearance of the ITB.

In-out asymmetry with He influx in the divertor has been controlled by changing of neutral beam (NB) power and plasma current (I_p). The effect of the ion grad-B drift direction and I_P and B_T (q_{eff}) dependence on He exhaust was investigated in ELMy H-mode and L-mode. The asymmetry with the He flux profiles do not depend on the ion grad-B drift direction. The asymmetry seems to be determined by β_P (including edge parameters: n_e, T_e, T_i et al.) and not be explicitly determined by NB power and I_p. Helium ash exhaust could be actively controlled in combination with the control of the asymmetry with He flux and He removal due to the Solid Target Boronization.

The value of the helium particle confinement time τ_{pHe} was estimated based on the measurements of He I emission combined with the computer simulation using the DEGAS code. It was found that the ratio of the wall source to the divertor source was evaluated to be about 0.5, and the helium ion source in the main plasma due to the wall source was larger than due to the divertor source. Based on the analyses, τ_{pHe} was estimated to be 0.12 s.

The profile of He I line has been observed to investigate the velocity distribution of the helium atoms in the divertor region. The temperature corresponding to the the width of the He I spectra is 1.3 eV and it is much higher than the surface temperature of the divertor tiles. Using the DEGAS code, the probability of penetration into the main plasma is estimated to be 0.1% and 2.7% for helium atoms with energy of 0.05 eV (the surface temperature of the divertor tiles) and 2 eV, respectively.

The present open divertor will be modified to the W-shaped pumped divertor in February - May, 1997, aiming to develop a new compact radiative divertor compatible with the good performance of the main plasma. The inclined target divertor with a dome was adopted because of its effectiveness in achieving dense and cold divertor plasmas, and baffling the back flow of neutral particles. The neutral particles will be exhausted through the inner gap between the divertor plates and the dome.

2. Reversed Shear Discharges

2.1 Achievement of High Fusion Performance in JT-60U Reversed Shear Discharges [1]

S. Ishida and many co-authors

Fusion performance of reversed shear discharges with an L-mode edge has been significantly improved in a thermonuclear dominant regime up to 2.8 MA of plasma current in JT-60U. The core plasma energy is efficiently confined due to the existence of persistent internal transport barriers formed for both ions and electrons at a large minor radius of r/a~0.7 near the boundary of the reversed shear region. In an assumed deuterium-tritium fuel, the peak fusion amplification factor defined for transient conditions involving the dW/dt term is calculated to be 1.05.

Plasmas which could have been produced in an assumed D-T fuel are simulated by using the TOPICS code and TRANSP code simply considering the full D beams with the experimental beam energy into a 50:50 D-T mixture of plasmas. Good agreements are obtained with confidence among these analyses for both D-D analysis and D-T simulation. The projected fusion power is equivalent to 10.7 MW with 83% from thermonuclear reactions. A simple ratio of the fusion power to the actual beam absorption power, P_{DT}/P_{abs} would be 0.68. For the transient plasmas as discussed here, the fusion amplification factor can be defined to the loss power from the plasmas subtracting the dW/dt term instead of the beam power only. Following this definition, the equivalent fusion amplification factor Q_{DT}^{eq} would reach 1.05 with a high fusion triple product of $n_D(0)\tau_E T_i(0)=7.8\times10^{20}$ m^{-3}•s•keV. The remarkable progress in fusion performance can be attributed to stable increase in plasma current maintaining a vast reversed shear region up to r/a~0.7-0.8 and controlling the beam deposition profile during the current ramp-up. The high performance discharges are repeatedly produced under the reliably injected beams, in which the defined Q_{DT}^{eq} value reached 1.05 for the two shots at ~2.8 MA.

In conclusion, the fusion performance has been so improved for reversed shear discharges with an L-mode edge in a thermonuclear fusion regime that the fusion amplification factor Q_{DT}^{eq} is in excess of unity; this represents the achievement of equivalent plasma conditions for break-even under the present definition of Q_{DT}. While stability and plasma purity are presently concerned for the reversed shear discharges, pressure profile broadening with an H-mode edge and/or effective plasma shaping with a high triangularity would improve the stability and the closed divertor to be installed in JT-60U would suppress the plasma dilution.

Reference:

[1] S. Ishida, T. Fujita et al., submitted to Phys. Rev. Lett.

2.2 High Performance Reversed Shear Plasmas with Large Radius Transport Barrier in JT-60U [1)]

T. Fujita, T. Hatae, T. Oikawa, S. Takeji, H. Shirai, S. Ide, Y. Koide, Y. Kawano, R. Yoshino, O. Naito, Y. Kamada, Y. Neyatani, S. Ishida and the JT-60 Team

The operation of reversed shear plasmas in JT-60U has been extended to low q, high I_p region, where high fusion performance has been obtained. The record values of DT-equivalent power gain in JT-60U have been achieved with dominant thermal fusion; $Q_{DT}^{eq} = 1.05$, $\tau_E = 0.97$ s, $n_D(0) = 4.9 \times 10^{19}$ m^{-3} and $T_i(0) = 16.5$ keV. Large confinement improvement resulted from the formation of internal transport barrier (ITB) with a large radius, which was characterized by steep gradients in electron density, electron temperature and ion temperature just inside the position of q_{min}.

To obtain high performance plasmas, it is essential to form q profiles with large radius of q_{min} (up to 80% of plasma minor radius) in low q regime ($q_{min} \sim 2$). This was accomplished by plasma current ramp-up with the persistent ITB while controlling pressure and current profiles to avoid collapses with low beta. The large bootstrap current and high electron temperature due to the formation of ITB enhanced the negative shear. Without the ITB, the negative shear weakened during the ramp-up and the discharge suffered from collapses which resulted in shrink of negative shear region. The ITB was formed by on-axis beam heating into a low density target plasma with reversed shear that was formed by current ramp-up without beam heating. The toroidal rotation shear near the axis, which originated from tangential beam injection, was also important for the formation of ITB in addition to the on-axis heating. The foot (outer edge) of ITB was formed at 0.45a at first and moved outward up to 0.8a while the position of q_{min} also moved outward from 0.65a to 0.8a. The foot of ITB was located where $-1<s<0$ (s is the magnetic shear).

Large confinement improvement was obtained at $q_{min} < 2.4$. The energy confinement times were mainly determined by q_{min} and the radius of ITB. High H factors up to 3.3 were obtained with an L mode edge. The effective one-fluid thermal diffusivity (χ_{eff}) in the ITB was less than the neoclassical ion thermal diffusivity and decreased with q_{min}. Though χ_{eff} had its minimum in the region with the largest negative shear, the causality of transport and shear has not been confirmed since the large pressure gradient caused by the transport reduction generates large bootstrap current that enhances the negative shear. The values of H/q_{95} and β_t increased with the decrease of q_{95} and the highest performance was achieved at $q_{95} = 3$ (2.8 MA). The performance was limited by disruptive beta collapses with $\beta_N = 1.8 - 2$ at $q_{min} = 1.8 - 2$.

1) Fujita T. et al., to be submitted to Nucl. Fusion.

2.3 Enhanced Core Confinement in JT-60U Reversed Shear Discharges [1)]

T. Fujita, S. Ide, H. Kimura, Y. Koide, T. Oikawa, S. Takeji, H. Shirai,
T. Ozeki, Y. Kamada, S. Ishida and the JT-60 Team

A new type of internal transport barrier (ITB) was observed in the negative magnetic shear region in JT-60U. It accompanies clear internal pedestals for n_e, T_e and T_i and reduction of electron and ion energy transport ; χ_e^{eff} sharply drops by a factor of 20 within 5 cm while χ_i^{eff} is less than the neoclassical value [2)]. The internal T_e pedestal and clear reduction of χ_e^{eff} are distinctive features that were not seen in TFTR or DIII-D reversed shear discharges or in the JT-60U high β_p mode.

High performance reversed shear experiments were carried out at high current regime with B_T = 4.3 T. The formation of ITB at the initial stage of NB injection was effective to suppress MHD instabilities during I_p ramp. The flat profile is formed in spite of centrally peaked power deposition. When q_{min} became 3, MHD fluctuations with low toroidal mode numbers and an inward movement or shrink of ITB were observed. After q_{min} passed 3, the position of ITB moved outward again and the outer edge of ITB extended to 70% of the plasma minor radius. The stored energy, neutron production rate and the central electron density continued to increase and the discharge terminated into a β collapse when q_{min} reached 2.0.

Both of τ_E and W_{dia} increased with plasma current. At 2.4 MA, highest τ_E (1.08 s) and W_{dia} (9.56 MJ) were obtained in separate shots. Both of these are record values of JT-60U. High confinement was obtained with high density; the confinement was determined by mainly density and the I_p dependence on τ_E was small for the fixed density. High performance was obtained with lower beam power and with lower $T_i(0)/T_e(0)$ than in high β_p H mode plasmas. The H factor increase with ρ_{ITB} (the radial position of ITB): the highest ρ_{ITB} was 0.68 where the H factors of 3.4 were obtained.

Very high fusion performance has been achieved in reversed shear discharges with thermonuclear dominant regime. We could succeed in renewing the Q_{DT}^{eq} record in JT-60U [3)] substantially. The plasma parameters for one of the best shots are I_p = 2.47 MA, q_{95} = 3.46, P_{NB} = 12.2 MW, $n_D(0) = 4.5\times10^{19} m^{-3}$, $T_i(0)$ = 15 keV, τ_E = 1.01s and Q_{DT}^{eq} = 0.82. The thermal-thermal reactions account for 82% of the total neutron emission of 3.0×10^{16} n/s. These results prove that the reversed shear configuration is very promising for improved performance of tokamaks.

1) Fujita T. et al., to appear in Plasma Phys. Contrl. Nucl. Fusion Research (Proc. 16th IAEA Fusion Energy Conf., Montréal, 1996), paper A1-4.
2) Fujita T. et al., Phys. Rev. Lett. **78,** 2377 (1997).
3) Nishitani T. et al., Nucl. Fusion **34,** 1069 (1994).

2.4 MHD Activity in Reversed Shear Plasmas in JT-60U

S. Takeji, T. Fujita, T. Ozeki, S. Ishii, Y. Kamada, G.J. Kramer, Y. Neyatani, S. Ishida,
T. Oikawa, S. Ide, R. Yoshino, and The JT-60 Team

1. Introduction

A tokamak operation with a configuration of reversed magnetic shear in the central region is attractive for a steady state tokamak reactor since the reversed shear configuration is consistent with a steady state with a high bootstrap current fraction. Advantages of stability, confinement, and transport in reversed shear plasmas have been revealed in several tokamak devices. The highest fusion performance in JT-60U was recorded in a reversed shear plasma [1]. Reversed shear discharges are, however, disruptive and the steady state sustainment with the improved performance is not yet achieved in JT-60U. Well-understanding of MHD activity in reversed shear plasmas is indispensable to achieve the much improved fusion performance and the steady state. In this experimental review, MHD behavior in reversed shear plasmas in JT-60U is reported.

2. Overview of MHD Activity

A time evolution of plasma parameters in a high performance reversed shear discharge is shown with a contour map of magnetic fluctuations on the frequency-time plane in Fig.1. Details of the operation scenario to the improved performance is described in Ref.[2]. The internal transport barrier was formed at about 0.6 s after neutral beam (NB) injection. Reversed shear plasmas with $B_T > 4$ T (B_T: toroidal magnetic field) didn't have the H-mode transition.

We observed minor collapses which released energy from the inner region of the internal transport barrier to the outer one when q_{min} crossed integer values and the steep pressure gradient was generated near $\rho(q_{min})$. Here, q_{min} is the minimum safety factor and $\rho(q_{min})$ is the normalized plasma minor radius, ρ, at q_{min}. Reversed shear discharges seemed to be often terminated with a disruption in such situation. In the case of the discharge shown in Fig.1, minor collapses occurred at $t \approx 4.9$ s with $q_{min} \approx 4$ and at $t \approx 5.9$ s with $q_{min} \approx 3$. We could avoid the disruption which might follow the minor collapses by a skilled operation such that decreasing in the plasma pressure and increasing in the plasma internal inductance when q_{min} reached to four and three [2].

After the active MHD phase at $t \approx 4.9$ s and $t \approx 5.9$ s, the stored energy, W_{dia}, and the electron density, n_e, in the central region began to increase again and the performance was improved significantly. Higher frequency magnetic fluctuations ($f \gtrsim 17$ kHz) with low toroidal mode number, n, (n = 1,2, and 3) appeared in the improved performance phase after $t \approx 5.9$ s. These fluctuations are resistive modes since their growth times were longer than 1 ms ($\gtrsim 10^4 \tau_A$, τ_A is Alfvén transit time). The high performance reversed shear discharge was terminated by a disruption at $q_{min} \approx 2$.

MHD fluctuations at the frequency $f \approx 6$ kHz were often observed with the toroidal mode number $n = 1$ throughout the discharge. The mode frequency was close to the plasma toroidal rotation frequency at $\rho \approx 0.4$ or near the plasma surface.

3. Characteristics of Resistive Modes

Resistive modes observed in reversed shear plasmas in JT-60U can be classified by their localization in minor radius. One is that localized near $\rho(\nabla p^{ITB})$, ones are that localized at distinctly inside and outside of $\rho(\nabla p^{ITB})$, and the other is that near the plasma surface. Here, $\rho(\nabla p^{ITB})$ is ρ at the steep pressure gradient generated owing to the internal transport barrier. It is usual that $\rho(\nabla p^{ITB}) \lesssim \rho(q_{min})$.

Resistive modes localized near $\rho(\nabla p^{ITB})$ were observed when ∇p^{ITB} and β was large enough and q_{min} was between integer values. In the case of the discharge shown in Fig.1, $m/n = 3/1$ mode appeared near $\rho(\nabla p^{ITB})$ when q_{min} decreased below three. After the appearance of 3/1 mode, 5/2 and 7/3 modes appeared in association with the evolution of q_{min}. The different n modes appeared at the different frequency like that $n = 1$ with $f \approx 20$ kHz, $n = 2$ with $f \approx 40$ kHz, and $n = 3$ with $f \approx 60$ kHz. These mode frequencys can be attributed to the plasma toroidal rotation near $\rho(\nabla p^{ITB})$.

Figure 2 shows radial profiles of electron temperature, T_e, fluctuations of T_e, $\tilde{T}_e/T_e$, and q profiles when resistive modes of $f \gtrsim 17$ kHz were observed. The T_e fluctuations are localized near $\rho(\nabla p^{ITB})$. The T_e fluctuation profiles denoted with open circles and closed squares have large amplitudes at the outer region of the steep ∇T_e. On the other hand, the fluctuation profile denoted with closed circles has large amplitudes at both inside and outside of the steep ∇T_e. An in-out asymmetry was observed in the amplitude of the former fluctuations and no clear in-out asymmetry was observed in the latter fluctuations. Plausible candidates for the resistive modes in reversed shear plasmas are resistive interchange modes [3], neoclassical tearing modes [4], and double tearing modes. We can probably say that the latter is $m/n = 3/1$ double tearing modes since the MHD fluctuations were observed near two $q = 3$ surfaces across $\rho(q_{min})$ at the same time without the in-out asymmetry. Detailed measurements of radial profiles of MHD fluctuations and q profiles are crucially important for identification of these resistive modes.

4. Hard Collapse for Termination

Most reversed shear discharges with L-mode edge were terminated with a hard collapse which resulted in the disruption. The occurring region of the hard collapse is shown in comparison with that of the β_p-collapse in the high-β_p mode in Fig.3. Here, $\beta_N = \beta_t(a[\mathrm{m}]B_T[\mathrm{T}]/I_p[\mathrm{MA}])$ is normalized beta, β_t is toroidal beta, a is plasma minor radius, and I_p is plasma current. The upper limit of the achieved β_N in the reversed shear discharges lies in the same region with that in the high-β_p mode. On the other hand, hard collapses in the reversed shear discharges often occurred even in the quite lower β_N region. The hard collapses in the low β_N region sometimes occurred at $q_{min} \approx 4$ or $q_{min} \approx 3$ with the growth time of the ideal MHD instabilities.

Some of the low β_N collapses seemed to be associated with surface modes such as external kink modes since the low β_N collapses sometimes occurred when the NB injection power was reduced by some reasons and the surface q was close to integer values. We also observed a growth of the rotating mode near the plasma surface and the mode locking for the hard collapses. Since most low β_N collapses occurred in the region where the low ℓ_i disruptions have been observed in JT-60U [5], the study of locked modes seems to be a key issue for the stable operation of the reversed shear discharges to the improved performance.

The hard collapses in the high performance reversed shear plasmas had different MHD feature from that in the low β_N plasmas. Figure 4 shows waveforms of T_e and magnetic fluctuations right before the collapse in the highest fusion performance discharge in JT-60U shown in Fig.1. The β_N reaches to 1.9 with q_{eff} of 4.3 at the highest fusion performance phase. The amplitude of the T_e fluctuations increased with the growth time longer than 1.5 ms, which is the growth time of resistive MHD instabilities. The frequency of the T_e fluctuations decreased from $\approx$ 17 kHz to $\approx$ 13 kHz right before the collapse. The T_e fluctuations had a higher frequency component ($f \approx 60$ kHz) at the same time with smaller amplitude. The mode analysis of the magnetic fluctuations showed that the MHD fluctuations were $n = 1$ at $f \approx 15$ kHz and $n = 3$ at $f \approx 60$ kHz. Both of the $n = 1$ and $n = 3$ modes were localized near $\rho(q_{min})$ and seemed to have the in-out asymmetry in the T_e fluctuations. The hard collapse followed these resistive modes with the growth time of several 10 μs, which is the growth time of ideal MHD instabilities. Ideal MHD stability analysis showed that the experimental β-limit ($\beta_N \approx 1.9$ at $q_{min} \approx 2$) is close to the theoretical one of the ideal low n ($n = 1$) kink modes [6].

5. Summary

Various MHD fluctuations were observed in JT-60U tokamak plasmas with reversed central magnetic shear configurations. Resistive modes without in-out asymmetry in the fluctuations seem to be double tearing modes. Resistive modes localized near $\rho(\nabla p^{ITB})$ with in-out asymmetry in the fluctuations are not yet identified.

The stability limit in a condition that a steep ∇p is generated near $\rho(q_{min})$ and q_{min} just crosses an integer value is important for the performance improvement and for the steady state since hard collapses seemed to occur in the situation. Study for locked modes is also important to establish a reliable operation scenario to the improved performance.

References

[1] S. Ishida et al., Sec.2.1 in this Review.

[2] T. Fujita et al., Sec.2.2 and 2.3 in this Review.

[3] M.S. Chu et al., Phys. Rev. Lett. **77** 2710 (1996).

[4] R. Carrera et al., Phys. Fluids. **29** 899 (1986).

[5] R. Yoshino et al, J. Plasma Fusion Res. **70** 1081 (1994).

[6] S. Ishii et al, Sec.2.5 in this Review.

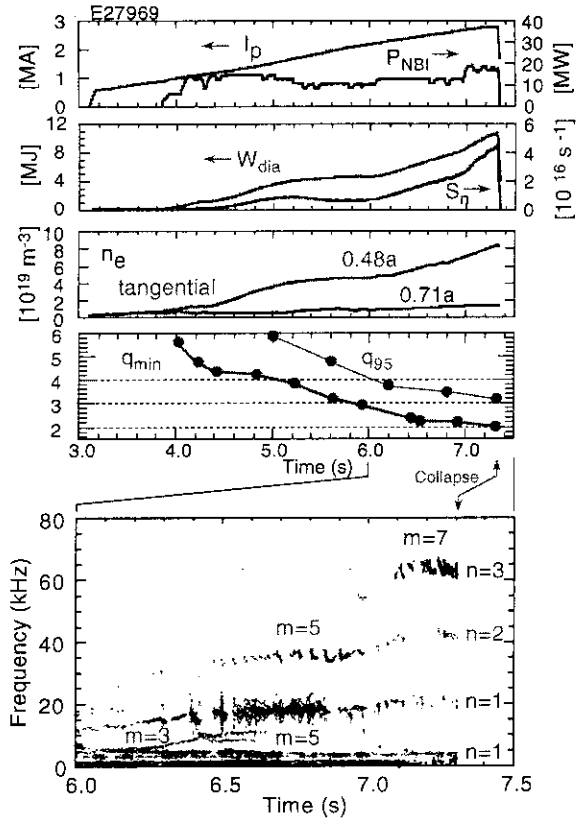

Fig.1: Evolution of a high performance reversed shear discharge (B_T = 4.2 T).

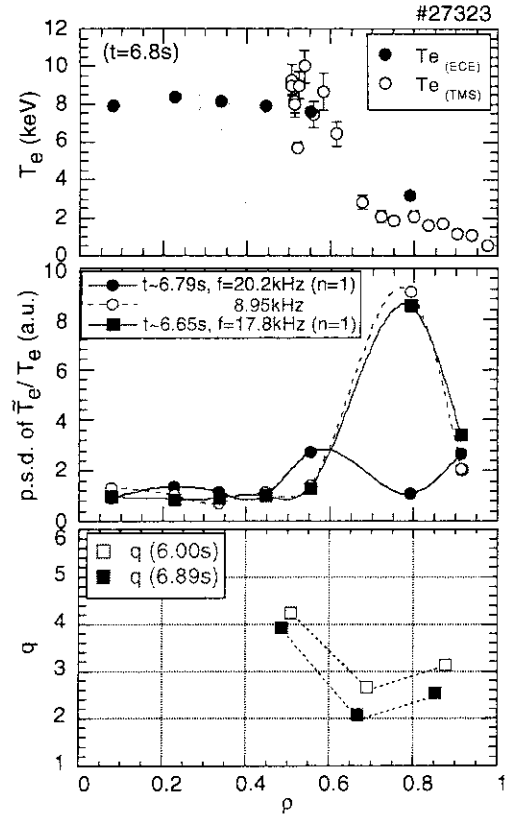

Fig.2: Radial profiles of T_e, power spectrum density (p.s.d.) of T_e fluctuations and safety factor q.

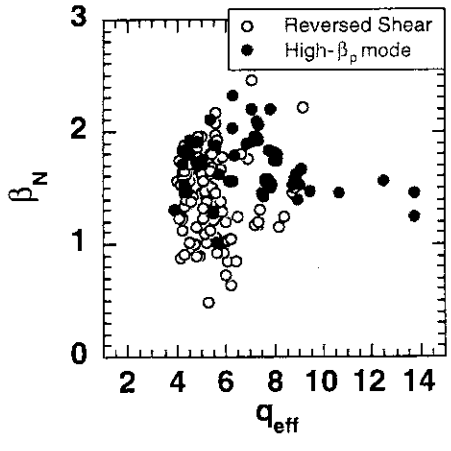

Fig.3: The β_N-q_{eff} region where the hard collapse occurs in the reversed shear discharges (open circles). The region of the β_p-collapse in the high-β_p mode is also shown (closed circles).

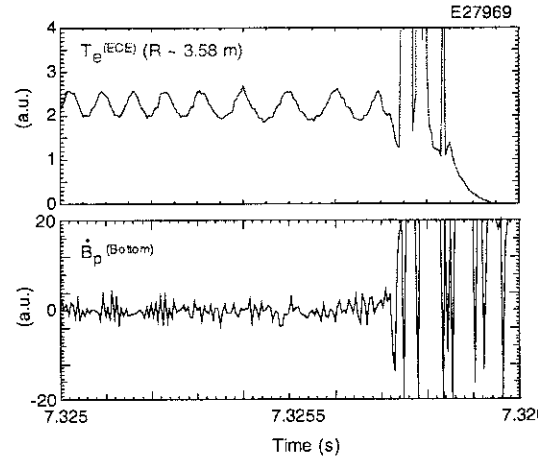

Fig.4: Waveforms of T_e and time derivative of poloidal magnetic field $\dot{B}_p$ at the collapse in the high performance reversed shear discharge shown in Fig.1.

2.5 Ideal MHD Stability in Negative Shear Plasma

Y.Ishii, T.Ozeki, S.Tokuda and S.Takeji

1. Introduction

Recently, the high performance plasmas have been obtained in the negative shear discharges in JT-60U[1]. In most of the negative shear discharges, the β_p collapse occurs and limits the β -value. Though the mechanism of the β_p collapse is not clear, MHD activities with the fast growth rate of about $100\mu s$ are observed in JT-60U experiments[2]. Therefore, it is important to clarify the feature of the ideal MHD stability and to achieve higher plasma performance. In this paper, effects of the safety factor profile, the triangularity and the conducting wall on the ideal MHD stability limit of negative shear plasma are investigated.

2. Ideal MHD Stability Limit

To analyze ideal MHD instabilities in negative shear plasmas, we use MEUDAS code and ERATOJ code[3]. Profiles of pressure and safety factor are shown in Fig. 1. These profiles are modified experimental data of JT-60U. The pressure profile is characterized that the steep pressure gradient locates just inside the radial position of q_{min}. To get the stability limit against the low n mode, the σ-scaling method[3] is used for the parameter scanning. If we scale $\psi \rightarrow \sigma\psi$ and $P \rightarrow \sigma P$, q scales approximately as q/σ, and β_p remains fixed. Figure 2 shows the stability limit against β_N and $q_{\min}$. Here, β_N is normalized beta, $\beta_N = \frac{aB_{T0}}{I_p}\beta_t$ (a : minor radius, B_{T0}: vacuum toroidal magnetic field at plasma center, I_p: plasma current, β_t : toroidal beta). A solid line shows the stability limit of n=1 mode(n is the toroidal mode number). An area above the solid line is unstable for the n=1 ideal MHD mode. A feature of the stability limit is that when $q_{\min}$ is just below a rational surface, the stability limit becomes lower. The n=2 mode becomes more unstable than n=1 mode in the region of $q_{\min} \leq 1.5$. The higher-n modes(n=3, 4, ...) also may appear in the region of $q_{\min} \leq 1.5$[4]. Therefore, the infernal mode may not appear in the region of $q_{\min} > 1.5$.

Figure 3 shows the radial mode structures of the n=1 mode at the point A in Fig. 2. In Fig. 3, the m=2 mode located around $q_{\min} \cong 1.8$ is the dominant mode. The radial mode structure shows that the main mode(m=2) becomes zero at the plasma boundary, but the higher modes($m \geq 3$) have finite values at the plasma boundary. Figure 4 shows the radial profile of the potential energy of the mode at the point A in Fig. 2. The following expression of the potential energy is used,

$$W_p = \frac{1}{2}\int\left[\frac{1}{\mu_0}\vec{Q}_\perp^2 + \frac{1}{\mu_0}\left(\vec{Q}_\parallel - \mu_0\frac{\vec{\xi}\cdot\nabla p}{B^2}\vec{B}\right)^2 + \Gamma p\left|\nabla\cdot\vec{\xi}\right|^2 - \frac{\vec{j}\cdot\vec{B}}{B^2}\vec{Q}\cdot\left(\vec{\xi}\times\vec{B}\right) - 2\left(\vec{\xi}\cdot\nabla p\right)\vec{\xi}\cdot\vec{\kappa}\right]d\tau .$$

The first three terms are stabilizing terms. The fourth term is the current driven term and the fifth term is the pressure driven term. The potential energy is negative(driving the instability)

in the region of $0.38 \le r \le 0.68$, and positive in the plasma edge region of $0.68 \le r$. In Fig. 4, it is seen that the instability is mainly induced by the current driven term.

For such a low-n mode, which determines the ideal stability limit in negative shear plasma, the effects of the triangularity, δ, and the conducting wall are investigated. The conducting wall effect is shown in Fig. 5. In this calculation, the conducting wall is set the value of REXT fixed at any poloidal angle. Here, the parameter REXT is defined as $REXT \equiv r_b / r_a$, where r_b is the minor radius of the conducting wall and r_a is the plasma minor radius. There is no difference between the β-limit of REXT=1.5 and that of REXT=∞. However, the conducting wall effect on β-limit becomes clear for REXT$\le$1.4. At $q_{min} = 2$, the critical β_N increases up to 3.1, when REXT is 1.3. It is clear that the conducting wall has a strong stabilizing effect on the ideal β-limit. Then, Fig. 6 shows the β-limits for three cases of δ(0.03,0.38,0.59). In this calculation, we fixed the ellipticity, κ, and REXT=∞. In these three cases, there is almost no change of the β-limit.

The feature and stability limit of the ideal MHD stabilities in negative shear plasma depend on the relative relation of the P-profile and q-profile. In this paper, the q-profile effect on the stability limit is investigated. Figure 7 shows the effect of the q-profile inside the radius of q_{min}. As q_0 becomes lower(i.e. the q-profile inside q_{min} becomes flatter), the β -limit decreases. At $q_{min} = 2.2$, the critical β_N decreases from 2.8 to 2.2 by changing q_0 from 7.0 to 4.0. Figure 8 shows the effect of the q-profile outside the radius of q_{min}. The plasma current I_p is changed to change the q-profile outside q_{min}. As I_p becomes higher(i.e. the q-profile outside q_{min} becomes flat), the β-limit decreases. At $q_{min} = 2.2$, β_N decreases from 2.8 to 2.6 by changing q^* from 10.1 to 6.1. Here, $q^* = \left(5a^2B_t / 2RI_p\right)\left[1+\kappa^2\left(1+2\delta^2-1.2\delta^3\right)\right]$ is the safety factor at the plasma edge. Therefore, in both the inside and outside region of q_{min} , the stronger magnetic shear has higher β-limit.

3. Summary

The feature and stability limit of the low-n mode in the negative shear plasma were investigated. The triangularity, δ, has almost no effect on the β-limit at REXT=∞. The conducting wall has a strong stabilizing effect on the β-limit for REXT$\le$1.4. In real devices, the parameter REXT changes in poloidal direction depending on the plasma shape. The plasma shape is changed by not only triangularity, δ, but also the ellipticity, κ. Therefore, it may need to study the combination effects of wall distance and plasma shape, which includes the δ and κ effects, on the β-limit. About the q-profile effect on the β-limit, it was shown that the stronger magnetic shear has higher β-limit. However, in this paper, the pressure profile was fixed. It needs to investigate the pressure profile effect on the β-limit.

References

[1] S.Ishida et al. : section 2.1 in this review
[2] Y.Neyatani et al. : Plasma Phys. and Control. Fusion 38(1996)A181.
[3] T.Takeda et al. : J.Comp.Phys. vol.93(1991)1.
[4] M.W.Phillips et al. : Phys. Plasmas 3(1996)1673.

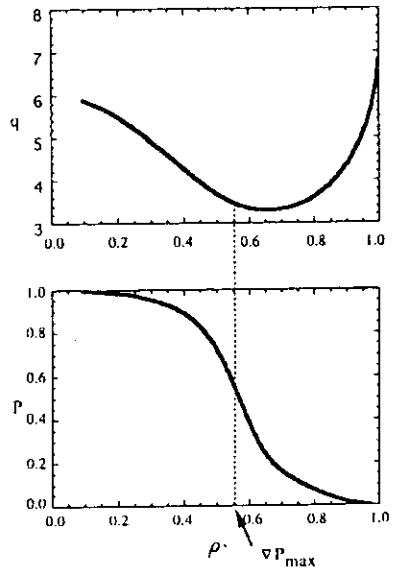

Fig.1 Radial profiles of P and q.

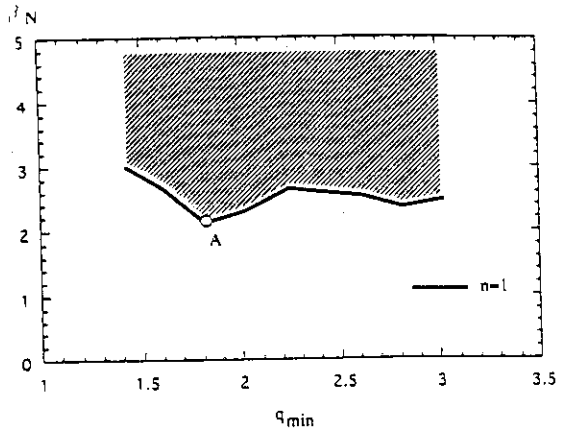

Fig.2 Ideal stability limit of n=1 mode.

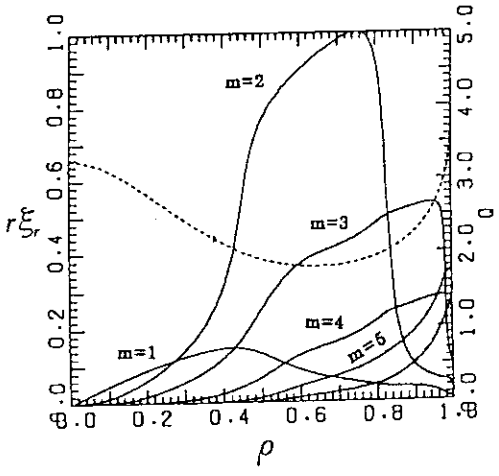

Fig.3 Radial mode structure at point A in Fig.2.

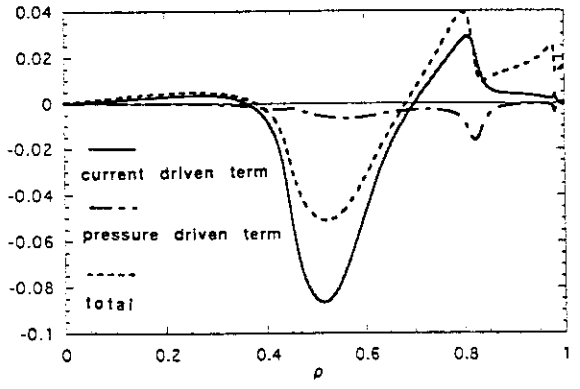

Fig.4 Radial profile of the potential energy at point A in Fig.2.

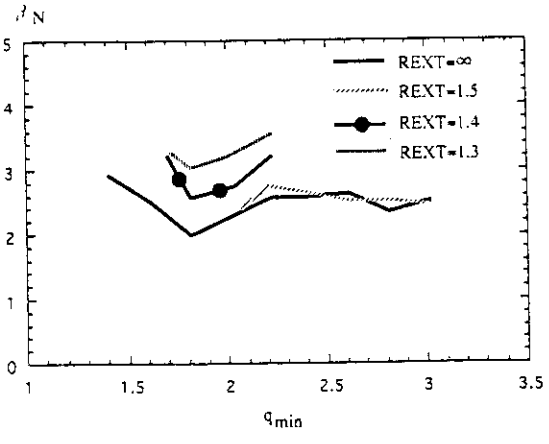

Fig.5 Conducting wall effect on the ideal β-limit.

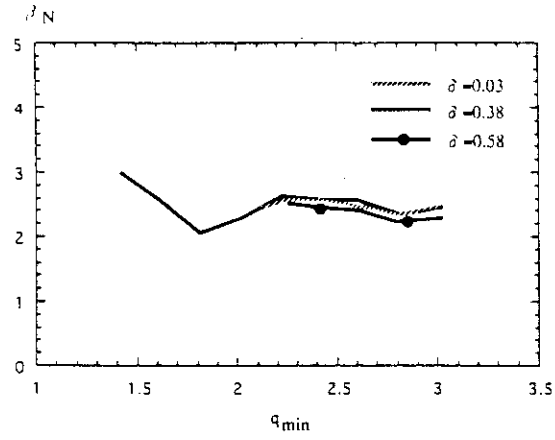

Fig.6 Triangularity effect on the ideal β-limit.

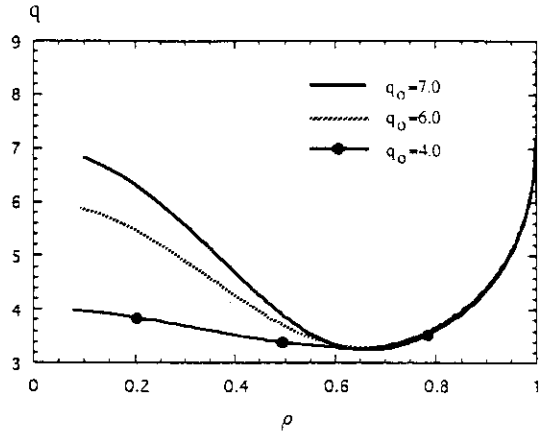

Fig.7(a) q-profiles changing the inside region of q_{min}.

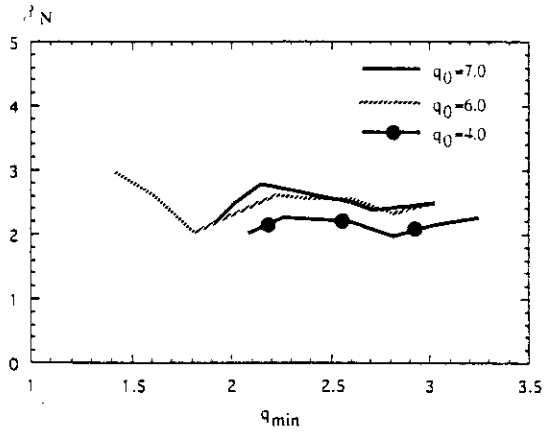

Fig.7(b) Effect of the q-profile inside the radius of q_{min} on the ideal β-limit.

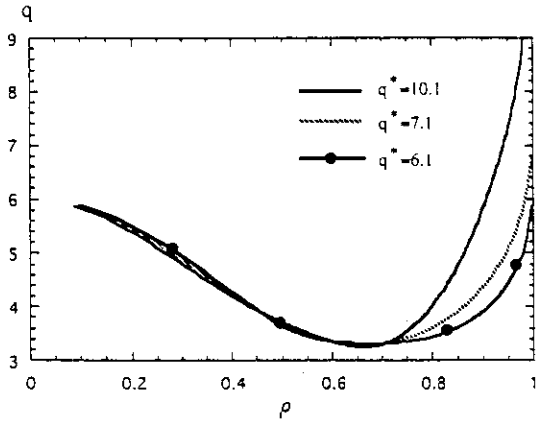

Fig.8(a) q-profiles changing the outside region of q_{min}.

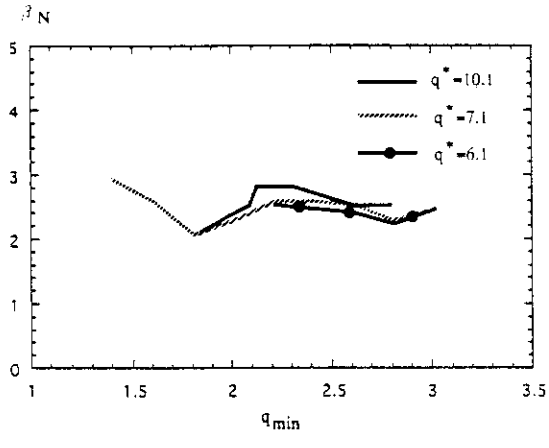

Fig.7(b) Effect of the q-profile outside the radius of q_{min} on the ideal β-limit.

2.6 Discontinuity formation in toroidal ITG mode structure under reversed magnetic shear configuration and consequence for internal transport barrier [1]

Y. Kishimoto, J. Y. Kim, T. Tajima, W. Horton, T. Fujita, T. Fukuda and S. Ishida

The turbulent structure of drift waves in a toroidal geometry is getting clearer due to recently developed toroidal siumulation and theory [1-2]. According to these studies, the drift modes in a toroidal geometry form a radially extended nonlocal structure whose correlation length Δr is given by $\Delta r \cong (\rho_i L)^{\alpha}$ with $\alpha \cong 0.5$, i.e. the geometrical mean between the ion Larmor radius ρ_i and the equilibrium scale length L (such as $L \cong a$: plasma minor radius or $L \cong L_T \equiv -\left(\partial \ln T_i / \partial r\right)^{-1}$: ion temperature scale length). Such a nonlocal mode shows a twisted thin eddy structure with up-down asymmetry characterized by a finite tilted poloidal angle θ_0 from the midplane (θ_0=0) [θ_0 is the Bloch shift parameter which represents the most unstable poloidal angle]. The basic characteristics in a typical L-mode such as (i) Bohm-like diffusion, (ii) radially increasing fluctuation and heat diffusivity, (iii) near marginal properties and (iv) profile resilience are considered to belong to one physical category which originates from the nonlocal modes. This understanding leads to a strategy that improved modes can be achieved by suppressing such a mode structure. In this paper, in order to obtain improved modes, we investigate the role of negative/weak magnetic shear and plasma shear rotation on these nonlocal modes using toroidal numerical simulation and also theory. Specifically, we present a model of the internal transport barrier (ITB) as formed in recent JT-60U reversed shear experiments [3] and perform toroidal particle simulation. Negative magnetic shear actually has a stabilizing effect on the toroidal drift mode, but not enough to form the ITB which is sharply localized in space. We found that the weak and/or zero magnetic shear breaks up the toroidal coupling and associated global mode staructure, leading to a *discontinuity* (or *gap*) in the mode excitation inside and outside the q-minimum (q_{min}) surface. Namely, the weak and/or zero magnetic shear plays a crucial role in forming the ITB.

It is also found that the discontinuity (or gap) efficiently works as a thermal barrier when the q-minimum surface locates just outside the maximum pressure gradient and this is consistent with the experimental result. A shear flow structure is found to enhance the character of the discontinuitywhen the flow shear is the same direction as the mode rotation as the case of the experiment [3] and significantly suppresses the mode activity in the gap region. Resultantly, a strong stabilization near the q_{min}-surface is achieved.

Reference

[1] Y. Kishimoto et. al., 16th IAEA Fusion Energy Conf., Montreal, IAEA-CN-64 / DP-10.

[2] Y.Kishimoto, et. al. Phys. Plasmas 3, (1996) 1289.

[3] T.Fujita et.al. 16th IAEA Fusion Energy Conf., Montreal, IAEA-CN-64 / A1-4.

2.7 Time Evolution of Internal Transport Barrier in JT-60U Reversed shear plasmas

T. Hatae, Y. Kamada, T. Fujita, S. Ishida, T. Oikawa,
Y. Kawano, Y. Koide, H. Shirai, H. Yoshida, A. Nagashima and JT-60 Team

1. Introduction

The high performance negative shear plasmas in JT-60U, in which the core plasma confinement is improved due to the formation of internal transport barrier, achieved break-even plasma condition [1]. These plasmas are characterized by the rapid change (formation of the internal transport barrier) in the profiles of both ion temperature, electron temperature and electron density [2][3]. This study is paid attention to the internal transport barrier, and done the following research; (1) time and spacial changing of the internal transport barrier for the time evolution of ion temperature profile, electron temperature profile, electron density profile etc. (2) correlation between the internal transport barrier and the safety factor profile, the toroidal rotation velocity profile for carbon.

2. Formation of Internal Transport Barrier

We used the diagnostics below to investigate the internal transport barrier. The time evolution of ion temperature profile $T_i(r)$ and the toroidal rotation velocity profile for carbon $V_t(r)$ are measured by the charge exchange recombination spectroscopy system (CXRS). The time evolution of electron temperature profile $T_e(r)$ and safety factor profile q(r) are measured by ECE Fourier spectrometer (ECE) and Motional Stark effect polarimeter (MSE), respectively. Profiles of electron temperature $T_e(r)$ and density $n_e(r)$ are measured by Ruby laser Thomson scattering system (Ruby Thomson) and newly installed YAG laser Thomson scattering system with time resolution of 100 ms (YAG Thomson). The measuring points of these diagnostics on the high performance negative shear plasma are shown in Fig.1.

A typical time evolution of ion temperature profile for the early phase of high performance negative shear plasma (E027302) is shown in Fig.2(a). The plasma current was initiated at t=3.0s and was ramped up to 2.47 MA in this discharge. The main heating of 12.2 MW by neutral beam was started at 4.1 s. In this figure, the ion temperature profile changes from the center peaked profile to the profile with steep gradient (internal transport barrier) at a certain radius. And the profile within the internal transport barrier becomes gradually flat. This is a profile evolution peculiar to the negative shear plasmas in JT-60U. The internal transport barrier is formed at r~0.4m from t=4.4s, then moves to r~0.6m. Meanwhile the temperature gradient becomes larger and larger. On the other hand, the ion temperature profile when the internal transport barrier was not formed under the similar condition (E027304) is shown in Fig.2(b). The ion temperature profile remains center peaked, and does not show a internal transport barrier.

Next we discuss time and spatial behaviors of internal transport barrier. The time evolution of temperature and density with a fixed location (r~0.49m) on Fig.2(a)(b) is shown in Fig.3. In the discharge with internal transport barrier (E027302), ion temperature, electron temperature and density increase at almost the same time within time and spatial resolutions of diagnostics in contrast with the similar discharge without internal transport barrier (E027304). Although the behavior for T_i, T_e is the same, the electron density increases behind increasing of T_i, T_e in the similar shot of E027302 with the internal transport barrier (E027306). Hence, time and spatial behavior of internal transport barrier for T_i, T_e is almost the same. For the electron density, it is possible that the internal transport barrier changes behind the changing for T_i, T_e.

3. Relationship between Internal Transport Barrier and Safety Factor Profile

Ion and electron temperature, electron density and safety factor profiles of two q_{min} position (r_{min}) cases are shown in Fig.4(a)(b). For a wide r_{min} case (E027302) with r_{min}~0.8 m, the steep gradient for temperature and density is located at r~0.6m as shown in Fig.4(a). For narrow r_{min} case (E026753) with r_{min}~0.65 m, the steep gradient is located at r~0.5m as shown in Fig.4(b). We can see from both cases that the internal transport barrier is formed within r_{min}. We define here two values of r_{ITB} and $r_{ITB\text{-}foot}$ for the internal transport barrier as shown in Fig.5. The location of internal transport barrier r_{ITB} is defined as the radial position of middle point between the maximum and minimum of the temperature profile pedestal. $r_{ITB\text{-}foot}$ is defined as the radius of lower bend of the pedestal. Time evolutions of r_{min}, r_{ITB} and $r_{ITB\text{-}foot}$ of the ion temperature profile are shown in Fig.6. The internal transport barrier is formed within r_{min}. That position moves outward, and then remains at the same position. r_{min} behaves similarly to r_{ITB}. Hence, it seems that there is a strong correlation between the position of q_{min} (r_{min}) and the position of internal transport barrier (r_{ITB}).

Fig.7 shows time evolutions of safety factor and toroidal rotation velocity V_t for carbon and ion temperature profile with and without an internal transport barrier. In the case with a transport barrier, a transport barrier is formed after 4.5 s, a negative dip is observed in the V_t profile as shown in Fig.7(a). And for the case with a transport barrier, negative shear becomes stronger and stronger. The position of negative dip corresponds to the position of internal transport barrier. After transport barrier formation, the direction of V_t inside the position of internal transport barrier changed from counter to co-direction. Fig 7(b) shows a case of no internal transport barrier. Although the negative shear formation is shown from the q profiles, there is no steep gradient on the T_i profiles and no negative dip on V_t profiles.

Reference

[1] Ishida S. et al., section 2.1 in this review

[2] Fujita T., Plasma Phys. Contrrol. Nucl. Fusion Research (Proc. 16th IAEA Fusion Energy Conf., Montrèal, 1996), paper A1-4

[3] Fujita T. et al., Phys. Rev. Lett. **78**, 2377 (1997)

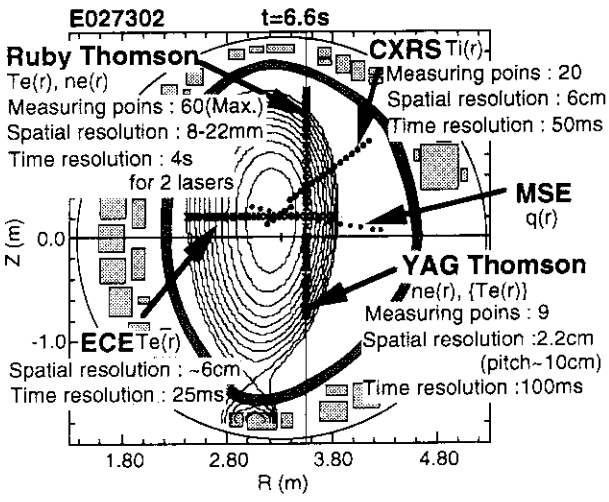

Fig.1 Diagnostics

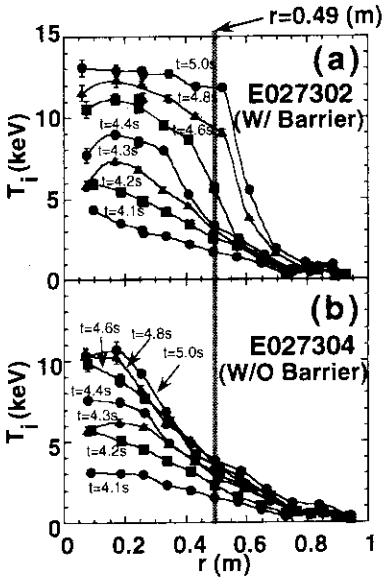

Fig.2 Time evolutions of ion temperature

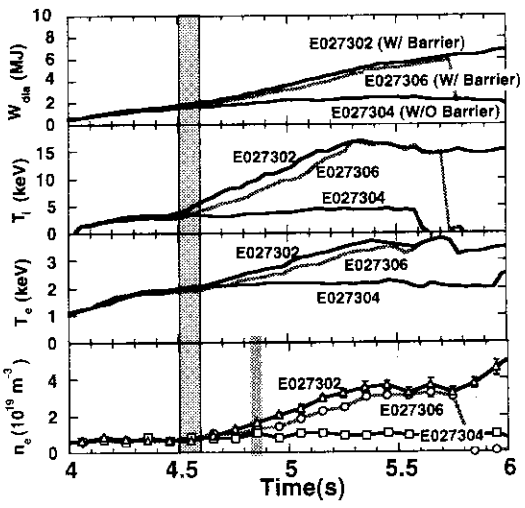

Fig.3 Time evolution at r~0.49m

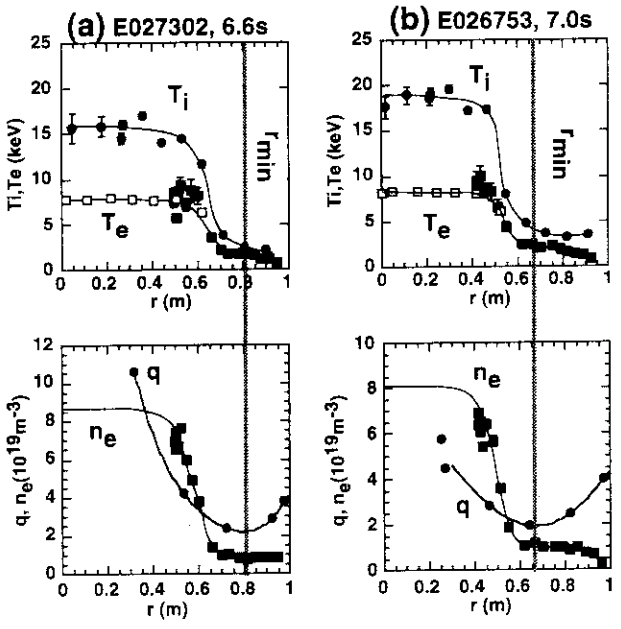

Fig.4 Location of q_{min} and internal transport barrier

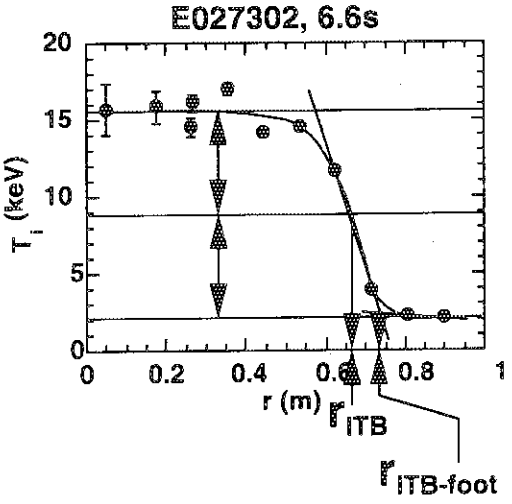

Fig.5 Definition of internal transport barrier position

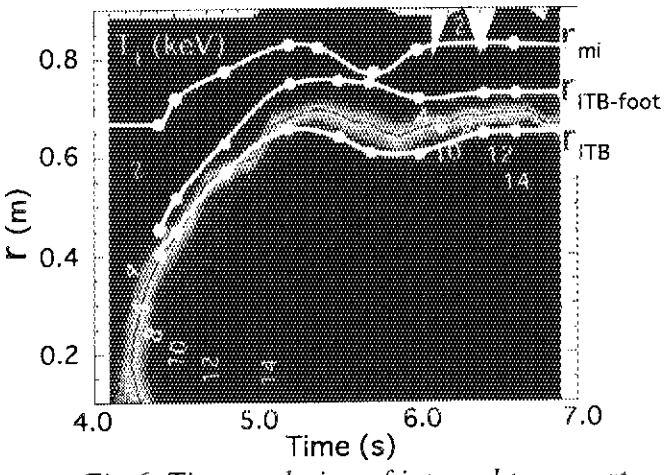

Fig.6 Time evolution of internal transport barrier position and r_{min}

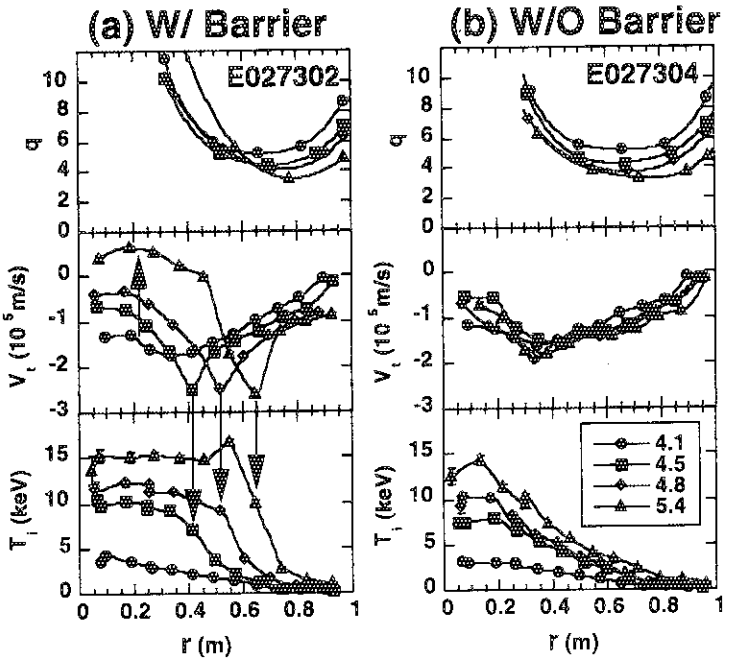

Fig.7 Correlation between q profile and toroidal rotation velocity for carbon

3. High-β_p H-mode and High Triangularity Discharges

3.1 High Performance Experiments in JT-60U High Current Divertor Discharges [1]

S. Ishida, Y. Neyatani., Y. Kamada, A. Isayama, T. Fujita, T. Oikawa, Y. Koide,
H. Shirai, T. Ozeki, T. Nishani, S. Takeji, H. Kimura, T. Hatae, T. Fukuda, N. Isei
and the JT-60 Team

Hot-ion H-mode and high-β_p H-mode regimes in JT-60U have been extended up to 4.5 MA with q_{95}=2.0 and 2.7 MA with q_{95}=2.5, respectively, with intense neutral beam injection power of up to 41 MW. The optimal safety factor was searched for improving the plasma performance in such high current low-q regimes, so that the maximum performance was found to be commonly attained around q_{95}~3 in support of ITER as shown in Fig.1. In the high-β_p H-mode regime performance parameters of H/q_{95} and β_N/q_{95} reached ~1.2 and ~0.75, respectively, in the low q region where the highest fusion triple products of $n_D(0)\tau_E T_i(0)$~$1.5\times10^{21}m^{-3}$•s•keV was achieved with a very high ion temperature $T_i(0)$=45 keV. The limitation for the hot-ion H-mode performance was due to a non-disruptive ELM event at a low Troyon factor during persistent m=1 modes with significant toroidal mode couplings. The high-β_p H-mode discharges have encountered disruptive β limits around q_{95}~3 in which the simultaneous growth of low-m internal modes was observed just prior to the disruption near the stability limit for ideal kink-ballooning modes. Successive ELM activity near the β limit induced an m=3/n=1 mode and turned into non-local collapses followed by the disruptions, which limited the sustainment of ELMy high-β_p H-mode discharges. The limitation features observed in the two high performance regimes are characterized by the difference in pressure profiles and the attainable stability.

Reference:

[1] S. Ishida, Y.Neyatani, Y. Kamada, A. Isayama, T. Fujita et al., in Plasma Physics and Controlled Nuclear Fusion Research 1996 (Proc. 16th Int. Conf. Montreal, Canada 1996), IAEA, paper IAEA-CN-64/A3-1.

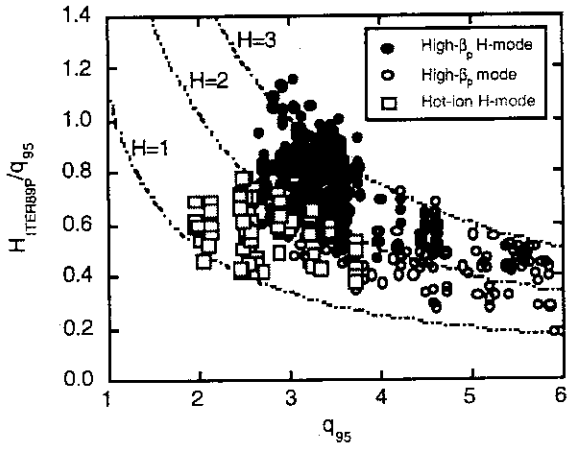

Fig.1 H/q_{95} as a function of q_{95} for high-β_p and hot-ion H-mode discharges along with contour lines in terms of the H-factor where H is against the ITER89-P scaling

3.2 Optimization of high-β_p H-mode confinement at high current with high power neutral beam injection

S. Ishida, Y. Kamada, S. Takeji and Y. Neyatani

1. Introduction

In JT-60U, high performance experiments for high-β_p H-mode discharges have been conducted in 1996 to demonstrate high reactivity plasmas and show reactor potentials in such a low-q regime by progressive extension of plasma current and heating power with improving plasma performance, and to address the subject of optimal safety factor for maximizing the fusion energy production at a maximum toroidal field strength of the tokamak [1]. The high current low-q regime is increasingly of importance to envisage whether the operation scenario in ITER towards self-ignition is workable at q_{95}~3.

2. Progress in optimization

The high-β_p H-mode discharges are configured to achieve a peaked beam deposition profile with a large A~4.3 and a low δ~0.05 [2,3]. The maximum plasma current in the high-β_p plasma configuration was limited by the divertor coil current restriction. It is essential for achieving the high-β_p H-mode confinement to create a sawtooth-free target plasma with a central q slightly above unity by injecting the main beams before the sawtooth onset, which would have produced a weak central magnetic shear configuration.

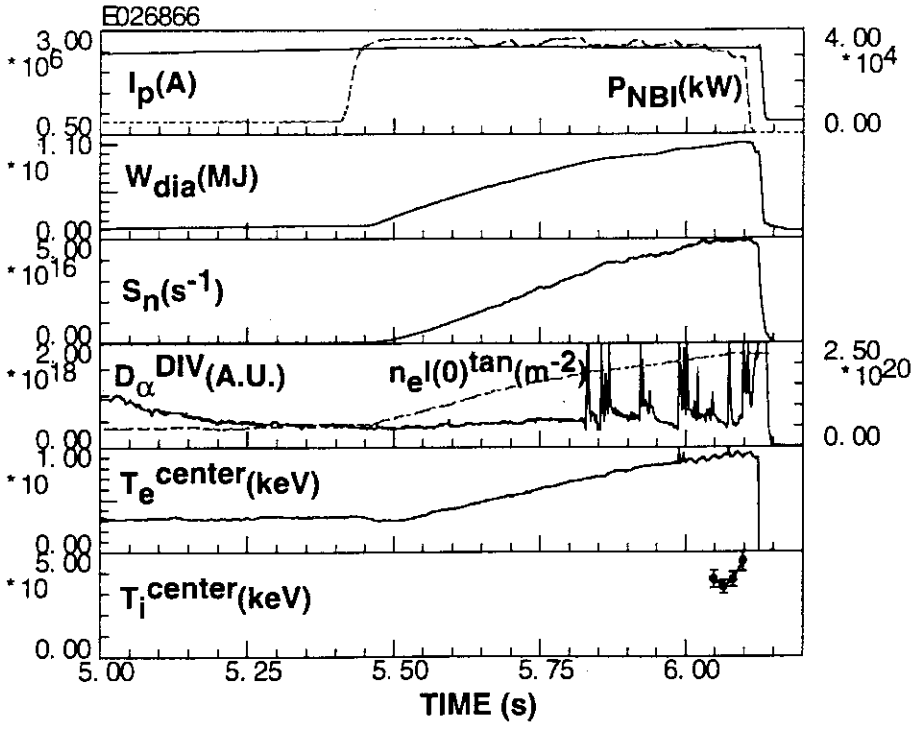

Fig.1 Discharge waveforms of a record shot to show the highest stored energy in high-β_p H-mode

In 1995, the modification of the neutral beam injection (NBI) system has been made for increasing the beam fueling rate by high current density beams as well as the injection power at the same acceleration voltage by means of narrowing the distance between extraction electrodes from 10 mm to 8 mm. In 1996, the high-β_p H-mode confinement has been successfully achieved at up to 2.7 MA with q_{95}=2.5 utilizing the intense NBI power up to 41 MW. The new technical advancements contributed to high-β_p H-mode experiments in 1996 are as follows: 1) fast current ramp-up operation allowing the main beams to be injected in the current flat top phase at high currents up to 2.7 MA. 2) intense beam power of up to 41 MW at 90-95 keV. Consequently, the high-β_p H-mode confinement has been achieved at up to I_p=2.7 MA with which W_{dia} reached 9.4 MJ at 2.6 MA as shown in Fig.1.

3. Optimal q for maximizing fusion performance

Comparison of the achieved stored energy and neutron emission rate among the high performance campaigns in '92-'94, 4-5 July '96 and 17-19 July '96 is shown in Fig.2. It is clearly shown that the confinement has been improved in the high current region above 2.2 MA. The neutron rate was not in excess of the level at 2.2 MA, but the stored energy was slightly improved up to 2.6 MA. At 2.7 MA, the discharge went to a soft landing sequence during the beam heating since the divertor coil current reached an operational limit. The diamagnetic β_N divided by the plasma inductance achieved in the '96 campaign is compared to the values in the '92-'94 campaigns against the cylindrical equivalent safety factor q* (mostly the same as the q_{95} value) in Fig.3. Substantial improvement in the stability of the high-β_p H-mode discharges in the low-q region below q*=3 is shown to be achieved mainly due to the pressure profile optimization [1].

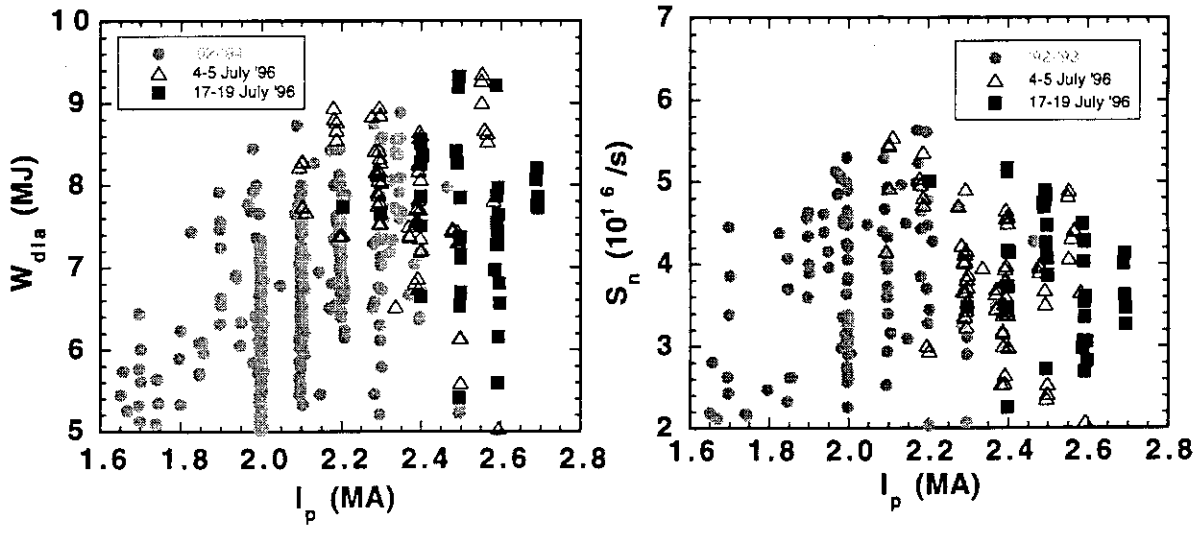

Fig.2 Stored energy and neutron rate as a function of the plasma current

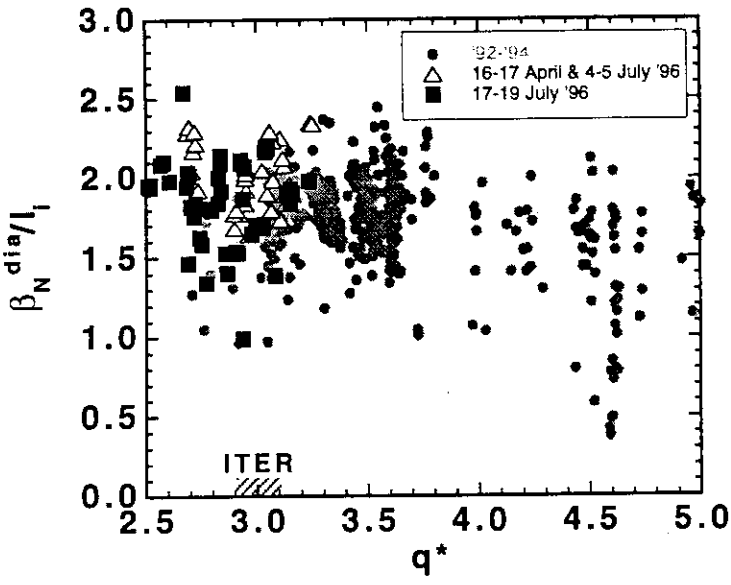

Fig. 3 β_N^{dia}/l_i as a function of q with an ITER operational region*

The ratio of H-factor to the safety factor, H/q, is a useful figure of merit for ignition margin since $(H/q)^2$ is proportional to the fusion product; $H/q_{95} \geq 0.6$ is required for sustained ignition in ITER [4]. The H/q_{95} reaches 1.16 at q_{95}=3.0 in high-β_p H-mode regime. The highest fusion triple product was transiently achieved with high power injection of 37 MW at peak and Z_{eff}~2.2 at q_{95}=2.9 during an ELM-free high-β_p H-mode, where $n_D(0)\tau_E T_i(0)$ reached ~$1.5\times10^{21}m^{-3}$•s•keV with T_i=45±5 keV, W_{dia}=8.6 MJ, and $S_n=5.2\times10^{16}$ /s at peak. The high performance high-β_p H-mode plasma was also sustained at q_{95}=3.0 with successive ELMs. During the ELMy high-β_p H-mode, high stored energy and neutron rate of W_{dia}~8-9 MJ and S_n~$4\text{-}5\times10^{16}$ /s are shown to be sustained with $H/q_{95}\sim\beta_N/q_{95}$~0.67 for ~1.5 times energy confinement times. At peak, W_{dia} and S_n reaches 9.3 MJ and 4.9×10^{16} /s, respectively, where $n_D(0)\tau_E T_i(0)\sim5.1\times10^{20}m^{-3}$•s•keV was achieved. These experimental evidences showing that the fusion performance is peaked around q_{95}~3 independent of transient, stationary states (dW/dt~0) support the argument that the fusion performance can be maximized around q_{95}~3 where ITER would have achieved self-ignition [1].

4. Edge and internal transport barriers

The high-β_p H-mode confinement to produce the high performance as shown above are characterized by the combination of high-β_p mode with an internal transport barrier and H-mode with an edge transport barrier. In the high-β_p mode phase just before the H-mode transition, the presence of internal transport barrier is clearly indicated in the electron density and ion temperature profiles at r/a~0.7 while the q profiles measured from mortional Stark effect spectroscopy reveals the central q value of ~1.4 slightly above unity with a weak central shear [1]. After the H-transition, the ion temperature tends to be significantly increased in the high-β_p H-mode confinement particularly at the edge of the plasma. The highest edge

T_i value observed is shown in Fig.4 to reach ~10 keV during an ELM-free period for a high-β_p H-mode discharge at 2.3 MA.

It is also of importance to know whether the internal transport barrier can be sustained in combination with the edge transport barrier in H-mode. Preliminary observations have shown that the T_i gradient at the internal transport barrier becomes weakened in time during an ELM-free H-mode period (shorter than the energy confinement time) once the H-mode transition occurs. In a short time, however, the substantial temperature gradient at the barrier appears to remain in an overall increase in the T_i profile during the ELM-free H-mode phase as shown in Fig.5.

The combined formation of the internal and edge transport barriers was a key operational issue to achieve the high performance in the high-β_p H-mode discharges. So far, the measurement of the density profile around the barrier location was so limited for the high-β_p discharge configuration that the identification of the barrier was usually made only from the measured ion temperature profile. More detailed investigation on the transport barrier behaviors would be possible with the data from the YAG laser Thomson scattering measurement for the plasma configurations optimized for the measurement rather than for the plasma performance.

References

[1] S. Ishida, Y.Neyatani, Y. Kamada, A. Isayama, T. Fujita et al., in Plasma Physics and Controlled Nuclear Fusion Research 1996 (Proc. 16th Int. Conf. Montreal, Canada 1996), IAEA, paper IAEA-CN-64/A3-1.

[2] S. Ishida et al.,ibid. (Proc. 14th. Int. Conf. Würzburg, 1992), Vol.1, p.219.

[3] Y. Koide et al.,ibid. (Proc. 15th. Int. Conf. Seville, 1994), Vol.1, p.199.

[4] F. Perkins et al., IAEA-CN-60/E-1-I-3 (Proc. 15th. Int. Conf. Seville, 1994).

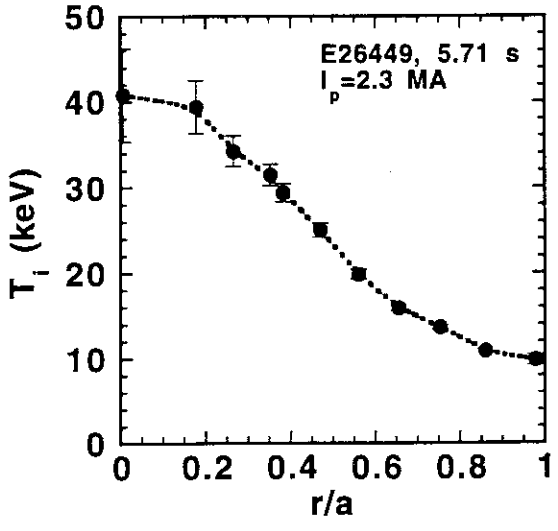

Fig.4 Ion temperature profile showing a high edge ion temperature of 10 keV

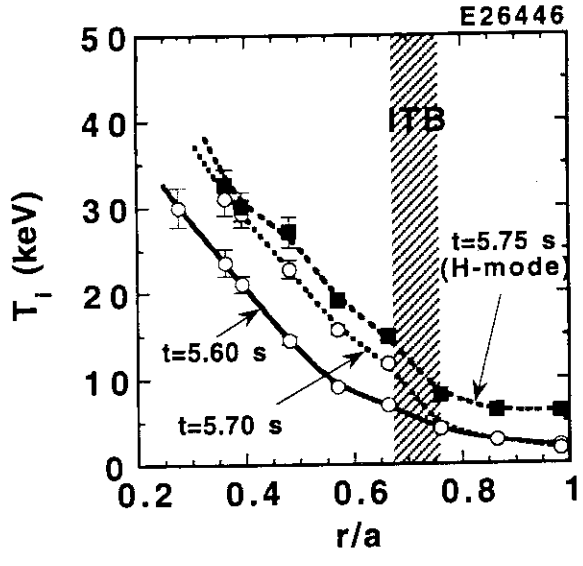

Fig.5 Ion temperature profiles showing an internal transport barrier and edge transport barrier

3.3 High Triangularity Discharges with Improved Stability and Confinement in JT-60U [1)]

Y. Kamada, R. Yoshino, K. Ushigusa, Y. Neyatani, T. Oikawa, O. Naito, S. Tokuda, H. Shirai, T. Takizuka, T. Ozeki, M.Azumi, T. Hatae, T. Fujita, S. Takeji, M. Matsuoka, Y. Koide, T. Fukuda, S. Ishida and JT-60U Team

In JT-60U, energy confinement, stability and the integrated performance including non-inductive current drive were much improved by a new high triangularity (δ) operation where δ was increased from the original value of ~0.1 to ~0.48. In JT-60U, δ is defined as the average of upper and lower triangularities at the outermost flux surface and δ_{95}~0.85δ. The advantage of the high-δ operation was demonstrated for the enhanced integrated performance required for the steady-state tokamak operation: 1) The edge pressure limit at the onset of giant ELMs was improved by a factor of 2. The improvements were 30-50% for edge electron density, ~50% for edge electron and ion temperatures and ~100% for the normalized edge pressure gradient (α-parameter)[2)]. The attainable normalized edge density in ELMy H-mode with H-factor > 2 was increased by a factor of 2. We also observed grassy ELMs at δ>0.3 with β_p>2. 2) The H-factor (= $\tau_E/\tau_E^{ITER89P}$) increased with δ at a given heating profile. 3) Achievable β_N values increased with δ by ~50% and a high value of β_N=3.1 was obtained at a high field of B_t=3.6T without I_p ramp down (q_{95}=4.0, δ=0.34). At a fixed q_{95} (=2.8-4.2), the value of β_N/l_i was almost constant over a wide range of B_t (1.5T- 4.5T) and β_N/l_i ~2.5 at δ <0.1 and ~3.5 at δ >0.3-0.4. 4) At fixed values of q_{95} and l_i, the maximum β_N was obtained at a medium peakedness of the pressure profile determined by the edge stability (giant ELMs) and the fast central collapse. The optimum peakedness at high-δ was smaller than that at low-δ mainly because of improved edge stability. 5) The integrated performance with H-factor=2-2.5 and β_N=2.6-3.1 was sustained for ~2s (~10τ_E) at I_p=1MA/B_t=3T under the full non-inductive current drive (NB driven ~40% and bootstrap ~60%). At I_p=1.5MA, a high fraction (70-80%) of non-inductive current was sustained for 2.5s with β_N~2.5 and H-factor~2.5. At I_p=1.8MA and Bt=3.6T a quasi-steady ITER-like ELMy discharge was sustained for 0.7s (~2τ_E) with β_N=2.7-2.9, H-factor~2.5, H/q_{95}=0.74 with dW/dt=0 and Q_{DT}=0.25-0.3 (q_{95}=3.4, δ=0.3, κ=1.5). These normalized parameters almost satisfy the ITER-requirements.

One of the large issues is that the b-limit in the quasi-steady state is limited by slowly growing (~resistive) low-n modes and the values are lower than the transiently achievable values limited by β-collapses with a fast (~ideal) growth rate.

1) Kamada Y., et al., to appear in Plasma Phys. Control. Nucl. Fusion Research (Proc. 16th IAEA Fusion Energy Conf., Montreal, 1996), A1-6

2) Kamada Y., et al., Plasma Phys. Control. Fusion **38** (1996) 1387.

3.4 Optimization of High Triangularity Discharges for Steady-State High Performance

Y. Kamada, R. Yoshino, K. Ushigusa, Y. Neyatani, T. Oikawa, S. Tokuda, T. Ozeki, M.Azumi, T. Hatae, T. Fujita, S. Takeji, S. Ishida and JT-60U Team

3.4.1 Introduction

The major goal of JT-60U is the *simultaneous* achievement of i) high confinement, ii) high β, iii) full noninductive current drive with a high bootstrap fraction and iv) high efficiency of heat and particle exhaust in the *steady-state*. The JT-60U experiments have been devoted to satisfy the integrated performance by optimizing profiles and plasma shape [1,2]. The recent achievements were reported in ref.2) and Sec.3.3. This section reports how we have been optimizing the discharges, where increase in the triangularity δ is the key factor. In JT-60U, the range of δ is from - 0.06 to + 0.6 at I_p=1MA and up to 0.3 at I_p=2MA (see Figs.1 and 2).

3.4.2 Optimization for Quasi Steady High Integrated Performance

In JT-60U, limits of β_N and H-factor are affected by major radius R_p (Fig.3) because NB-heating profiles and loss of fast ions by toroidal field ripple are functions of R_p. In this section, the ripple loss (~15% for the typical high-δ plasmas) is not subtracted in estimating H-factor. For a high-β limit, it is required to make the peakedness of pressure profile medium [1,2], for which off-axis heating is suitable. However, in the previous discharges with low-δ, H-factor with off-axis heating (R_p~3.3m) became ~70% compared to on-axis heating. This limitation had been the issue of combining high confinement and high β. However, as shown in Figs.3 and 4, the H-factor is increasing with δ at a fixed R_p (3.25-3.3m) and can be comparable to the level of on-axis heating. Moreover, the β-limit is much higher than that of on-axis heating. These high confinement discharges was obtained by keeping q(0) above unity. At high δ, the internal transport barrier similar to the high-β_p mode was formed even with off-axis heating [2].

Figure 5 shows the limit of β_N/l_i increases with δ (β_p>1.6, H-factor>2, dW/dt =0).The upper boundary is limited by the fast collapses. Data A, B and C correspond to quasi-steady full non-inductive current drive at I_p=1MA. The sustainable duration of the integrated performance with the high values of β_p, β_N and H-factor was extended with increasing δ : A:0.3s, B:0.7s and C:2.0s. The life time is finally limited by growth of the low-n resistive modes [1,2] .The main

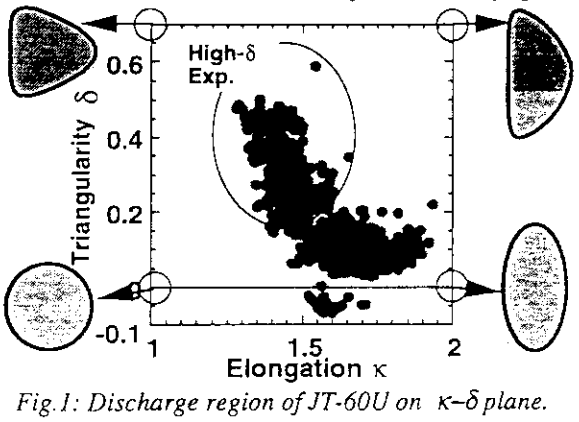

Fig.1: Discharge region of JT-60U on κ–δ plane.

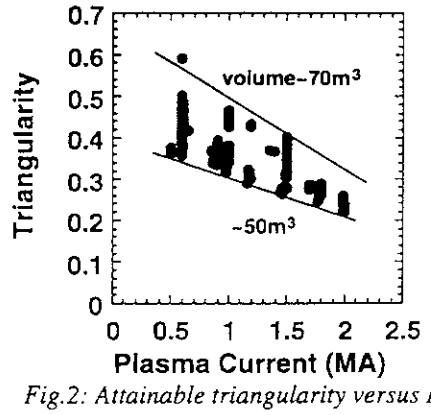

Fig.2: Attainable triangularity versus Ip.

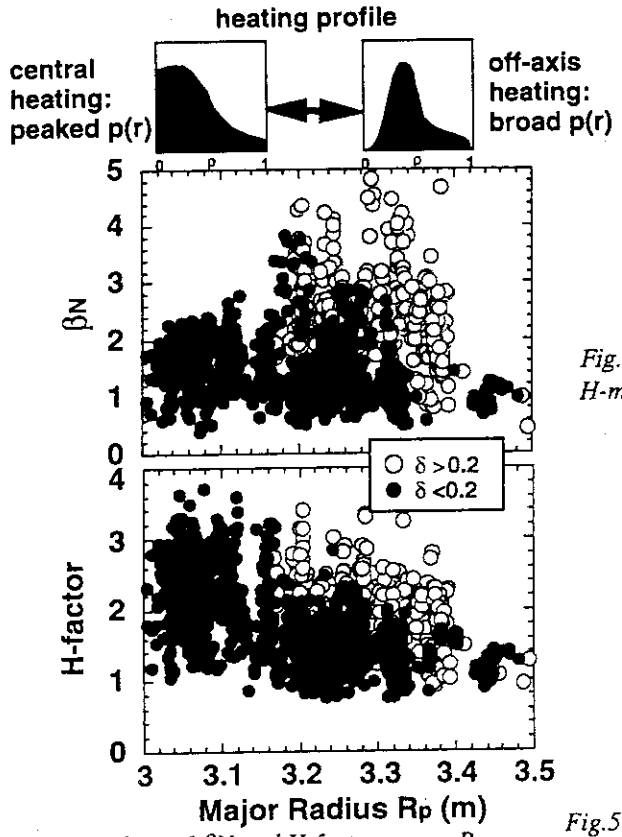

Fig.3: Values of βN and H-factor versus Rp for high-δ(○) and low-δ(●) discharges.

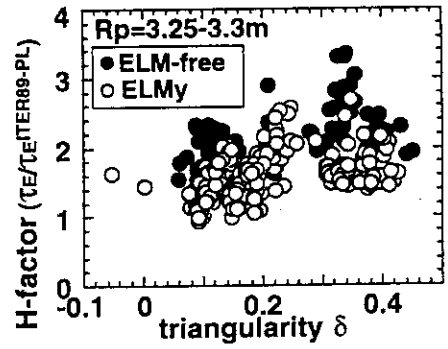

Fig.4: Increasing H-factor with δ in ELM-free and ELMy H-modes at a fixed Rp (off-axis heating).

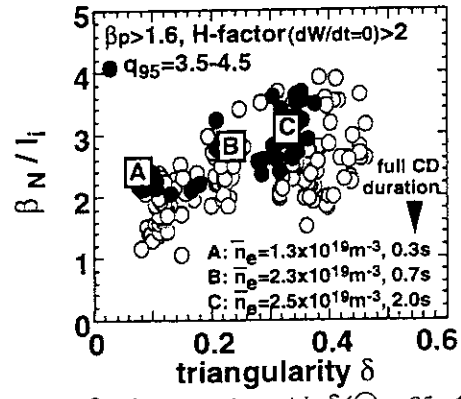

Fig.5: Limit of βN /li increasing with δ(○: q95=4.5-6, ●: q95=3.5-4.5). A, B and C: Quasi-steady full non-inductive current drive cases at Ip=1MA (NB driven=30-40% and bootstrap=60-70%). Sustainable duration of the full current drive state becomes longer with increasing δ.

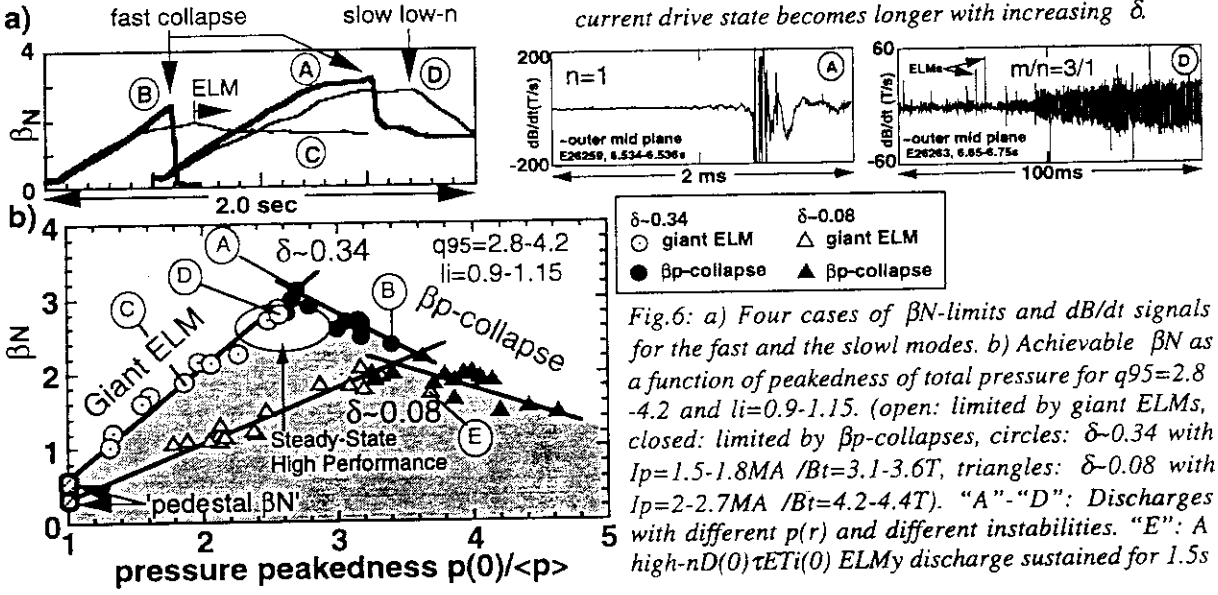

Fig.6: a) Four cases of βN-limits and dB/dt signals for the fast and the slowl modes. b) Achievable βN as a function of peakedness of total pressure for q95=2.8 -4.2 and li=0.9-1.15. (open: limited by giant ELMs, closed: limited by βp-collapses, circles: δ~0.34 with Ip=1.5-1.8MA /Bt=3.1-3.6T, triangles: δ~0.08 with Ip=2-2.7MA /Bt=4.2-4.4T). "A"-"D": Discharges with different p(r) and different instabilities. "E": A high-nD(0)τETi(0) ELMy discharge sustained for 1.5s

reason of the improved β-limit at high-δ can be understood by the improved edge pressure limit for giant ELMs [2] and the dependence of β-limit on the pressure profile [1,2]. For achieving high-β_N, there is an optimum peakedness for p(r). Figure 6a) gives four cases of the β_N-limit with different p(r) and different instabilities, and signals of dB/dt for the fast collapse "A" (growth time <50μs) and for the slowly growing (order of ~10ms) low-n mode "D". As shown in Fig. 6b), for both high-δ and low-δ, β_N-values are limited by the fast collapses (closed) at higher

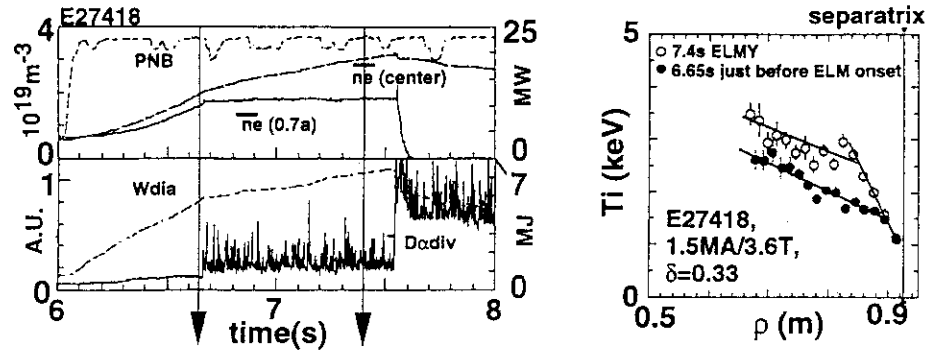

Fig.7: Difference in edge pedestal width between ELM-free and ELMy phases.

p(0)/<p> and by giant ELMs (open) at smaller p(0)/<p>. The improved β-limit seems mainly due to the improved edge stability against giant ELMs. The favorable quasi-steady high performances (Figs 8 and 9) were obtained around the optimum p(r) with β_N~(0.8-0.9)xβ_N^{max}.

Here it should be noted that the width edge pressure pedestal Δ is affected by giant ELMs. In the ELM-free H-mode, Δ depends on the poloidal gyro radius of thermal ions (Δ~(3.3±0.5)$\varepsilon^{0.5}\rho_p$) [3]. In the giant-ELMy phase, the edge pressure gradient is almost similar to that in the ELM-free phase. While, Δ becomes 2 - 3 times as wide as that in the ELM-free phase (Fig.7).

Figure 8 shows a discharge with a high fraction (70-80%) of non-inductive driven current sustained for ~2.6s (~8τ_E) with dl_i/dt~0 where high values of β_N~2.5 and H-factor~2.5 were sustained even at a small value of l_i~0.8. At t=7.1s, Q_{DT}=0.27, H-factor=3, bootstrap=0.85MA, beam driven=0.39MA. The β_N value was set at ~80% of the transiently achievable β_N-limit. The sustainable duration of such discharges becomes shorter at higher β_N. In this region, a gradual

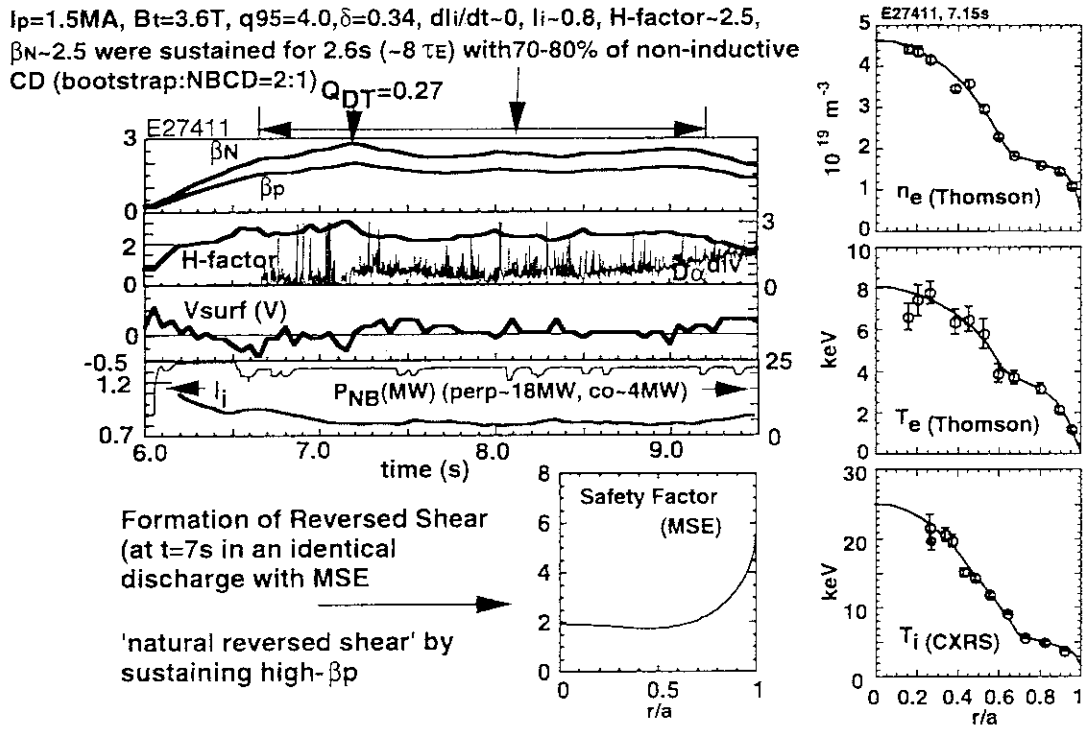

Fig.8: Time traces and profiles of the discharge with a high fraction (70-80%) of non-inductive driven current sustained for 2.6s (~8 τE) with βN~2.5 and H-factor~2.5. At t=7.1s, Q DT=0.27, bootstrap=0.85MA, beam driven =0.4MA (82% non-inductive) and H-factor=3. The q-profile was measured in an identical discharge with MSE.

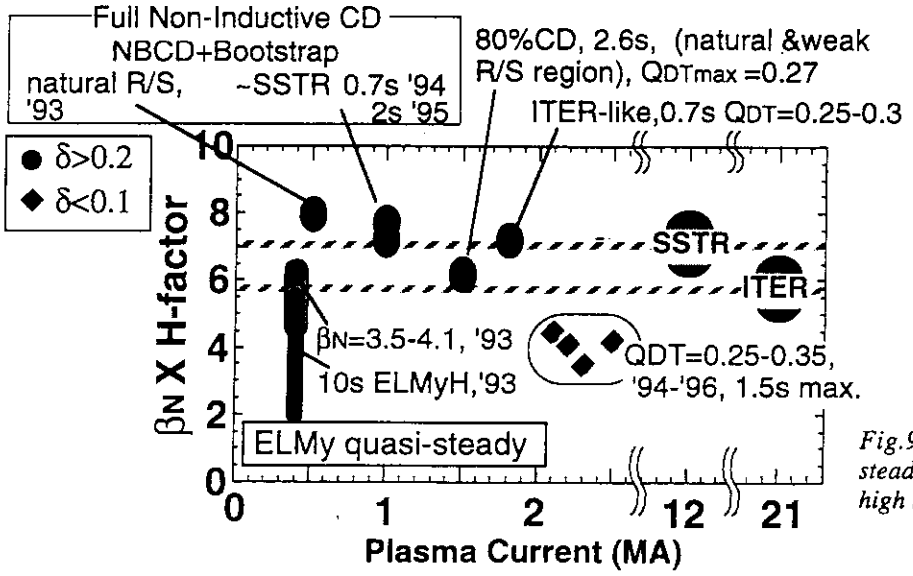

Fig.9: Progress of quasi-steady ELMy discharges with high integrated performances

reversal of central shear was observed due to a high bootstrap fraction (50~60%) [2], which is suitable for sustainment of reversed shear in steady-state by self reversal. In Fig.8, the q-profile with reversed shear is shown for an identical discharge with MSE. The density and temperature profiles have internal barriers at r/a~0.6. Although the central shear is reversed, the ITB located in the weak positive shear (<~1) region [2] which is similar to the standard high-β_p H-mode.

3.4.3 Conclusion

The integrated performance including non-inductive current drive were much improved by optimizing shaping (high-δ), pressure profile and current profile. Figure 9 summarizes progress of quasi-steady ELMy plasmas (dW/dt=0, sustained longer than $2x\tau_E$). The values of $\beta_N xH$ required in ITER and SSTR have been satisfied at I_p up to 1.8MA. Up to I_p=1MA, full non-inductive current drive was obtained with a large bootstrap fraction (60-74%). Up to 1.5MA, we have sustained high β_p values sufficient for natural shear reversal. The β-limit in the quasi-steady state is limited by resistive low-n modes and the values are lower than the ideal limit. The neoclassical tearing mode is one of the candidates. In JT-60U, ITER-like discharges were demonstrated at I_p=1.8MA, where high β_N (2.7-2.9) value was sustained at a low collisionality (ν^*~0.03-0.05) close to ITER [2]. In JT-60U, sustained β_N values at the low collisionality region are high compared to other tokamaks [4]. The largest issue is to sustain the above core plasma performance at a high density required for remote radiative cooling, for which we will continue the optimization research by using new W-shaped divertor and negative ion-based NBI.

References

1) Kamada Y., et al., to appear in Plasma Phys. Control. Nucl. Fusion Research (Proc. 16th IAEA Fusion Energy Conf., Montreal, 1996), A1-6
2) Kamada Y., et al., in Plasma Physics and Controlled Nuclear Fusion Research 1994 (Proc. 15th Int. Conf. Seville, 1994), Vol. 1, IAEA, Vienna (1995) 651.
3) Hatae T.,et al., JAERI-Research 96-018 p68-71, submitted to Plasma Phys. Control. Fusion
4) Sauter O., et al., "Beta Limit in Long-Pulse Tokamak Discharges" to appear Phys. Plasmas.

3.5 Ideal MHD Instabilities with Low Toroidal Mode Numbers Localized near An Internal Transport Barrier in JT-60U High-β_p Mode Plasmas [1]

S. Takeji, Y. Kamada, T. Ozeki, S. Ishida, T. Takizuka, Y. Neyatani, and S. Tokuda

A minor collapse localized near an internal transport barrier has been observed in high-β_p mode plasmas in JT-60U. We referred to the minor collapse as the *"barrier localized mode"* (BLM). Experimental observations revealed that the BLM is an ideal MHD instability with low toroidal mode numbers, n, (n = 1 is dominant). The occurring mechanism of the BLM seems to be associated with the steep pressure gradient at the internal transport barrier, ∇p^{ITB} [2].

Linear analysis of ideal MHD stability was applied to study the effects of ∇p^{ITB} on the stability. We employed equilibria based on the experimental ones for the stability analysis. Then, ideal low n modes were found to be destabilized with localized displacements near the internal transport barrier. The plasma condition for destabilization of the ideal localized low n modes was that the large ∇p^{ITB} induces a bootstrap current, j_{BS}^{ITB}, the magnetic shear, s^{ITB}, is reduced to be negative, and the safety factor, q^{ITB}, is right close to an integer value (The superscript "ITB" means local values at the internal transport barrier). Stability boundary of the low n (n = 1, 2, 3) modes are shown on the $\beta_p - \alpha^{ITB}$ plane in Fig.1. The stability boundary in the lower α^{ITB} (< 1.5) region was determined by the infernal mode destabilized in the central region in the plasma. The β_p-limit of the low n (especially n = 1) modes decreased significantly in the region of $\alpha^{ITB} \gtrsim 1.5$, in which region s^{ITB} was reduced to be negative. Then the radial displacement of each low n mode changed from the global distribution to the localized one. The n = 1 mode became the most unstable low n mode at $\alpha^{ITB} \gtrsim 1.9$. On the other hand, the infinite n ballooning mode was not destabilized near the internal transport barrier since s^{ITB} was very weak or negative.

Time response of j_{BS}^{ITB} driven by ∇p^{ITB} was simulated by using TOPICS code. The numerical results supported our assumption that j_{BS}^{ITB} flows immediately after the formation of the internal transport barrier and reduces s^{ITB}.

The MHD feature and the destabilization condition of the localized ideal low n instabilities found in this stability analysis are qualitatively consistent with the experimental ones of the BLM.

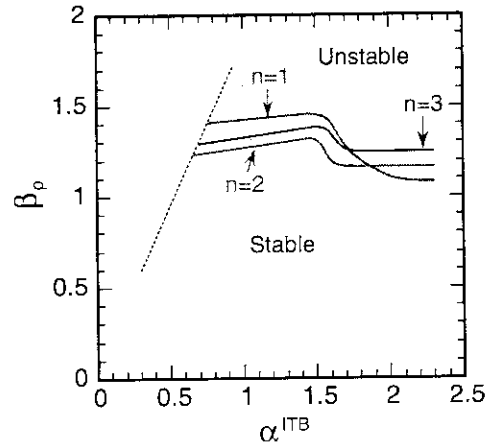

Fig.1. *Stability boundary on $\beta_p - \alpha^{ITB}$ plane against the low n (n = 1, 2, 3) modes (α=$-2\mu_0 q^2 R\nabla p/B^2$). s^{ITB} is negative in the region $\alpha^{ITB} \gtrsim 1.5$.*

References

[1] S. Takeji et al, submitted to Phys. Plasmas.

[2] S. Takeji et al, in *Review of JT-60U Experimental Results from February to October, 1995* JAERI-Research 96-018, 52 (1996).

4. H-mode Confinement

4.1 H-mode Transition and Power Threshold in JT-60U [1]

T. Fukuda, M. Sato, T. Takizuka, K. Tsuchiya, Y. Kamada and H. Takenaga

Based on the results of deliberate experimental investigations at JT-60U, we have first demonstrated that the edge neutral density literally determines the degree to which the threshold power depends on the density. Therefore, information on the edge neutral density can integrate the different density dependencies observed in various tokamaks.

As a result of the intensive experimental campaign, following heuristic results have been obtained. (1) Being indicative of the significance of the wall conditions, the threshold power continuously decreased at the beginning (the first 15 to 20) of the series of discharges, and only the early pulses were consistent with our previous results at JT-60U [2]. The threshold power scaling $P_{th}[MW] = 0.18 \times n_e^{0.5}[10^{19}m^{-3}]B_T^{1.0}[T]R^{1.5}[m]$ was obtained with an assumption of the nondimensional constraints, and it predicts $\approx$ 53 MW for ITER at $n_e = 5 \times 10^{19} m^{-3}$. The JT-60U results reside in a similar region as JET in the P_{net} vs $n_e^{0.75} B_T S$ diagram. However, it does not seem congenial to $n_e^{1.0} B_T^{1.0} R^{2.5}$. (2) The edge ion collisionality at $r/a = 0.95$ ($\nu_{i\,eff}^{*\,95}$), which includes the impurity contribution [3], is around unity only in a limited density range of minimum threshold, whilst conventional theory requires unconditional unity [4].

In order to elucidate the physics of density dependence, we have evaluated the flux averaged neutral density at $r/a \geq 0.95$ (n_o^{95}) with DEGAS. (3) It was found that $\nu_{i\,eff}^{*\,95}$ starts decreasing above a given boundary of n_o^{95}/n_e^{95}, regardless of the $\bar{n}_e$ range. This heuristic feature is quite consistent with the characteristic density dependence of P_{th} and $\nu_{i\,eff}^{*\,95}$; as a consequence of increased n_o^{95}/n_e^{95}, higher critical edge temperature and larger heating power are required for the transition, to which degree is moderate when $\bar{n}_e \geq \bar{n}_{min}$ and substantial when $\bar{n}_e < \bar{n}_{min}$. The role of neutral particles can be interpreted in such a way that larger number of trapped ions experience charge exchange in a region where neutrals are abundant and lose their energy to result in the reduced number of orbit loss ions. The neutral density limit, above which H-mode bifurcation cannot occur, estimated with the charge-exchange assumption [5] is quite consistent quantitatively with our result.

[1] FUKUDA, T. et al., to appear in Plasma Phys. Control. Nucl. Fusion research (Proc. 16th IAEA Fusion Energy Conf., Montréal, 1996) IAEA-CN-64/AP2-9.
[2] KIKUCHI, M. et al., Proc. 14 th Int. Conf. on Plasma Phys. and Contr. Nucl. Fusion Research, Vol. 1(1992)189; M. Sato et al., Proc. 15 th Int. Conf. on Plasma Phys. and Contr. Nucl. Fusion Res., IAEA-CN-60 (1994) A-2-II-4.
[3] FUKUDA, T. et al., Plasma Phys. and Contr. Fusion, 36 A (1994) 87.
[4] SHAING, K. C., CRUME, E. C., Jr., Phys. Rev. Lett. 63 (1989) 2369.
[5] SHAING, K. C., HSU, C. T., Phys. Plasmas **2** (1995) 1801.

4.2. Scaling of H to L Back Transitions in JT-60U [1]

T. Fukuda, T. Takizuka, K. Tsuchiya, Y. Kamada, H. Takenaga and M. Mori

"Hysteresis" of the threshold power is theoretically predicted [2] and observed in several tokamaks [3]. However, as Ref. 2 puts it, H-L boundary in threshold is higher with gas puffing, and we have not yet established an reliable scaling of back transitions. This issue is lately highlighted in a viewpoint of the compatibility of H-modes with the "cold radiative mantle." Therefore, we have carried out an intensive experiment, in which the NB power was decreased in a staircase fashion, and edge plasma quantities including the neutral particle density were analyzed to the detail. In this work, only the spontaneous back transitions were treated by restraining the heating power at an amount "barely enough" to attain the H-mode, in order to reduce the impurity influx as well as to exclude the ELM-induced back transitions.

Contrary to the theoretical predictions, the net heating power [$P_{net}=P_{abs}+P_{OH}$ $-\dot{W}-P_{rad}$] at the back transition was similar to that for the L to H transition, and apparent hysteresis was not observed. Here, the density was real-time feedback controlled with the gas puffing in a range $0.86\text{-}3.6\times10^{19}\,m^{-3}$. This result may imply that the edge transport is deteriorated nearly down to the L-mode quality right before the back transition in JT-60U [H-factor ($\tau_E/\tau_E^{ITER\text{-}89P}$) averaged over the database was 1.1]. The effective edge ion collisionality [4] right before the back transition was also similar to that of the forward transition both in the functional form and values in the ν^*-n_e plane. The back transition threshold is scaled as $P_{th}^b[MW]=1.45B_T[T]\times n_e^{0.5}[m^{-3}]/I_p^{0.5}[MA]$ which incorporates a Greenwald-formed expression. Reproduction of the L to H transition scaling which was established in the previous year was confirmed, viz: $P_{th}^f[MW]=1.02B_T[T]n_e^{0.5}[m^{-3}]/I_p^{0.5}[MA]$, as well. For back transitions, sawteeth seem to play more influential roles than for the L to H transitions, which is relevant to the q-dependence. A speculative interpretation of the H to L scaling above is that the edge quantities, represented by a nondimensional parameter $\eta_G^*=R^{1.75}n_e/I_p$, may be the potential determinant. Accordingly, the value of Z_{eff} was similar at the back transition i.e., even at a higher density, and so was the divertor D_α intensity by a noticeable amount, in spite of the significant reduction of n_o^{95} right after the L to H transition. The n_o^{95}/n_e^{95}-ν^* diagram is described in the subsequent subsection.

[1] FUKUDA, T., et al., to be submitted to Nucl. Fusion.
[2] ITOH, S-I, ITOH, K., Phys. Rev. Lett. **60** (1988) 2276.
[3] FUKUDA, T., KIKUCHI, M., KOIDE, Y., et al., Plasma Phys. Controll. Fusion, **36** A (1994) 87.
[4] RYTER, F., ALEXANDER, M., FUCHS, J. C., et al., in Controlled Fusion and Plasma Physics (Proc. 21st Eur. Conf. Montpellier, 1994), Vol. 18B, Part I, European Physical Society (1994) 330.

4.3 Effect of edge neutrals on H-L back transition in JT-60U [1]

K. Tsuchiya, T. Fukuda, H. Takenaga, Y. Kamada,
S. Ishida, M. Mori and T. Takizuka

In the past study, we found that edge neutrals affect the condition of H-mode transition in JT-60U [2,3]. Threshold power scaling of H-mode transition was obtained in the case of $n_e^{av} > 1.2 \times 10^{19} m^{-3}$. But this threshold power P_{th} steeply become large with decrease of density under the condition of lower density. In this situation, edge collisionality become lower than unity. This collisionality correlated closely with edge neutral density. This means that threshold power becomes higher with increase of edge neutral density. It was reasoned by analogy that neutrals also affect the condition of back transition.

It is theoretically predicted that net input power (P_{net}) at back transition tends to be lower than at H-mode transition [4]. This prediction was experimentally evidenced in ASDEX-U [5]. In JT-60U, however, this hysteresis phenomenon was not clearly obtained. Density dependence of edge collisionality ($\nu_i^*{}_{eff}$) at back transition was similar to this dependence at H-mode transition. $\nu_i^*{}_{eff}$ - n_0/n_e relationship of back transition case was similar to that of H-mode transition case. This means that edge confinement just before back transition is similar level to that just before H-mode transition. Therefore it was clarified from viewpoints of global (P_{net}) and local ($\nu_i^*{}_{eff}$, n_0/n_e) parameters that H-mode confinement just before back transition was close to L-mode confinement just before H-mode transition in JT-60U.

References

1) Tsuchiya K., Fukuda T., Takenaga H., Kamada Y., *et al.*: to be submitted in Plasma Phys. Controlled Fusion.
2) Tsuchiya K., Takenaga H., Fukuda T., Kamada Y., *et al.*: Plasma Phys. Controlled Fusion 38 (1996) 1295.
3) Fukuda T., Sato M., Takizuka T., Tsuchiya K., *et al.*: 16th IAEA Fusion Energy Conference IAEA-CN-64/AP2-9 (1996).
4) Itoh S. -I. and Itoh K.: Phys. Rev. Lett. 60 (1988) 2276.
5) Ryter F., Alexander F., Fuchs J. C., Gruber O., *et al.*: Controlled Fusion and Plasma Physics (Proc. 21st Eur. Conf., Montpellier, 1994) vol.18B, Part I, Europian Physical Society (1994) 330.

4.4 Characteristics of Edge Pedestal Width in JT-60U ELM-free H-mode Plasmas [1]

T. Hatae, S. Ishida, Y. Kamada, T. Fukuda, T. Takizuka,
H. Shirai, Y. Koide, M. Kikuchi, H. Yoshida, O. Naito and JT-60 Team

In H-mode plasmas, there is a bend in the temperature and density profiles near the plasma surface (separatrix). The distance from the bend to the separatrix is called a pedestal width. In this study, the pedestal width in H-mode was investigated in peripheral T_e and T_i profiles, and $1/B_P$, edge T_i and ion poloidal gyroradius ρ_{Pi} dependence of the pedestal was investigated. In order to obtain a wide range of ρ_{Pi}, these experiments were carried out with plasma current from 1 MA to 4.5 MA. Note that the pedestal width in the ELM free H-mode phase is treated in this study. Since the pedestal width of ELMy phase is different from that of ELM free H-mode phase, the pedestal width of ELMy phase is beyond the scope of this study.

New data set of the pedestal width was obtained with wide ranges of edge T_i and B_p in the ELM free H-mode plasma, where ranges of T_i and B_p were 1.45 – 3.9 keV and 0.18 T – 0.74 T, respectively. The range of pedestal width, which was obtained from temperature profile of T_e and T_i, was from 2.6 cm to 8.1 cm. Initial scaling studies proved that the pedestal width can not be simply expressed by the inverse poloidal field. The pedestal width, however, is still showing a positive correlation with the inverse poloidal field. The spreading of data seems to be due to variation of ion temperature. When the edge T_i was fixed, the pedestal width was proportional to $1/B_P$. On the other hand, for the edge T_i dependence, the pedestal width normalized by $1/B_P$ showed a linear dependence on the square root of edge ion temperature. Hence, it is clear that the pedestal width is dependent on $1/B_P$ and $\sqrt{T_i}$, suggesting poloidal gyroradius dependence of the pedestal width. Shaing proposed the following pedestal width [2].

$$\Delta r \sim \sqrt{\varepsilon}\left(\rho_{Pi}/\sqrt{S}\right), \qquad S=\left|1-\frac{1}{B_P\Omega_P}\frac{dE_r}{dr}\right|, \qquad (1)$$

where ε, ρ_{Pi} S, Ω_P and E_r are inverse aspect ratio, poloidal gyroradius of thermal ions, squeezing factor, poloidal gyro-frequency and radial electric field, respectively. Since the orbit squeezing factor is around 1, we consider that the theoretical width is comparable to $\sqrt{\varepsilon}\rho_{Pi}$ as a banana width. The measured pedestal widths of T_e and T_i, with a range from 2.6cm to 8.1cm, showing a clear dependence on $\sqrt{\varepsilon}\rho_{Pi}$. The value of pedestal width, however, is found to be a factor ~3.3 larger than the theoretical prediction of $\sqrt{\varepsilon}\rho_{Pi}$.

[1] Hatae T., et al., to be submitted to Plasma Phys. Control. Fusion
[2] Shaing K. C., Phys. Fluids **B 4** (1992) 290.

4.5 Degradation of energy and particle confinement in high density ELMy H-mode plasmas[1]

N Asakura, K Shimizu, H Shirai, Y Koide and T Takizuka

ELMy H-mode discharges have been produced in high density regime of the divertor tokamaks. These discharges had a cold and dense divertor or detached divertor plasma, produced by strong puffing of deuterium gas[2] and/or an impurity gas such as neon[3]. However, H-factor (the enhancement factor of τ_E larger than ITER89P L-mode scaling) has been shown to decrease with increasing neutral gas pressure in the main vacuum chamber, and the mechanism causing the degradation of enhanced energy confinement was not determined.

Degradation of energy and particle confinement was investigated under the high recycling divertor condition with high power neutral beam injection of 18−19 MW. The plasma parameters were fixed at $I_p/B_t/q_{95}$ = 1-1.2 MA/ 2-2.1 T/ 3.3-3.5. The global energy confinement time τ_E decreased continuously from 0.13 to 0.078 s with increasing $\bar{n}_e$ from $(2.2-2.4)\times10^{19}$ m^{-3} (medium density regime) to $\simeq n^{Gr}$ ($\sim 4.7\times10^{19}$ m^{-3}). The reduction was due to a reduction in the stored energy of fast ions W_{fast}, and the constancy of the thermal plasma energy W_{th} with increasing $\bar{n}_e$. Thermal energy confinement time τ_{th} decreased slightly from 0.088−0.092 s (medium density regime) to 0.083 s (at onset of the X-point MARFE). The reduction in τ_{th} occurs when a fraction of $P_{rad,div}$ increases and neutral recycling in the divertor region is enhanced.

Edge profiles of n_e (Thomson scattering system) and T_i (CXRS) were measured. The local maximum in $|d(n_eT_i)/d\rho|$ was observed at ρ = 0.96−0.99 for the medium and high densities. The width of the region with the large pressure gradient decreased at the high density (at ρ = 0.95−0.97), resulting in the reduction in the thermal energy confinement. However, a large pressure gradient was maintained within the separatrix (ρ = 0.98−1.0).

τ_p^G decreased greatly from 0.13 to 0.08 s due to the increase in the neutral influx from the divertor region. Combining the results, ratios of τ_p^G/τ_{th} and τ_p^G/τ_E decreased from 1.5 to 1 and from 1.0 to 0.8 with increasing $\bar{n}_e$, respectively. The ratios were favorable by a factor of 2−4 for achievement of a cold and dense divertor plasma as compared to the results reported for the ELM-free H-mode plasmas.

The increase in neutral density inside the separatrix, n_0, was evaluated under the attached divertor condition. n_0 near the X-point, $(1-2.5)\times10^{16}$ m^{-3}, was larger by a factor of 10 than that at the midplane due to recycling neutrals from the divertor. Comparison to theoretical models[4] showed that n_0 over most of the circumference (at and above the midplane) was less than the critical level, n_{0c}, to affect the L-H bifurcation mechanism, while the maximum n_0 near the X-point reached n_{0c}. This is consistent with the fairly constant value of τ_{th} and the maintenance of the large pressure gradient and a radial electric field within the separatrix. Increased n_0 and the enhanced asymmetry in the poloidal direction had less effect on maintaining the edge transport barrier as long as the attached divertor condition was maintained.

The present conclusions were obtained only for the relatively low I_p and B_t. The study of the high density ELMy H-mode plasmas for higher I_p and B_t discharges is an important issue for future study.

[1] N. Asakura, *et al.*, Plasma Physics and Controlled Fusion (1997).
[2] N. Asakura, *et al.*, Proc. 15th IAEA Conf. **Vol. I** (IAEA, Vienna, 1995) 515.
[3] K. Itami, *et al.*, Proc. 16th IAEA Conf.
[4] S. -I. Itoh, *et al.*, Nucl. Fusion **29** (1989) 1031.
K. C. Shaing, *et al.*, Phys. Fluids **B 5** (1993) 3841.

4.6 Nondimensional Transport Study on ELMy H-mode Plasmas in JT-60U

H. Shirai, T. Takizuka, Y. Kamada, T. Fukuda, Y. Koide

1. Introduction

The study of heat transport in tokamaks has been carried out from various points of view, such as transport analyses of experiments, transport theory and transport simulation. Recently the transport analyses based on the nondimensional plasma parameters [1-5] have been regarded as more general method to predict the transport properties of next generation tokamaks such as ITER. The important nondimensional parameters related to the plasma confinement and transport are the plasma geometrical values ,i.e., aspect ratio, $A=R/a$, the elongation, κ, the triangularity, δ and the safety factor, q, the shear parameter, $s=\left(r/q\right)dq/dr$ and the normalized Larmor radius, $\rho^* = \rho_L/a = \sqrt{2mT_e}/eBa$, the thermal component of beta value, $\beta_{th} = 2\mu_0\left(n_eT_e+n_i^{th}T_i\right)/B^2$, the normalized collision frequency, $\nu^* = \nu_{ei}/\left(\nu_b\varepsilon^{1.5}\right)$, the ratio of the electron to the ion temperature, T_e/T_i, and so forth. Here n_i^{th} is the thermalized ion density, $\varepsilon = r/R$ is the local inverse aspect ratio, ν_{ei} is the electron-ion collision frequency, and $\nu_b = V_{th}/qR$ is the electron bounce frequency. The normalized thermal diffusivity, χ^*, is expressed by nondimensional plasma parameters as follows,

$$\chi^* = \chi/\chi_{Bohm} = C\left(\rho^*\right)^{\mu}\left(\nu^*\right)^{\xi}\left(\beta_{th}\right)^{\zeta}q^{\gamma}\cdots \quad , \tag{1}$$

where $\chi_{Bohm} = T_e/eB$ denotes the Bohm diffusion coefficient. The exponent μ, ξ, ζ, γ and so forth should be clarified by the systematic experiments of nondimensional parameter scan.

Values of q, s, β_{th}, ν^* in the present large tokamaks such as JT-60U are already similar to those of ITER. However, the ρ^* value of ITER is much smaller than that of large tokamaks. Therefore the ρ^* dependence of χ is an important subject to predict the transport properties of ITER plasmas. The special cases of μ=0, μ=0.5 and μ=1 are called "Bohm type diffusion", "weak gyroBohm type diffusion", and "gyroBohm type diffusion", respectively. The gyroBohm type diffusion is considered to have a short wave length structure, $k_\perp\rho_i \sim 1$, where $k_\perp$ is the perpendicular wave number of the dominant turbulence and ρ_i is the ion Larmor radius. On the other hand, the Bohm type diffusion is considered to have longer wave length structure, $k_\perp\rho_i << 1$.

We have been studying the nondimensional transport properties in L-mode plasmas [5] and ELMy H-mode plasmas in the high elongation configuration [6]. In L-mode plasmas χ_e and χ_i show weak gyroBohm type diffusion and Bohm like diffusion, respectively. Therefore the normalized thermal energy confinement time, $\tau_E^{th}T_e/B_t$, becomes proportional to $1/\left(\rho^*\right)^{0.4-0.5}$. In ELMy H-mode plasmas, on the other hand, $\tau_E^{th}T_e/B_t$ is almost independent of ρ^* because the strong ELM activity occur in the high field shot. In order to make clear the transport properties hidden by MHD activity, we try nondimensional transport study in high triangularity (δ) configuration, which is effective for the suppression of ELM activity comparing with low δ configuration.

2. Experimental and Numerical Calculation Method

In order to make clear the ρ^* dependence of χ by eq. (1), two plasmas which have almost the same nondimensional parameters except for ρ^* are compared with each other. In these plasmas R, a, κ and δ should be the same. The ρ^* value can be changed by magnetic field, B. It is necessary to change the plasma density, the temperature and the plasma current as a function of B like $n \propto B^{1.33}$, $T \propto B^{0.67}$ and $I_p \propto B$ to have similar profiles of q, s, β_{th}, ν^* in spite of different B. The density and the temperature are adjusted by gas puffing and the NBI injection power. In order to avoid the hot ion mode plasma and to realize $T_e/T_i \sim 1$, NBI injection power is kept low. NBI injection timing is adjusted in order to keep the same l_i value. By taking the division of eq.(1) for the different magnetic field, $B=B_1$ and $B=B_2$, we obtain the following formula,

$$\frac{\chi^*(B_1)}{\chi^*(B_2)} = \frac{\chi(B_1)/\chi_{Bohm}(B_1)}{\chi(B_2)/\chi_{Bohm}(B_2)} = \frac{\left(\rho^*(B_1)\right)^{\mu}}{\left(\rho^*(B_2)\right)^{\mu}} . \tag{2}$$

The exponent μ is evaluated as follows,

$$\mu_{eff}(r) = \frac{\ln\left(\dfrac{\chi_{eff}^{\exp}(B_1)/\chi_{Bohm}(B_1)}{\chi_{eff}^{\exp}(B_2)/\chi_{Bohm}(B_2)}\right)}{\ln\left(\rho^*(B_1)/\rho^*(B_2)\right)} , \tag{3}$$

$$\mu_e(r) = \frac{\ln\left(\dfrac{\chi_e^{\exp}(B_1)/\chi_{Bohm}(B_1)}{\chi_e^{\exp}(B_2)/\chi_{Bohm}(B_2)}\right)}{\ln\left(\rho^*(B_1)/\rho^*(B_2)\right)} , \tag{4}$$

$$\mu_i(r) = \frac{\ln\left(\dfrac{\chi_i^{\exp}(B_1)/\chi_{Bohm}(B_1)}{\chi_i^{\exp}(B_2)/\chi_{Bohm}(B_2)}\right)}{\ln\left(\rho^*(B_1)/\rho^*(B_2)\right)} . \tag{5}$$

The profiles of effective thermal diffusivity, $\chi_{eff}^{\exp}$, electron and ion thermal diffusivities, $\chi_e^{\exp}$ and $\chi_i^{\exp}$, are calculated by the steady-state power balance equation of electron and ion by using the profile data of JT-60U experiment. The power deposition profile of NBI is calculated by OFMC (Orbit Following Monte-Carlo) code [7] in order to evaluate the ripple loss of fast ions.

3. Results of Nondimensional Transport Study

We have examined a pair of NBI heated ELMy H-mode shots; shot E26177 (B_t=1.86 T, I_p=0.86 MA, $\bar{n}_e$=1.4×10^{19} m^{-3}, P_{abs}=4.9 MW, l_i=1.15, W_{th}=0.50 MJ, τ_E^{th}=0.13 s) and shot E26276 (B_t=3.08 T, I_p=1.5 MA, $\bar{n}_e$=2.9×10^{19} m^{-3}, P_{abs}=7.5 MW, l_i=1.11, W_{th}=1.50 MJ, τ_E^{th}=0.19 s). They have R=3.33 m, a=0.88 m, a_V (volume averaged minor radius)=1.0 m, κ=1.35, δ=0.35, V=64 m^3 and q_{eff}=4.5 .

Figure 1 shows the comparison of the measured profiles of n_e, T_e, T_i, and the calculated ohmic and NBI heating profiles, Q_{OH}, Q_{NBI}^e and Q_{NBI}^i, between 1.86 T shot (solid lines and

closed symbols) and 3.08 T shot (broken lines and open symbols). The n_e profile is flat like L-mode plasmas. Temperature profiles are fairly similar between these shots, and T_e/T_i is 0.95±0.05 in the region $a/3 \leq r \leq 2a/3$ for both shots. The deposition profile of NBI is rather off-axis. In this configuration the ripple loss of fast ions is evaluated about 20 % of injected power. Therefore the Q_{NBI} rapidly tends to zero in the plasma outer region. The point of maximum Q^i_{NBI} in 1.86 T shot locates slightly near the plasma central region comparing with that in 3.08 T shot due to the different density. Profiles of β_e, β_i^{th} and ν^* in shots E26177 and E26276 are compared in Fig. 2. They show fairly good agreement.

Profiles of $\chi_e^{\exp}$ (broken line) and $\chi_i^{\exp}$ (solid line) of E26177 and E26276 are presented in Fig. 3. The values of $\chi_i^{\exp}$ is larger than $\chi_e^{\exp}$, and both increase from the plasma central region toward the outer region. The values of both $\chi_i^{\exp}$ and $\chi_e^{\exp}$ in the high field plasma (E26276) are smaller than those in the low field plasma (E26177).

The profile of exponent μ_e (broken line) and μ_i (solid line); the ρ^* dependence of χ_e and χ_i, is summarized in Fig. 5. It is found that the ρ^* dependence of χ_e in ELMy H-mode plasma is almost the same or somewhat stronger than that in L-mode plasmas, i.e. weak gyroBohm type diffusion. The ρ^* dependence of χ_i in ELMy H-mode plasma is almost gyro Bohm type diffusion, which is much stronger ρ^* dependence than that in L-mode plasmas. Therefore the normalized thermal energy confinement time has strong ρ^* dependence, $\tau_E^{th} T_e / B_t \propto (\rho^*)^{-0.8}$, which is favorable for the future reactor. This results is similar to those obtained in JET [8] and DIII-D [9].

It is very interesting and very important subject to clarify the reason that the property of ion heat transport changes dramatically from L-mode phase to H-mode phase. We will study further the different transport mechanism between L-mode and H-mode plasmas from the view point of the effect of the plasma rotation and the radial electric field. We are also planning to carry out nondimensional transport analyses of hot ion H-mode plasmas and high density H-mode plasmas in JT-60U.

References

1) B. B. Kadomtsev : Sov. J. Plasma Phys. **1** (1975) 295.
2) J. W. Connor and J. B. Taylor : Nucl. Fusion **17** (1977) 1047.
3) F. W. Perkins, C. W. Barnes, D. W. Johnson, et al. : Phys. Fluids B **5** (1993) 477.
4) J. P. Christiansen, P. M. Stubberfield, J. G. Cordey, et al. : Nucl. Fusion **33** (1993) 863.
5) H. Shirai, T. Takizuka, O. Naito, et al. : J. Phys. Soc. Jpn. **64** (1995) 4209.
6) T. Takizuka, H. Shirai, Y. Kamada, et al. : JAERI-Research 95-075 (1995) 22.
7) K. Tani, M. Azumi and H. Kishimoto : J. Phys. Soc. Jpn. **50** (1981) 1726.
8) JET Team : in Proc IAEA 16th International Conference on Plasma Physics and Controlled Nuclear Fusion Research 1996, Montréal, Canada (1996) IAEA-CN-64/A2-1.
9) C. C. Petty, T. C. Luce, K. H. Burrell, et al. : Phys. Plasmas **2** (1995) 2342.

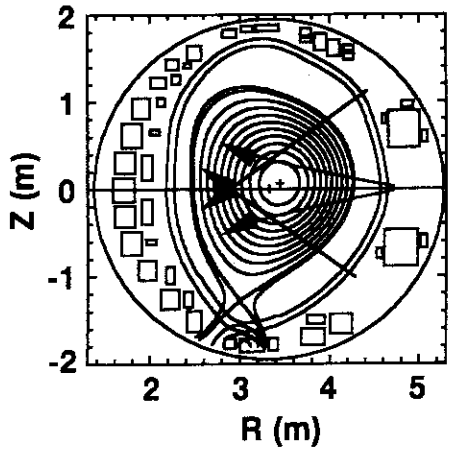

Fig.1 Poloidal cross section of shot E26177.

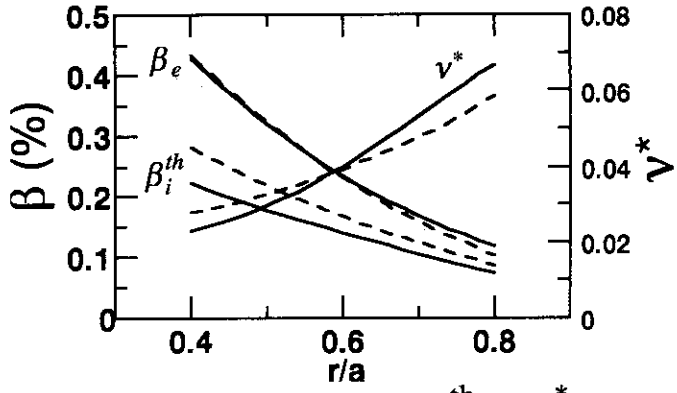

Fig. 3 Profiles of β_e , β_i^{th} and ν^* in shot E26177 (solid line) and shot E26276 (broken line).

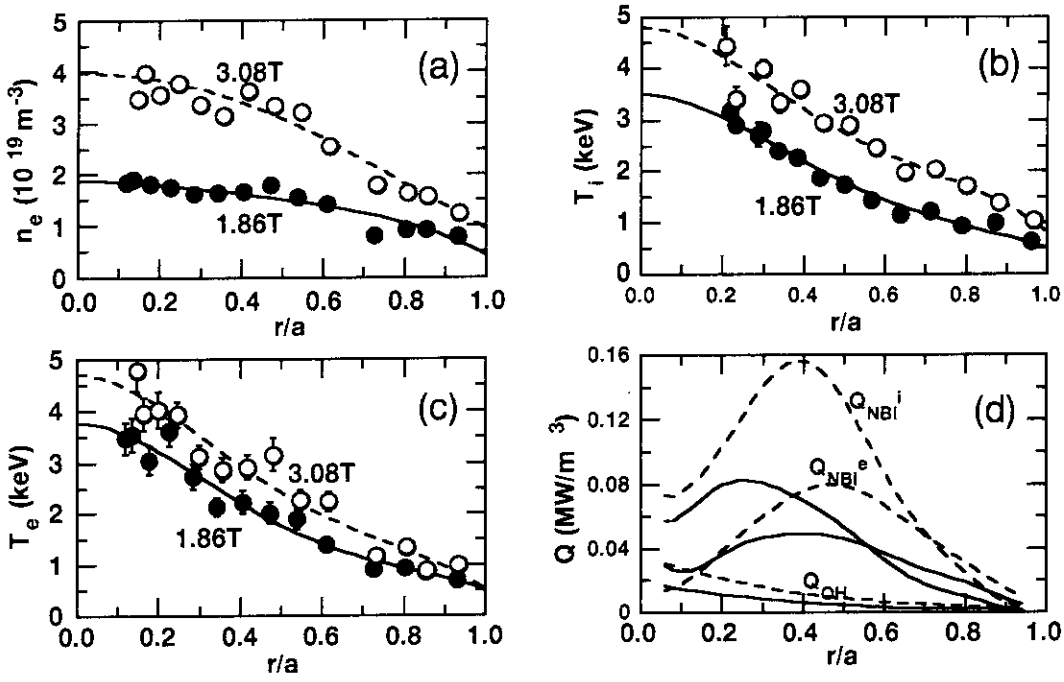

Fig. 2 Profiles of (a) n_e, (b) T_e, (c) T_i and (d) heating profile in shot E26177 (solid line) and shot E26276 (broken line).

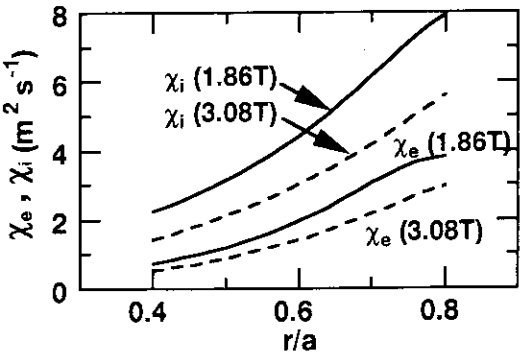

Fig. 4 Profiles of χ_e and χ_i in shot E26177 (solid line) and shot E26276 (broken line).

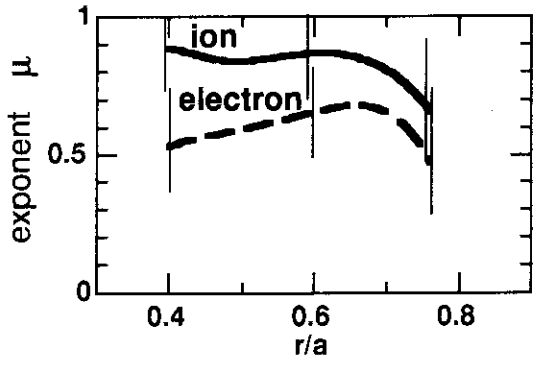

Fig. 5 Profiles of μ_e (broken line) and μ_i (solid line).

4.7. Exploration of Ohmic H-mode Regime in JT-60U

K. Tsuchiya, T. Fukuda, Y. Kamada and T. Takizuka

1. Introduction

Although the transition physics of ubiquitous H-mode has been intensively investigated in terms of the edge plasma quantities i.e., radial electric field and resultant flow shear formation [1], determinants of the global threshold power have not yet been adequately resolved. In order to establish a comprehensive picture of the H-mode transition itself, as well as to relate the edge dynamics with the global scaling parameters, integration of the threshold for the NB heated H-modes with that of ohmic H-modes would remain as one of the most efficient approaches.

Ohmic H-modes are often observed in relatively small-sized tokamaks e.g., Alcator C-Mod, TCV, TUMAN-3 and COMPASS-D, seemingly due to the size-dependent reduction of the threshold power [2-5]. In larger tokamaks, except for the low-q discharges in DIII-D [6], ohmic H-mode has not been either produced or examined carefully. Though Ref. 5 claims that the ohmic H-mode threshold is no less than additionally heated H-mode scalings [7] predict, direct investigation in a single device has not been performed before. Whilst a well favored paradigm of the H-mode transition is the orbit excursion of trapped ions [8], ohmic power is deposited mainly to the electrons in the edge. Other potential differences with the NB H-modes are that NB may introduce a large amont of neutral flux and impurities via strong wall interactions of energetic ions.

2. Estimate of the ohmic input and threshold power

With the aid of the expression for the JT-60U thermal confinement scaling in Ref. 9 and Spitzer resistivity, ohmic heating power can be scaled as

$$P_{\mathrm{OH}}[\mathrm{MW}] = 5.2\times10^{-5} I_{\mathrm{P}}^{2}[\mathrm{A}] R_{\mathrm{P}}[\mathrm{m}](\kappa a^{2}[\mathrm{m}])^{-1} Z_{\mathrm{eff}} T_{\mathrm{e}}^{-1.5}[\mathrm{eV}]$$

$$= 1.7 q^{-0.83} \kappa^{0.29} R_{\mathrm{P}}^{0.79}[\mathrm{m}] A^{-1.39} B_{\mathrm{T}}^{0.44}[\mathrm{T}] n_{\mathrm{e}}^{0.5}[\mathrm{m}^{-3}] Z_{\mathrm{eff}}^{0.67}, \qquad (1)$$

where κ, R_{P} and A respectively represent ellipticity, major radius and aspect ratio. The JT-60U power threshold scaling for the NB-heated plasmas, on the other hand, is described as [10]

$$P_{\mathrm{th}}[\mathrm{MW}] = 0.18\, n_{\mathrm{e}}^{0.5}[10^{19}\mathrm{m}^{-3}] B_{\mathrm{T}}^{1.0}[\mathrm{T}] R_{\mathrm{P}}^{1.5}[\mathrm{m}]. \qquad (2)$$

For a parameter set of (κ, A, R_{P}, B_{T}, Z_{eff}, n_{e})= (1.6, 3.7, 3.3, 2.0, 2.5, 1.5), the expected ohmic power and the threshold are 1.0 MW and 3.3 MW, respectively. For COMPASS-D and

DIII-D, the parameter sets of (1.6, 3.3, 0.56, 1.4, 1.5, 6.0) and (1.6, 3.3, 0.56, 1.4, 1.5, 6.0) respectively yield P_{OH}/P_{th} = 0.35 / 0.16 and 1.0 / 0.85. Therefore, the chances of obtaining an ohmic H-mode for JT-60U are larger plasma current under the reduced magnetic field and major radius, the operational regime of which we may suffer from the vigorous MHD instabilities. In addition, current ramp would have to be employed as well, in order to increase the ohmic input, expecting the inductive contribution [V_i], viz:

$$[V_i] = \frac{\mu_0 R_P}{4}(\dot{l}_i I_P + 2 l_i \dot{I}_P) + \mu_0 R_P (\ln\frac{8R_P}{a} - 2)\dot{I}_P \qquad (3)$$

An increase of the time derivative of l_i can thereby contribute to the heating efficiency.

3. Experiment

The parameter set (κ, A, R_P, B_T, Z_{eff}, n_e) was chosen at (1.54, 4.4, 3.0, 2.5, 2.25, 1.0); plasma volume was reduced to 40 m^3, and I_P/B_T of 1.12 MW / 2.5 T was intended to retain q_{eff} [$= 0.5(5a_P^2 B_T/R_P I_P)(1+\kappa^2)\{1+(a_P/R_P)^2(1+0.5(\beta_P+l_i/2)^2)\}\{1.24-0.54\kappa+0.3(\kappa^2+\delta^2)+0.13\delta\}$] above 4. The density was real-time feedback controled with gas puffing, and current scan under a fixed-q was also performed. In addition, the current ramp-up rate dI_P/dt was increased up to 3.0 MA/sec.

A few of the discharges suffered from the vertical instabilities, as the plasma resided in the region of negative n-index less than -2.0. However, though transient, an apparent sign of the H-mode transition was observed as shown in Fig. 1. The top subpanel shows the plasma current, where its ramp rate of 3.0 MA/sec is indicated. In the 2nd column, an increase of the diamagnetic stored energy and averaged density at ρ = 0.46 are shown, together with a reduction of the divertor D_α signal in the bottom subpanel. H-mode transition occurs at 10.54 s, in the middle of the current ramp, as indicated with a dotted line. Edge electron temperatures right before the transition measured with the ECE diagnostic at 95% poloidal flux were much less i.e., nearly a half of the NB-heated H-modes with a similar density and magnetic field, which is inconsistent with the NB-heated H-mode cases.

Another indication of H-mode was obtained with the edge density fluctuation, measured with a heterodyne reflectometer at 98% poloidal flux. The expanded time lag, shown as a broad autocorrelation function, is directly relevant to the reduction of the decorrelation frequency and the suppression of turbulent fluctuations in the H-mode [11].

The ohmic input power was evaluated with FBI code, since TOPICS code [12] was not

applicable because of the deficiency of the ion temperature profile. As can be anticipated from eq. (1), the ohmic input power increased with density and plasma current. It also increased with the current ramp rate. However, the ohmic heating power did not clearly exceed the predicted threshold, in spite of the fact that fair evidence of H-mode transition was indeed observed.

4. Discussion

Indication of ohmic H-mode was observed with the ohmic input less than the prediction of the additionally heated H-mode scaling, when the plasma current was ramped up. Speculative interpretation of the above result is that reduction of the edge magnetic shear, which can increase the number of trapped ions lost from the orbit, may possibly the cause of a reduced threshold. However, as the reduction of the edge magnetic shear can produce adverse effect on the edge confinement properties, further investigation is still necessary.

References

[1] BURRELL, K.H., CARLSTROM, T.N., DOYLE, E.J., *et al.*, Plasma Phys. Control. Fusion, **34** (1992) 1859.
[2] SNIPES, J.A., HUBBARD, A.E., GARNIER, D.T., *et al.*, Plasma Phys. Control. Fusion, **38** (1996) 1127.
[3] WEISEN, H., HOFMANN, F., DUTCH, M.J., *et al.*, Plasma Phys. Control. Fusion **38** (1996) 1137.
[4] ANDREJKO, M.V., ASKINAZI, L.G., *et al.*, Plasma Phys.Control. Fusion **36** (1994) A165.
[5] CAROLAN, P.G., FIELDING, S.J., GERASIMOV, S., *et al.*, Plasma Phys. Control. Fusion **36** (1994) A111.
[6] SCHISSEL, D.P., *et al.*, in Controlled Fusion and Plasma Physics (Proc. 16th Eur. Conf. Venice, 1989), Vol. 13B, Part I, European Physical Society (1989) 115.
[7] RYTER, F., ALEXANDER, M., FUCHS, J. C., *et al.*, in Controlled Fusion and Plasma Physics (Proc. 21st Eur. Conf. Montpellier, 1994), Vol. 18B, Part I, European Physical Society (1994) 330.
[8] SHAING, K. C., CRUME, E. C., Jr., Phys. Rev. Lett. 63 (1989) 2369.
[9] SHIRAI H., TAKIZUKA, T., NAITO, O.,*et al.*, J. Phys. Soc. Japan **64** (1995) 4209.
[10] FUKUDA, T., SATO, M., TAKIZUKA, T.,*et al.*, in Plasma Phys. Control. Nucl. Fusion research (Proc. 16th IAEA Fusion Energy Conf., Montréal, 1996) IAEA-CN-64/AP2-9.
[11] FUKUDA, T., KIKUCHI, M., KOIDE, Y., *et al.*, Plasma Phys. and Contr. Fusion **36** (1994) A87.
[12] HIRAYAMA, T., SHIMIZU, K., TANI, K., *et al.*, Experimental Transport Analysis Code System in JT-60, JAERI Report No. JAERI-M-88-043 (1988).

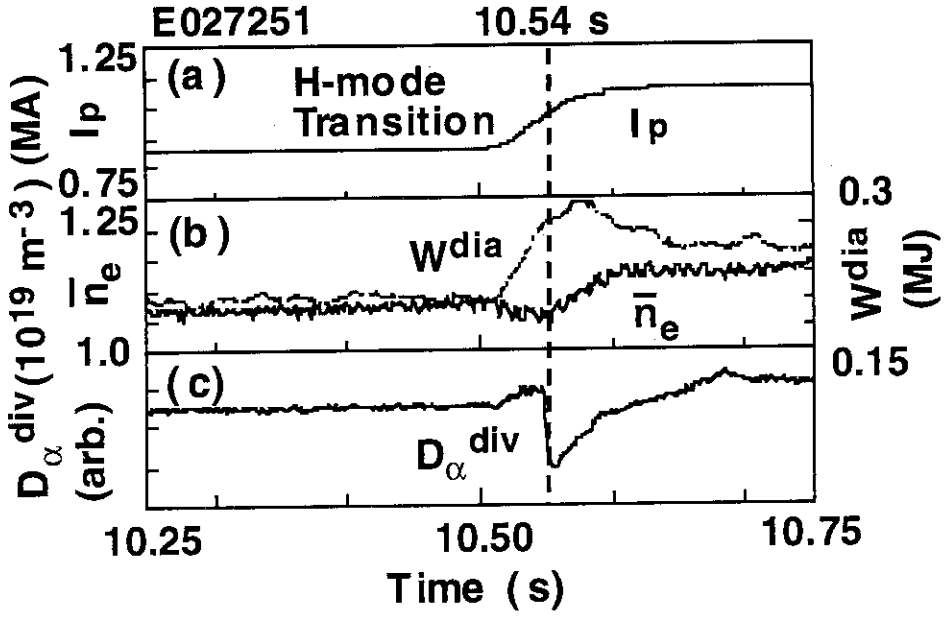

Fig. 1 (a) Plasma current , (b) diamagnetic stored energy and averaged density at $\rho = 0.46$ are shown,together with (c) the divertor Dα signal. H-mode transition occurs at 10.54 s, in the middle of the current ramp, as indicated with a dotted line.

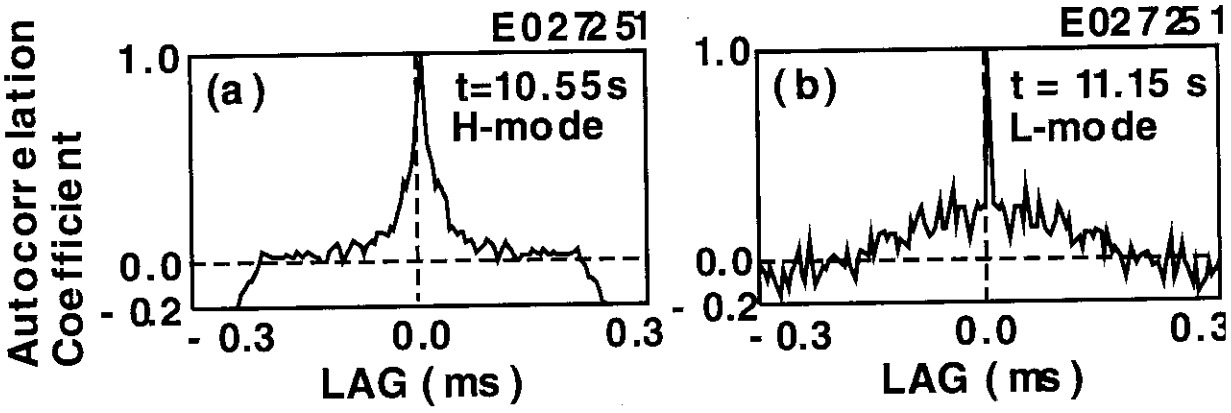

Fig. 2 Autocorrelation coefficients for(a) OH H-mode and (b) L-mode.

5. High Energy Particle

5.1 Transport and Loss of Energetic Ions in JT-60U

K. Tobita, T. Nishitani, H. Harano, K. Tani, M. Isobe, T. Fujita, Y. Kusama,
G. Wurden, H. Shirai, T Oikawa, T. Fukuda, K. Hamamatsu, S. Ishida, M. Nemoto,
T. Kondo, A. Morioka, H. Kimura, M. Saigusa, S. Moriyama, O. DaCosta,
V.I. Afanassiev, JT-60 Team

In reversed magnetic shear plasma, fast ion confinement is anticipated to be deteriorated because of weak poloidal magnetic field in the core. As a matter of fact, JT-60U experiment indicated that confinement of energetic ions in reversed magnetic shear was inferior to that in the normal shear with positive magnetic shear [1, 2]. The experimental triton burnup in the reversed shear was a half or a third of the expected, while that in the normal shear almost agreed with the calculation. The results indicate that a significant fraction of energetic tritons escaped the plasma in the reversed shear, raising a concern on serious MeV ion losses in reversed shear operations of steady state tokamak reactors. Stochastic and collisional ripple losses are a probable explanation for the significant triton losses.

Up-down asymmetric ripple experiment confirmed the earlier prediction on ITER that the ripple up-down asymmetry did not enhance energetic ion loss at a significant degree, and that the loss was independent of the ion drift (or B_t) direction [3]. The result encourages flexible B_t reversal operation in next step fusion reactors with up-down asymmetric ripple in terms of ripple loss.

Reference:

[1] K. Tobita, T. Nishitani, H. Harano, K. Tani, M. Isobe, et al., in Plasma Physics and Controlled Nuclear Fusion Research 1996 (Proc. 16th Int. Conf. Montreal, Canada 1994), IAEA, paper IAEA-CN-64/A5-6.

[2] K. Tobita, H. Harano, T. Nishitani, T. Fujita, K, Tani, et al., ' Losses of fast tritons in JT-60U reversed magnetic shear discharges', submitted to Nuclear Fusion.

[3] M. Isobe, K. Tobita, et al., to be published in Nucl. Fusion.

5.2 CX Measurements of d-d Triton Distribution Function in High Power NB Heating

F.V.Tchernychev*, Y.Kusama, M.Nemoto, A.Morioka, K.Tobita, S.Ishida
**A.F.Ioffe Physical-Technical Institute, St.Petersburg, 194021, Russia*

1. Introduction

The study of fusion products is an important task for the further tokamak development. By this time the significant populations of fusion particles are created during the experiments in d-d tokamak plasmas even without tritium technology and the distribution functions of fusion products can be studied in these tokamaks. The measurements of d-d tritons in comparison with observation of other fusion particles is most promising because of the following reasons:

- relatively high triton density due to long slowing down time in the plasma;
- high neutralization probability;
- gyroradius of 1 MeV triton is approximately equal to gyroradius of 3.5 MeV alpha-particle, so the orbital effects of fusion tritons are similar to those of alpha-particles.

In this section the first results of triton measurements in JT-60U using MeV-range NPA are presented.

2. Possibilities of Triton Measurements

The triton measurements were performed during experiments in high-beta plasmas, which had significant d-d reactivity due to interaction of bulk ions with deuterium beams. The main plasma parameters are presented in Table 1 and their time evolutions are shown in Fig.1. Unfortunately NPA detectors were overloaded by neutron background during the injection (from 5.0 to 7.0 sec). Therefore the particle measurements were impossible during NBI and even some time after NBI. The only possibility for the measurements was to detect the slowing down tritons after the decrease of neutron background (about 0.5 sec after the turn-off of NBI).

The characteristics of fusion tritons, estimated for the plasma parameters during and after NBI, are listed in Table 2. Since the critical energy of tritons E_{CR} is much lower than their birth energy E_0, it is expected that the collisions with electrons predominate and high energy tritons decelerate practically without scattering in pitch angle.

The slowing down tritons can be neutralized due to electron capture on plasma neutral deuterium and on hydrogen-like carbon impurity C^{5+}[1]. After neutralization the outgoing tritium atomic flux can be detected by NPA.

Table 1. The main plasma parameters during and after NBI.

Plasma parameters	during NBI (5.8-7.0 sec)	after NBI (8.0 sec)
Toroidal field, B_t	4 T	
Plasma current, I_p	2.4 MA	
Central electron density, $n_e(0)$	$2.5 \cdot 10^{19}$ m^{-3}	$1.2 \cdot 10^{19}$ m^{-3}
Central electron temperature, $T_e(0)$	(7.5-8.5) keV	3.5 keV
Total plasma neutron yield, S_n	$(2.5\text{-}3) \cdot 10^{16}$ 1/sec	
Total NBI power, P_{NBI}	25 MW	

Table 2. Characteristics of fusion tritons during and after NBI.

Triton characteristics	during NBI (5.8-7.0 sec)	after NBI (8.0 sec)
Birth energy, E_0	1.01 MeV	
Gyroradius, r_c	6.2 cm	
Critical energy, E_{cr}	220 keV	100 keV
E_0 / E_{cr}	4.5	10
Slowing down time on electrons, τ_{sl}	3.4 sec	2.9 sec
Time of thermalization, τ_{th}	2.6 sec	3.4 sec

The time of deceleration of 1 MeV tritons to the energy E_S, assuming that $E_S >> E_{cr}$, can be determined as $\tau_S(E_S) = - 0.5\ \tau_{sl}\ \ln(E_S / E_0)$. According to Table 2 the estimated triton slowing down time is (2.9-3.4) sec, hence the tritons with energies E_S = (0.3-0.6) MeV could be observed in about (1 - 2) sec after termination of NBI.

3. Experimental Arrangement

The triton measurements were performed by NPA of MeV energy range [2]. The NPA was installed near tokamak midplane with its sight line directed tangentially to the plasma [3]. The top view of JT-60U plasma with the analyzer sight line is shown in Fig.2a. It is important for the triton measurements that the NPA overlooked the central region of plasma where the d-d reactivity was expected to be high. The values of plasma minor radius, crossed by the analyzer sight line, are presented in Fig.2b. The pitch angles of particles which could be detected by NPA along the sight line are also shown. Since the trapped particles have the pitch angles greater than 54 deg (this value is taken for the outer boundary of the plasma as a lower limit), only the passing particles could be detected.

4. Results

The data obtained by one of the NPA energy channels is shown in Fig.3. The picture presents pulse height distribution of the detector signal measured from 7.6 to 8.1 sec of the plasma shot ((0.6-1.1) sec after NBI termination). The peak around ADC channels 7-8 can be related to the triton signal and the left shoulder on the distribution corresponds to the residual neutron background. The analyzer was tuned to the energy range (0.26-1.0) MeV to detect the tritons with birth energy by highest energy channel and the slowing down particles by other channels. Right below birth energy (0.7 -1) MeV no triton signal has been observed and one can connect this fact with triton deceleration after termination of NBI. The low signal in the intermediate energy range (0.5 - 0.7) MeV can be explained, assuming that the charge-exchange on the neutral deuterium is a dominant process of triton neutralization, because the charge-exchange cross section is dramatically dropping with these energies. Assuming that, the energy distribution of tritons can be evaluated:

$$f_t \propto dJ / dE \; / \; \langle \sigma_{CX} v \rangle,$$

where dJ / dE is the tritium flux entering NPA and $\langle \sigma_{CX} v \rangle$ is the rate coefficient of charge-exchange on deuterium. The triton spectrum inferred from the measurements in NPA low energy channels is shown in Fig.4. To increase the statistics the data presented in the picture were collected during 0.5 sec. The total numbers of particles detected by each channel are also shown in Fig.4.

Assuming that the triton spectrum does not change much after the termination of NBI, the data obtained by NPA can be compared with the measurements of neutron emission and the value of plasma neutral density can be estimated. The level of neutral density which is necessary to produce such count rates in NPA channels should be about $6 \cdot 10^{13}$ m^{-3} (for the neutron yield $S_n \sim 3 \cdot 10^{16}$ 1/sec) which seems to be a reasonable value.

5. Summary

- the passive signal of neutralized d-d tritons was reliably detected and the energy spectrum of tritons in the plasma core was measured in 1 sec after the termination of NB-heating;

- the mechanism of triton neutralization in the plasma has been determined as the electron capture on residual neutral deuterium.

References

[1] Korotkov A.A. et al., 21 EPS Conference on Controlled Fusion and Plasma Physics 18B(I) (1994) 226.

[2] Y.Kusama et al., Rev.Sci.Instrum. 66 (1995) 339.

[3] Y.Kusama et al., to be published in Fusion Engineering and Design.

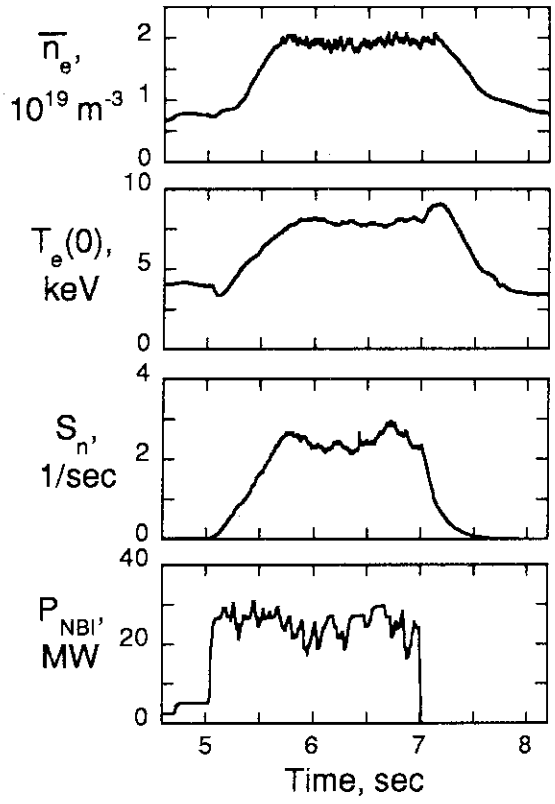

Fig.1. Time evolution of plasma parameters. #26439

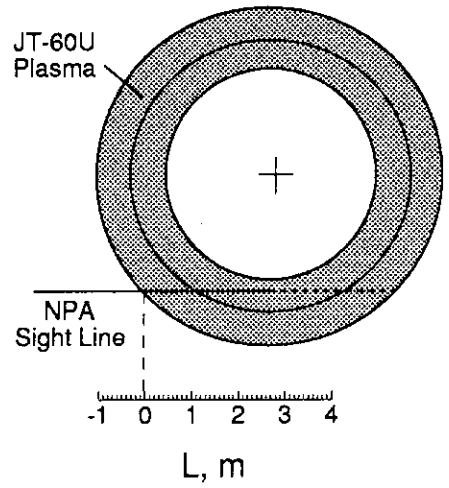

Fig.2a. NPA arrangement.

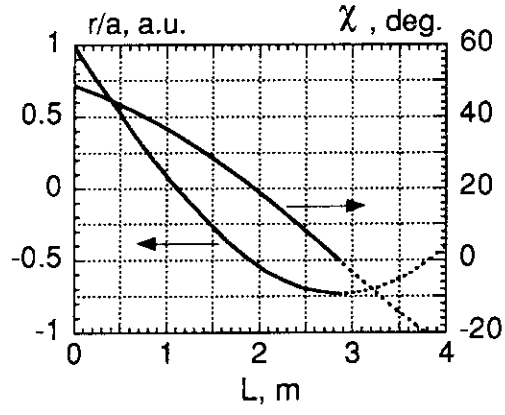

Fig.2b. Minor radius and pitch angle along NPA sight line.

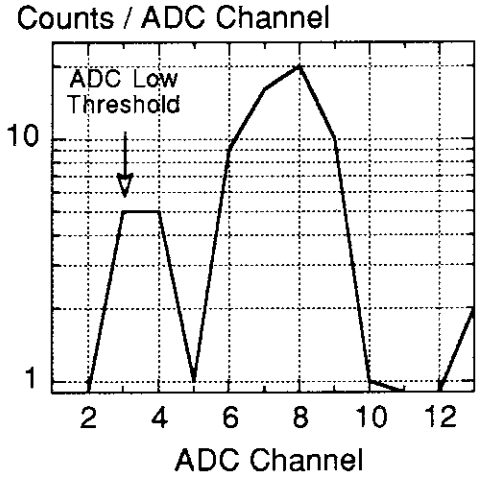

Fig.3. Pulse height distribution of detector signal in one of the NPA energy channels. E_{CH} = 0.43 MeV; #26439; (7.6-8.1) sec.

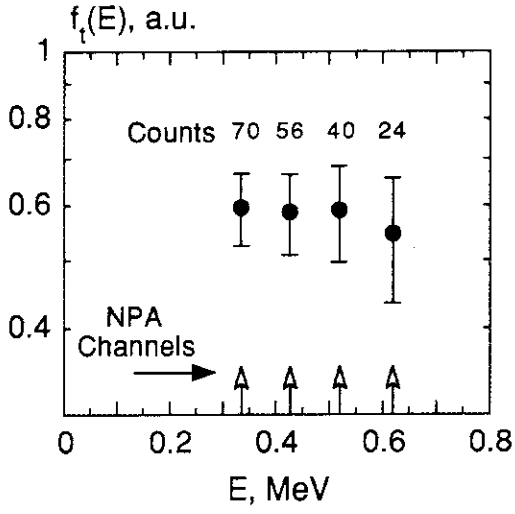

Fig.4. Triton energy distribution. #26439; (7.6-8.1) sec.

5.3 ICRF Heating and TAE Modes in Reactor-Relevant JT-60U Discharges [1]

H.Kimura, S.Moriyama, M.Saigusa, Y.Kusama, T.Ozeki, G.J.Kramer, T.Fujita, T.Oikawa, T.Fujii, M.Nemoto, K.Hamamatsu, O.DaCosta, S.Ishida, Y.Kamada, T.Kondoh, A.Morioka, Y.Neyatani, K.Tobita, V.I.Afanassiev[1], G.Y.Fu[2], C.Z.Cheng[2], R.Nazikian[2] and the JT-60 Team

Applicability of ICRF minority heating in negative shear (N/S) discharge is an important subject for the development of a steady-state tokamak reactor. Fast ions should be well confined inside the transport barrier to heat the bulk plasma efficiently with relatively weak poloidal field. In JT-60U, second harmonic ICRF minority heating in deuterium negative shear discharges was found to efficiently heat bulk plasmas inside the transport barrier. A typical example is shown in Fig. 1. The plasma stored energy, the electron and ion temperatures in the plasma core remarkably increased after start of the ICRF injection and reached 5 MJ, ~7 keV and ~12 keV, respectively. However, a change of the electron density due to ICRF is negligebly small, as is seen from almost equal temporal evolution of the line average electron density between with and without ICRF. The result reflects characteristics of RF heating (no particle fuelling). H-factor ($\equiv\tau_E/\tau_E^{ITER89P}$) increased from 1.4 before ICRF to 2.0 at the end of the ICRF pulse without correction of ripple-induced fast ion losses. A steep gradient layer appeared in the pressure profile, indicating formation of an internal transport barrier (ITB) associated with the negative shear operation. A normalized radius of the position of the steep gradient layer (r_{ITB}/a) was ~0.65, which almost coincides with the position of the minimum value of q (q_{min}).

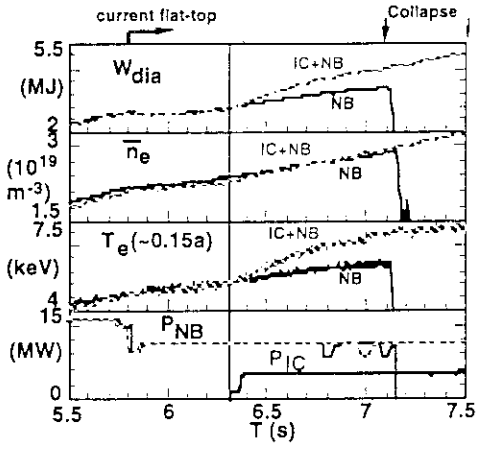

Fig. 1 Typical time evolution of negative shear experiment with combined ICRF (4 MW) and NBI (9 MW) heating, or NBI heating (9 MW) alone at I_P=2 MA and B_T=3.3 T. The negative shear configuration was produced by current ramp-up with early beam injection (pre-NBI heating). The plasma current reached the flat-top at 5.8 sec, and the NBI power was reduced from 13 MW (for pre-heating) to 9 MW (for main heating). Then 4 MW of ICRF power was injected in the combined heating case. It should be noted that while the plasma collapsed at 7.1 s in the NBI only case, it survived up to 7.5 s i.e., just after the ICRF was turned off.

The tail ion stored energy due to ICRF heating was comparable to that of a positive shear discharge. While TAE modes were unstable in the positive shear discharge, they were stable when a strong ITB was formed in the negative shear discharges. TAE modes (90-110 kHz, n=5-8) were observed only after the density profile broadened, due to sequential partial collapses. The mode frequency range is consistent with theoretical TAE mode frequency assuming q~2, which is close to the value of q_{min}. The behaviour of TAE modes in negative shear plasmas was analyzed with the NOVA-K code. It was found that the stability of TAE modes is sensitive to the gap alignment just inside q_{min} and that the calculations agree qualitatively with the experimental results.

Reference

[1] H. Kimura et al., Proceedings of the 16th IAEA Fusion Energy Conference, Montreal, 1997, paper F1-CN-64/E-6 (IAEA, Vienna, to be published).

---

[1] Ioffe Physical-Technical Institute, Russia

[2] Princeton Plasma Physics Laboratory, U.S.A.

5.4 ICRF Coupling at 102 MHz

S. Moriyama, H. Kimura, N. Asakura, and M. Saigusa

5.4.1 Frequency Change to 102 MHz from 116 MHz

The frequency of ICRF system was changed to 102 MHz from 116 MHz in December 1995, in order to keep up with the low toroidal magnetic field (B_T) operation in JT-60U. The resonant B_T of the second harmonics of hydrogen on the axis of JT-60U plasma was reduced from 3.8 T to 3.34 T. From January 1996, RF power at 102 MHz had been injected to the JT-60U. Impedance matching between the antenna and the transmission line using the stub tuners and the high power phase shifters, adjustment of the phase control, and the antenna conditioning were taken place.

5.4.2 Impedance Matching and Antenna Aging at 102 MHz

About 80 shots were devoted to impedance matching and antenna aging after the frequency change. Figure 1 shows the history of impedance matching and antenna aging after the frequency change. After precise impedance matching, the power reflection coefficient reached ~ 5 % which is low enough to couple 5 MW, for the RF generator.

As the results of antenna aging, 4.3 MW (short pulse) was coupled in 80 shots and 4.6 MW for 1 sec at last in November 1996. The maximum voltage stand-off in the antenna was ~ 34 kV and is close to the maximum voltage achieved at 116 MHz. It means that low coupling resistance limited the power.

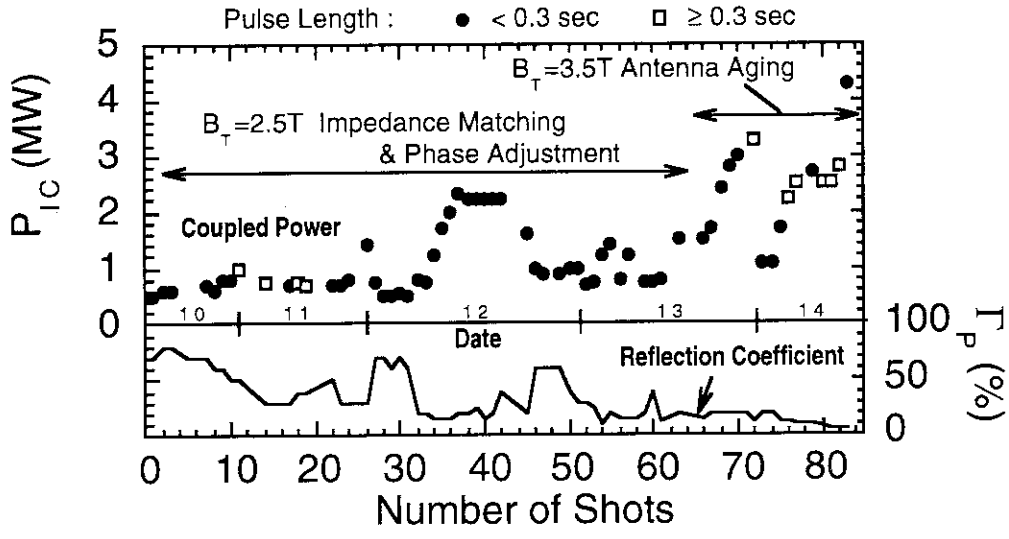

Fig. 1 Impedance matching and antenna aging in the first ~80 shots after the frequency change

5.4.3 Coupling Resistance

After the frequency change to 102 MHz, the coupling resistance of the antenna, R_C, was 60 - 70% of that at 116 MHz. Figure 2 shows the R_C against the gap between the Separatrix and first wall of the vacuum vessel on equatorial plane. The Faraday shield of the ICRF antenna is ~ 3 cm behind the first wall surface. As a result of the reduction of R_C, the voltage stand-off in the antenna was larger at 102 MHz at the same coupled power, P_{IC} as sown in Fig. 3. It is clear that the P_{IC} was limited by the antenna voltage stand-off at 102 MHz. In contrast with at 102 MHz, P_{IC} was limited mainly by the generator capability at 116 MHz[1]. Reason of the R_C reduction is examined in 5.6.5.

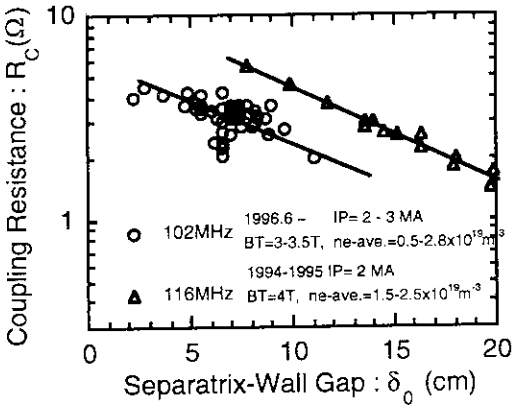

Fig. 2 Coupling resistance at 116 and 102 MHz

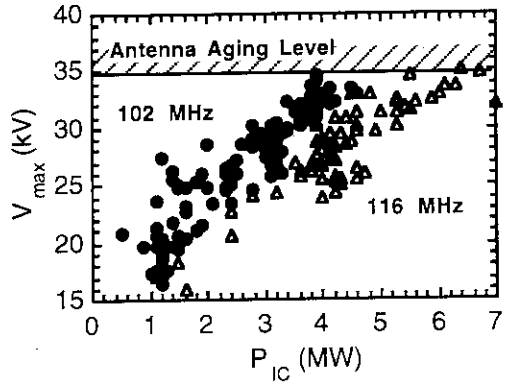

Fig. 3 Coupled power limited by the antenna voltage stand-off at 102 MHz.

5.4.4 Coupling to High n_e Plasma

Coupling to high electron density (n_e) plasma was tried in order to obtain higher coupling resistance at 102 MHz expecting increase of the second scrape off layer (SOL) density. However, improvement in R_C was small probably due to highly elongated configuration of the plasma (Fig. 4). The reciprocating probe[2] measurement shows that the second SOL did not change significantly with $\overline{n_e}$. Probably the second SOL was scraped off by the first wall at above and below the antenna because of the difference in the shape of Separatrix and the first wall due to the plasma configuration. In addition, no difference in Rc was observed between He and D plasma.

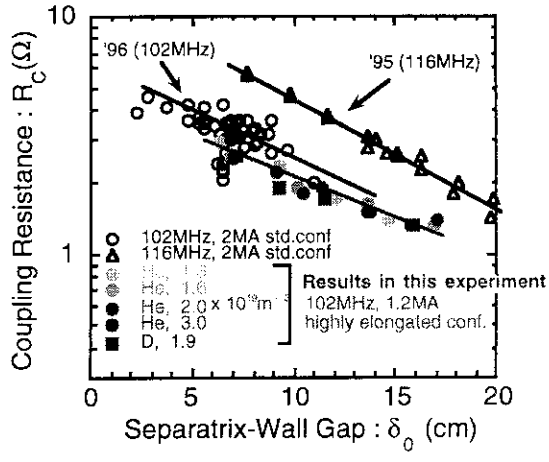

Fig. 4 Coupling to high density, highly elongated configuration I plasma.
I_P = 1.2 MA, B_T = 3.5 T, $\overline{n_e}$ ~ 1.3 - 3.0 x 10^{19} m^{-3} (He), $\overline{n_e}$ ~ 1.9 x 10^{19} m^{-3} (D) (up to near density limit)

5.4.5 SOL Profile and Coupling Calculation

Antenna coupling resistance is calculated using a coupling code[3] in order to examine the reason of low R_C at 102 MHz (Fig. 5). An example of the assumed plasma density profile based on the reciprocating probe measurement is shown in Fig. 6. The calculated R_C is close to the measurement as shown in Fig. 5. Some differences between the calculation and measurement in 116 MHz case are probably due to the low density limitation of the coupling code. Though the code cannot calculate wide second scrape off with $\overline{n_e} < \overline{n_e}^c$, where $\overline{n_e}^c$ is the cut off density of the first wave, narrower second scrape off is assumed in such cases.

The toroidal magnetic field, B_T, is different in 102 and 116 MHz operations, because the ICRF resonance is normally on axis. Difference in R_C due to the difference in q which comes from difference of B_T, is small as shown in Fig. 6. This results show the reduction of R_C at 102 MHz is due to RF characteristics of the ICRF antenna itself which was designed to obtain best coupling at around 120 MHz.

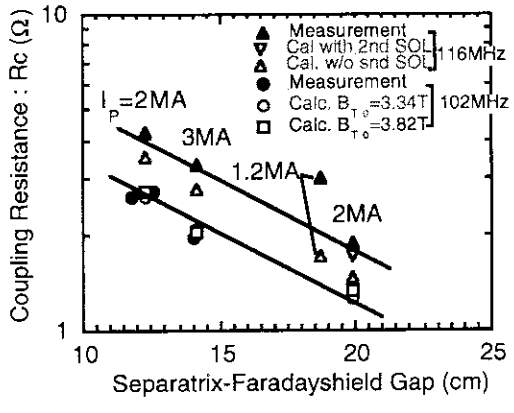

Fig. 5 Comparison between observed and calculated coupling resistance at 102 and 116 MHz

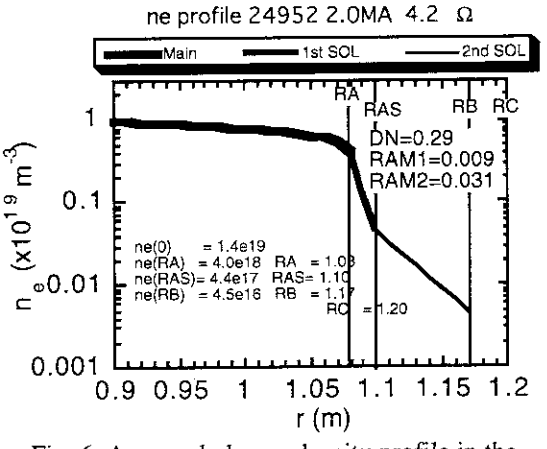

Fig. 6 Assumed plasma density profile in the coupling calculation. The profile is based on the reciprocating probe measurement.

5.4.6 Summary

4.6 MW of ICRF power (P_{IC}) was successfully coupled at 102 MHz. P_{IC} is limited by the antenna voltage limit (aging level) because of low Coupling resistance (R_C). Reduction of R_C comes from RF characteristics of the antenna which was designed to obtain best coupling at ~ 120 MHz. For the closed divertor plasma expected in the operation in 1997, a little larger antenna-sparatrix gap and lower SOL density due to the baffle plate is foreseen. Lower R_C is expected, however modification of stub tuner will enable trials for higher antenna voltage stand-off. Improvement of antenna voltage stand-off limit is effective to couple higher power.

References

1) S. Moriyama, et al., "ICRF Coupling Study and Technology Development for JT-60U", Proc. US-Japan workshop for RF technology, Florida, Dec. 1995.

2) N. Asakura, S. Tsuji-Iio, Y. Ikeda, Y. Neyatani, M. Seki, "Fast reciprocating probe system for local scrape-off layer measurements in front of the lower hybrid launcher on JT-60U", Rev. Sci. Instrum.

3) M. Saigusa, T. Fujii, H. Kimura, S. Moriyama, et al., "Electrical Design and Test of ICRF Antenna for JT-60U", Fusion Engineering and Design, 24, (1994)47-64.

5.5 Neutron sawtooth behavior in ICRF Heating

A. Morioka, K. Tobita, H. Kimura, S. Ishida, T. Nishitani,
H. Harano, N. Isei, Y. Kusama

1. Introduction

In fusion reactor, the fast ions spewed by sawtooth crashes from plasma can damage the first wall. It is important to understand the effect of sawtooth instability on fast ions transport. The research from both experiment and theory are advanced about the mechanism of disorption of fast ions without well understanding on sawtooth instability. It is reported that neutron emission by considering fast ions behavior at sawtooth crashes can explain[1]. The behavior of neutral beam ions (NB ions) spewed by giant sawtooth crash from plasma center is examined by measurement of 2.45MeV neutrons (beam-thermal reaction dominant) formed in DD reaction. In this section, 2.45MeV neutron sawtooth behavior in ICRF heating is reported.

2. Experiment

In the minority ions(proton) ICRF heated deuterium plasmas, the giant sawtooth crash is always observed. The parameter of discharges ranges the plasma current I_p=2MA, the magnetic field B_t=3.5T, electron density $\overline{n_e}$=1.3~1.9x$10^{19}m^{-3}$, central electron temperature $T_e(0)$=2.5~7keV and neutral beam power P_{NB}=10MW. The line averaged electron density was measured by FIR and CO_2 interferometers. The electron density profile was measured by Ruby and YAG Thomson scattering. The electron temperature profile was measured by Thomson scattering and ECE grating polychromatar. The ion temperature profile was measured by charge-exchange recombination spectroscopy(CXRS). The neutron emission was measured by collimated plastic scintilator[2] and uncollimated fission chambers[3].

3. Experimental results

A time evolution of plasma with giant sawtooth crash is shown in Fig.1. The neutron emission profile before giant sawtooth crash calculated by using TOPICS code[4] is shown in Fig.2. The central neutron emission(I_n) which dominated by beam-thermal reaction is proportional to the product of deuterium density (n_D) of thermal component, NB ion's density (n_b) and fusion cross section ($<\sigma v>_{DD}$). The time evolution of central neutron emission and total neutron emission(S_n : mainly contributed from the regime of ρ=0.3-0.6) after sawtooth crashes is shown in Fig.3. Though the central neutron emission decreases, when the inversion radius(R_{inv}) is under 0.4, total neutron emission is almost constant. In the case of $R_{inv} \cong 0.5$, both central and total neutron emission decrease. In the sawtooth crash where the n_b component in plasmas is almost same, the fractional changes of central neutron emission for the

fractional changes of averaged electron density is shown in Fig.4. It is assumed that becomes $\Delta\overline{n_e}/\overline{n_e} \propto \Delta\overline{n_D}/\overline{n_D}$, when Z_{eff} is constant around sawtooth crash. From this results, fractional changes of the central neutron emission can be explained by fractional changes of the bulk ion density. However, when the inversion radius is about 0.5, fractional changes of central neutron emission become 2 or 3 times longer than the amount of fractional changes of the bulk plasma, and it indicates the disorption from plasma center of the n_b component.

4. Conclusion

The behavior of NB ions was examined by the measurement of time evolution of neutron emission in sawtooth crashes observed in minority ion ICRF heating experiment. The central neutron emission decreases with sawtooth crashes, when the inversion radius is under 0.4. It is considered that there are small effects of fast ions transport, because total neutron emission are almost fixed. Both centers and total neutron emission decrease about 10% with a sawtooth crash, when the inversion radius is 0.5. When sawtooth crash generated in outside from this region, the effect of fast ions transport is large, and then there is some possibility of the loss to outside of the plasma.

References

[1] J.A. Loberg, W.W. Heidbrink,et al.: PPPL-2558 (1988) ;
Phys. Fluids B**1**, 4, 874(1988)
[2] A. Morioka, T. Nishitani, et al.: Section 10.8 in this review.
[3] T. Nishitani, et al.: Rev. Sci. Instrum., **63**, 5270 (1992)
[4] Naka fusion reseach establishment, JAERI-M 91-159 (1991)

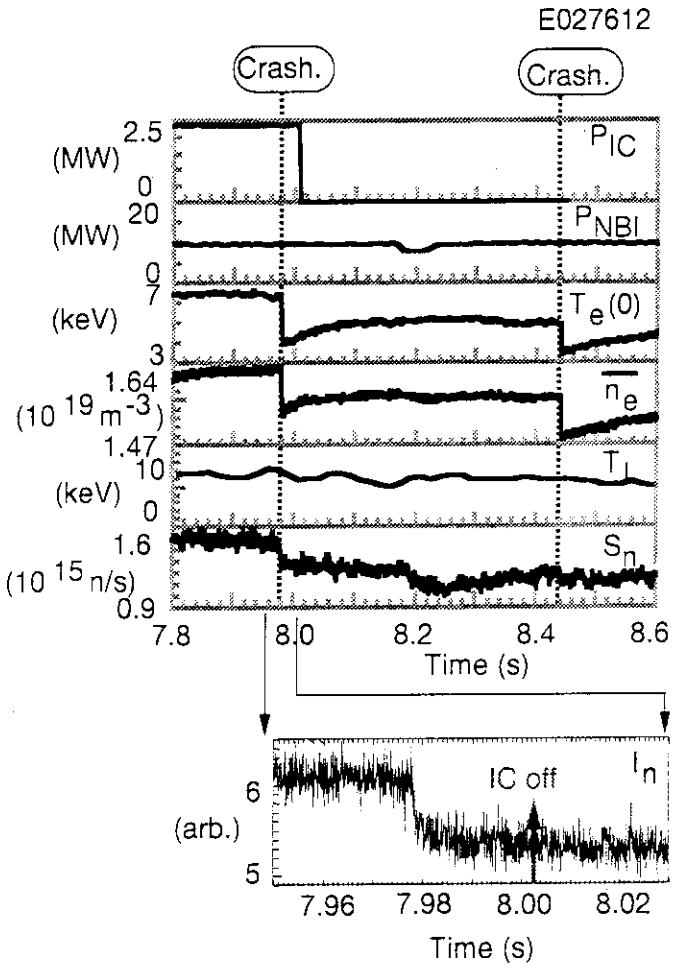

Fig.1. The time evolution of the plasma including the giant sawtooth crash

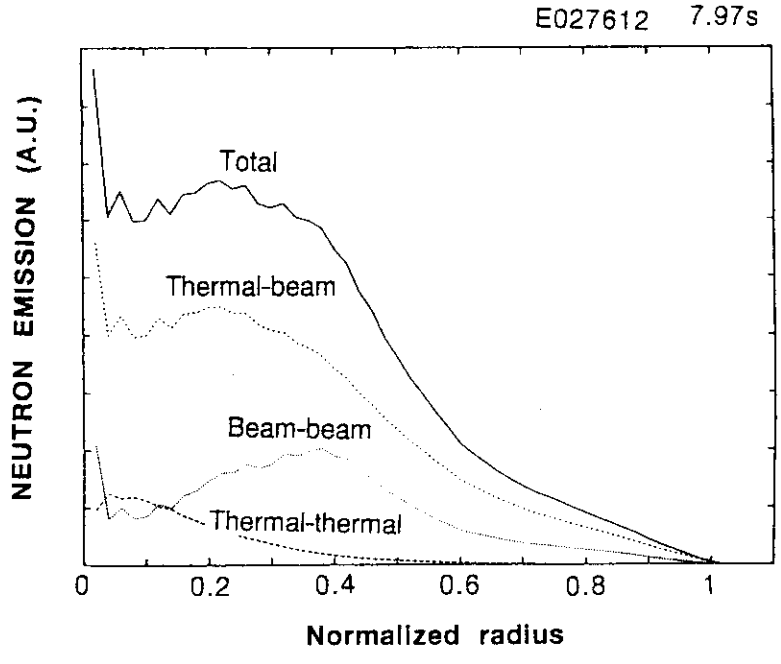

Fig.2. Neutron emission profile calculated by TOPICS code

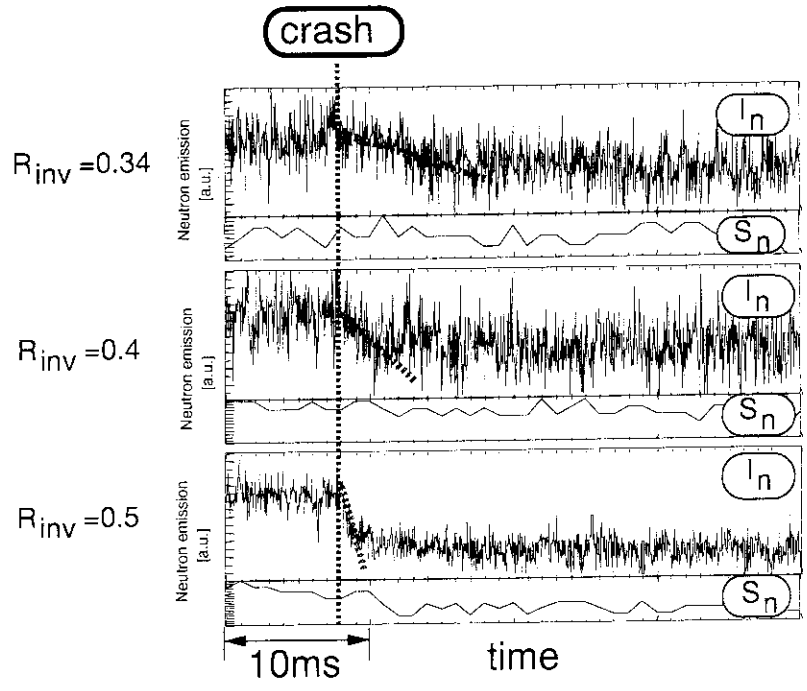

Fig.3 The time evolution of central neutron emission and total neutron emission after the sawtooth crash

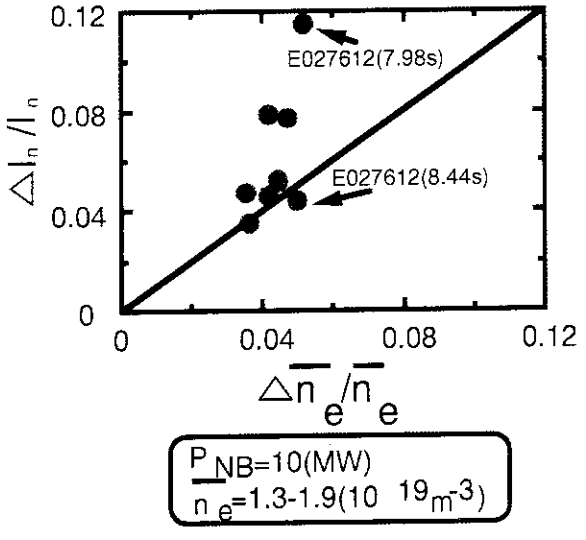

Fig.4 Fractional drop in central nutron emission versus fractional drop in average electron density for ICRH discharges.

5.6 TAE modes in low-q plasmas

M. Saigusa, H. Kimura, G. J. Kramer, Y. Kusama, S. Moriyama, T. Oikawa, T. Kondoh, N. Isei

Abstract Toroidicity-induced Alfvén eigen (TAE) modes excited by ICRH were studied in low-q plasma. Low shear TAE modes and bi-directional TAE modes were observed for the first time. The location of TAE modes shifted from the outside to inside q=1 surface following the expansion of q=1 surface caused by current diffusion into core region. The TAE modes inside q=1 surface (tornado modes) are much more harmful for energetic ion confinement than the TAE modes outside q=1 surface.

Toroidicity-induced Alfvén eigen (TAE) modes are expected to be excited by energetic fusion products, whose speeds are comparable to the Alfvén speed[1]. The degradation of the energetic particle confinement due to TAE modes has been investigated in JT-60U [2]. For study the behavior of TAE modes in a low-q plasma like ITER's target plasma (q_{95}~3), TAE mode experiments in low-q discharges have been performed by using second harmonic hydrogen minority ion cyclotron resonance heating (ICRH) in helium (^{4}He) majority plasma at a frequency of 102 MHz in JT-60U. The parameters of target plasma are a plasma current of 2.6 MA, a safety factor (q_{95}) of 2.8, and a toroidal magnetic field on axis of 3.3 T, where the hydrogen ion concentration is about 10 %.

Figure 1 shows the time evolution of the TAE mode frequency spectra in the typical low-q discharge. The toroidal mode number of observed TAE modes increased one by one during the first and second ICRH pulses, while they decreased one by one during the third and forth ICRH pulses. The main reason of the behavior of the toroidal mode number of the TAE modes can be explained with the expansion of the q=1 surface due to the current diffusion into core region.

Sequence of the appearance of observed TAE modes on the Alfvén continuum gap (ACG) map [3] in the low-q discharge is shown in Fig. 2. The open symbols show the Alfvén continuum gap on the safety factor against the toroidal mode number plane. The closed circles show the observed TAE modes estimated from the measured frequencies. The curved arrows indicate the order of the TAE mode appearance in a low-q discharge. The horizontal hatched region indicates the assumed high pressure gradient layer (ΔP_h) of the energetic particles, where TAE modes can be excited by the pressure driven diamagnetic drift of the energetic ions via inverse Landau damping. The n behavior of the observed TAE modes can be explained by our physical model. The safety factor in the high ΔP_h region decreased gradually due to the current diffusion into core plasma, so that the toroidal mode numbers of the excited TAE modes increased one by one outside q=1 surface, while they decreased one by one inside q=1

surface. By the way, the lower n TAE modes might be excited more easily than higher n one as long as within high ΔP_h region in JT-60U.

The typical two discharges for the TAE modes outside q=1 surface and inside q=1 surface are shown in Figs. 3(a) and 3(b), respectively. Both discharges have almost the same plasma conditions except the start time of ICRH and NBI pulses. ICRH was applied for exciting the TAE modes and the perpendicular NBI unit (#14) was applied for measuring the profiles of the toroidal rotation velocity and the ion temperature with charge exchange recombination spectroscopy (CXRS). Counter tangential NBI (#7b) was applied for measuring the q profile with the motional stark effect (MSE), where the accelerated beam voltages were about 85 keV. The injection angles of the tangential and perpendicular NB units are -35.5° and -75° with respect to the magnetic axis, respectively. The signals shown in Fig. 3 are the TAE mode frequency spectra measured with the Mirnov coil array, the plasma stored energy evaluated with diamagnetic loop coils (W_{dia}), the line averaged electron density ($\overline{n_e}$), the central electron temperature ($T_e(0)$) measured with electron cyclotron emission, the neutron count produced by the nuclear reaction between high energy protons over 3 MeV and the impurity boron ions: $^{11}B(p, n)^{11}C$, which means 3 MeV proton population [4], the coupled ICRH power (P_{IC}) of about 3.8 MW, and the total hydrogen NBI power (P_{NBI}) of about 1.5 MW. In addition, the hatched periods indicate the appearance of TAE modes.

There are the significant differences of the effect of TAE modes on the energy confinements between inside and outside q=1 surface. The low-n TAE modes (n=3 and 4) estimated to be outside q=1 surface has no effect on the plasma parameters except small vibration of the neutron signal. On the other hand, the plasma stored energy, the central electron temperature and the 3 MeV proton population cramped or decreased during the high-n multiple TAE modes (we call tornado mode) in Fig. 3(b).

Figures 4(a) and 4(b) show the calculated Alfvén continua at the appearance of the n=3 TAE mode outside q=1 surface in Fig. 3(a) and the n=6 TAE modes inside q=1 surface in Fig. 3(b), respectively. The solid waved lines show the Alfvén continua calculated by the code: MEUDASGC using the measured plasma parameters. The horizontal straight line and closed circle show the observed TAE mode frequencies considering Doppler shift due to toroidal rotation and the estimated gap for the TAE modes. The vertical dotted line in each figure shows the location of q=1 surface. Both figures indicate that the radial location of the tornado mode is inner than that of TAE modes outside q=1 surface. The overlapping resonance like "domino" between multiple high-n TAE modes may occur to enhance stochastic diffusion. These may be the reasons why the tornado mode is more harmful for energetic ions in core region than normal TAE modes outside q=1 surface.

The typical frequency spectra of the low shear TAE modes predicted by J. Candy [5] are shown in Fig. 5. The theory predicted the many TAE modes in the same Alfvén continuum gap, that is, many odd and even TAE modes with the same toroidal mode number and the

different radial mode numbers. We obtained the target low shear plasma by making low-q and low-li plasma. Many TAE modes appeared from 6.3 s and disappeared at the end of ICRH pulse (6.27-7.14 s). Especially, three n=4 TAE modes adjacent frequencies appeared, and only one mode survived at 7.1 s, probably due to the increase in the magnetic shear. These phenomena agree with the theoretical prediction, qualitatively.

Figure 6 shows the typical frequency spectra of tornado modes including bi-directional modes (n=4 and 5) at a high electron density ($\overline{n_e}$~$2.8\times10^{19}m^{-3}$) in low-q and higher-li discharge. The frequency differences between co-propagating mode and counter-propagating one are proportional to the toroidal mode number. The angular frequency difference ($\Delta\omega$) between co-propagating mode (ω_{+n}) and counter-propagating mode (ω_{-n}) was predicted by the following formula [6]: $\Delta\omega = \omega_{+n} - \omega_{-n}=\omega^*_i+2\omega_t$ (5.6-1), where ω^*_i is diamagnetic drift angular frequency of the energetic ions, and ω_t is toroidal rotation angular frequency. If the driving mechanism is inverse Landau damping due to diamagnetic drift of energetic ions, the bi-directional TAE modes could not be observed in the same radial position. However, the observed bi-directional TAE modes were proved to be located on the same Alfvén continuum gap by the Eq. (5.6-1) using measured data. In shot E28255, the observed frequency differences were 21.0 kHz and 24.7 kHz at n=5 and n=6 bi-directional TAE modes, respectively. Then, the estimated frequency differences of both bi-directional TAE modes, which are 19.8 kHz in n=5 and 23.7 kHz in n=6, almost agree with the observed frequency differences. The bi-directional modes have been observed only at a high electron density plasma ($\overline{n_e}$> $2\times10^{19}m^{-3}$). Therefore, the bi-directional TAE modes may be excited by non-linear coupling between both modes.

As a summary, the new type TAE modes excited by trapped energetic ions were observed in low-q discharge (q_{95}~2.8), which is similar with the target plasma in ITER (q_{95}~3). Low shear TAE modes predicted by theory were observed outside q=1 surface in low-li plasma (li~1.0), while the bi-directional TAE modes were observed inside q=1 surface in high-li (li~1.25) and high electron density plasma (>$2\times10^{19}m^{-3}$) for the first time. The TAE modes shifted from outside to inside q=1 surface due to the expansion of q=1 surface in low-q discharge. The high-n multiple TAE modes inside q=1 surface (tornado modes) are much more harmful for energetic ion confinement than the low-n TAE modes outside q=1 surface.

References

1) C.Z. Cheng et al., Ann. Phys. NY 161, 21(1984).
2) H. Kimura et al., Journal of Plasma and Fusion Research, **71**, 1147 (1995).
3) M. Saigusa et al., Plasma Phys. Control. Fusion Res., **37**, 295 (1995).
4) T. Kondoh et al., Journal of Plasma and Fusion Research, **72**, 1397 (1996).
5) J. Candy et al., Physics letters A, **215**, 299 (1996).
6) L.E. Sugiyama et al., Bulletin of 38 th APS meeting, Denver, **41**, No.7, 1584 (1996).

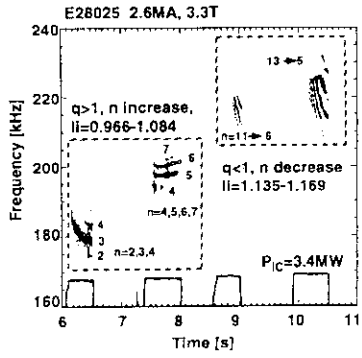

Fig. 1 Time evolution for TAE mode frequency spectra in low-q discharge.

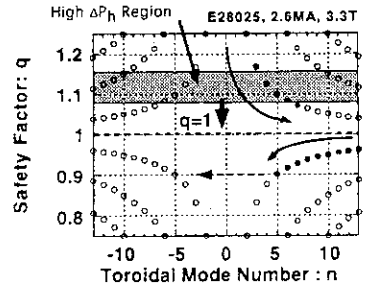

Fig. 2 Sequence of the appearance of TAE modes on the ACG map in low-q discharge. TAE modes move from high-q to low-q region due to current diffusion into core region.

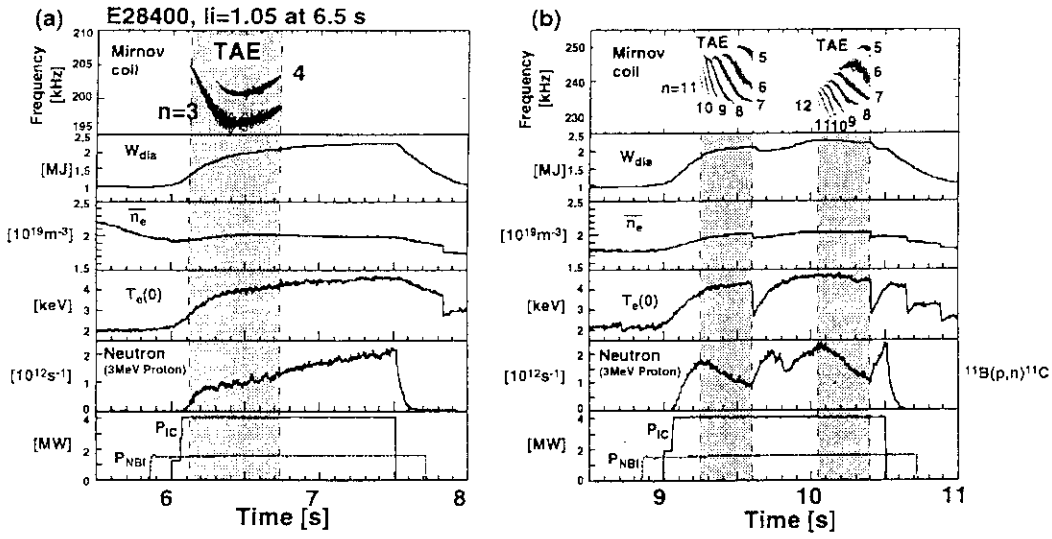

Fig. 3 Typical discharges for (a) TAE modes outside q=1 surface and (b) the TAE modes inside q=1 surface (tornado mode). Both discharge has almost the same plasma condition except start time of ICRH and NBI.

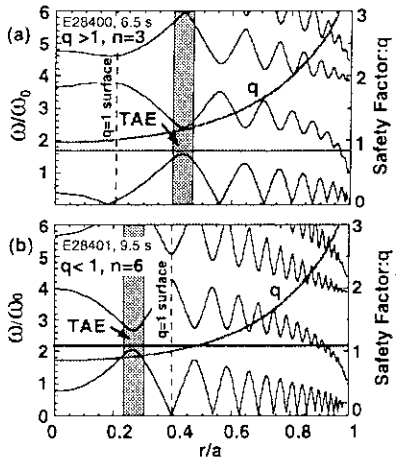

Fig. 4 Alfvén continua at the appearance of TAE modes in Fig. 3. (a) TAE modes outside q=1 surface. (b) TAE modes inside q=1 surface. Horizontal lines show the observed TAE mode frequencies.

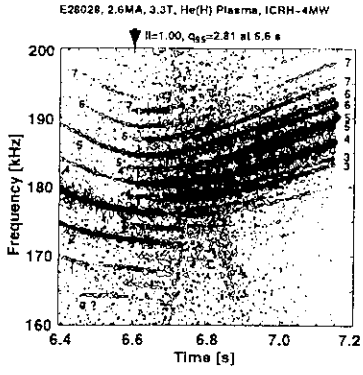

Fig. 5 Typical frequency spectra of the low shear multiple TAE modes outside q=1 surface.

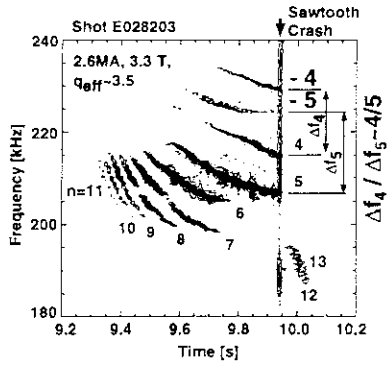

Fig. 6 Typical frequency spectra of tornado modes including bi-directional modes (n=4 and 5) in low-q and higher-li discharge.

5.7 Noncircular triangularity and Ellipticity induced Alfvén eigenmodes observed in JT-60U [1].

G.J. KRAMER, M. SAIGUSA, T. OZEKI, Y. KUSAMA, H. KIMURA, T. OIKAWA, K. TOBITA, G. FU†, C.Z. CHENG†.

†*PPPL, Prinston University, Prinston, New Jersey 08543, U.S.A.*

Toroidicity induced Alfvén Eigenmodes (TAE) which can exist in the lowest gap of the shear Alfvén continuum, where the poloidal harmonics with mode numbers m and $m+1$ couple, have been studied in the past [2]. In the next higher gap, which is created by the coupling of poloidal harmonics with mode numbers m and $m+2$, Ellipticity induced Alfvén Eigenmodes (EAE) can reside. They were observed in DIII-D [3] and JET [4]. The third gap is created by coupling of the poloidal harmonics with mode numbers m and $m+3$ and these modes are called Noncircular triangularity induced Alfvén Eigenmodes (NAE). The NAE modes have been seen in JT-60U for the first time ever.

The frequency of the AE modes is approximately given by: $\omega = v_A \Delta m/2qR$, with $\Delta m = 1, 2, 3$ for the TAE, EAE, and NAE modes, respectively, v_A the Alfvén velocity, R the major radius and q the q-surface where the mode has its maximum amplitude.

Ion Cyclotron Resonance Frequency (ICRF) heating was used create an energetic ion population that can excite the AE modes. The AE modes were detected with the fast sampled (sampling frequency: 1 MHz) Mirnov coil system. From phase differences of these signals, obtained from a Fast Fourier Transform, toroidal mode numbers were determined.

In Fig. 1 a discharge is shown in which TAE, EAE and NAE activity was observed. The TAE modes with mode toroidal mode numbers between one and five were observed between 160 and 220 kHz. One EAE mode was observed with toroidal mode number one at 430 kHz and one NAE mode at about 505 kHz with toroidal mode number three was seen.

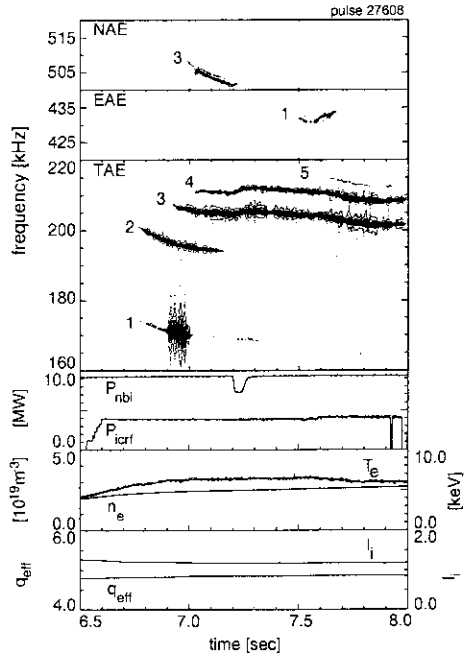

FIG. 1 Time traces of a shot where AE modes were observed. From the top to the bottom are shown: The Mirnov coil signal of the NAE mode, the EAE mode and the TAE modes, the NBI and ICRF power, the line averaged density and the central electron temperature from the ECE polychromator, and the internal inductance, ℓ_i, and q-effective. The AE modes are labeled with their toroidal mode number.

1. G.J. Kramer *et al.* submitted to Phys. Rev. Lett.
2. M. Saigusa *et al.* Plasma Phys. and Contr. Fusion, **37** (1995) 295.
3. A.D. Turnbull *et al.* Phys. Fluids, **B5** (1993) 2546.
4. A. Fasoli *et al.* Nucl. Fusion **35** (1995) 1485.

5.8 Ion Cyclotron Emission (ICE) Measurements in JT-60U

O. Da Costa, H. Kimura, S. Moriyama, K. Tobita, M. Saigusa and the JT-60 Team

In a fusion reactor, the highly energetic α-particles created by the D-T fusion reactions will provide the main heating by collisions with the background electrons or ions. Diagnostics of fast ions are therefore essential in a tokamak. Among the various methods, Ion Cyclotron Emission (ICE) is one of the simplest and most promising[1]. It consists in measuring the radiation emitted by the ions rotating around the magnetic field lines at the first harmonics of cyclotron frequency ($f \sim$ 10-200 MHz). The radiation detected is principally due to the fast ions, even if they are in a very small minority in comparison with the thermal ions.

In JT-60U, the electric field of this wave is measured by 3 RF probes located below an ICRF antenna on the outer wall of the vacuum vessel[2]. The system was recently modified so as to measure independently the parallel and perpendicular electric fields by combining the signals of the 3 probes[3]. The signals are processed using spectrum with fast repeated sweeps in frequency (10-200 MHz in 5 ms with a small resolution bandwidth of 0.3 MHz) to study the frequency of emission peaks or set at fixed frequencies (with a large bandwidth of 5 MHz) to study the time evolution of ICE with discharge parameters, the correlation with MHD activity and the correlation between emissions at low and high harmonics...

In NBI-heated plasma, the perpendicular electric field spectra are formed of narrow, regularly spaced peaks [fig. 1]. Their frequencies correspond to the cyclotron harmonics of the main ion species taken at the plasma outer edge. This is similar to the previous results in other tokamaks. In high β_p discharges we detect emission peaks corresponding to the first 3 cyclotron harmonics of fusion tritons at the plasma center ($R \approx$ 3.1-3.2 m) [fig. 2]. This is the first time that emission from the plasma center and from fusion tritons is detected in a tokamak.

The parallel electric field spectra are almost flat. This is compatible with the hypothesis that the wave received is the Alfvén Magnetoacoustic mode.

The measurement of ICE during ICRF heating shows the redistribution of the emission peaks due to parametric instabilities [fig. 3].

We observe correlations between ICE at fixed frequencies and elms [fig. 4]. We also observe oscillations in ICE due to the expulsion of fast ions from the plasma center during fishbone-type instabilities [fig. 5]. We do not observe any evidence of correlation with TAE modes.

References

1) O. Da Costa and H. Kimura, 3rd Public Seminar on Basic Research of Atomic Energy in JAERI, Tokyo, 1996.
2) O. Da Costa et al, International Conference on Plasma Physics, Nagoya, 1996.
3) O. Da Costa et al, International Energy Agency Tripartite Workshop on TAE Modes and Energetic Particle Physics, Naka, 1997.

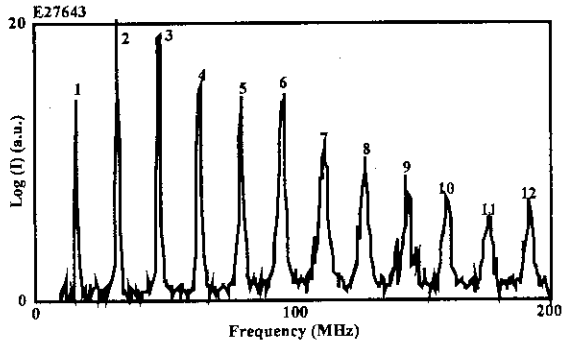

Fig. 1: ICE spectrum from 10 to 200 MHz. Emission from deuterons at mid-plane outer edge.

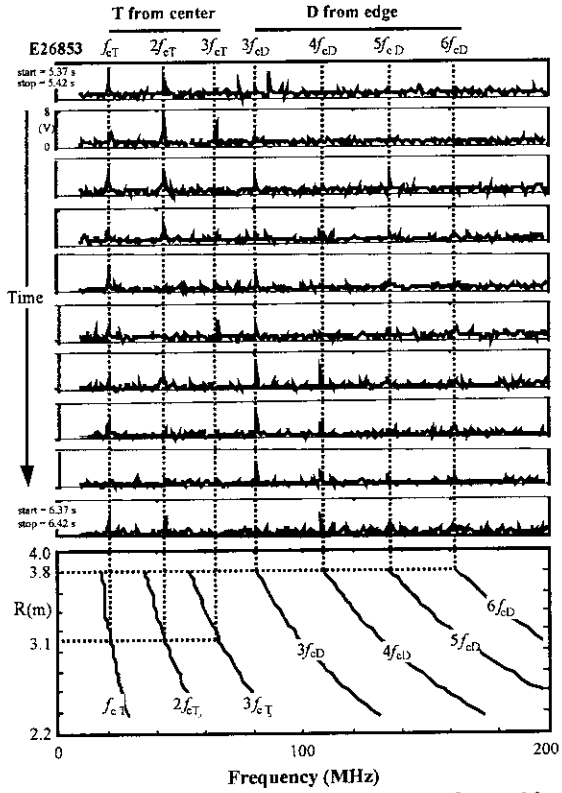

Fig. 2 : 10 consecutive ICE spectra from 10 to 200 MHz with emission peaks from fusion tritons at the plasma center (R = 3.1 m) and from NB-injected deuterons at mid-plane outer edge (R = 3.8 m).

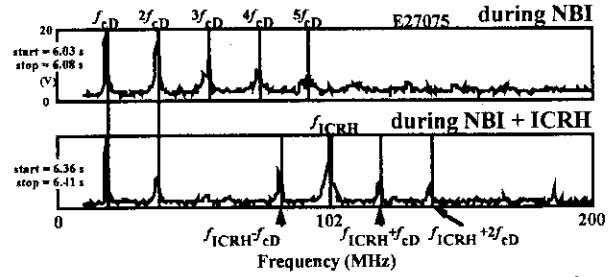

Fig. 3 : ICE spectra showing the redistribution of emission peaks during ICRH due to the parametric decay wave.

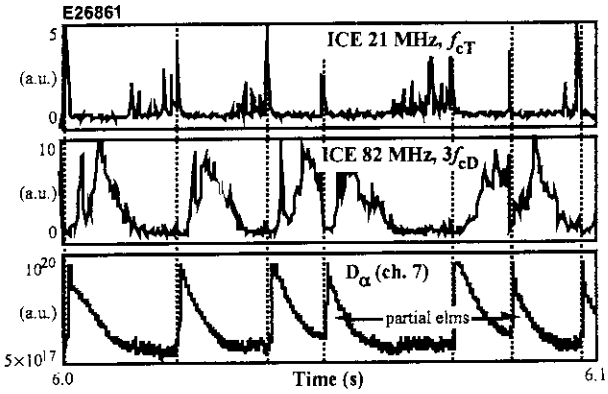

Fig. 3 : Correlation of first harmonic of Tritium (21 MHz) and anticorrelation of third harmonic of Deuterium (82 MHz) with D_α showing elms.

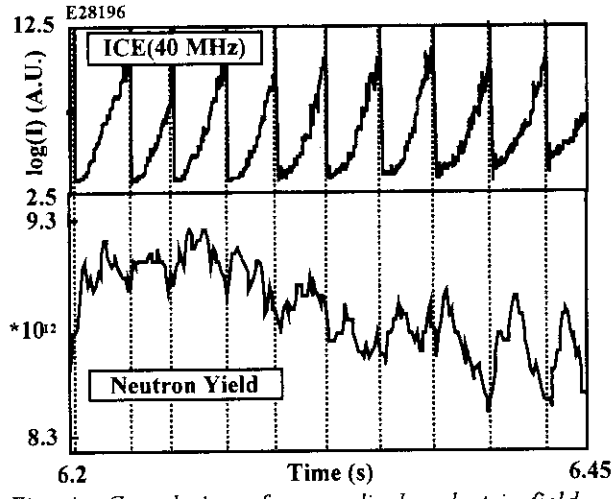

Fig. 4 : Correlation of perpendicular electric field (40 MHz) with Neutron Yield during (n=1) Fishbone-Type instability.

6. Current Drive

6.1 Steady-State Operation Research in JT-60U[1]

K. Ushigusa and the JT-60 Team

1. INTRODUCTION

Objectives of the JT-60 research are to establish the physics basis for a steady-state tokamak fusion reactor and to contribute to the ITER physics R&D. Significant progress in key physics issues such as improved confinement, radiative divertor, non-inductive current drive (CD), profile control, stable high normalized beta, fast particle physics was achieved in JT-60U in the recent years. Two important systems have been newly installed in JT-60U. To improve the stability at the plasma edge and to allow high fusion performance in a higher density regime, the triangularity control system has been installed in JT-60U. The triangularity δ can be controlled from -0.06 to 0.6 at I_p=1MA, and from -0.03 to 0.3 at I_p = 2MA with no large change of the plasma volume. The negative-ion based NBI (N-NBI) with a beam energy of 0.5MeV and the injection power of 10MW was installed in JT-60U in order to demonstrate efficient core heating and current drive in a reactor relevant plasma. This paper introduces recent progress on steady-state operation research the initial results of an N-NBI in JT-60U.

2. PROGRESS IN STEADY-STATE OPERATION RESEARCH

2.1 High β_p H-mode regime

With careful control of MHD activities during the current ramp-up phase at a low density, the high β_p H-mode was realized at the high current up to 2.7MA (q_{95} = 2.53). A fusion triple product of $n_D(0)\tau_E T_i(0)$ =1.53x10^{21}keVsm^{-3} with H-factor ~3.3 was achieved at Ip=2.4MA (q_{95}=3.9). A quasi steady-state high β_p ELMy H-mode with $n_D(0)\tau_E T_i(0)$ =0.51x10^{21}keVsm^{-3} (W_{dia} ~ 9.3MJ, H-factor = 2.05, and β_N ~ 2.0) was sustained for a duration of around 1.5τ_E.

An effect of the triangularity δ of the plasma shape has been studied to improve the edge stability and to enlarge the operational region of the high β_p H-mode to a higher density regime. In high δ operation (δ = 0.35), the normalized beta value of β_N ~ 2.5 and H-factor ~2.3 were sustained for 2.5 seconds without causing any large impurity influx from the divertor during high power NB pulses. With increase of δ up to 0.33 from 0.08, a fully non-inductive discharge with a high performance; a high bootstrap current fraction (I_{BS}/I_p ~ 60%), H-factor =2.0-2.5, β_N=2.6-3, and $n_D(0)\tau_E T_i(0)$ = 0.1x10^{21}keVsm^{-3} was sustained for 2 s (10τ_E). The duration of full CD condition in similar discharges with a low δ (δ =0.08) were limited to 0.6s due to a growth of low-n modes or carbon impurity influx from the divertor plates.

2.2 Reversed shear discharges

A wide negative shear region (r/a < 0.6) was produced by the NB injection into current ramp-up phase. The steep gradient in temperature and density at around the q_{min}

has been observed and a significant high fusion performance ($n_D(0)\tau_E T_i(0) = 0.68 \times 10^{21}$ keVsm^{-3}, W_{dia} =9.56MJ, Q_{DT} = 0.83) was realized in reversed shear plasmas. Lower hybrid current drive(LHCD) was examined to sustain a reversed shear configuration. A non-inductive hollow current was produced with a careful control of multi-peaked wave spectra excited by two different multi-junction launchers. The MSE measurement has indicated that q_o decreased gradually during LHCD. However, the reversed shear was kept for 7.5s until the end of LH pulse. It has been demonstrated that the magnetic shear and the core confinement of high power NB heated plasmas can be controlled by changing the launched wave spectra. Radiative divertor plasma with the internal transport barrier was produced by the neon gas injection into a reversed shear plasma. Results observed have indicated that the reversed shear is one of the attractive candidates for an advanced steady-state operation scenario.

2.3. Initial results of N-NBI experiments

The JT-60U N-NBI system was completed in March, 1996. After beam-conditioning since then, N-NB power of 2.5MW at a beam energy of 350keV was injected into JT-60 plasmas. Within uncertainty of the measured shine-through and Z_{eff}, the shine-through power could be explained by the theoretical prediction based on both a single-step and multi-step ionization cross-section. A characteristic time of the neutron decay after switch-off of the N-NB pulse was consistent with the theoretical prediction where the classical slowing down process was assumed. Giant sawteeth appeared during N-NBI and a peaked electron temperature profile was observed. Strongly anisotropic pressure and a total incremental energy confinement time longer compared with the positive-ion based NBI at E_B=80keV were observed, which indicated a significant contribution from energetic parallel beam ions. An effective core heating by N-NBI in high density reversed shear plasmas was also confirmed.

Current drive by N-NBI (350keV) was examined by injecting N-NBI into partially (~70%) current-driven discharge by positive-ion based NB(4MW of co-tangential beams and 4MW of perpendicular beams). During the N-NB pulse, the surface loop voltage became negative, indicating a fully non-inductive current drive. The neutron emission increased by a factor of 2. The surface voltage, the total stored energy and the neutron emission rate were reproduced by a 1.5D transport code TOPICS and ACCOME code. The code simulation predicted 0.28MA of N-NB driven current, which corresponds to the CD efficiency of ~0.8×10^{19}m^{-2}A/W with 27% of the shine-through power, while ~0.48×10^{19}m^{-2}A/W for P-NBI(80keV). These results indicate effectiveness of N-NBI as a core heating and current drive method in reactor relevant plasmas.

REFERENCES

[1] K. Ushigusa and the JT-60 Team, in proc. of the 16th IAEA Fusion Energy Conference (Montreal 1996), F1-CN-64/01-3.

6.2 Initial Result of Negative-Ion Based NBI in JT-60U

K. Ushigusa, O. Naito, M. Nemoto, Y. Kamada, T. Oikawa, T. Fujita, K. Tobita, Y. Kusama, M. Kuriyama, T. Itoh and the JT-60 Team

1. Introduction

As is well known, negative-ion based NBI (N-NBI) with an energy of MeV-class is required in a fusion reactor, to realize a high neutralization efficiency with an enough high beam energy to penetrate high density core plasmas. In order to develop heating and current drive method in a reactor, a negative-ion based NB system was installed in JT-60U. The first injection was made in Mar. 1996. The initial results of N-NBI experiments in JT-60U performed from Mar. to Oct. 1996 to survey the heating and current drive capability will be shown in this paper(1).

2. N-NBI System

A schematic drawing of the JT-60U N-NBI system is shown in Fig.1. A beam energy of 0.5MeV is adopted for a good central penetration in high density operation, with shine through below 5% in the density range of 0.5- $1x10^{20}m^{-3}$. An injection power of 10MW is determined to obtain clear N-NBI effects on heating and CD performance in high density and improved confinement modes produced by high power positive-ion based NBI (P-NBI). The total system efficiency of N-NBI system is estimated to be 40% including losses on power supply, a neutralization efficiency (60%), a geometrical efficiency (90%) and a re-ionization loss (2%). Extracted ions with a cross-section of $1.1x0.45m^{-2}$ from a negative ion generator (a volume production type) are accelerated up to 0.5MeV by electrostatic acceleration grids and focused on the JT-60U plasma of 24m away from the ion source. The distance between ion sources and the plasma center is around 27 m. Negative-ion beam is neutralized in the neutralizer tank where deuterium gas is fed at a gas line density of $7.5x10^{15}$ molecules/cm^2. The magnetic field in the ion passage from the ion source to the neutralizer cell is kept to be <0.05gauss against a large leakage field. The beam tangential radius is 2.6m while the typical plasma major radius is 3.4m. The beam profile is a Gaussian profile with around 15cm and 18cm e-folding width horizontally and vertically, respectively. The temperature increase in the beam target plates of the first wall during N-NB pulse with 2MW, 0.2 s injection without plasma was measured by both IRTV and thermo-couples. These temperature increases are roughly consistent with the values expected by heat propagation analysis. The heat load profile for lower ion source agreed with the designed profile, while there was another peak of heat load for upper ion source. Further adjustment is required for the upper beam line. Figure 2 shows the beam energy dependence of the neutralization efficiency. Results of JT-60 positive beams are shown as the solid symbols, while open

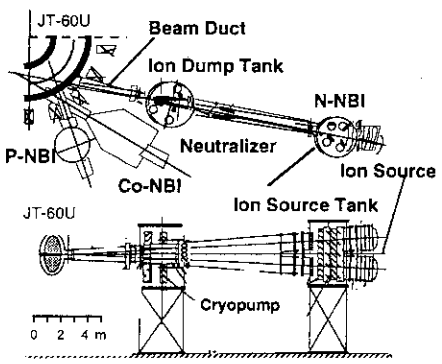

Fig.1 The JT-60U N-NBI System ; 0.5MeV, 10MW, 10s, D/H, Two ion sources.

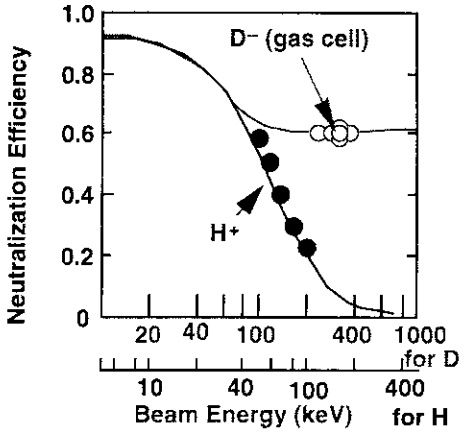

Fig.2 Neutralization efficiency of beam ion against the beam energy.

symbols show the N-NB data. Two lines are the theoretical prediction of neutralization efficiency for positive and negative ions. It was confirmed that the neutralization efficiency of the negative beam ions with the energy of 0.4MeV is around 60%, which is consistent with the theoretical predication. In the commissioning, the adjustment and the experiment of N-NBI for about half year, the injection power of 2.5MW(350keV), the maximum beam energy of 400keV, the pulse length of 1 second have been achieved in the plasma injection.

3. N-NB heating and beam ion behaviors

Typical example of N-NB injection into an OH discharge (1.15MA/2,24T) is shown in Fig.3a where 2.3MW of NNB power with the beam energy of 350keV was injected at the density of $1.5 \times 10^{19} m^{-3}$. It was found that the poloidal beta value evaluated by Shafranov lambda β_p^{equ} is much larger than the diamagnetically measured one β_p^{dia}, indicating a significant pressure anisotropy during N-NB injection. A giant sawtooth appears at t ~ 10.7s, and a peaked electron temperature is formed before the sawtooth crash as shown in Fig. 3b.

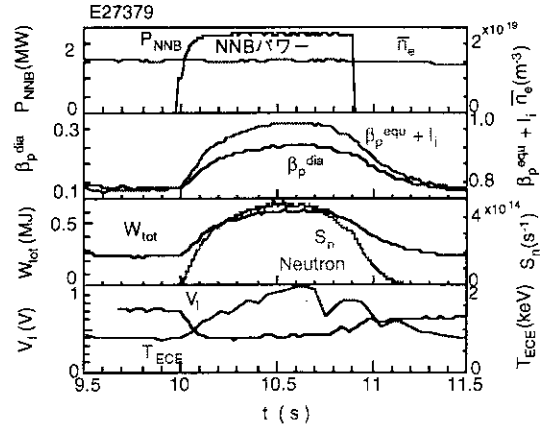

Fig.3a Time evolution of plasma parameters during N-NB Injection. Ip=1.15MA, BT=2.24T.

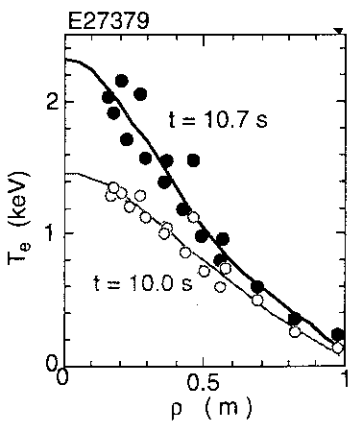

Fig. 3b Electron temperature profile with and without N-NBI.

The total incremental energy confinement time of N-NBI was longer than that of the positive NBI with the beam energy of 80keV by a factor of 1.5 at n_e ~$10^{19}m^{-3}$. This discrepancy dissappeard at higher density region (>$3x10^{19}m^{-3}$). Similar density dependence was seen in the pressure anisotropy during N-NBI, suggesting a significant contribution of the parallel beam energy component on the total energy content at low density regime in the case of N-NBI.

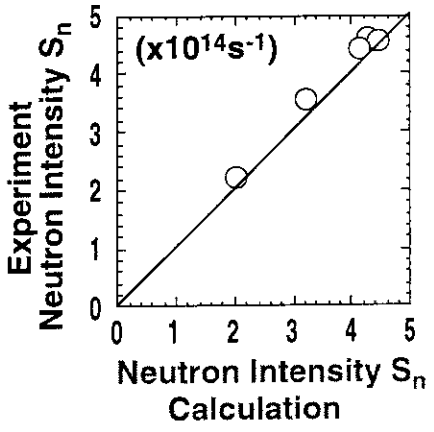

Fig.4a Comparison of neutron emission rate between experiment and calculation. E_B=350keV, n_e=(0.5-2.8)x$10^{19}m^{-3}$.

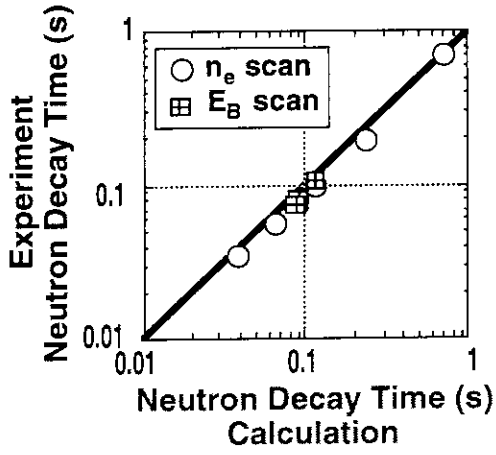

Fig. 4b Comparison of decay time of neutron signal between experiment and calculation. circles;E_B=350keV, n_e=(0.5-2.8)x$10^{19}m^{-3}$ squars; E_B=200-300keV, n_e=1.5x$10^{19}m^{-3}$

Dominant part of the neutron rate during N-NB injection at low density regime is due to the beam-thermal reaction. Therefore, the behaviors of the injected beam ions can be studied by analyzing the neutron signal. The neutron emission rate and the decay time are studied by changing the electron density and the beam energy. In Fig. 4, the observed neutron rate during N-NB and the decay time after N-NB switched off are compared with the theory. Here we use the time dependent 1.5D transport code, TOPICS, to estimate the time evolution of the neutron signal. Both the neutron emission rate and the decay time agree with the classical theory, indicating the classical behavior of the injected beam ions in this experimental parameter regime.

In order to confirm an effective core heating in high density plasmas, NNB was injected into a reversed shear plasma. After forming the reversed shear configuration with 11MW of the positive NB, the injection of 2MW NNB power increase the energy content by around 1MJ and the neutron signal by $3x10^{15}s^{-1}$. Increase in the energy content mainly comes from the increase in the thermal energy content, while the dominant part of the increase in neutron signal is due to the increase in beam-thermal reaction,. The βp collapse appeared during NNB pulse, indicating effective heating of NNB in reversed shear plasmas.

4. Current drive performance

Current drive capability has been also studied. In the combined current drive with positive (4MW, 80keV) and the negative (1.9MW, 350keV) tangential beams at n_e=0.5x10^{19}m^{-3}, more than 80% of the total plasma current (1MA) was driven by the neutral beams where >0.2MA was driven by the N-NBI. estimated. An example of fully non-inductive discharge with NBCD and the bootstrap current is shown in Fig.4. In order to increase the bootstrap current, 4MW of perpendicular beams were injected in to 4MW of positive beam CD plasma. After that, 2MW of negative beams were injected. The surface loop voltage becomes slightly negative value. In this figure, the experimentally measured signals are plotted as the black lines. To estimate the non-inductive driven current, the ACCOME code and the time dependent 1.5D transport are used to reconstruct the all plasma parameters such as the stored energy, neutron emission rate and the loop voltage. Codes indicates that 0.28MA is driven by NNB. Current of 0.46MA and 0.27MA are driven by the positive beams and the bootstrap current, respectively. This NNB driven current corresponds to the CD efficiency of 0.8x10^{19}m^{-2}A/W with 27% of shinethrough loss, while the positive beams with 80keV has the CD efficiency of 0.5x10^{19}m^{-2}A/W in this conditions.

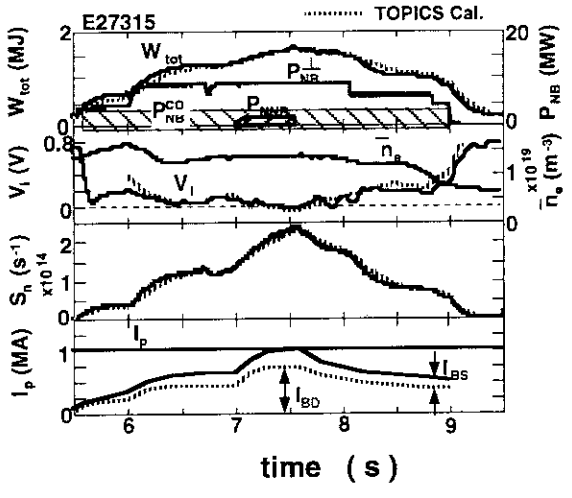

Fig.5 Time evolution of fullly non-inductive discharge with NBCD by N-NBI and P-NBI. E_B=350keV, n_e=(0.5-2.8)x10^{19}m^{-3}.

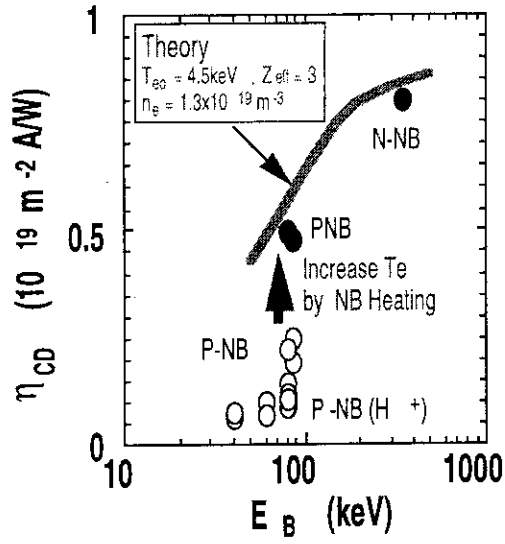

Fig. 6 Current drive efficiency against the beam energy. Solid line is the calculated value with Teo=4.5keV.

The current drive efficiency is plotted against the beam energy where symbols show experimental results and the line is the calculated efficiency by ACCOME code with T_{eo}=4.5keV, Z_{eff}=3, n_e=1.3x10^{19}m^{-3}. This figure indicates that higher CD efficiency will be obtained at next experimental campaign with a high temperature target and 0.5MeV N-NBI.

REFERENCES

(1) K. Ushigusa and the JT-60 Team, in proc. of the 16th IAEA Fusion Energy Conference (Montreal 1996), F1-CN-64/01-3.

6.3 Shine-through measurement and multi-step ionization processes of NNB

M. Nemoto, K. Tobita, K.Ushigusa, Y. Kusama, M. Kuriyama, K. Kodama, K. Masaki, A. Sakasai and Y. Kamada

1. Introduction

Establishment of high performance plasma in steady state with controlled current-drive is an important issue in a fusion reactor like ITER. A negative ion based neutral beam (NNB) is an effective tool to control the plasma current distribution and to heat the plasma at the same time. Thus the NNB is one of the candidates for plasma heating and current dive on ITER. In order to design the high power NNB system, theoretical predictions on the ionization processes of NNB in plasma should be verified by experiments.

Until the early 1980s, it had been considered that the ionization of neutral beam could be explained with the single-step ionization processes. However, recent numerical calculations have revealed that multi-step processes can enhance the cross section of beam ionization in plasma[1,2]. The multi-step processes of beam particles consist of excitation processes and the following ionization and charge-exchange processes. Their predictions show that ionization of a neutral beam in plasma is determined by the multi-step ionization processes in addition to the single-step processes and that the cross-sectional enhancement for the multi-step processes is strongly influenced by plasma parameters such as plasma density and the effective charge of plasma. The problem is that the individual predictions on the enhancement are not in agreement. Therefore, the shine-through measurements of a high energy NNB up to 500 keV on JT-60U would be very important to conclude the degree of the cross-section enhancement. Because no experimental data over 140 keV/amu have been obtained so far[3,4] and the cross-sectional enhancement will be identified more clearly than the previous experiments.

In this section, we report the experimental results on the shine-through of a 350 keV hydrogen beam and the deduced enhancement factor .

2. Experimental set up

The NNB system on JT-60U has two beamlines. In order to measure the shine-through of the two NNBs, two sets of thermo-couple arrays are installed crosswise on the first wall, which measured the heat flux of the traversed NNB. Each array consists of 11 thermo-couples and each of them are sheltered by a molybdenum cap. In order to avoid increase in the temperature by influence of ripple loss ions, the caps are installed 5 mm below the first wall surface.

Calibration of thermo-couple arrays is carried out during the conditioning phase of the NNB. Then the NNB is injected into the vacuum vessel without plasma. An infrared TV (IRTV) also measures wall temperature rise due to the traversed NNB. The surface temperature is consistent with one of the first wall measured with IRTV.

3. Shine-through and cross-sectional enhancement

The NNB generated in the upperside ion source was injected into hydrogen plasma. The plasma parameters were I_p=0.8-1.8 MA, $B_T(0)$=1.2-3.5 T, P_{NNB}=1.0-2.4 MW and $\overline{n_e}$=(1.0-4.1)×10^{19} m^{-3}. The shine-through is deduced from the thermo-couple data obtained at a specific channel whose temperature rise is the highest.

Figure 1 shows $\overline{n_e}$ dependence of the shine-through obtained in a fixed plasma configuration. Scatter of the data is caused by ambiguity of Z_{eff} and/or density profile. The shine-through expected from the single-step processes is shown with a dotted line in the figure. It is found that the shine-through obtained in density range over $\overline{n_e}$=3×10^{19} m^{-3} is smaller than that expected from the single-step processes. The enhanced attenuation of NNB is probably attributed to the multi-step processes.

We estimate the cross-sectional enhancement caused by the multi-step ionization processes, using the experimental shine-through and the cross sections assembled by Janev et al.[5]. In the calculation of the ionization, it is assumed that impurity in plasma is carbon only, based on spectroscopy measurement. Figure 2 shows the cross-sectional enhancement as a function of $\overline{n_e}$. It is found that the cross-sectional enhancement increases clearly with $\overline{n_e}$ over 3×10^{19} m^{-3}. This trend is the same as the prediction from the numerical calculations[1]. In low density range of (1.0-1.6)×10^{19} m^{-3}, the cross-sectional enhancements are scattered around zero due to the error of Z_{eff} measurement.

4. Summary

Using a hydrogen beam with the energy of 350 keV, the shine-through in hydrogen plasma was measured and the cross-sectional enhancement was estimated. The shine-through decreases with $\overline{n_e}$ and its degradation is larger than that caused by the single-step ionization processes. The cross-sectional enhancement increases clearly with $\overline{n_e}$ over 3×10^{19} m^{-3}.

References

1) R. K. Janev et al., Nuclear Fusion 29 (1989) 2125.
2) A. A. Korotkov, Sov. J. Plasma Phys. 15(1989)817.
3) K. Tobita et al., Plasma Phys. Contr. Fusion 32(1990)429.
4) Equipe TFR, Plasma Phys. Contr. Fusion 29(1986)37.
5) R. K. Janev et al., Suppl. to Nuclear Fusion, 4 (1993).

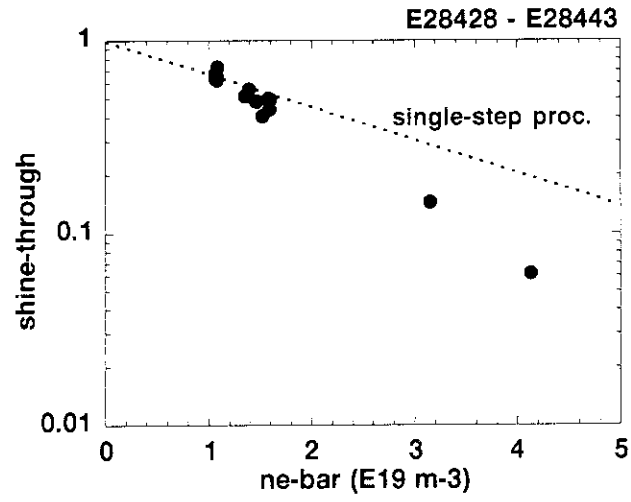

Fig. 1 : Dependence of shine-through on line-averaged electron density.

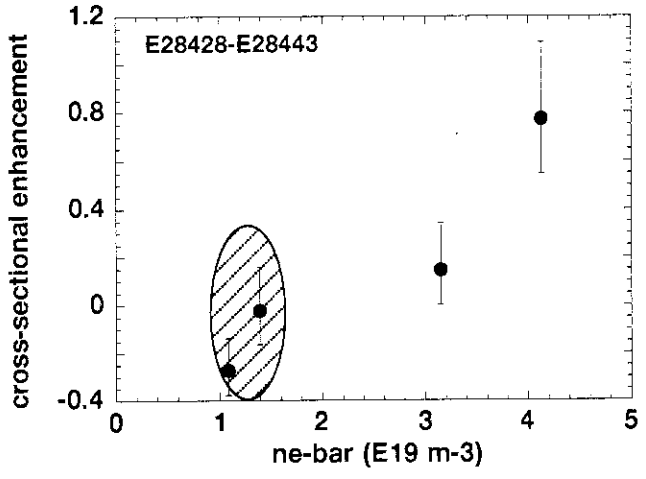

Fig. 2 : Dependence of the cross-sectional enhancement on line-averaged electron density. Cross-sectional enhancements in range of (1.0-1.6)×10^{19} m^{-3} are in hatched area.

6.4 Neutron decay following N-NB injection

A. Morioka, K. Tobita, H. Harano, Y. Kusama, T. Nishitani

1. Introduction

In JT-60U, 14 positive-neutral beam injectors(P-NBI) are installed. 4 beams of those are injected into the plasma tangentially and the other beams are injected perpendicularly. Negative-neutral beam injector(N-NBI) was installed in 1996. The deceleration process and ripple loss of beam ions have been investigated by using short pulse P-NB injection[1,2]. One of quantitative checks of beam ions loss is to measure the decay of neutron emission following short pulse neutral beam injection[3]. In N-NB injection, first results was reported[4]. In this experiment, the loss of N-NB ions studied measuring the decay of neutron emission after the N-NBI turn-off.

2. Experiment

A N-NB with the beam pulse width(t_{beam}) 300ms, the beam energy(E_b) 350keV and the beam power(P_{NNB}) 2.5MW was injected into OH plasma with $T_e(0)$=1.4~1.7keV, $\overline{n_e}=1\times10^{19}$ m^{-3} and Z_{eff}=1.4 at the plasma current I_p=1MA and the toroidal magnetic field B_t=2.5T. Neutron emission arising from DD reaction was measured by using uncollimated fission chambers [5]. The electron temperature profile was measured by Thomson scattering and electron cyclotron emission diagnostics. The line averaged electron density was measured by FIR and CO_2 interferometers. The electron density profile was measured by Thomson scattering. The value of Z_{eff} was evaluated by using a measurement of bremsstrahlung. The time evolution for N-NB injection is shown Fig.1.

3. Comparison with calculation

To assess the neutron decay, we used a 1D code which assumed the classical slowing down without ion loss and no radial diffusion. The calculation code employed the fitted function to the measured electron temperature and density profiles and the fitted function to the fusion cross section. Plasma parameters such as n_e, T_e, T_i, Z_{eff} were assumed constant in time at every 10ms. The comparison between measured neutron emission and calculated neutron emission by assuming the classical slowing down without ion loss and no radial diffusion is shown Fig.2. The measured neutron decay roughly agree with the classical slowing down. Since the electron temperature rises during N-NB injection, the slowing-down time of fast ions is a little longer the temperature used in the calculation. If the temporal change in T_e is included, therefore, the calculation decay should match better than the present result. The rough agreement of the neutron decays indicates that N-NB ions are confined well in the plasma on JT-60U.

References

[1] K. Tobita, K. Tani, T. Nishitani, et al.: Nucl. Fusion, **34**, 8, 1097 (1994)

[2] K. Tobita, K. Tani, Y.Kusama, et al.: Nucl. Fusion, **35**, 12, 1585 (1995)

[3] W. W. Heidbrink, J. Kim, R. J. Groebner: Nucl. Fusion, 28, 10, 1897 (1988)

[4] Y. Neyatani and the JT-60 Team : Plasma Phys. Cont. Fus., **38**, A181 (1996)

[5] T. Nishitani, et al.: Rev. Sci. Instrum., **63**, 5270 (1992)

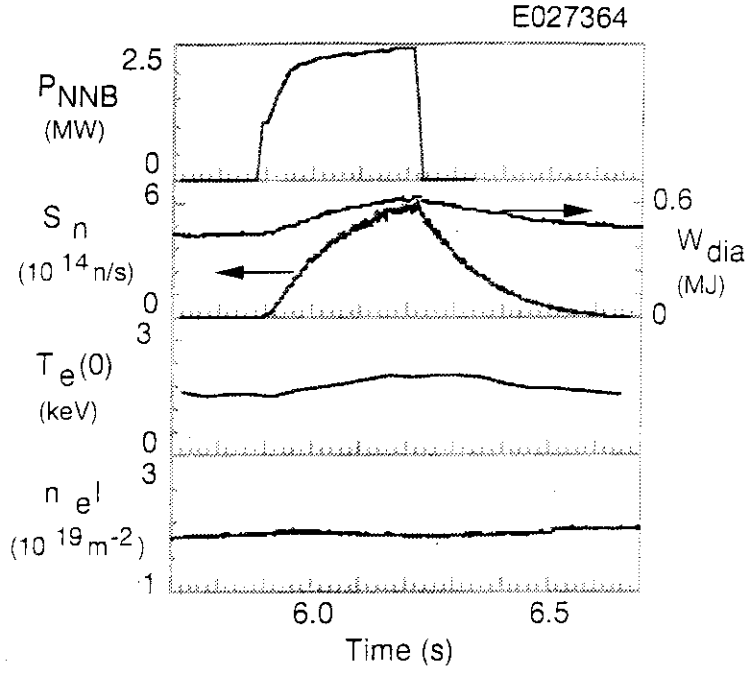

Fig.1 Time evolution for NNB pulse injection

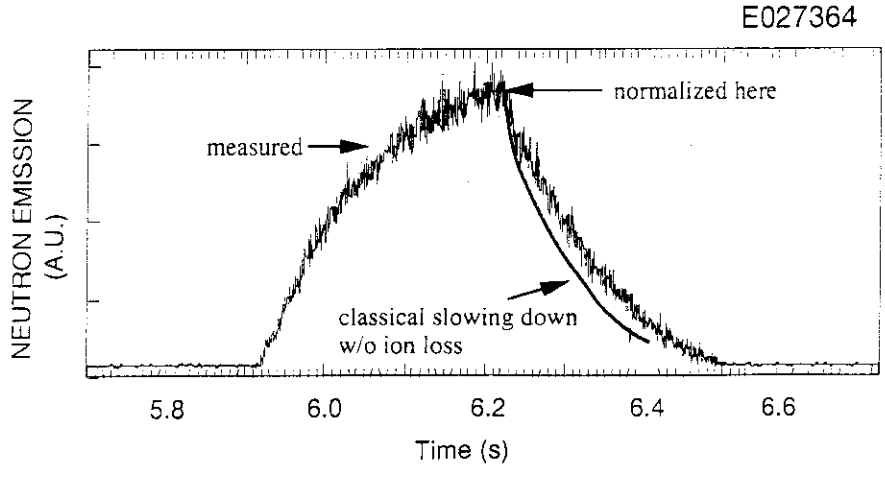

Fig.2 Comparison between the neutron emission decay and the calculated neutron emission decay by assuing the classical slowing down and no radial diffusion.

6.5 Application of LHCD for Sustainment and Control of a Reversed Magnetic Shear Plasma in JT-60U [1]

S. Ide, O. Naito, T. Fujita, T. Oikawa, M. Seki and theJT-60 team

In JT-60U, it has been demonstrated experimentally that reversed magnetic shear can be maintained, controlled[2] and even formed by using lower hybrid wave (LHW) current drive (LHCD). In the experiment the reversed shear configuration was sustained for about 7.5 s (Fig.1), and it was concluded that it reached nearly quasi-steady state. Furthermore, the experimental results show that the area of better confinement can be changed in coincidence with the reversed magnetic shear control by LHCD (Fig.2). Formation of a reversed magnetic shear configuration by an LHW injection alone was successfully demonstrated (Fig.3). Strongly reversed magnetic shear, even stronger than one formed by a normal scenario (NBI heating at current ramp-up), with large area of shear reversal was formed by LHW alone. Furthermore, strong gradient was found in the electron temperature profile, suggesting improvement of confinement. Moreover, attainable β_N, the normalized plasma beta, in this discharge was found to be comparable to that of normal reversed shear discharge (Fig.3). Considering recent success of improving plasma performance in reversed magnetic shear discharges with high power heating in TFTR, D-IIID and JT-60U, our results should have an impact not only on enhancement of performance but also on investigating the physics involved.

References

[1] S. Ide et.al., Proc. 16th IAEA Fusion Energy Conf., Montrèal, 1996, IAEA-CN-64/E-3
[2] S. Ide, T. Fujita, O. Naito, and M. Seki, 1996, Plasma Phys. Controlled Fusion, **38**, 1645

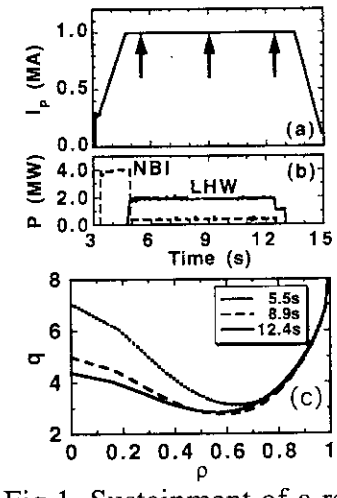

Fig.1. Sustainment of a reversed shear by LHCD. Waveforms of (a) Plasma current, (b) NBI and LHW powers. (c) Safety factor profiels measured at three timing showm by arrows in (a).

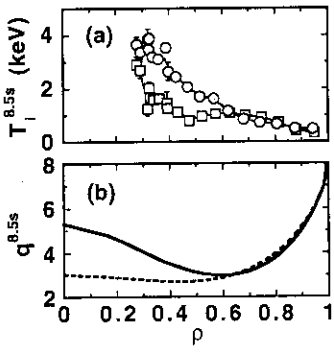

Fig.2. Control of better confinement region by LHCD. (a) Ion temperature profiles of discharges in which LHW drives hollow current profile (scircles) and peaked one (squares) (b) Corresponding q profile for the hollow driven current profile case (solid curve) and the other (dashed curve).

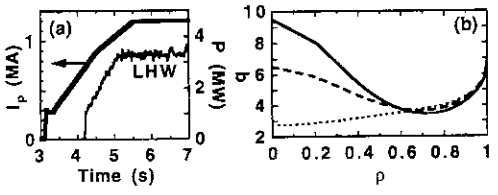

Fig.3. (a) Waveforms of I_p and P_{LH}. (b) The q profile evaluated at 5.5s is shown by a solid curve, ones in NBI only (dashed curve) and OH cases (dotted curve) are shown for references.

7. Radiative Divertor and SOL

7.1 Radiative divertor with improved core plasma confinement in JT-60U[1]

K. Itami, N. Hosogane, N. Asakura, A. Sakasai, H. Kubo, S. Konoshima,
T. Fujita, T. Oikawa, M. Shimada, R. Yoshino

Radiative divertor in reversed shear plasmas with high ion temperature

In order to obtain the reversed shear plasmas [2] with high Ti, it is necessary to reduce particle recycling levels and to apply beam heating with P_{NB} = 15 MW to the target plasmas with edge plasma denisty $n_e \leq 5 \times 10^{18}$ m^{-3} during the ramp-up phase of plasma current. The discharges were deuterium plasmas with I_p = 1.8 MA, B_T = 4 T and the plasma volume V_p = 60 m^3. The neutral beam power was stepped down to P_{NB} = 10 MW before the flat top of the plasma current. Neon and deuterium gas injection was applied at t = 5.3 s, 500 milliseconds after the transport barrier started to grow up. Radiation loss from the divertor increased by 20 % of the input power after the neon and deuterium gas puff. The central Ti = 10 keV was sustained during the gas puff. While the neutron rate decreased by 30%, the H-factor = 1.8 was sustained until the collapse of the reversed shear discharge.

Sustainement of transport barrier with divertor MARFE

Full detachment in the divertor was obtained only in the reversed shear plasma with high edge density [3]. The plasma conditions were I_p = 1.2 MA, B_T = 3 T. It was also found that the internal transport barrier in the reversed shear plasma is compatible with the divertor MARFE. The internal transport barrier was sustained during the divertor MARFE phase for 1.8 second in the shot 27708. The total radiation loss from the divertor and the main plasma increased from 3 MW to 8 MW, reaching 80% of the input power. The improved confinement inside the ITB terminated by a beta collapse at t = 7.5 s. Significant drops of the stored energy, plasma density, electron temperature at the beta collapse is observed. Profiles of safety factor at t = 6.15 s and t = 7.5 s shows that the negative shear was sustained during the radiative divertor phase while the reversal of the shear became shallow. A careful adjustment of the gas puff sequence and amount of deuterium puff was required to produce the radiative divertor without a beta collapse and to maintain improved plasma confinement inside the internal transport barrier.

Radiative divertor plasma in ELMy H-mode plasmas with high beam power

Low particle recycling level ($\Phi_{div} < 2 \times 10^{22}$) was required to obtain good energy confinement in ELMy H-mode plasmas of JT-60U. Target heat flux density q_d exceeded 5 MW/m^2 and the electron temperature in the divertor plasma T_{ed}, reached ~80 eV and it was difficult to produce dense amd cold plasmas only by deuterium puffing. With the neon and deuterium gas puffing, quasi steady sustainement of the divertor detachment was obtained up to P_{NBI} = 20MW in ELMy H-mode plasmas. In such a discharge, the total radiation loss from the plasma increased from 6 MW to 14 MW.

References

[1] K. Itami et al., Proc of 16th IAEA conference, Motreal(1996).
[2] T. Fujita et al., Proc of 16th IAEA conference, Motreal (1996).
[3] K. Itami et al., Phys. Rev. Lett. 78, 1267(1997).

7.2 Radiative divertor experiment with Nitrogen gas injection

K. Itami, S. Konoshima, N. Hosogane

1. Introduction

Neon, argon and nitrogen gas have been used in radiative divertor experiment as seed gases to enhance radiation loss from the plasma. Impurity ions in the main plasma dilute hydrogen ions and cool down the main plasma and it is preferable to confine the impurity ions as effectively as possible in the divertor plasma region and to increase the radiation loss mainly in the divertor plasma. It has been reported in the paper from JET [1] that the largest radiation loss in the divertor against the radiation loss in the main plasma was obtained by the N_2 gas injection among Ar, Ne and N_2 gas injection. In that paper, the smallest deterioration of the H-factor in the radiative divertor experiment with the N_2 injection was also reported. We tried several discharges with N_2 gas puff in 1995. This paper reports the N_2 gas puff experiment for radiative divertor in February in 1996.

2. Results

Significantly larger amount of the N_2 gas was necessary to increase radiation loss from the plasma than Neon gas. This originates from lower recycling rate of nitrogen than that of neon. Neon level in the main plasma is determined by the total amount of the neon gas and the level is kept at a constant value even after the injection. This suggests the neon impurity level in the main plasma is dominated by the recycling in the vessel. On the other hand, nitrogen impurity level decays when the N_2 gas injection is terminated. Since JT-60U doesn't have active divertor pump at present, this decay of nitrogen level is attributed to the wall pumping. Fig. 1 shows a typical discharge with N_2 gas puff. N_2 gas rate as large as 6 Pa m^3/s was injected for 1 second. Total amount of N_2 gas is larger by a factor of 10 than the amount of Ne gas routinely used in the radiative divertor experiments . While ELM activity disappeared at the end of N_2 gas puff and plasma confinement went back to L-mode, ELM activity reappeared within 0.5 second along with the decay of N VII intensity after N_2 gas turn-off. The stored energy started to increase again when ELMs reappeared.

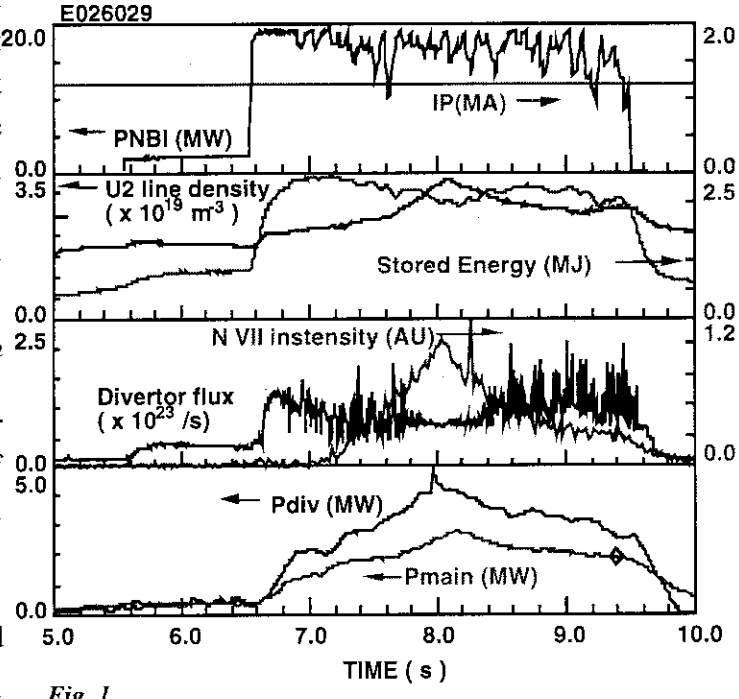

Fig. 1
Typical waveforms of a discharge with nitrogen gas puff.

In the discharges, both the divertor and main radiation was increasing during N_2 gas injection. Total radiation power increased from 1.5 MW to 2.8 MW in the main plasma and

increased from 2 MW to 4.2 MW in the divertor plasma. Therefore 50% of the beam power was radiating from the plasma. The increase in radiation power density was the largest at the inner divertor. This is the common feature with discharges with neon injection. However there seemed to be the minimum N_2 puff rate to increase the divertor radiation loss. N_2 gas puff rate larger as large as 4 Pa m^3/s was required to increase the radiation loss from the divertor Fig. 2 exhibits the existence of the minimum N_2 gas puff rate for increasing the radiation loss from the divertor. Radiation loss rate at the bolometer chord viewing the inner divertor is shown as the most sensitive indicator in this figure.

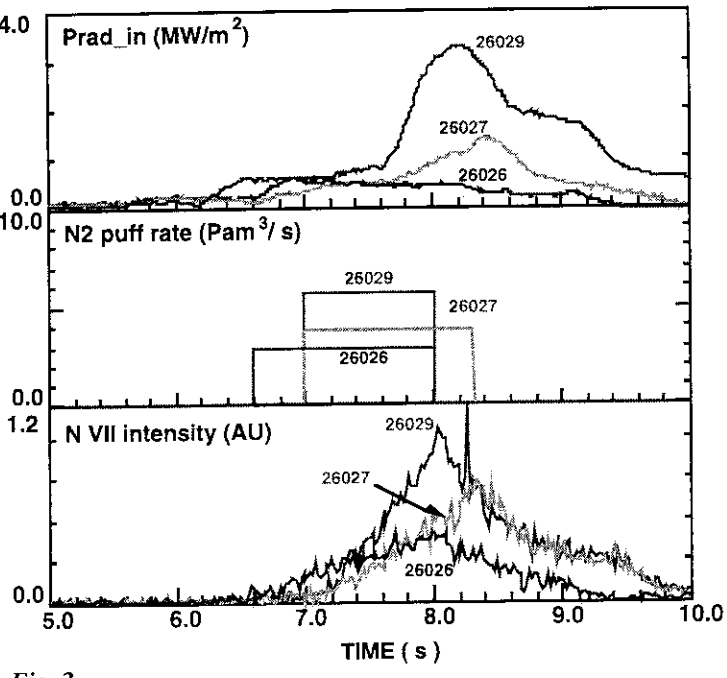

Fig. 2
Radiation loss at the chord viewing the inner divertor, N2 gas puff rate and nitrogen line intensity are shown for three discharges.

Withn the limited number of the discharges in this experiment, we did not have an opportunity to puff N_2 and D_2 gas at the same time to obtain divertor detachment.
From the result shown above, we expect N_2 gas rate as large as 6 Pa m^3/s more for the detached divertor experiment by N_2 gas injection. Nitrogen is much more easily accumulate than Neon inside the vacuum vessel and the background level of the nitrogen line is gradually increasing. We had to shoot a conditioning discharge after every discharge with N_2 gas puff in this experiment. Therefore divertor pumping is necessary to carry out the detached divertor experiment that requires N_2 gas amount larger by a factor of 3 ~ 4 than this experiment. We expect to do N_2 gas puff experiment after the modification to w-shaped divertor with pumps.

Reference

[1] JET Team Plasma Phys. Controlled Fusion **36**, Supplement 11A, A3(1995).

7.3 Comparison of the radiative divertors with different impurity gases

H. Tamai, S. Konoshima, N. Hosogane, K. Itami, and N. Asakura

1. Introduction

The radiative cooling in the divertor region is one of the key issue to eliminate the large heat load onto the divertor plate, so that the sustainment of radiative divertor plasma is one of the urgent tasks for the ITER divertor design. The way to control the radiative divertor in the steady state is tested in many tokamaks. In the various trials to produce a stable radiative divertor, it is found that the sustainment of the radiative divertor at the higher radiation level is comparably not easy to control since the instabilities by the high radiation loss, such as MARFE, are occasionally driven in the high recycling region.

In addition to producing the enhanced divertor radiation, the compatibility with the high performance of the main plasma confinement is recognised as the key issue. Trials for producing the radiative divertor plasma compatible with high confinement performance by the different impurity gases are operated in JT-60U tokamak.

This paper describes the comparison of the profile behaviour of the divertor radiation depending on the impurity gas puffing into divertor during the enhanced remote radiative cooling phase.

2. Diagnostics

Divertor radiation loss power is observed by two bolometer arrays. Figure 1 illustrates the poloidal location of those bolometer arrays. Two bolometer arrays cover the whole divertor region, and are labelled as the top array, and the side array, respectively. Total power of the divertor radiation is estimated by the summed signals of six central channels of the top array.

Bolometer arrays are installed on the toroidal port sections of P-8 and P-9, apart from the gas valve installed on P-15 and P-18, which conducts the impurity gas into the divertor region. Therefore, the bolometric measurement is considered to be not affected by the toroidal asymmetry caused by the intense gas fuelling.

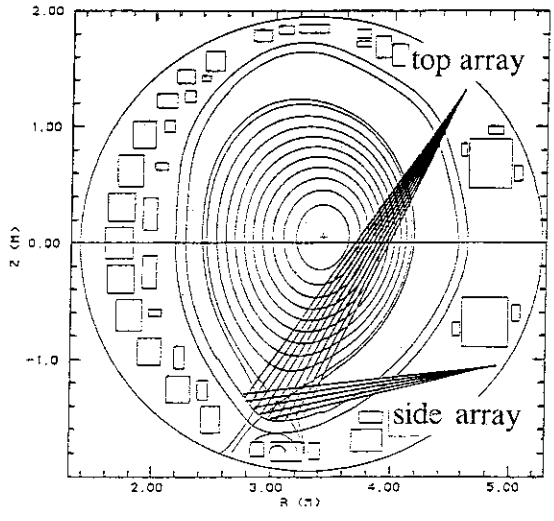

Fig. 1 Poloidal location of the bolometer arrays for the measurement of the divertor radiation.

3. Profile of the divertor radiation

The radiative divertor is performed in the neutral-beam hated plasmas by the puffing gas of neon, nitrogen, and the compound of those gases with deuterium.

Figure 2 shows the temporal evolution of the radiation loss from the divertor and from the main plasma in the radiative divertor plasma produced by neon puffing. Neon is puffed twice with each duration of 0.4 seconds. Only by short gas puffing, the intensity of the line emission of NeX from the divertor region are maintained during the radiative divertor phase. Divertor radiation continues to increase up to about 9MW, which is 25% of the input power. The radiation loss from the main plasma also increases, which might be partly contributed by the neon flux into the main plasma.

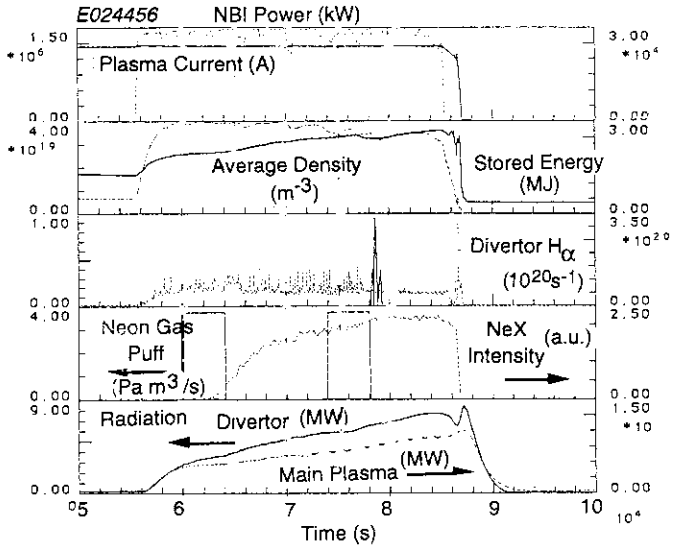

Fig. 2 Temporal evolution of the typical plasma parameters in the radiative divertor by neon puffing.

Figure 3 plots the profile of the divertor radiation at the timing before the first neon puff (6s), the midterm (7s), and after the second puff (8s). The equatorial plane around the divertor x-point and the each chords of bolometer channel are also illustrated. A peak in the side array shifts towards the x-point after the neon puffing. Outside peak in the top array also indicates the upward shift, while the inside peak keeps the position during the increase of the intensity.

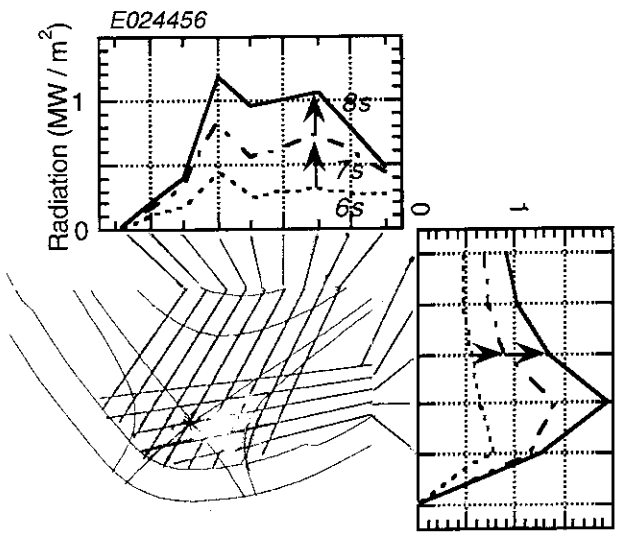

Fig.3 Profile of divertor radiation by Ne puffing.

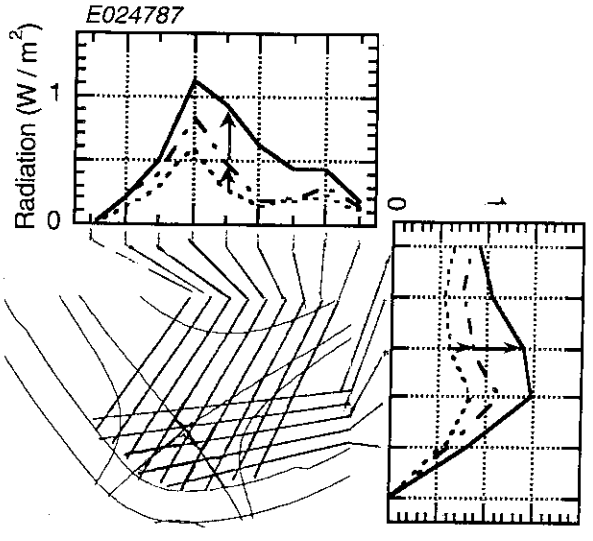

Fig.4 Profile of divertor radiation by N_2 puffing.

The radiative divertor by the nitrogen puffing is compared. During the continuous nitrogen puffing of 0.3s, the total power of divertor radiation continues to increase up to 28% of the input power. On the other hand, the main plasma radiation gradually decreases. Figure 4 plots the profile of the divertor radiation by nitrogen puffing. Though the intensity also gradually increases, peaks of the radiation keep the position in both the arrays, and the intense radiation is localised around the inside peak.

4. Influence on the confinement performance

Additional gas puffing of deuterium into the radiative divertor, which is produced by impurity gas, is also performed in order to increase the fuelling efficiency. The compound puffing with deuterium results the enhancement of the divertor radiation in the high density region. In Fig.5 the power ratio of the divertor radiation to the total input is plotted against the electron density averaged over the central chord of the main plasma. In both impurity gas puffing of neon and nitrogen, the power fraction of the divertor radiation enhances with the increase of the density. By the compound puffing of impurity gases with deuterium, higher fraction of divertor radiation in a high density region can be achieved.

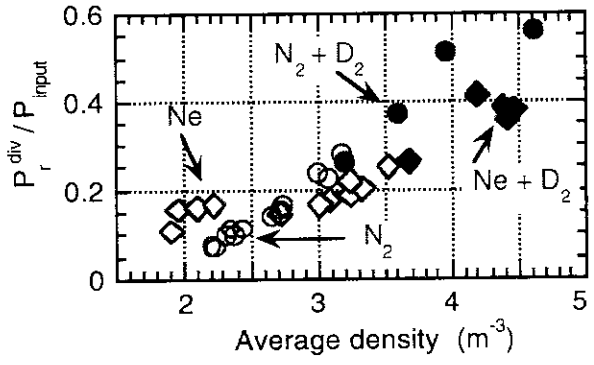

Fig. 5 Divertor radiation versus the average electron density, for the puffing gas of neon(◇), nitrogen(○), and compound with deuterium(◆,●).

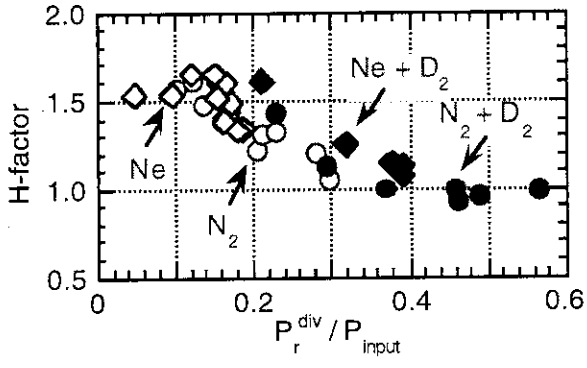

Fig. 6 H-factor versus the divertor radiation, for the puffing gas of neon(◇), nitrogen(○), and compound with deuterium(◆,●).

Figure 6 shows the dependence of the H-factor on the power fraction of the divertor radiation. H-factor is referred to the ITER-89 L-mode scaling. Confinement performance gradually degraded as the power fraction of the divertor radiation goes up, and no improvement is observed at around 50% of the divertor radiation.

5. Summary

The radiative divertor plasma by the different puffing gas is compared. The power ratio of the divertor radiation to the total input of 25-30% is performed by neon, or nitrogen puffing. Outside peak of the divertor radiation shifts towards the x-point by the neon puffing. While by the nitrogen puffing, intense peak in the inside keeps the position. Because of the large cooling

rate and high recycling rate, neon puffing of short pulse is sufficient for maintaining the divertor radiation. Increase of the main plasma radiation might be contributed by the neon flux. Compound gas puffing with deuterium enhances the divertor radiation in a high density regime. The confinement performance is degraded with the increased divertor radiation.

References

1) S. Konoshima *et al.*, JAERI-Research *96-018* (1996) 190.
2) N. Asakura *et al.*, Nucl. Fusion *36* (1996) 795.
3) K. Itami, *et al.*, Phys. Rev. Lett. *78* (1997) 1267.

7.4 SOL Plasma Profiles in High Density Discharge[1]

N. Asakura, Y. Koide, K. Itami, N. Hosogane, K. Shimizu, S. Tsuji-Iio, S. Sakurai, and A. Sakasai

Radial profiles of electron density $n_{e,mid}$, temperature $T_{e,mid}$, and ion temperature $T_{i,mid}$ in the scrape-off layer (SOL) were investigated under radiative and detached divertor conditions in L-mode discharges. $T_{e,mid}$, and $n_{e,mid}$ profiles were measured with a fast reciprocating Langmuir probe system[2] installed at the midplane with a spatial resolution of 1−2 mm. $T_{i,mid}$ profile in the edge plasma was measured with charge exchange recombination spectroscopy system (CXRS) with a spatial resolution of 6−7mm.

Since the ratio of $T_{i,mid}/T_{e,mid}$ was about 3 over a wide range of $\bar{n}_e$, the ion pressure was dominant. It was expected that $T_{i,mid}$ is higher than $T_{e,mid}$ due to the low parallel thermal conductivity of ion by a factor of $(m_i/m_e)^{1/2}$ ~60 for deuterium plasma. The measured value of $T_{i,mid}/T_{e,mid}$ ~3 at the separatrix was consistent with $T_{i,mid}/T_{e,mid}= (m_i/m_e)^{1/9}$ ~2.5, which is predicted by the SOL/divertor two-point model assuming cross-field heat conductivity and the power into the SOL, P_{SOL}, are the same for the ion and electron[3].

Ion pressure plays an important role in the pressure balance between the midplane and the divertor targets. The ratio of the static and dynamic pressure at the divertor separatrix ($2(p_{i,div} + p_{e,div}) = 4p_{e,div}$, assuming $T_{i,div} = T_{e,div}$ and Mach number $M = 1$) to the total plasma pressure at the midplane ($p_{i,mid} + p_{e,mid}$) was observed to be unity. The total plasma pressure balance was maintained along open field lines at $\bar{n}_e$ lower than the occurrence of an X-point MARFE. When the X-point MARFE occurs, however, the ratio was reduced by a factor of 5−50.

Two (i.e. first and second) SOL regions with different characteristic lengths were observed both in the $n_{e,mid}$ and $T_{e,mid}$ profiles. The first SOL extended up to 10−15 mm outside the separatrix. The profile had a small e-folding length provided that the attached divertor condition was maintained. Effect of the connection length on the decay lengths of $n_{e,mid}$ and $T_{e,mid}$, λ_{T_e} and λ_{n_e}, was determined. A regression analysis for $T_{e,sep} \geq$ 45 eV suggested that $\lambda_{n_e} \propto q_{eff}^{\alpha} T_{e,sep}^{\beta}$, where $\alpha = 0.85 \pm 0.12$ and $\beta = 0.23 \pm 0.15$, and $\lambda_{T_e} \propto q_{eff}^{\alpha} T_{e,sep}^{\beta}$, where $\alpha = 0.5 \pm 0.1$ and $\beta = -0.3 \pm 0.2$. λ_{T_e} was by a factor of 1.5−2 larger than λ_{n_e}. At the occurrence of the X-point MARFE, $T_{e,sep}$ at the midplane was between 40 and 45 eV. The critical $T_{e,sep}$ was the same for the discharges with different connection lengths.

At the same time, λ_{T_i} was compared to λ_{T_e} and λ_{n_e}. λ_{T_i} was by a factor of 2.5−3 larger than λ_{T_e} at the first SOL. $T_{i,mid}/T_{e,mid}$ was 3.5−4.5 at the outer flux surfaces. λ_{T_i} increased with the connection length; $\lambda_{T_i} \propto q_{eff}^{\alpha} T_{i,sep}^{\beta}$, where $\alpha = 0.8 \pm 0.2$ and $\beta = -0.3 \pm 0.2$ for $T_{e,sep} \geq 45$ eV. The results were consistent with the prediction of the SOL two-point model, i.e. $\lambda_{T_i}/\lambda_{T_e} = (m_i/m_e)^{1/9}$ ~2.5, due to the low parallel thermal conductivity of ion.

During the X-point MARFE, λ_{T_e}, λ_{n_e} and λ_{T_i} increased substantially with a reduction in $T_{e,mid}$, $T_{i,mid}$ and $n_{e,mid}$ at the plasma edge and in the first SOL, due to the penetration of the maximum radiation region into the main plasma near the X-point.

[1] N. Asakura, *et al.*, "SOL plasma profiles under radiative and detached divertor conditions in JT-60U", J. Nual. Matter. (1997).
[2] N. Asakura, *et al.*, Rev. Sci. Instrum. **66** (1995) 5428.
[3] C.S. Pitcher, P.C. Stangeby, to be published in Plasma Physics and Controlled Fusion.

[1]Present address: Research Laboratory for Nuclear Reactors, Tokyo Institute of Technology.

7.5 Parallel current driven in the high density SOL

A. Kumagai *, N. Asakura, K. Itami, M. Shimada, and M. Nagami
*Plasma Research Center, University of Tsukuba,Tsukuba-shi, Ibaraki-ken 305, Japan

1. Introduction

Parallel currents passing between the two strike zones in the scrape-off layer of single null divertor discharges is called a SOL current. In JT-60U low and moderate densities discharges with the ion grad-B drift towards the X-point, the SOL current flows from the outboard divertor to the inboard divertor[1]. The observed direction of SOL currents corresponded to the direction of thermoelectric currents, which flows from high electron temperature side to low electron temperature side. A temperature difference between the two target plates would cause a current in order to compensate the difference in the sheath potential[2,3]. In this paper, we investigate the relation between the asymmetry in plasma parameters on the divertor plate and observed SOL currents under the detached divertor condition and during the X-point MARFE on JT-60U.

2. Experimental results

The SOL currents have been investigated in JT-60U high density plasmas with the ion grad-B drift towards the X-point. Langmuir probes mounted on the divertor tiles were used to measure the SOL current. The SOL current $J_{\parallel}$ at each probe position was obtained by the probe current when the applied voltage was equal to zero. Profiles of electron temperature T_e^{div} and SOL current $J_{\parallel}$ under the attached and detached divertor conditions are shown in figure 1(a), (b). A positive sign is assigned to positive charge flow from the SOL to the target tile. Under the detached divertor condition, the direction of $J_{\parallel}$ was reversed compared to attached case, accompanied by the reversal of the in-out asymmetry in T_e^{div}. The direction of $J_{\parallel}$ corresponded to the direction of the thermoelectric current. However, under the detached divertor condition and during the X-point MARFE, the magnitudes of SOL currents at the outboard target were 2-6 times larger compared with those at the inboard target, and exceeded the theoretical prediction[3].

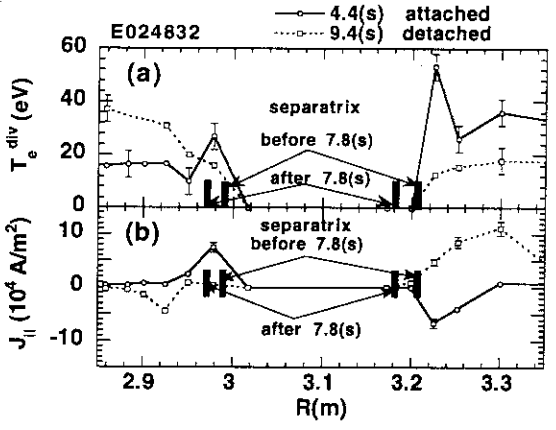

Figure 1. Profiles of (a) electron temperature T_e^{div} and (b) SOL current $J_{\parallel}$ at t=4.4 and 9.4 s of the discharge E024832.

References

[1] K. Itami et al., 1992 Proc. 14th Int. Conf. on PlasmaPhysics and Controlled Nuclear Fusion Research (*Würzburg*) IAEA-CN-56/A-6-5.
[2] P. J. Harbour et al., Contrib. Plasma Phys. **28** (1988) 415.
[3] G. M. Staebler and F. L. Hinton, Nucl. Fusion **29** (1989) 1820.

7.6 SOL Plasma Profiles in high density OH discharges with deuterium and helium gas puffing

N. Asakura

$n_{e,mid}$ and $T_{e,mid}$ profiles at the midplane SOL were investigated in ohmic heating discharges with deuterium (D) and helium (He) gas puffing. Profiles were measured in high safety-factor discharges ($q_{eff} = 7.0$, $I_p = 1.2$ MA, $B_t = 3.5$ T), and two combinations of I_p and B_t ($I_p/B_t = 1.2$ MA/2.1 T and 2 MA/3.5 T) were chosen for the low-q_{eff} discharges ($q_{eff} = 4.4$−4.5).

Figure 1 shows $n_{e,mid}$ at the separatrix, $n_{e,s}$, as a function of $\bar{n}_e$. Over the density range of $\bar{n}_e$, $n_{e,s}$ in **D** plasma was larger than that in **He** plasma by a factor of 1.3−1.7 at the same q_{eff}. Thus, detachment of the divertor plasma occurred at lower $\bar{n}_e$ for **D** plasma compared with **He** plasma. $n_{e,s}$ at high q_{eff} (~7) was lower than $n_{e,s}$ at low q_{eff} (4.4~4.5) for the same $\bar{n}_e$; $n_{e,s}$ decreased with the connection length. The ratio of $n_{e,s}$ to $\bar{n}_e$ depending on I_p, B_t and ion species is summarized in Table 1.

Two (i.e. first and second) SOL regions with different characteristic lengths were observed both in the $n_{e,mid}$ and $T_{e,mid}$ profiles. In the high density discharges, the first SOL extended up to 10−15 mm outside the separatrix. Figure 2 shows e-folding length of the $n_{e,mid}$ profile, λ_{n_e}, as a function of $\bar{n}_e$. Here, the first SOL region is very small (5−10 mm) for the **He** plasma at high q_{eff}, and λ_{n_e} may include the second SOL region. λ_{n_e} is relatively constant with varying $\bar{n}_e$ (except for the high q_{eff} **He** plasma) as long as the attached divertor plasma was maintained. When the detachment of the divertor plasma occurs, λ_{n_e} increases largely. λ_{n_e} in **He** plasma was larger than that in **D** plasma by a factor of 1.3−1.5. Dependence of λ_{n_e} on I_p, B_t and ion species is summarized in Table 2.

Fig. 1

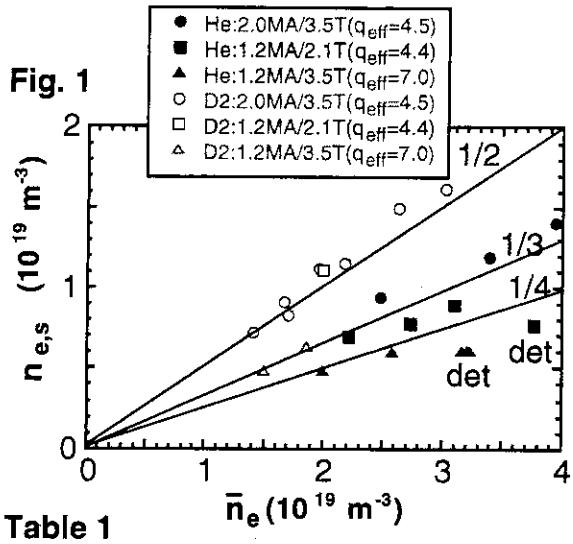

Table 1

$n_{e,s}/n_e$	D2	He
2.0MA/3.5T(qeff=4.5)	0.5	0.35
1.2MA/2.1T(qeff=4.4)	0.5	0.30
1.2MA/3.5T(qeff=7)	0.33	0.25

Fig. 2

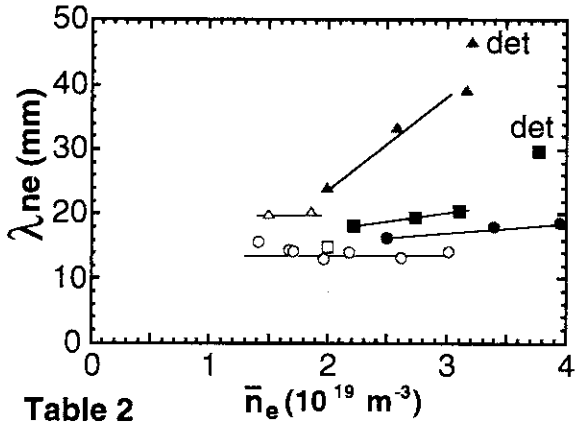

Table 2

λ_{n_e}	D2	He
2.0MA/3.5T(qeff=4.5)	1.2-1.4 cm	1.6 ->1.8 cm
1.2MA/2.1T(qeff=4.4)	1.4 cm	1.8 -> 2 cm
1.2MA/3.5T(qeff=7)	~2 cm	2.4 ->3.9 cm

Figure 3 plots $T_{e,mid}$ at the separatrix, $T_{e,s}$, as a function of $n_{e,s}$. $T_{e,s}$ is similar for **D** and **He** plasmas at the same $n_{e,s}$. Thus, electron pressure at the separatrix, $n_{e,s} \times T_{e,s}$, is comparable for **D** and **He** plasmas, and Fig. 3 also shows that $n_{e,s} \times T_{e,s}$ increases with input power P_{OH}, which is large at high I_p. The detachment of the divertor plasma occurs when $T_{e,s} \leq 40$ eV, which was similar for the L-mode cases. When the detachment of the divertor plasma occurred, $n_{e,s}$ was not increased or decreased with $\bar{n}_e$. In particular for the case of deuterium gas puffing, the main plasma was detached at slightly higher $\bar{n}_e$, causing the high density disruption.

Figure 4 shows e-folding length of the $T_{e,mid}$ profile, λ_{T_e}, as a function of $T_{e,s}$. λ_{T_e} increases with a reduction in $T_{e,s}$ due to a reduction in the electron parallel conductivity. λ_{T_e} in **He** plasma was larger than that in **D** plasma by a factor of 1.3－1.6. λ_{T_e} increases with the connection length (q_{eff}). q_{eff} dependence of λ_{T_e} and the ratio of λ_{T_e} for **He** SOL to that for **D** SOL are similar to those for λ_{n_e} as shown in Fig. 2. Dependence of λ_{T_e} on I_p, B_t and ion species is summarized in Table 3.

Figure 5 compares λ_{T_e} and λ_{n_e}. λ_{T_e} is by a factor of 1.4－2.0 larger than λ_{n_e} at the relatively high $\bar{n}_e$. Ratio of λ_{T_e} to λ_{n_e} increases with the reduction in $T_{e,s}$ (increase in $n_{e,s}$). When the divertor plasma is detached, the ratio of $\lambda_{T_e}/\lambda_{n_e} \sim 2$ is observed for **He** plasma although both λ_{T_e} and λ_{n_e} increase as shown in Fig. 2 and Fig. 4. For the case of high $T_{e,s}$, λ_{T_e} is comparable to λ_{n_e}.

Fig. 3

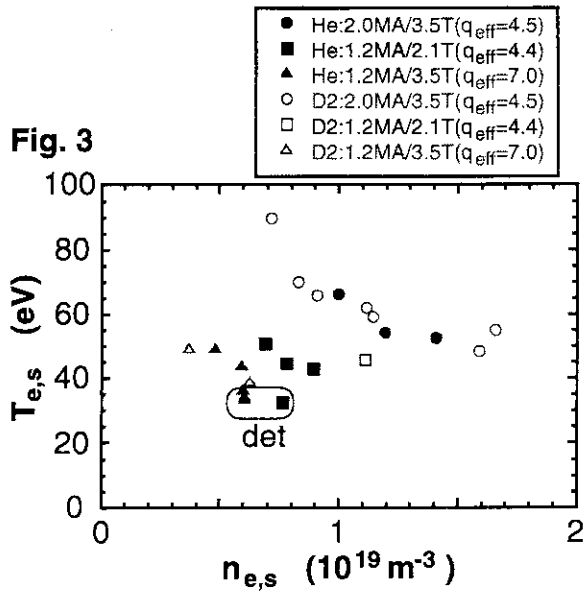

Fig. 4

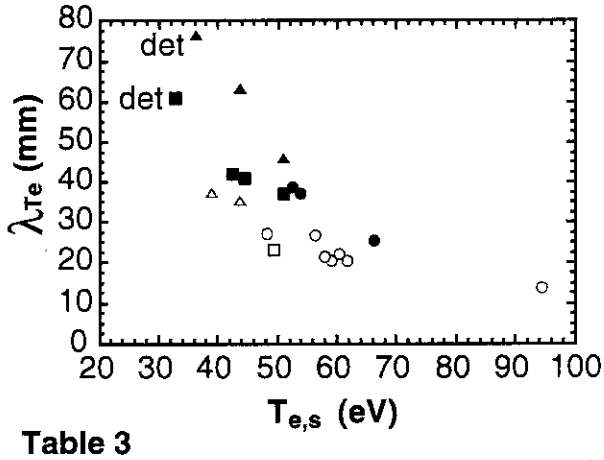

Table 3

λ_{T_e}	D2	He
2.0MA/3.5T(qeff=4.5)	2-2.7 cm	2.7-3.8 cm
1.2MA/2.1T(qeff=4.4)	2.3 cm	3.6 cm
1.2MA/3.5T(qeff=7)	3.5-3.8 cm	5.5-6.5 cm

Fig. 5

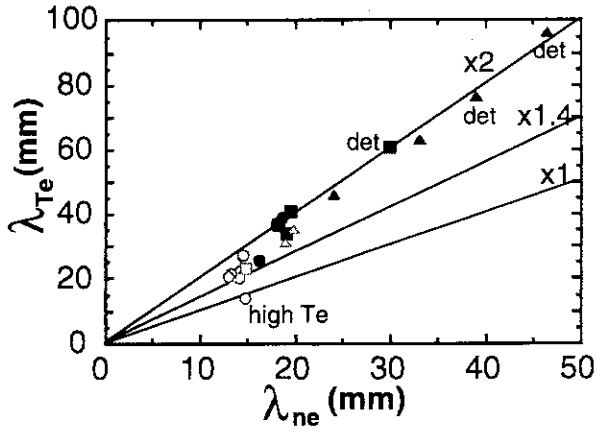

As a result, $n_{e,s}$ in the **He** plasma was lower than that in **D** plasma at the same $\bar{n}_e$; electron density profile is peaked in the **He** discharge. On the other hand, in the SOL region broader density profile was observed. Radiation power becomes large in the deuterium discharge at lower $\bar{n}_e$. Figure 6 (a) and (b) show the radiation fraction of the main plasma, $P_{rad,main}/P_{OH}$, and that of the divertor plasma, $P_{rad,div}/P_{SOL}$, respectively. Here, the power into SOL, P_{SOL}, is given by $P_{OH}-P_{rad,main}$. Whereas q_{eff} dependence of the radiation power is not seen in the main plasma, $P_{rad,div}$ increases with q_{eff} and $\bar{n}_e$. This is because the particle recycling is enhanced in the divertor region due to the longer connection length, causing the lower temperature at the divertor[1]. The radiation fraction in the divertor at an onset of the plasma detachment is 0.45－0.50 for **He** and **D** plasmas. The values are comparable to those in the deuterium L-mode and H-mode discharges[2].

Fig. 6 (a)

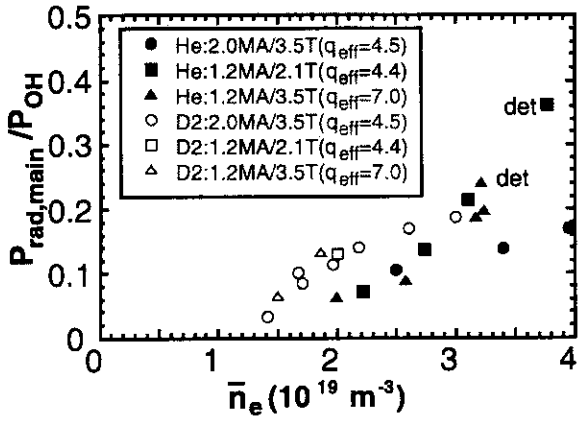

Fig. 6 (b)

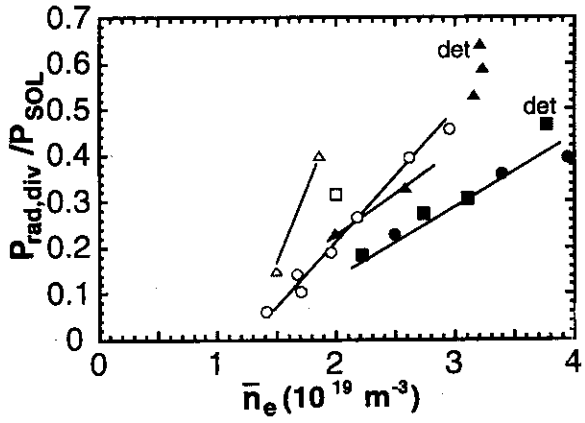

The database will be used to analyze the plasma detachment condition for **He** and **D** plasmas, using a two point model of the SOL and divertor plasmas.

[1] N. Asakura, *et al.*, Nucl. Fusion, **35** (1995) 381.
[2] N. Asakura, *et al.*, Nucl. Fusion, **36** (1996) 795;
N. Asakura, *et al.*, Plasma Physics and Controlled Fusion (1997).

7.7 Edge Plasma Profiles in high density ELMy H-mode

N. Asakura, Y. Koide

1. Introduction

ELMy H-mode discharges have been operated in high density regime with strong puffing of deuterium gas. These discharges produced a cold and dense divertor or detached divertor plasma. Database of the plasma profiles at the SOL and edge, in particular, for the ELMy H-mode discharges is very few, and it is of great practical importance to design the ITER divertor. Density scan of the ELMy H-mode plasma was performed, for the first time in JT-60U, in the relatively low B_t (2.1 T) and I_p (1.2 MA) with P_{NBI} of 6 MW since heat load to an midplane reciprocating Langmuir probe was tolerable to repeat a series of the discharges. In this section, changes in $T_{e,mid}$ and $n_{e,mid}$ profiles in the SOL region are shown, and they are compared to those in the L-mode plasma[1]. Density was increased from 1.8×10^{19} (with small gas puffing of 1 Pa) to 3.4×10^{19} m^{-3} (just below the onset of the X-point MARFE) on a shot-to-shot basis, using feedback control of deuterium gas puffing to keep $\bar{n}_e$ at a constant level during the probe measurement. (Total number of the discharges was six).

2. SOL profiles in ELMy H-mode plasma

$T_{e,mid}$, and $n_{e,mid}$ profiles were measured with the reciprocating Langmuir probe system[2] installed at the midplane with a spatial resolution of 1−2 mm. Rate of the voltage scan of the double-probe (±300 V) was 333 Hz with the sampling rate of 200 kHz, which is faster than the ELM frequency of 100−170 Hz. Large probe current, I_{probe}, produced by a ELM pulse was eliminated using a numerical filter in the analysis process. Fluctuations in I_{probe} (caused by edge plasma fluctuations) were larger than those in L-mode discharge, which influence an estimation of the electron temperature. A method of the noise reduction is now being developed. $T_{i,mid}$ profile in the edge plasma was measured with charge exchange recombination spectroscopy system (CXRS) with a spatial resolution of 6−7mm.

Figure 1 shows $n_{e,mid}$ and $T_{e,mid}$ profiles at $\bar{n}_e = 1.8\times10^{19}$, 2.8×10^{19} and 3.4×10^{19} m^{-3} (just below the X-point MARFE onset). Two (i.e. first and second) SOL regions with different characteristic lengths are observed both in the $n_{e,mid}$ and $T_{e,mid}$ profiles. The first SOL extends up to 10−15 mm outside the separatrix. Using an exponential function in the first SOL region, electron density at the separatrix, $n_{e,s}$, and the e-folding length, λ_{n_e}, are calculated to be 0.570×10^{19}, 0.904×10^{19}, 1.42×10^{19} m^{-3}, and 18.4, 15.1, 16.2 mm,

respectively. Although there is large uncertainty in the electron temperature at the first SOL region due to the large fluctuations, e-folding length, λ_{T_e}, is evaluated to be 18.5, 16.3, 15.4 mm. Ratio of λ_{T_e} to λ_{n_e} is unity (smaller the that in the L-mode: $\sim$1.5), which was caused by the small λ_{T_e} in the ELMy H-mode (This is not conclusive).

Fig.1(a)

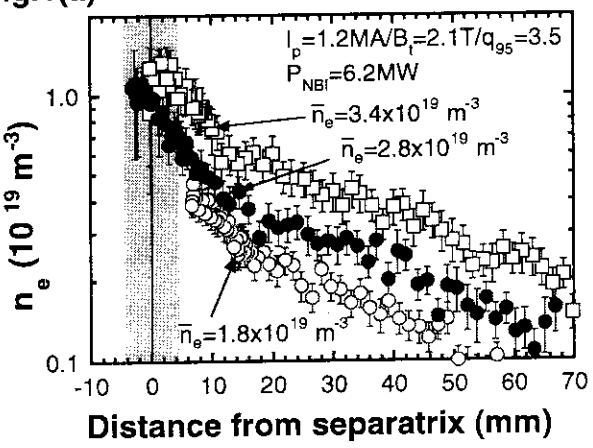

Fig.1(b)

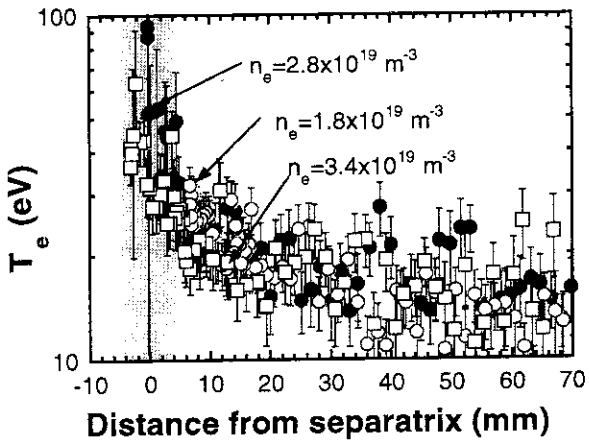

Fig.2 (a)

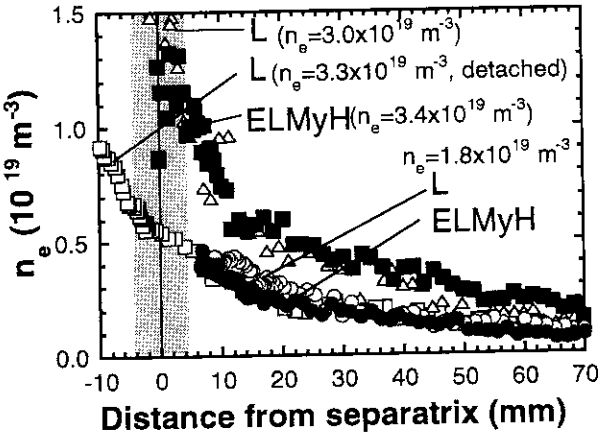

Fig.2 (b)

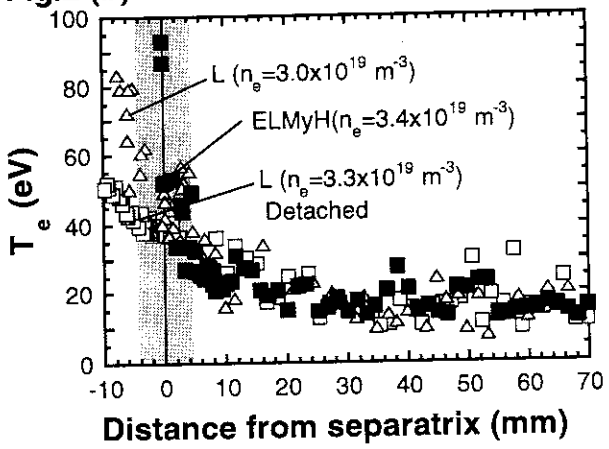

Fig.2 (c)

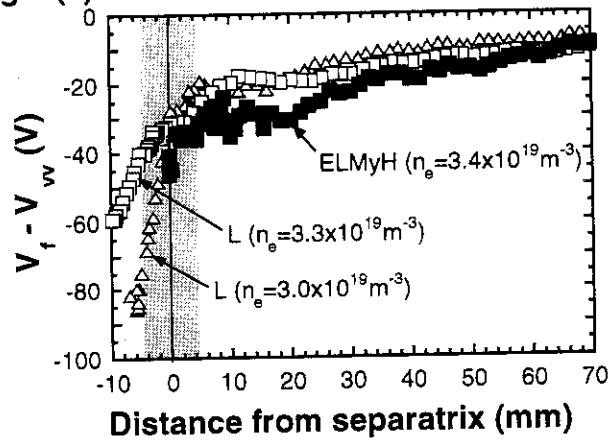

Fig.2 (d)

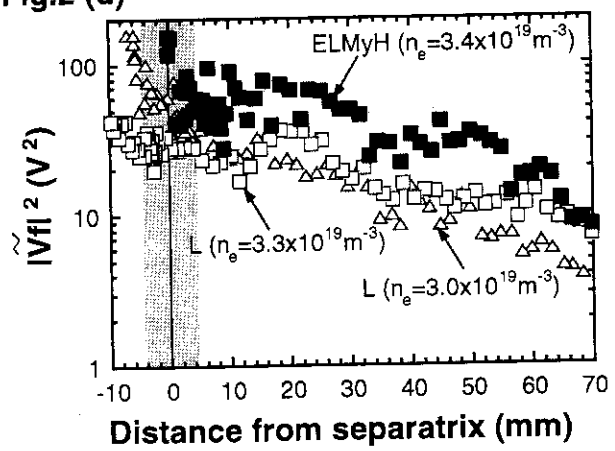

3. Comparison between ELMy H- and L-modes plasmas

$n_{e,mid}$ and $T_{e,mid}$ profiles for L-mode and ELMy H-mode are shown in Fig. 2(a) and (b). SOL plasma profiles were obtained in the L-mode at low $\bar{n}_e$ (1.8×10^{19} m^{-3}) and at high $\bar{n}_e$ ($3.0 - 3.4 \times 10^{19}$ m^{-3}) with lower $P_{NBI} = 4$ MW. For the L-mode plasma at high $\bar{n}_e$ of 3.3×10^{19} m^{-3}, divertor plasma is detached and X-point MARFE occurs, causing large reduction in $n_{e,s}$ (as shown in Fig. 2(a)). The divertor plasma is attached at $\bar{n}_e$ of 3.0×10^{19} m^{-3} for the L-mode and at $\bar{n}_e$ of 3.4×10^{19} m^{-3} for the ELMy H-mode. $n_{e,mid}$ profiles in the first and second SOL regions are similar between L-mode and ELMy H-mode when $n_{e,s}$ is the same as shown in Fig. 2(a). $T_{e,mid}$ profile has a large gradient at the separatrix compared to that in the L-mode, while at the outer region $T_{e,mid}$ are similar. Figures 3(c) and (d) shows that floating potential, V_f, is slightly lower compared to that in the L-mode, while power of V_f fluctuations, $\langle \tilde{V}_f^2 \rangle$, is larger than that in the L-mode. Here, large V_f caused by an ELM pulse and power level of low frequency ($\leq$1 kHz) induced by V_{probe} sweep are not included in $\langle \tilde{V}_f^2 \rangle$.

4. Edge plasma profiles

Electron density profiles in the edge regions corresponding to those in Fig. 2(a) are shown in Fig. 3. Large gradient and clearer pedestal of n_e profile are observed at the inside of the separatrix in the ELMy H-mode plasma. In the SOL region, n_e profiles are similar between the L- and H-modes within the large error bars of the measurement (20－30%) and spatial ambiguity of 5 mm. Values of n_e at the separatrix, $n_{e,s}$, (0.5×10^{19} and 1×10^{19} m^{-3} at low and high densities, respectively), are consistent with the results of the reciprocating probe measurements. When the X-point MARFE occurs, n_e decreases at inside of the separatrix ($r/a = 0.91$－1).

Ion and electron temperature profiles, T_i and T_e, corresponding to the n_e profiles are shown in Fig. 4(a) and (b). With increasing $\bar{n}_e$ from 1.8×10^{19} to $(3.3 - 3.4) \times 10^{19}$ m^{-3}, T_i at the separatrix, $T_{i,s}$, decreases from 430 to 220 eV for ELMy H-mode and from 220 and 80 eV for L-mode. T_e at the separatrix, $T_{e,s}$, decreases from 160 and 80 eV for L-mode, which have large errors of 80 and 50 eV, respectively. These values of $T_{e,s}$ are larger than 50 and 38 eV measured with the reciprocating probe. $T_{e,s}$ for ELMy H-mode has a larger error of 100%, and they are not shown in Fig. 4(b).

5. Summary

In the SOL region, T_e profile at the separatrix had a larger gradient compared to that for

the L-mode plasma. In the first and second SOL regions, fluctuation power in floating potential, $\langle \tilde{V}_f^2 \rangle$, was larger compared to that in the L-mode. However, n_e and T_e profiles for the ELMy H-mode were similar to those for L-mode plasma. The database will be used to analyze SOL/divertor plasma transport and the plasma detachment condition for ELMy H-mode plasmas, using a two point model of the SOL plasma.

[1] N. Asakura, *et al.*, "SOL plasma profiles under radiative and detached divertor conditions in JT-60U", J. Nual. Matter. (1997).

[2] N. Asakura, *et al.*, Rev. Sci. Instrum. **66** (1995) 5428.

Fig.3

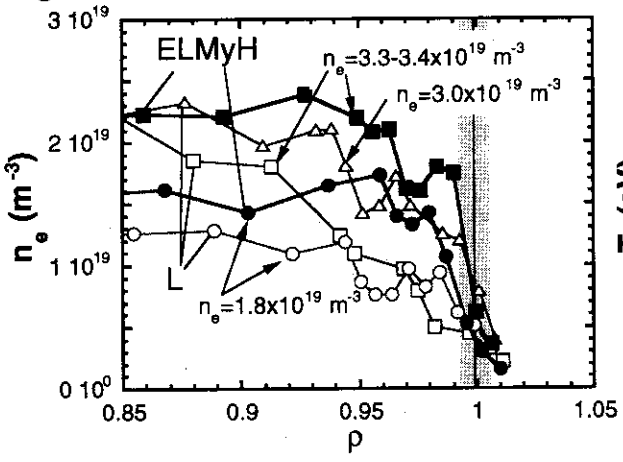

Fig.4 (a)

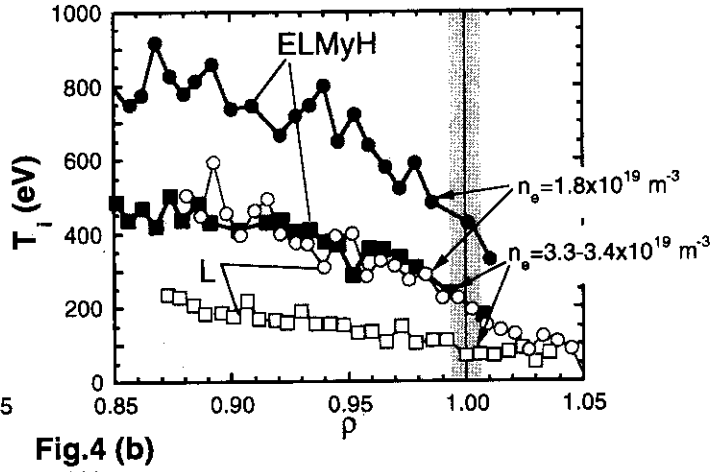

Fig.4 (b)

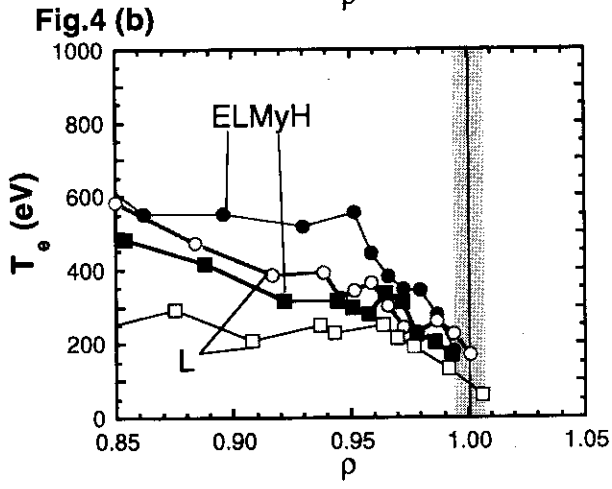

7.8 A Compact W-Shaped Pumped Divertor Concept For JT-60U[1]

N. Hosogane, S. Sakurai, K. Shimizu, S. Tsuji -Iio[1)], M. Shimada,
K. Kodama, K. Masaki, N. Asakura, K. Itami and T. Takizuka
1) Tokyo Institute of Technology

In JT-60U, the present open divertor will be modified to the W-shaped pumped divertor(Fig. 1) in February-May, 1997, aiming to develop a new compact radiative divertor compatible with the main plasma performance. The new divertor consists of inclined divertor plates and a dome arranged in a W-shaped configuration, as well as inner baffles and outer baffles for pumping duct. The inclined target type divertor with a dome was adopted because of its effectiveness in achieving dense and cold divertor plasmas and baffling the back flow of neutral particles. The neutral particles will be exhausted through the gaps between the divertor plates and the dome. The net pumping speed is in a range of 35 m^3/s to 70 m^3/s at 0.1-1 Pa at 300°C. For active control of particle exhaust, fast shutter valves, with an aperture changeable during a shot, will be installed to the three pumping ports.

The performance of this divertor was assessed with numerical simulations. In the W-shaped divertor, even with large pumping, divertor electron temperature as low as 10 eV is obtained with smaller particle flux than the open divertor under the same heating condition of P_{SOL}=12 MW, indicating the effectiveness in achieving a dense and cold divertor plasma. At the same time, the neutral particle density at the periphery of the main plasma is remarkably reduced(more than 1/50) by the baffling effect of the inclined targets. With the dome, the throughput from the private region is increased by a factor of about 2, and is controlled by changing the gap between the separatrix and the dome. Moreover, according to the calculation with impurity transport cord(IMPDV), the dome is found to reduce the influx of methane gas to the X-point region.

[1] N. Hosogane et al., in 16th IAEA Fusion Energy Conference, Montreal, Canada, 1996.

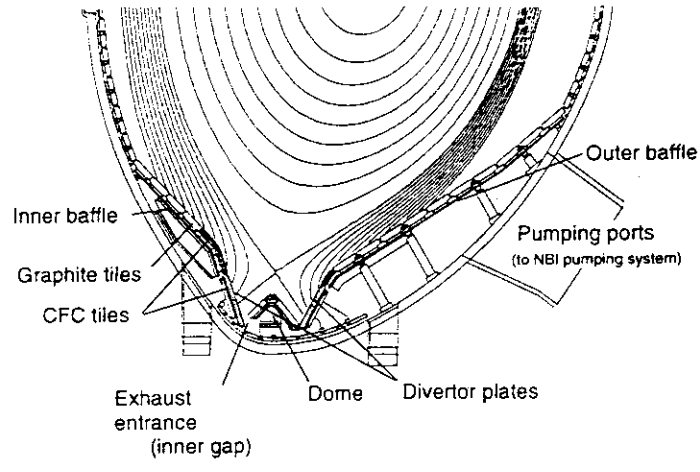

Fig. 1 Cross-sectional view of W-shaped divertor

8. Particle Confinement and Impurity Behavior

8. 1 Effects of source distribution and edge density on particle confinement[1, 2)]

H. Takenaga, N. Asakura, K. Shimizu, K. Nagashima, H. Kubo and A. Sakasai

In order to understand the effects of the particle source distribution and the edge density on the global particle confinement, the particle balance has been quantitatively analyzed. The dependence of the particle confinement time on the ratio of the NBI source to the wall recycling and gas-puffing sources was investigated. The particle confinement time increased with this ratio for the L-mode and ELMy H-mode plasmas, while, for the ELM-free H-mode plasma, the dependence of the particle confinement time on this ratio was not obvious. Furthermore, the confinement times of the NBI particles (τ_p^{NB}) and the wall recycling particles (τ_p^{R}) were separated for the L-mode plasma from the global particle balance analysis. The value of τ_p^{NB} was about 3 times longer than τ_p^{R}, although the penetration depth of the NBI source was 10 times longer than that of the wall recycling source.

In order to clarify above results, the local particle transport has been analyzed. The density in the main plasma is maintained by not only the particle source in the main plasma but also the edge density. When the edge density is not zero, the density in the main plasma becomes some value, even if there is no particle source in the main plasma. We call this density, which is not related with the particle source in the main plasma, a "base density". In this analysis, the densities maintained by the NBI and wall recycling sources and the base density were separated, and τ_p^{NB} and τ_p^{R} were estimated. First, from the analysis in the steady state phase and the perturbed phase, the particle diffusion coefficient was estimated to be 1.0 m^2/s at the plasma edge and 0.1 m^2/s at the plasma center, and also the large inward pinch velocity of 20 m/s was estimated at the plasma edge. Then, the effects of the source distribution and the base density was investigated using the estimated transport coefficients. It was found that the edge density and the strong inward pinch give the small ratio of τ_p^{NB}/τ_p^{R}. The values of τ_p^{NB} and τ_p^{R} estimated from the local analysis were smaller by 60% than those estimated from the global analysis, because in the global analysis the effect of the base density was not taken into account. These results indicated the particle confinement can not be represented by the particle confinement time estimated from the particle number and the particle source in the main plasma.

References

1) H. Takenaga, et al., to be published in J. Nucl. Mater. (12th PSI)

2) H. Takenaga, et al., submitted to Nucl. Fusion.

8. 2 Confinement time for pellet injected particles

H. Takenaga, K. Nagashima

1. Introduction

Pellet injection is a most promising method for the particle fuelling in the main plasma of a fusion reactor. It is expected that the pellet is injected in the plasma edge region of the fusion reactors because of the high edge temperature and the large plasma size. In order to understand the effect of the edge injection, it is important to investigate the dependence of the particle confinement on the ablation depth of the pellet injection. In this report, the effective confinement time for the pellet injected particles was estimated from the decay time of the electron density after the pellet injection, and its dependence on the ablation depth was discussed. Furthermore, in order to understand the global confinement of the pellet injected particles, the local particle transport was simulated using the particle transport coefficients evaluated from the gas-puffing modulation experiment.

2. Method of analysis

The global balance for the particles fuelled by the pellet injection and wall recycling can be separately expressed using the effective confinement time for the pellet injected particles (τ_p^P) and the confinement time for the particles fuelled by the wall recycling (τ_p^R) as follows:

$$\frac{dN_p}{dt} = -\frac{N_p}{\tau_p^P} + S_P \qquad (1)$$

$$\frac{dN_R}{dt} = -\frac{N_R}{\tau_p^R} + S_R \qquad (2)$$

where N_p and N_R are the electron numbers fuelled by the pellet injection and wall recycling, respectively. S_P and S_R are the particle source of the pellet injection and wall recycling, respectively. After the pellet injection (S_p=0), the solutions of eqs. (1) and (2) can be obtained as follows:

$$N_p = N_p(0)\exp\left(-\frac{t}{\tau_p^P}\right) \qquad (3)$$

$$N_R = \exp\left(-\int \frac{1}{\tau_p^R}\,dt\right)\left\{\int S_R \exp\left(\int \frac{1}{\tau_p^R}\,dt\right)dt + N_R(0)\right\} \qquad (4)$$

Therefore, the total electron number after the pellet injection can be represented as follows:

$$N = N_p + N_R$$

$$= N_p(0)\exp\left(-\frac{t}{\tau_p^P}\right) + \exp\left(-\int \frac{1}{\tau_p^R}\,dt\right)\left\{\int S_R \exp\left(\int \frac{1}{\tau_p^R}\,dt\right)dt + N_R(0)\right\} \quad (5)$$

The value of τ_p^P can be estimated from the time decay of the electron density after the pellet injection, if τ_p^R and S_R are known. Here, τ_p^R was estimated from the ohmic phase and the total wall recycling source was estimated from the Dα emission intensities. The penetration probability of the wall recycling neutrals into the main plasma was calculated by the neutral particle transport simulation code DEGAS based on the measurements of the divertor probes.

3. Experimental results

The experiments were performed with the plasma current of I_p = 1.8 MA and the magnetic field strength of B_T = 3.5 T. Figure 1 shows the wave-forms of the averaged electron densities, the total particle source estimated from the Dα emission intensities and the particle flux onto the divertor plates measured with the divertor probes. The pellet was injected into the OH plasma at t = 5.5 s with the injection steed of about 1 km/s. In order to estimate the particle coefficients, the gas-puffing modulation experiment was also performed after 2 s from the pellet injection. This result is discussed in the next section. The ablation depth of the pellet was changed by the density scan for the target plasma. Figure 2 shows the electron density profiles just after the pellet injection for the edge ablation case (a) and the center ablation case (b). The position of the peak election density (r/a_{ne}^{peak}) was located at r/a=0.8 and 0.0 for the edge and central ablation cases, respectively.

First, the particle confinement time for the wall recycling source (τ_p^R) was estimated in the ohmic phase as shown in fig. 3. τ_p^R

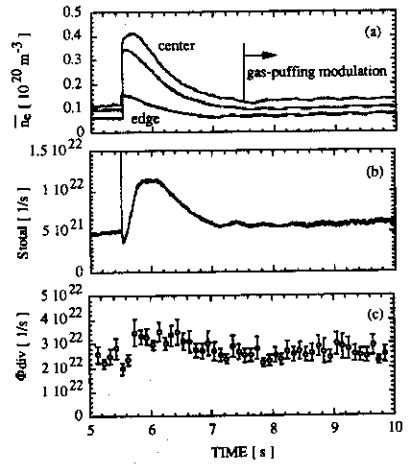

fig. 1 wave-forms of the averaged electron densities (a), the total particle source estimated from the D_α emission intensities (b) and the particle flux onto the divertor plates (c) with I_p =1.8MA and B_T =3.5T.

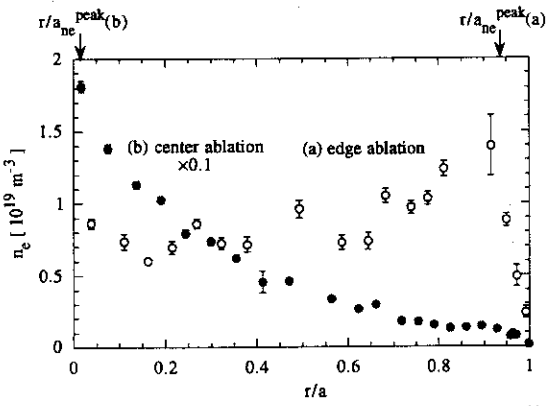

fig. 2 Electron density profiles just after the pellet injection for the edge ablation case (a) and the center ablation case (b).

increased with the electron density until $\bar{n}_e = 0.6\times10^{19}$ m^{-3}, however, τ_p^R was almost constant up to this value. The constant value of $\tau_p^R = 0.6$ s was used for the analysis model as mentioned in the section 2.

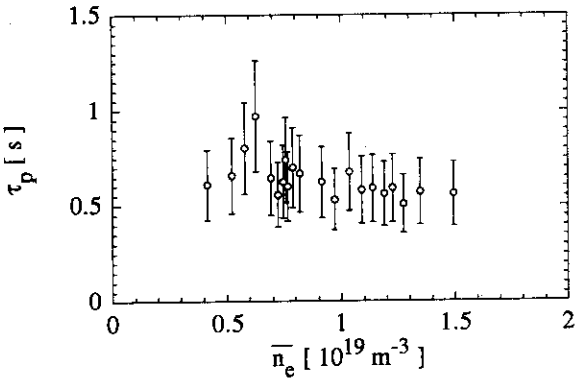

fig. 3 Particle confinement time in the ohmic phase.

In fig. 4, the results of the analysis are shown for the center ablation case. The value of N was evaluated based on the measurements (FIR and Thomson scattering), N_R was estimated using eq. (4) and N_p was estimated by the subtracting N_R from N. The value of τ_p^P was evaluated from the decay time of N_p. In this case, τ_p^P was evaluated to be 0.4 s. The dependence of τ_p^P on r/a_{ne}^{peak} is shown in fig. 5. τ_p^P is constant in the region of $r/a_{ne}^{peak} > 0.4$, and τ_p^P in the case of $r/a_{ne}^{peak} = 0$ is twice larger than that in the case of $r/a_{ne}^{peak} > 0.4$. It is expected that τ_p^P increases with the ablation depth, however, the results obtained here suggested that τ_p^P is constant until certain value. In the next section, the reason was discussed based on the local particle transport simulation.

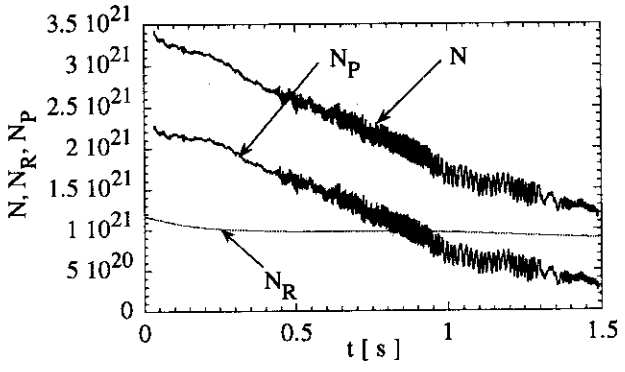

fig. 4 Time decay of electron numbers in the center ablation case evaluated using the model described in the section 2.

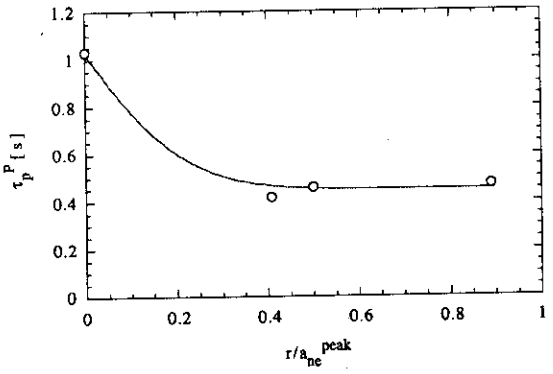

fig. 5 Dependence of τ_p^P on r/a_{ne}^{peak} .

4. Particle transport simulation

The particle transport coefficients were estimated from the gas-puffing modulation experiment[1]. Here, the particle diffusivity was assumed to be constant value and the inward pinch velocity was assumed to be $v=2DCv/a^2$ for the simplify. The value of D and Cv were estimated to be 1.16 m^2/s and 0.6, respectively.

Figure 6 shows the time evolution of the electron density profile for the pellet injected particles in the center ablation case using the estimated D and Cv. The ablation profile of the pellet was calculated using a theoretical formula. We estimated τ_p^P from the decay time of

the simulated N_p. Figure 7 shows the relationship between τ_p^P evaluated from the experiment and τ_p^P estimated from the simulation. The value of τ_p^P estimated from the simulation was almost constant, even if the ablation depth was changed. This result comes from the fact that the electron density profile becomes same during the sort time ($t < 50$ ms), even if the electron density profile just after the pellet injection was different due to the difference of the ablation depth. The value of τ_p^P evaluated from the experiment was also constant except for the central ablation case, however, the absolute value was twice lager than that estimated from the simulation. The value of τ_p^P evaluated from the experiment for the central ablation case is much larger than that estimated by the simulation. This might be come from the fact that D in the central region smaller than that in the edge region. We used the simple model of the particle transport, however, , in order to investigate these effect, more detail model should be used such as radial profile of D and v, T dependence of D and v. This should be investigated in future work.

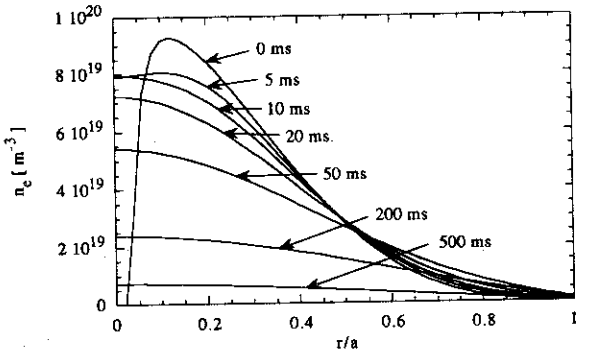

fig. 6 Time evolution of density profile in the center ablation case calculated using the estimated D and Cv.

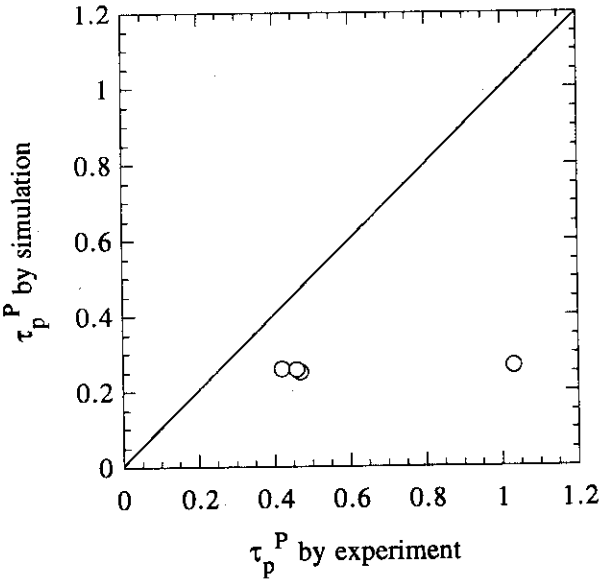

fig. 7 Relationship between τ_p^P estimated from experiments and simulations.

5. Conclusion

The value of τ_p^P was estimated from the decay time of the electron density after the pellet injection. It was found that τ_p^P is constant value of 0.4-0.5 s for the case of $r/a_{ne}^{peak} > 0.4$, and τ_p^P in the case of $r/a_{ne}^{peak} = 0$ is twice larger than that in the case of $r/a_{ne}^{peak} > 0.4$. Simulation using the simple model of the particle transport indicated the weak dependence of τ_p^P on the ablation depth.

Reference

1) K. Nagashima, et al., to be published in Plasma Phys. Control. Fusion.

8. 3 Neutral deuterium and helium behavior in JT-60U divertor plasmas[1)]

H. Takenaga, H. Kubo, T. Sugie, N. Asakura, A. Sakasai, S. Kuroda*,
K. Uchino* and K. Muraoka*

Neutral deuterium and helium behavior in JT-60U divertor plasmas has been studied based on measurements of the spectra and emission profiles of Dα and He I lines combined with computer simulations. The measured Dα spectrum shows a symmetrical profile and the contribution of the reflected particles with high energy was not observed. The peak of the spectrum shifted about 6 pm toward the short wavelength side. The calculated peak shift of the Dα spectrum was larger than that of the measurement. In order to adjust the simulation to the measurement, the simulation in which the Franck-Condon energy was taken as a free parameter was performed. The Franck-Condon energies of 0.03, 2, 5 and 10 eV should be taken into account for the adjusting.

The measured He I spectrum shows broad and narrow components. The broadening of the narrow component was almost the same as the wavelength resolution of the spectrometer. In this measurement, the wavelength resolution corresponds to the Doppler width of helium at a temperature of 0.2 eV. The width of the broad component was equal to the Doppler width of helium at a temperature of 1-2 eV. The narrow component can be ascribed to the desorbed helium. However, the mechanism which produces the broad component is yet to be understood.

The deuterium and helium density and the penetration probability into the main plasma were estimated based on the measurements of absolute Dα and He I emission intensity profiles and simulations. The deuterium and helium sources were estimated to be 3.3×10^{22} and 3.2×10^{21} s^{-1}, respectively. The deuterium and helium densities at the outboard strike point were estimated to be 1.6×10^{17} and 4.7×10^{17} m^{-3}, respectively. Although the total helium source released at the divertor plates was one order of magnitude smaller than the deuterium source, the helium density was higher than the deuterium density at the outboard strike point, because the helium source was localized around the outboard strike point compared with the deuterium source. The penetration probability of deuterium and helium were estimated to be 2 and 1.3%, respectively. The penetration probability of the helium strongly depends on its energy, and it is important for helium control to understand the mechanism which is responsible for the production of the broad component in the He I spectrum.

Reference

1) H. Takenaga, et al., in proceedings of the 1996 ICPP (Nagoya 1996) vol. 1, 642.

*Department of Energy Conversion, Kyushu University, Kasuga Fukuoka 816, Japan

8.4 Dα line profile in the divertor region

H. Kubo, H. Takenaga, T. Sugie

Understanding of behavior of deuterium atoms in divertor regions is necessary to control fueling and pumping in fusion plasmas. The velocity distribution of deuterium atoms determines their penetration depth into plasmas and includes the information on the recycling processes. In the divertor region of JT-60U, the profile of Dα line has been observed to investigate the velocity distribution of the deuterium atoms.

Dα line profile in the outboard divertor region measured with a high-resolution visible spectrometer [1] is shown in Fig. 1. The wavelength resolution is 0.011 nm for the present observation. The spectrum is split into three components due to the Paschen-Back effect. The line profile is symmetry and the shift in the wavelength is little. It suggests that the contribution of the reflection of deuterium ions at divertor tiles is not important. According to Ref. 2, the reflection coefficient is 0.15 and the mean reflection energy is 60 eV for D^+ with an incident energy of 100 eV on carbon materials. Such discrepancy between the tokamak observation and the atomic data is also found for He [3]. The spectrum can be fit by a sum of narrow and broad Gaussian components. The narrow component is attributed to the emission from Franck-Condon atoms before the charge-exchange with deuterium ions. The temperature corresponding to the width is 1.3 eV and this width has information on dissociation processes of deuterium molecules and molecular ions. The broad component is attributed to the atoms produced by the charge-exchange. The temperature corresponding to the width is 22 eV. It must be lower than the ion temperature, because atoms with the higher energy escape the divertor region in the shorter time and the probability of their emitting Dα line is the lower.

For more detail investigation, it is necessary to simulate the spectra using sophisticated code like DEGAS.

References

1) Kubo H. et al.: to be published in Fusion Eng. Des.
2) Eckstein, W.: Suppl. J. Nucl. Fusion Vol 1., 17 (1991).
3) Kubo. et al.: in this JAERI Report.

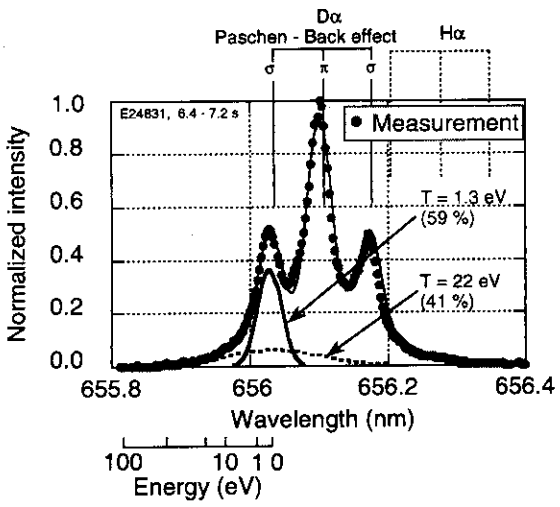

Fig. 1 Dα line profile in the outboard divertor region. Points indicate the measured spectrum and the lines indicate the fitted spectra. The toroidal field is 3.5 T, the NBI power is 8 MW, and the averaged electron density in the main plasma is 1.6 × 10^{19} m^{-3}. The electron temperature and the electron density measured by a Langmuir probe near the outboard strike point are 40 eV and 0.49 × 10^{19} m^{-3}, respectively.

8.5 A Review on Impurity Transport in Divertors [1]

K. Shimizu, T. Takizuka, A. Sakasai

Analyses with an impurity Monte-Carlo code IMPMC have elucidated impurity generation and shielding in JT-60U [2,3]. The impurity shielding effect of a dome in JT-60U divertor modification was also investigated [4]. Including such analyses, this paper reviewed the recent progress in experiments and simulations which have been made in JT-60U and other major tokamaks for understanding impurity transport in divertors.

Power exhaust is one of the most crucial requirements for future fusion reactors, like ITER. It is widely recognized that impurity injection is needed to significantly reduce the heat load to the divertor plates. By means of strong gas puffing and introduction of light impurities, the compatibility of high confinement core plasma (H-mode) with strong radiative divertor has been demonstrated in DIII-D [5], JET [6], Alcator C-mod [7] and ASDEX-Upgrade [8]. In negative shear discharges in JT-60U, the detached divertor has been recently achieved for 1.6 s by neon gas puffing with the internal transport barrier sustained [9]. Impurity injection plays an essential role in achieving high confinement core plasmas with the radiative divertor. However, the core impurity contamination was high (Z_{eff} ~ 3) compared to the value required for ITER (Z_{eff} < 1.6). Therefore, a scheme for impurity retention in the divertor region should be established for fusion research. The issues contained in the paper are impurity generation, shielding and cross field diffusion. As for the impurity generation, chemical sputtering and wall source are discussed with emphasis on the characteristics of their transport and shielding. Impurity control with plasma flow induced by gas puffing and divertor pumping, and adequately designed divertor geometry is also presented.

Simulation analyses with Monte-Carlo codes of DIVIMP [10] and IMPMC [2] have made progress in understanding the impurity behavior in divertors. The diagnostics have been developed remarkably in the last two years. In this conference (PSI-12), interesting experimental results were presented: the direct measurement of the parallel flow of carbon towards the divertor plate in the Alcator C-mod [11], and the impurity enrichment factor evaluated by absolutely calibrated charge exchange recombination spectroscopy for Ne^{+10} in DIII-D puff and pump experiments [12]. Major findings obtained from such recent advances in simulations and diagnostics are as follows:

-- The production mechanism of carbon, which is the dominant impurity in most of the present tokamaks with carbon divertor plates and/or walls, has been investigated extensively. It was found that in the low recycling divertor, physical sputtering and self sputtering are the main causes of carbon generation [2]. It is confirmed that chemical

sputtering from the wall and/or the target plates becomes dominant in the carbon production mechanism in high recycling and detached divertor plasmas [3].

-- The wall source is found to contribute to the core impurity content because of a large penetration probability [13]. Influx of the wall source into the main plasma can be suppressed by a high density and high temperature SOL plasma.

-- Impurity retention in the divertor is determined basically by the balance between the thermal force and friction force. From the measured C IV radiation profile, the impurity diffusion coefficient was evaluated as ~1 m^2/s in JT-60U [2].

-- One of the most promising methods for impurity control is to enhance the plasma flow with gas puffing and pumping. In puff and pump experiments in DIII-D [14] and ASDEX-U [15], impurity retention in the divertor was improved. There are two candidates for the mechanism: the upstream plasma flow induced externally or recirculation of neutrals in the divertor chamber. The dominant mechanism is yet to be identified. Direct measurement of the plasma flow is needed.

-- Methane sputtered from the private region is found to enhance the radiation around the X-point in an open divertor, such as JT-60U, and has a possibility to cause an X-point MARFE. A dome to close the private region effectively suppresses the carbon impurity flux into the upstream SOL and the temperature dependence of its radiation power becomes favorable to thermal stability ($\delta P_{rad} < 0$ for $\delta T_e < 0$), suggesting that the dome is effective in stabilization of a MARFE caused by chemical sputtering [4].

References

[1] Shimizu K., Takizuka T., Sakasai A.: to be published in J. Nucl. Mater. (PSI-12).

[2] Shimizu K. et al., J. Nucl. Mater. 220-222 (1995) 410.

[3] Shimizu K. et al.: in Plasma Physics and Controlled Nuclear Fusion Research 1994 (Proc. 15th Int. Conf. Seville, 1994), Vol.3, IAEA, Vienna (1996) 431.

[4] Shimizu K. et al.: J. Plasma and Fusion Research 71 (1995) 1227.

[5] Allen S.L. et al.: J. Nucl. Mater. 220-222 (1995) 336.

[6] Matthews G.F. et al.: Plasma Phys. Control. Fusion 37 (1995) A227.

[7] Lipschultz B. et al.: to be published in J. Nucl. Mater. (PSI-12).

[8] Gruber O. et al.: Phys. Rev. Lett. 74 (1995) 4217.

[9] Itami K. et al.: Phys. Rev. Lett. 78 (1997) 1267.

[10] Stangeby P.C. and Elder J.D.: J. Nucl. Mater. 196-198 (1992) 258.

[11] Jablonski D. et al.: to be published in J. Nucl. Mater. (PSI-12).

[12] Schaffer M.J. et al.: to be published in J. Nucl. Mater. (PSI-12).

[13] Matthews G.F. et al.: J. Nucl. Mater. 196-198 (1992) 374.

[14] Mahdavi M.A. et al.: J. Nucl. Mater. 220-222 (1995) 13.

[15] Bosch H.-S. et al.: Phys. Rev. Lett. 76 (1996) 2499.

8.6 Study of carbon impurity generation by chemical sputtering in JT-60U [1]

S. Higashijima, H. Kubo, T. Sugie, K. Shimizu, N. Asakura, K. Itami,
N. Hosogane, A. Sakasai, S. Konoshima, S. Sakurai and H. Takenaga

8.6.1 Introduction

Production of hydrocarbons is still important even if the electron temperature of the divertor plasma is so low that physical sputtering can be negligible. To reduce the quantity of carbon impurity generated by chemical sputtering processes is an important issue for the long operation such as in ITER to suppress the erosion of divertor tiles. The chemical sputtering dependence on the deuterium ion flux and the surface temperature of divertor tiles has systematically been studied.

8.6.2 Results

In the divertor region, CD-band intensity attributed to methane has been measured in L-mode high density plasmas, and the chemical sputtering yield of methane was estimated as functions of the surface temperature and deuterium ion flux. Bremsstrahlung, C II and Dα intensities were measured at the same time and the relations between the production of methane and them were investigated. The conclusions were summarized as follows;

(1) The chemical sputtering yield for CFC tiles was typically from 10^{-3} to 10^{-2} for 350K < $T^{Surface}$ < 600K and 10 eV < T_e < 50 eV.

(2) The chemical sputtering of B4C-converted CFC tiles was small in comparison with normal CFC tiles. Especially the yield was ~10^{-3} in the range of 350K < $T^{Surface}$ < 850K and 10 eV < T_e < 50 eV and 1.0 X 10^{19} m^{-3} < n_e < 1.5 X 10^{19} m^{-3}.

(3) The chemical sputtering yield of methane for CFC tiles was decreased from ~ 10^{-2} to ~ 10^{-3} when the deuterium ion flux increased from 1 X 10^{22} $m^{-2}s^{-1}$ to 1 X 10^{23} $m^{-2}s^{-1}$ between 10 eV < T_e < 50 eV.

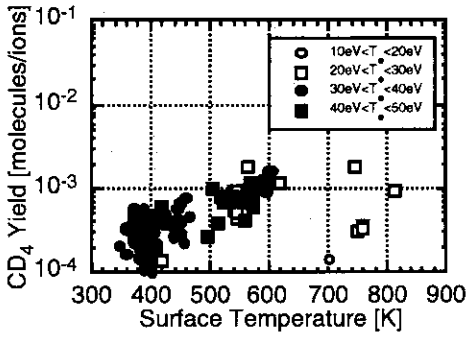

Fig. 1 Surface temperature dependence of chemical sputtering yield for B4C-converted CFC tiles for 1.0 X 10^{19} m^{-3} < n_e < 1.5 X 10^{19} m^{-3}. The electron temperature in the divertor was in the range from 10 eV to 50 eV.

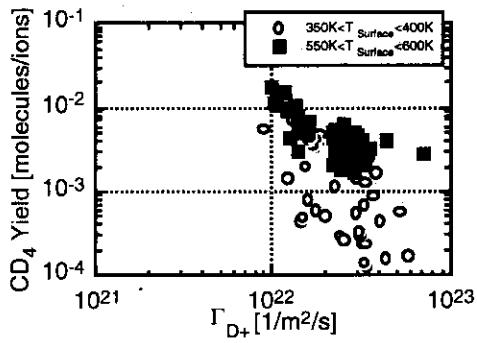

Fig. 2 Deuterium ion flux dependence of chemical sputtering yield of methane for CFC tiles. The open circles represent data with 350K < $T^{Surface}$ < 600K and the closed squares represent data with 550K < $T^{Surface}$ < 600K and 10 eV < T_e < 50 eV.

References

[1] Higashijima S. et al., to be published in J. Nucl. Mater..

8.7 Effect of Particle and Heat Fluxes on Carbon Generation during ELMy Phase in JT-60U[1]

S. Sakurai, N. Asakura, K. Itami, Y. Kamada, H. Kubo and A. Sakasai

ELMy H-mode is considered as a steady-state operation mode in a tokamak reactor. Divertor targets are periodically exposed huge particle and heat fluxes at ELM events. It is very important to study the effect of particle and heat fluxes and divertor tile temperature on carbon generation during ELMy phase.

Burst of the emission from carbon impurities were observed just after the degradation of the good confinement (H-factor ~2) in a quasi-steady state high b_p ELMy H-mode discharge with high power (~28MW) NB heating in JT-60U. The measured temperature of the inboard target exceeded 1200°C at the burst, although the maximum point located beyond the view of the divertor diagnostics. Radiation of carbon impurities around the inboard target could not be obtained too. Large spikes of Dα signals and surface temperature at the inboard target show that heat and particle fluxes at a giant ELM pulse on the inboard target are much larger than those on the outboard target.

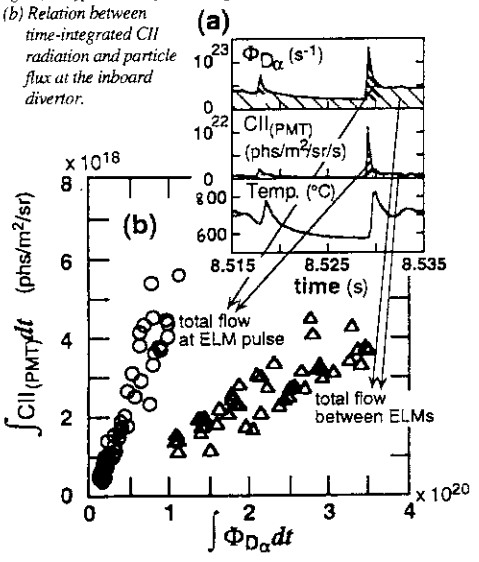

Fig.1 (a) Typical waveform at a giant ELM. (b) Relation between time-integrated CII radiation and particle flux at the inboard divertor.

The profiles of CII radiation in divertor region and surface temperature of target tiles were measured in long pulse NB heated (~22MW,6s) ELMy discharges with adjusted configuration for divertor diagnostics. The maximum temperature of divertor targets kept below 900°C and the burst was not observed in these discharges. CII radiation around the inboard target was much larger than that around outboard target. Particle and heat fluxes at each ELM pulse measured by fast sampling diagnostics confirm large in-out asymmetry. These results suggest that the inner divertor target is dominant carbon source and particle and/or heat fluxes at an ELM pulse affect the carbon generation during ELMy phase. Figure 1(a) shows Dα and CII radiation and the surface temperature of the inboard divertor measured by fast sampling PMT array (20μs) and IRTV (250μs). CII radiation is extremely enhanced at a giant ELM pulse. Figure 1(b) shows the relation between time-integrated CII radiation and particle flux at the inboard target. The ratio of CII radiation to the particle flux at an ELM pulse is much larger than that between ELMs. This suggests that the sputtering yield of carbon was enhanced at an ELM pulse. The effect of ELMs on carbon generation is not negligible.

[1] S. Sakurai, N. Asakura, K. Itami, Y. Kamada et al., in 1996 Int. Conf. on Plasma Physics (Proc. 1996 ICPP, Nagoya, 1996) Vol.1, Japan Soc. of Plasma Sci. and Nucl. Fus. Res., Nagoya (1997) 646-649

8.8 Active Control of Helium Ash Exhaust and Transport Characteristics in JT-60U[1]

A. Sakasai, H. Kubo, K. Shimizu, T. Fujita, N. Asakura, K. Itami,
S. Higashijima, S. Sakurai, H. Takenaga, N. Hosogane and the JT-60 team

In-out asymmetry with He flux in the divertor during ELMy H-mode has been successfully controlled by changing neutral beam (NB) power and plasma current (I_P). The effect of the ion grad-B drift direction, I_P and B_T (q_{eff}) dependence on He exhaust was investigated in ELMy H-mode and L-mode. The He flux is larger on the outer target than on the inner target in the cases of I_P=1.0 MA, B_T=2.5 T, P_{NB}=18 MW. On the other hand, the He flux is larger on the inner target than on the outer target in the case of I_P=1.7 MA, B_T=3.5 T, P_{NB}=18 MW. The in-out asymmetry with the outboard enhanced He flux is remarkable in ELMy H-mode with high NB power heating and low I_P. The in-out asymmetry in the He flux profiles do not depend on the ion grad-B drift direction. However, the in-out asymmetry in the D flux is changed with the ion grad-B drift away the divertor (reversed B_T and I_P). The asymmetry seems to be determined by β_P (including edge parameters: n_e, T_e, T_i et al.). It does not explicitly depend on NB power and I_P. Asymmetry control and solid target boronization (STB) enabled effective helium ash exhaust. This result suggests that the selective exhaust, for example He ash removal from the outboard and fueling particle removal from the inboard, is possible to control the burning of core plasma in future reactors.

Helium transport characteristics of reversed shear plasmas has been studied using a ^{4}He beam (central fueling) and a short pulse He gas puff (edge fueling). In reversed shear mode, the electron density in the central region is peaked and the confinement is remarkably enhanced inside the internal transport barrier (ITB), which is formed near the position of minimum q. $n_e(r)$, $T_e(r)$ and $T_i(r)$ profiles inside the ITB are peaked. The improvement of the He particle confinement was found inside the ITB. He density profile depends on a strength of ITB. He particle confinement is enhanced due to an ITB formation. The He transport in reversed shear plasmas was found to be characterized by a large inward velocity near the ITB. To summarize, helium accumulation was observed inside the ITB. This result indicates that it is difficult for He particles to purge He particles from inside the ITB. This behavior of helium in reversed shear mode is clearly different from those in ELMy H-mode and L-mode[2]. However, the profile of He concentration in reversed shear plasma is almost flat because the shape of $n_e(r)$ profile is almost the same as the He density profile.

References

[1] A. Sakasai et al., the 16th IAEA Fusion Energy Conf., Montreal 1996, AP2-1.
[2] A. Sakasai et al., Journal of Nuclear Materials 220-222 (1995) 405.

8. 9 Characteristic of Dα and He I emissions in ELMy H-mode plasma

H. Takenaga, S. Sakurai, N. Asakura, H. Kubo and A. Sakasai

It is expected that ELM activities encourage the helium ash exhaust from the main plasma in fusion reactors. In order to understand the exhaust property in ELMy H-mode plasmas, He I emission has been measured in the divertor region of JT-60U.[1] The in-out asymmetry has been found in He I emission and the asymmetry was changed by the scanning of the plasma parameters. However, because the time resolution of this measurement was longer than the cycle of the ELM pulses, time evolution of He I emission in each ELM pulse was not studied. In this report, Dα and He I (668nm) emissions in the ELMy H-mode plasma were simultaneously measured with a fast sampling around the inboard and outboard strike points, and the characteristic of Dα and He I emissions in each ELM pulse was discussed.

Figure 1 shows the sight lines and the plasma configuration used in this study. The Dα and He I emissions were measured with optical fibers. The light transmitted through the optical fibers was divided into 2 branches, and these were detected with a time resolution of 0.25 ms through the interference filters for Dα and He I, respectively.

Figure 2 shows the wave-forms of the NBI power, the averaged electron densities and the stored energy in the ELMy H-mode plasma analyzed here. The discharge was operated in deuterium with the plasma current of 1.4 MA, the toroidal magnetic field of 3.5 T and the NBI power of 17 MW. Helium was fuelled by the 60 keV ^{4}He beams. The heating due to the D beams was started at t = 5.0 s, and the He beam injection was started at t = 5.5 s. The electron density gradually increased and the stored energy gradually decreased during t = 6.0-8.0 s.

Upper figure of fig. 3 shows the time evolution of Dα and He I emissions around the inboard and outboard strike points during t = 5.0-8.0 s. In lower figure of fig. 3, the Dα and He I emissions during t = 5.5-5.6 s are shown on an enlarged scale. Here, we define the height of emission spike due to the ELM pulse ($H^{in,\,out}_{D\alpha,\,He\,I}$) and the base of emission ($B^{in,\,out}_{D\alpha,\,He\,I}$) as shown in lower figure. It can be seen from the upper figure of fig. 3, $H^{in}_{D\alpha}$ and $H^{out}_{D\alpha}$ decreased, while $B^{in}_{D\alpha}$ and $B^{out}_{D\alpha}$ gradually increased. On the other hand, $H^{in}_{He\,I}$ increased together with the increment of $B^{in}_{He\,I}$. In contrast, $H^{out}_{He\,I}$ seems to be constant, although $B^{out}_{He\,I}$ increased. In the period of t = 5.5-5.6 s, the spikes of Dα and He I emissions simultaneously appeared as shown in the lower figure. However, the spike of the He I emission around the inboard strike point was not obvious during t = 5.5-5.6 s.

The in-out asymmetry of He I emission for each ELM pulse is shown in fig. 4. The open circles show the ratio of $B^{in}_{He\,I}/B^{out}_{D\alpha}$, the closed circles show the ratio of $H^{in}_{He\,I}/H^{out}_{He\,I}$. It can be seen from this figure, the base and height ratios show the different tendency. The

ratio of $B^{in}_{He\,I}/B^{out}_{D\alpha}$ decreased, while the ratio of $H^{in}_{He\,I}/H^{out}_{He\,I}$ increased.

The ratio of the ELM height to the base (H/B) of the He I emission was plotted against that of Dα emission in fig. 5. The open circles show the data around the inboard strike point and the closed circles show the data around the outboard strike point. The H/B of He I emission around the outboard strike point was proportional to the H/B of Dα emission. The H/B of He I emission around the inboard strike point increased with the H/B of Dα emission until the H/B of Dα emission was equal to 1, however, the H/B of He I emission was saturated above this value.

In this analysis, our discussion was limited on the emission property of Dα and He I. In order to understand the helium behavior in the ELMy H-mode plasma, it is necessary to interpret the Dα and He I emissions to the particle flux.

Reference

1) A. Sakasai, et al., in Plasma Phys. Contrl. Nucl. Fusion Research (Proc. 16th IAEA Fusion Energy Conf., Montreal, 1996) AP2-1.

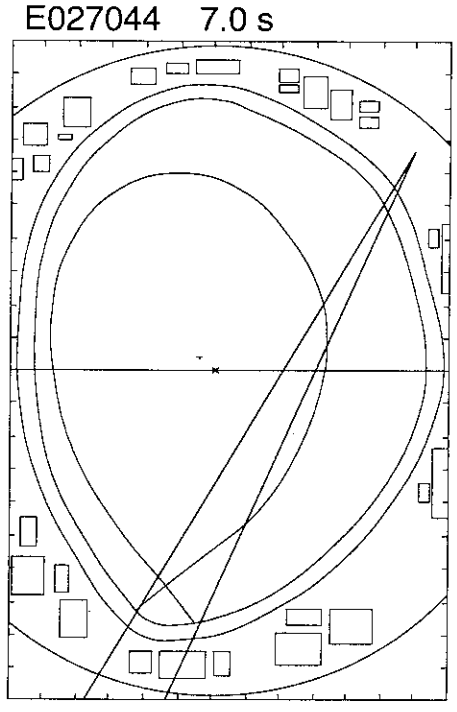

fig. 1 Sight lines of the measurements and the plasma configuration.

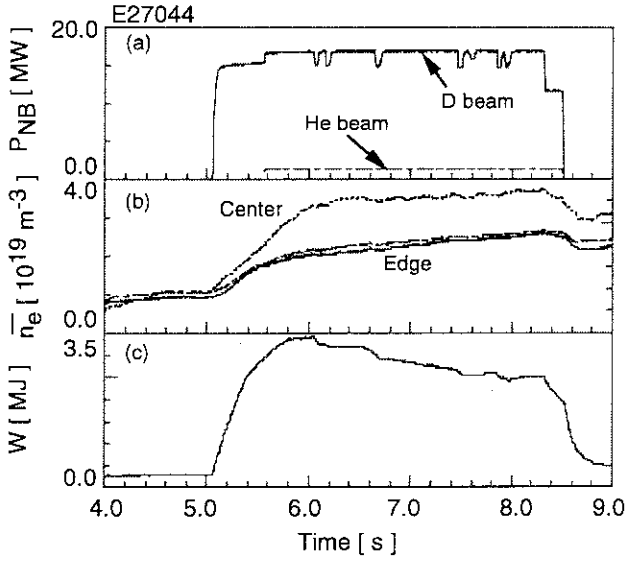

fig. 2 Wave-forms of the discharge: (a) the NBI power of the D and He beams, (b) the averaged electron densities and (c) the strored energy.

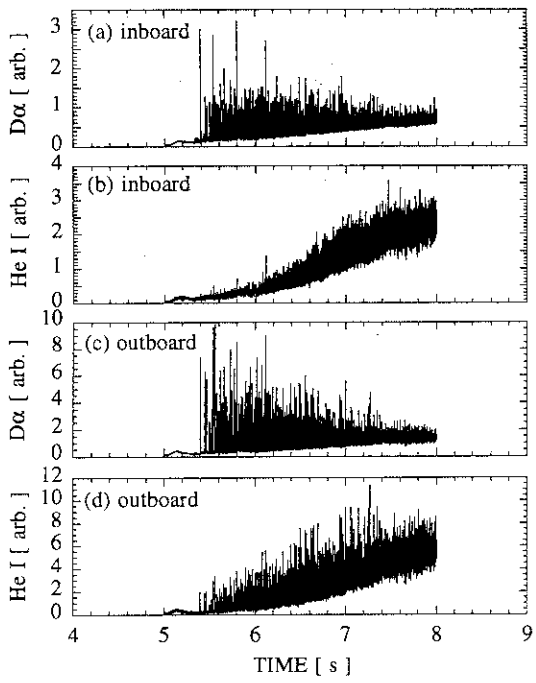

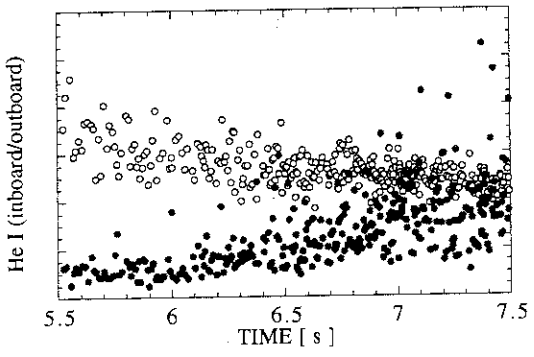

fig. 4 In-out asymmetry of base (open circles) and ELM height (closed circles) of He I emission.

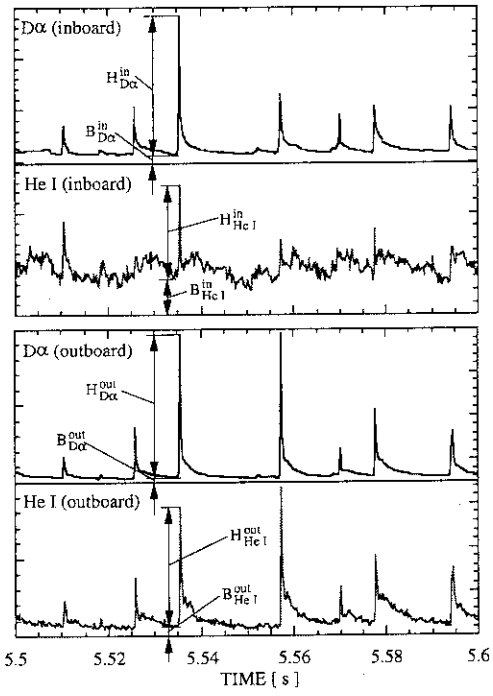

fig. 3 Time evolution of D α and He I emissions: (a) D α emission around the inboard strike point, (b) He I emission around the inboard strike point, (c) Dα emission around the outboard strike point and (d) He I emission around the outboard strike point. In lower figure, Dα and He I emissions during t = 5.5-5.6 s are shown on an enlarged scale

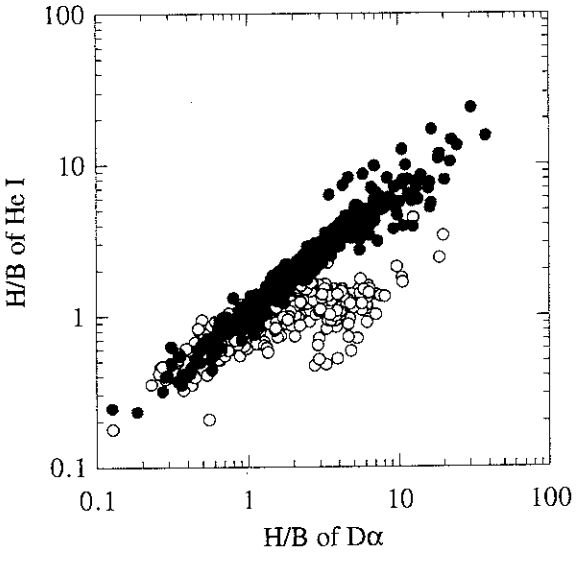

fig. 5 Relationship between H/B of Dα and He I. Open circles show the data around the inboard strike point, and closed circles show the data around the outboard strike point.

8.10 Helium Removal from Reversed Shear Plasmas

A. Sakasai, H. Kubo, T. Fujita, S. Higashijima

1. Introduction

In reversed shear mode, the electron density in the central region is peaked and the confinement is remarkably enhanced inside the internal transport barrier (ITB), which is formed near the position of minimum q. The electron temperature and ion temperature profiles ($T_e(r)$, $T_i(r)$) inside the ITB are also peaked in JT-60U[1]. Then reversed shear mode is attractive because of its improvement of particle and energy confinement at the core region as a new operation scenario for ITER. Helium ash exhaust from the revered shear plasma is a matter of concern. It is very important to make clear He removal from reversed shear plasmas because of an enhancement of He particle confinement.

2. Experimental Arrangement

A tangential viewing charge-exchange recombination spectroscopy (CXRS) system provides radial density profiles of fully ionized helium. CXR emission of He II 468.52 nm (n=4-3) is led to 0.5-m and 1.0-m Czerny-Turner spectrometers through 80-m pure quartz optical fibers. The detection system consists of image-intensified double linear photodiode arrays that have high sensitivity. The sensitivity calibration of the CXRS system was performed by the use of an integrating sphere.

Recycling influx profiles of D and He ions were derived, respectively, from the measured line intensities of D_α and He I (728.1 nm or 667.8 nm) with a 60-ch optical fiber array coupled to visible spectrometers. This diagnostics enabled measurements in ELMy H-mode discharges with high X-point configuration (X_P=20 cm). The measured electron temperature from the Langmuir probe array at the divertor target is used to calculate the He influx.

3. Helium Density Profiles

Helium transport characteristics of the reversed shear plasma was investigated using a ^4He beam (central fueling) and a short pulse He gas puff (edge fueling)[2]. Figure 1 shows the time evolution of a typical reversed shear discharge (I_P=1.2 MA, B_T=3.0 T, Vol=65 m^3 and P_{NB}=18 MW) with helium beam injection of $P_{He\text{-}NB}$=2.3 MW. The formation of the ITB started at t=5.4 s. Increase of He density in the core plasma (r/a=0.12) is much faster than one in the peripheral region (r/a=0.81) The He density in the core plasma is very peaked with the formation of the ITB. Two partial collapses occurred at t=6.1 s and t=6.3 s. In this discharge, the ITB was not eliminated and reformed. The He density in the core plasma was remarkably reduced by these partial collapses. However, the He density the peripheral region was not affected by the collapse and linearly increased.

Figure 2 shows (a): ion and electron temperature profiles, (b): an electron density profile and (c): He density profiles in reversed shear mode with He beam injection. In reversed shear mode, the electron density in the central region is peaked and the confinement is remarkably enhanced inside the ITB, which is formed near the position of minimum q. $n_e(r)$, $T_e(r)$ and $T_i(r)$ profiles inside the ITB are peaked. The ^{4}He beam injection started at t=5.0 s and lasted for 1.5 s. The H-factors are 1.5 at t=6.0 s and 2.0 at 6.5 s, respectively. The central ion temperature is 8 keV, the central electron temperature is 5 keV and the central electron density was 4×10^{19} m^{-3}.

In the case of He beam injection, the He density is higher inside the ITB than outside the ITB. The He density increase is much faster inside the ITB than outside the ITB. In the case of He gas puff, the He density profile is almost flat for 0.5 s after He gas puff start. Then, the He density inside the ITB continuously increases and reaches 1.4×10^{18} m^{-3} without regard to no He source. On the other hand, the He density outside the ITB reaches a saturation level of 0.8×10^{18} m^{-3} at t=0.5 s after He gas puff start.

To summarize, helium accumulation was observed inside the ITB. This result indicates that it is difficult for He particles to purge He particles from inside the ITB. This behavior of helium in reversed shear mode is clearly different from those in ELMy H-mode and L-mode[3]. However, the profile of He concentration normalized by the electron density in reversed shear plasma is almost flat because the shape of $n_e(r)$ profile is almost the same as the He density profile.

4. Helium Removal from Reversed Shear Plasmas

An enhancement of He particle confinement is not desirable for He exhaust. However, it was observed that He particles inside the ITB was expelled when a partial collapse occurred like particle exhaust due to ELMs. Figure 3 shows (a): the time evolution of helium density (r/a=0.18, 0.50, 0.81) and (b): the time evolution of He I brightness profile in the divertor in a reversed shear discharge with He beam injection. A partial collapse occurred at t=6.4 s in the discharge. The helium density at the center (r/a=0.18) and the half radius (r/a=0.50) was suddenly reduced to 65% after the partial collapse. On the contrary, one at the peripheral region (r/a=0.81) was not so changed and reduced to 95%. The helium density profile was flattening due to the partial collapse. At the same time, the line averaged electron density was reduced to 91%. Then the helium density at the center quickly recovered at t=7.0 s to the level just before the partial collapse.

He flux in the divertor is larger 3 times after a partial collapse (t=6.5 s) than before a partial collapse (t=6.4 s) as shown in Fig. 3 (b). The partial collapse terminated the ITB, He particle confinement was degraded. As the result, helium particles was expelled from the core plasma to the divertor. Therefore, helium can be removed from reversed shear plasmas due to frequent partial collapse. The partial collapse and safety factor q(r) control in reversed shear mode are expected to reduce He ash content in the core plasma.

5. Conclusions

Helium transport characteristics of reversed shear plasmas has been studied using He beam injection and He gas puff. The improvement of the He particle confinement was found inside the ITB. He particle confinement is enhanced due to an ITB formation. When a partial collapse occurred, He particles inside the ITB was expelled at the same time of the disappearance of the ITB. Helium can be removed from reversed shear plasmas due to frequent partial collapse.

References

[1] T. Fujita et al., Proc. of the 16th IAEA Fusion Energy Conf., Montreal 1996, IAEA-F1-CN-64/A1-4.

[2] A. Sakasai et al., Proc. of the 16th IAEA Fusion Energy Conf., Montreal 1996, IAEA-F1-CN-64/AP2-1.

[3] A. Sakasai et al., Journal of Nuclear Materials 220-222 (1995) 405.

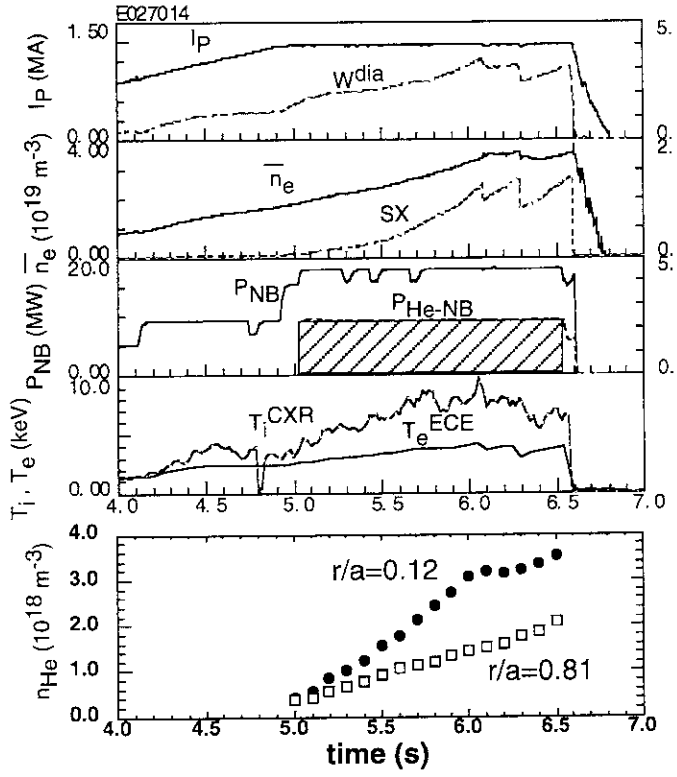

Fig. 1 The time evolution of a typical reversed shear discharge (I_P=1.2 MA, B_T=3.0 T, P_{NB}=18 MW) with helium beam injection.

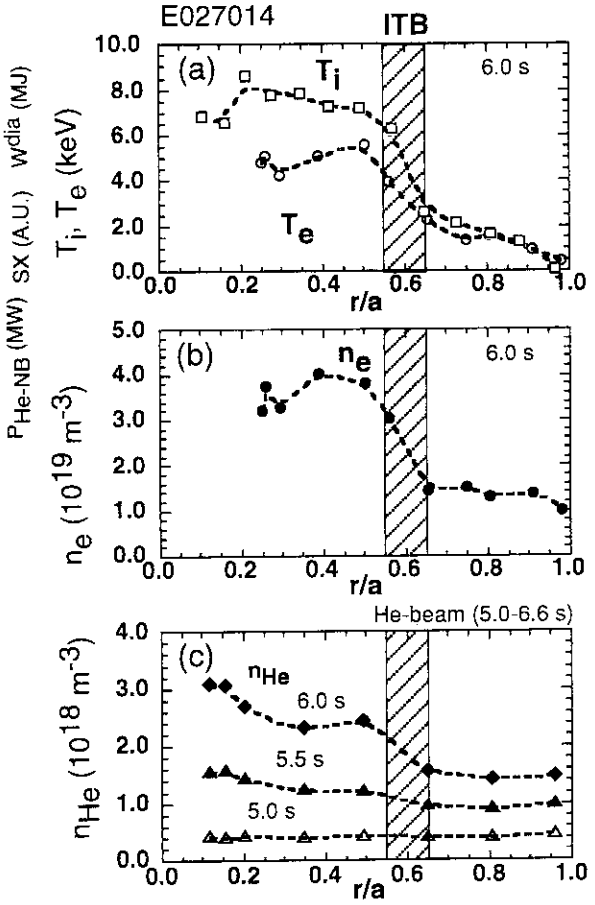

Fig. 2 (a): ion and electron temperature profiles, (b): an electron density profile and (c): helium density profiles in reversed shear mode with He beam injection.

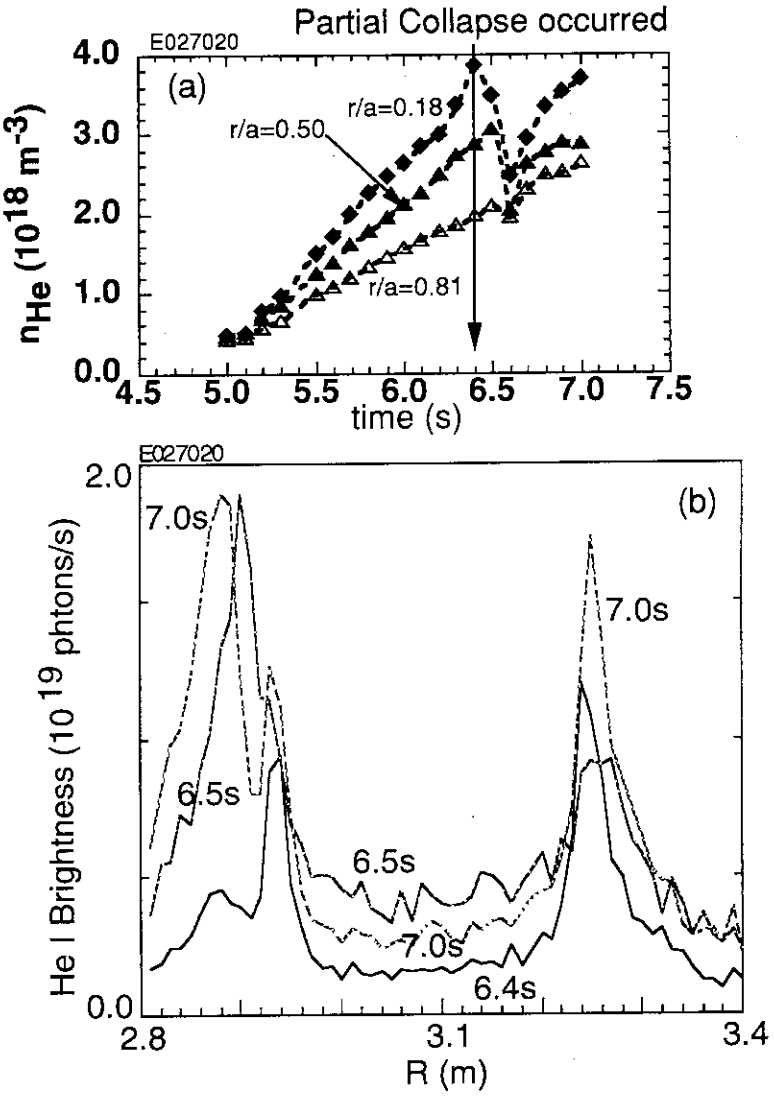

Fig. 3 (a): the time evolution of helium density (r/a=0.18, 0.50, 0.81) and (b): the time evolution of He I brightness profile in the divertor in a reversed shear plasma with He beam injection.

8. 11 Determination of particle transport coefficients in reversed shear plasma of JT-60U[1)]

H. Takenaga, K. Nagashima, A. Sakasai, T. Oikawa and T. Fujita

The improved confinement mode was recently found in the reversed shear plasmas with the internal transport barrier of the electron density. Two reasons for the steep gradient of the electron density can be considered. There are the reduction of the particle diffusivity and the strong inward pinch. It is very important to clarify whether the steep gradient of the electron density is based on both reasons or only one reason, because it is closely related with not only physical mechanism of the internal transport barrier but also the consistency of the improved confinement and the particle control such as fuelling and helium ash exhaust. In order to clarify the above points, the profiles of the particle diffusivity and the convection velocity should be separately evaluated.

We performed the helium gas-puffing modulation experiment in the reversed shear plasma with the plasma current of 1.2 MA and the toroidal magnetic field of 3 T. The particle diffusivity in the region of internal transport barrier was reduced by about factor of 2 compared with that in the inside region. The inward pinch velocity was observed in the region of internal transport barrier, while the outward velocity (inverse pinch) was observed in the inside region.

Reference

1) H. Takenaga, et al., to be submitted to Plasma Phys. Control. Fusion.

8.12 Broadening of He I line in the divertor region

H. Kubo, H. Takenaga, T. Sugie,
S. Higashijima, S. Suzuki and A. Sakasai

1. Introduction

Understanding of behavior of helium atoms in divertor regions is necessary to control helium-ash pumping in fusion plasmas. The velocity distribution of the helium atoms determines their penetration depth into plasmas and includes information on the recycling processes. In the divertor region of JT-60U, the profile of He I line has been observed to investigate the velocity distribution of the helium atoms.

2. Experiment

The profile of He I (668 nm, 1s2p ^{1}P - 1s3d ^{1}D) line from the divertor region has been observed by a high-resolution visible spectrometer [1]. The wavelength resolution was 0.014 nm for the present observation. The spatial distribution in the divertor region was obtained by simultaneous observation along 10 sight lines.

Time evolution of a discharge for this study is shown in Fig.1. He gas was puffed just before NB heating and the electron density was raised by a D_2 puff. Near the outboard strike point the electron density increased and the electron temperature decreased, as the electron density increased in the main plasma. The electron density near the separatrix decreased rapidly at 6.1 s due to the occurrence of partial detachment.

3. Results and Discussion

Fig. 2 shows the spectra of the He I line observed at the outboard strike point at times of 5.25 and 7.75 s of the discharge shown in Fig. 1. The spectra are split into three components due to the Zeeman effect. At 5.25 s, the spectrum is similar to the slit function and the line broadening is small. It suggests that helium atoms are dominantly desorbed with energy about the surface temperature of the divertor tiles and the reflection of helium ions is not important. The suggestion disagrees with the computer simulation of the reflection [2]. The simulation has presented that the particle reflection coefficient and the mean reflection energy are 0.091 and 24.7 eV for He^+ at an incident energy of 100 eV for carbon materials. Similar disagreement has been observed for hydrogen ions [3]. The disagreement might be attributed to the difference of the surface character between the tokamak experiment and the simulation. The spectrum at 7.75 s is obviously broader than the slit function. The temperature corresponding to the width is 1.3 eV and it is much higher than the surface temperature of the divertor tiles.

In this paper, we fit the spectrum by a sum of narrow and broad components (a delta function and a Gauss function) convoluted by the slit function. The time evolution

of the intensities of the two components and the temperature corresponding to the width of the broad component are shown in Fig. 1. The intensity of the narrow component decreases and the intensity of the broad component increases, as the electron density increases and the electron temperature decreases. The broad component is dominant in the partially detached plasma. The temperature of the broad component is 1 - 2 eV.

Fig. 3 shows the spatial distribution of the total intensity, the proportion of the broad component and the temperature corresponding to the width of the broad component. In the attached plasma (5.25 s), the intensity distribution has a clear peak and the proportion of the broad component is low near the strike point. The temperature is about 1.1 eV. In the detached plasma (7.75 s), the intensity distribution is broad and the broad component is dominant. The temperature is about 1.7 eV. In detached plasmas, the ionization length becomes longer, as the electron temperature decreases and the energy of helium atoms increases. It explain the spread of the spatial distribution of the intensity.

A possible heating mechanism to explain the broad component is the elastic collision with deuterium ions [4]. In a temperature range lower than 20 eV, as the temperature decreases, the ionization rate decreases rapidly while the elastic collision rate increases gradually. It can qualitatively explain the tendency that the line width increases as the temperature decreases. In attached plasmas, the temperature is higher at the separatrix than away from the separatrix. In detached plasmas, intensity ratios of He I lines suggested that the electron temperature around the divertor tiles to the null point is about 10 eV[5]. The spatial distributions of the proportion of the broad component shown in Fig. 2 might be attributed to the spatial distribution of the temperature.

Here we define an average temperature of helium atoms as T (broad) × I (broad) / I (total), where T (broad) and I (broad) are the temperature corresponding to the width and the intensity of the broad component, respectively. I (total) is the sum of the intensities of the narrow and broad components. The relation between the average temperature and the electron temperature near the strike point is shown in Fig. 4. The datum in a partially detached plasma is tentatively plot at an electron temperature of 10 eV according to the electron temperature estimated from intensity ratios of He I lines. The average temperature increases as the electron temperature decreases. If it is assumed that helium atoms are heated by the elastic collision before their ionization in an infinite area with temperature: T, and density: n, the average temperature of helium atoms to be observed: T_{He} (calculation), is expressed as

$$\overline{T_{He}}\,(\text{calculation}) = \frac{\int_0^{\infty} T_{He}(t) \exp\left(-S(T_e)\, n_e t\right) dt}{\int_0^{\infty} \exp\left(-S(T_e)\, n_e t\right) dt},$$

$$\frac{dT_{He}}{dt} = R\,(T_{He}, T_{D^+})\, n_{D^+}\ ,$$

where S and R are the ionization rate coefficient and the temperature relaxation rate coefficient by the elastic collision, respectively. The temperature relaxation rate coefficient is calculated using the diffusion crosssection for the elastic collision [4]. If it is assumed that the ion temperature is equal to the electron temperature and the deuterium ion density is equal to the electron density, the average temperature is given as a function of the temperature as shown in Fig. 4. The calculated temperature increases as the temperature decreases. The calculated temperature agrees with the measured temperature in electron regions around 10 eV and 70 eV. The calculated temperature is, however, lower than the measured temperature in the temperature range from 20 to 60 eV. The discrepancy is attributed to the spatial distribution, because the electron temperature is lower away from the separatrix than at the separatrix. And the discrepancy might be attributed to the definition of the measured averaged temperature, because the spectral line does not have a Gaussian profile and the width is close to the width of the slit function. For exact discussions, it is necessary to simulate the line shape using sophisticated codes.

Using a neutral particle transport code (DEGAS), that does not include the effect of the elastic collision, the probability of penetration into the main plasma is estimated to be 0.1 % and 2.7 % for helium atoms with energies of 0.05 (the surface temperature of the divertor tiles) and 2 eV, respectively [6]. The broad component affects significantly helium contamination of the main plasmas. Therefore, it is important to study the heating mechanism of the helium atoms using sophisticated transport code considering the effect of the elastic collision in their transport.

Acknowledgment

The authors are grateful to Dr. N. Tawara of National Institute of Fusion Research and Dr. T. Shirai of Japan Atomic Energy Research Institute for their useful suggestion about atomic data.

References

1) Kubo H. et al.: to be published in Fusion Eng. Des.
2) Eckstein W. and Verbeek H.: IPP 9/32 (1979).
3) Kubo H. et al.: in this JAERI research.
4) Bachmann P. and Reiter D.: Contrib. Plasma. Phys., 35, 45 (1995).
5) Kubo H. et al: JAERI-Research 96-018, 104, (1996).
6) Takenaga, H. et al.: "Proc. Int. Conf. on Plasma Physics", ed. Sugai H. and Hayashi T., Nagoya, 642 (1996).

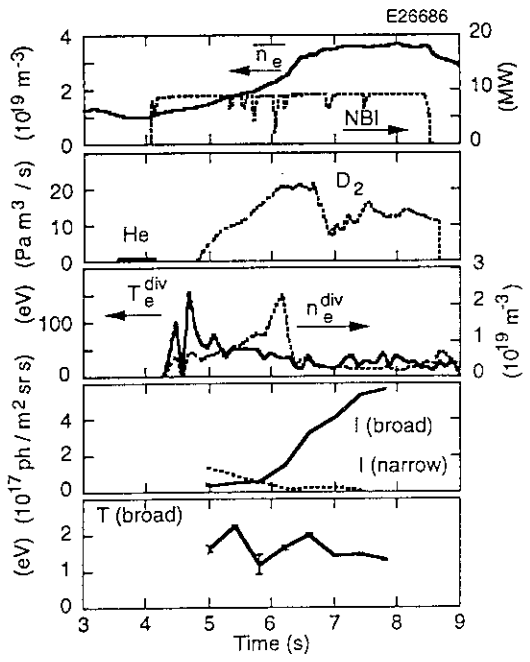

Fig. 1 Time evolution of a discharge with a He puff. The line-averaged electron density in the main plasma and the NBI power are shown in the first row. The puff rates of He and D_2 are shown in the second row. The third row shows the electron temperature and density obtained by a Langmuir probe near the outboard strike point. The forth and the fifth show intensities of the broad and narrow components and the temperature corresponding to the width of the broad component of He I line at the strike point.

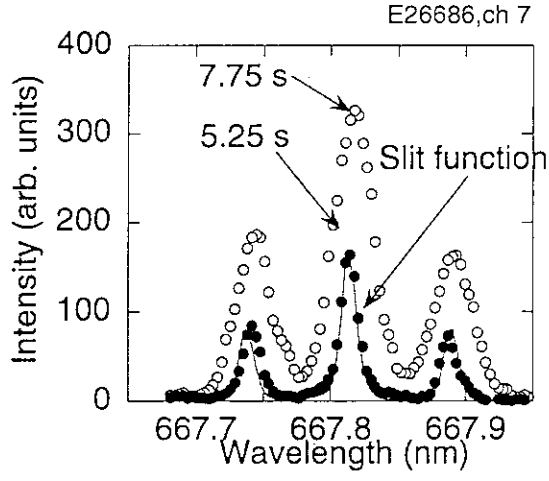

Fig. 2 Spectra of the He I line. The solid and the open circles indicate the spectra observed at the outboard strike point at times of 5.25 and 7.75 s of the discharge shown in Fig. 1, respectively. The line indicates the slit function of the spectrometer.

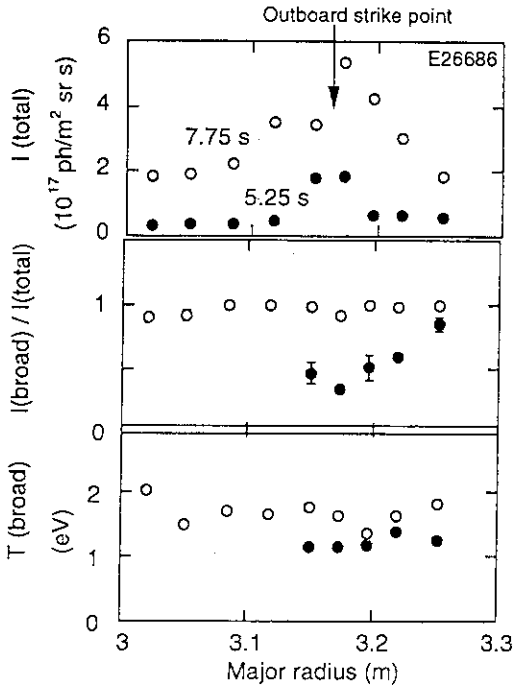

Fig. 3 Spatial distribution of the total intensity, the proportion of the broad component and the temperature corresponding to the width of the broad component of the He I line. The data were obtained at times of 5.25 (solids circles) and 7.75 s (open circles) in the discharge above.

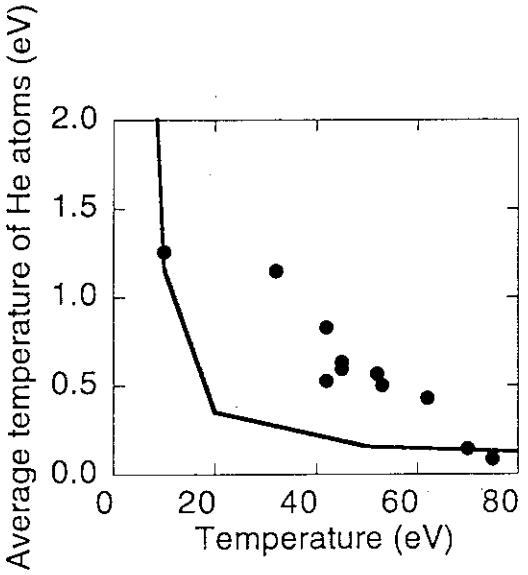

Fig. 4 Average temperatures of the helium atoms as functions of electron temperature. The points indicate the measurement and the line indicates the calculation. The datum measured in a partially detached plasma is tentatively plot at an electron temperature of 10 eV.

8. 13 Neutral helium behavior

H. Takenaga, S. Sakurai, N. Asakura, K. Nagashima, H. Kubo, K. Shimizu and A. Sakasai

1. Introduction

In order to fulfil the burning condition in a fusion plasma, the ratio of τ_{pHe}^{*}/τ_{E} should be smaller than 10, where $\tau_{pHe}^{*}=\tau_{pHe}/(1\text{-}R)$. The value of τ_{pHe}^{*} depends on the two mechanisms as shown in the equation: one is helium confinement in main plasmas, and the other is recycling of neutral helium atoms. The former is closely related to the performance of the main plasma, and the latter strongly depends on the divertor configuration and the pumping rate. These two mechanisms should be separately discussed for understanding of the helium ash exhaust property. In this report, neutral helium behavior was investigated based on the measurements of He I emission (668nm) combined with the computer simulations using the DEGAS code. The helium ion source in the main plasma was estimated, and the helium confinement time was evaluated.

2. Method of analysis

Figure 1 shows the sight lines of the He I emission measurements. In the divertor region, He I emission in the hatched region of fig. 1 was measured with 60ch fiber array. For the main plasma region, there are 6 measuring chords at the different poloidal cross section from the divertor measurement.

In order to interpret the measurement to the helium atom behavior, we used the neutral transport simulation code DEGAS. In the DEGAS code, the helium atom source distribution and the initial energy of the helium atom were given as initial conditions. Two kinds of helium atom source were taken into account. One is a divertor source which is localized around the strike points on the divertor plates and the other is a wall source which is uniformly distributed over the wall surface. In order to determine the absolute value of these sources, the He I emission profiles calculated using the DEGAS code

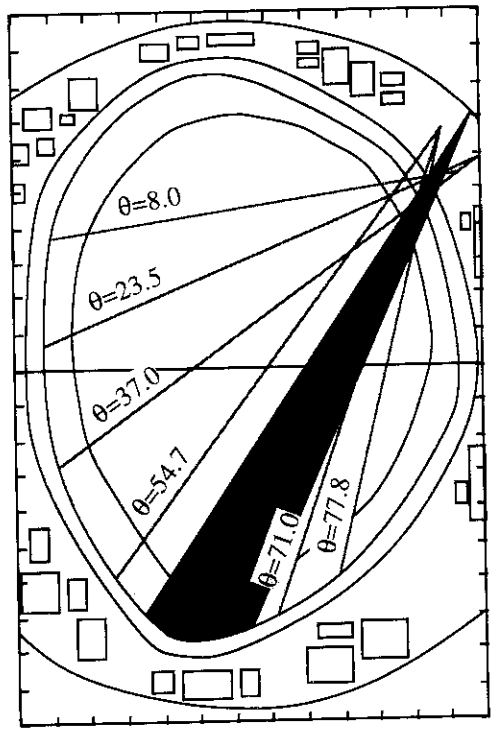

fig. 1 Sight lines of He I emission measurements. In the hatched region, He I emission was measured with 60ch fiber array. For the main plasma region, there are 6 measuring chords whose poloidal angles are shown in the figure.

were fitted to the measured profiles. The helium atoms were released at initial energys of the divertor plate temperature (0.05eV) and 2 eV, because the two components were observed in He I spectrum measurements.[1] The ratio of these components was assumed to be 1.

3. Results and discussion

In fig. 2, the open circles show the measured He I emission intensity profile in the main plasma region as a function of the measuring chord angle shown in fig. 1. The measurements were performed in the L-mode plasma with the plasma current of 1.2 MA and the toroidal magnetic field of 3.5 T. The discharge was operated in the deuterium with a small amount of the helium gas-puffing. The He I emission intensities in the upper region from the mid plane is one order of magnitude smaller than that in the lower region. The solid line in fig. 2 shows the calculated He I emission intensity with the wall source. It can be seen from this figure that the calculated He I emission intensity has the flat profile in the whole plasma region. In this figure, the absolute value of the calculation was determined by the adjusting the calculation to the measurements in the lower region. The wall source was estimated to be 1.8×10^{21} s^{-1}. However, because the calculation is one order of magnitude smaller than the measurement in the upper region, the wall source might be smaller by half. The penetration probability into the main plasma was estimated to be 1.8 and 30 % for the particles with the energy of the wall temperature and 2 eV, respectively. The helium ion source in the main plasma was estimated to be 2.9×10^{20} s^{-1}.

In fig. 3, the open circles show the measured He I emission intensity in the divertor region as a function of the major radius. The measured emission intensity shows peaks at the inboard and outboard strike points. The dashed line shows the calculation for the case of the wall source whose absolute value was determined based on the measurement in the main plasma region as mentioned above. In order to fit the calculation to the measurement around the strike points, the He I emission profile with the divertor source was calculated. We assumed that the width of the helium flux profile released from the divertor plates was a factor of 3 smaller than that of the deuterium flux profile measured with the divertor probes and the outboard helium flux was enhanced by 2.5 compared with the deuterium flux profile, so as to adjust the calculated emission profile to the measurement. The solid line shows the calculation with the divertor source, and thick line shows the sum of the calculations with the wall source and the divertor source. It can be seen from this figure that the calculation agrees well with the measurement. The divertor helium source was estimated to be 3.2×10^{21} s^{-1}. The divertor source was by a factor of 2 larger than the wall source. The penetration probability into the main plasma for the divertor source was estimated to be less than 0.1 and 2.7 % in the case of the initial energy of the wall temperature and 2 eV, respectively. The helium ion source in the main plasma was estimated to be 4.2×10^{19} s^{-1}. The helium ion source in the main plasma due to the divertor source was by a factor of 7 smaller than that

due to the wall source. This fact is disadvantage for the helium ash exhaust. The deuterium wall source is much smaller than the deuterium divertor source in L-mode plasmas[2]. The difference in the ratio of the wall source to the divertor source between deuterium and helium might come from the difference in transport of SOL plasma and/or recycling processes between deuterium and helium. This should be clarify in the future work.

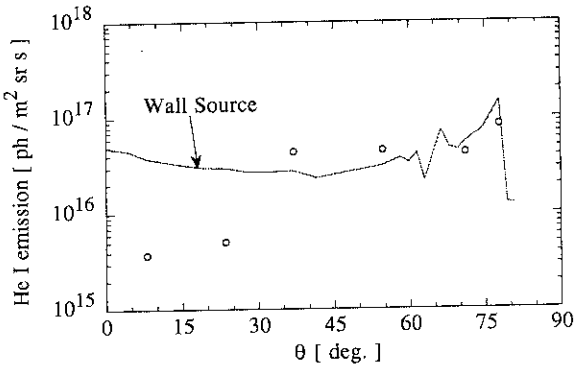

fig. 2 He I emission profiles in the main plasma region as a function of the measuring chord angle. Open circles show the measurements and solid line shows the calculation.

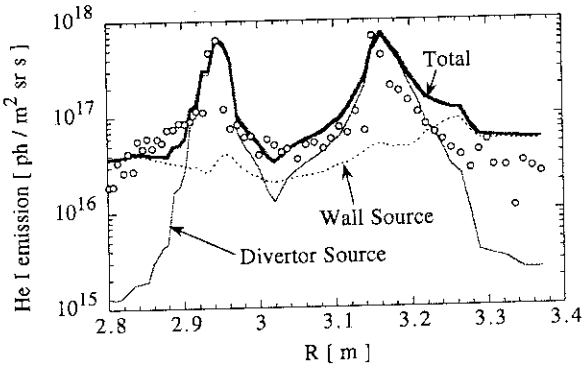

fig. 3 He I emission profiles in the divertor region. Open ciecles show the measurements. Dashed and solid lines show the calculation with wall source and divertor source, respectively. Thick line shows the sum of these calculations.

The total helium ion number was evaluated to be 3.9×10^{19} from the measurement of the helium ion density profile in the main plasma. The helium particle confinement time τ_{pHe} was estimated to be 0.12 s. If the wall source was estimated to be smaller by half because of the disagreement between the calculations and the measurements in the main plasma region, τ_{pHe} was estimated to be 0.2 s. In order to reduce the ambiguity in the estimation of τ_{pHe}, it is necessary to adjust the calculation to the measurement in the upper region from the mid plane by changing the wall source distribution. Furthermore, because the penetration probability strongly depends on the energy of the helium atoms, the mechanism which decides the helium atom energy should be investigated.

In this discharge, τ_E was estimated to be 0.13 s, therefore, the ratio of τ_{pHe}/τ_E was estimated to be 1-1.5. In order to obtain the condition of $\tau_{pHe}^*/\tau_E<10$, the recycling factor must be less than 0.85. The recycling factor can be expressed in the burning plasma during the steady state phase as follows:

$$R = \frac{P_W\Phi_W + P_D\Phi_D}{P_W\Phi_W + P_D\Phi_D + \bar{\Phi}},$$

where P_W and P_D are the penetration probability of the wall source and the divertor source, respectively, Φ_W and Φ_D are the wall source and the divertor source, Φ is the helium production

rate due to the fusion reactions. In the steady state, the pumping flux must equal to the production rate. Therefore, $\Phi=F_{pump}\Phi_D$, where F_{pump} is the pumping rate. If the ratio of Φ_W/Φ_D is expressed as α, R can be rewritten as:

$$R = \frac{P_W\alpha + P_D}{P_W\alpha + P_D + F_{pump}}.$$

In order to obtain the condition of $\tau_{pHe}^*/\tau_E<10$, F_{pump} should be larger than 0.02, if we use the values discussed above. This value gives the restriction for the divertor design. In order to obtain the condition of $\tau_{pHe}^*/\tau_E<10$ with the small value of F_{pump}, α should be smaller.

4. Conclusion

The value of τ_{pHe} was estimated based on the measurements of He I emission combined with the computer simulation using the DEGAS code. It was found that the ratio of the wall source to the divertor source was estimated to be about 0.5, and the helium ion source in the main plasma due to the wall source was by a factor of 7 larger than that due to the divertor source. Based on these analyses, τ_{pHe} was estimated to be 0.12 s.

References

1) H. Takenaga, et al., in proceedings of 1996 ICPP (Nagoya 1996) Vol. 1, 642.
2) H. Takenaga, et al., J. Nucl. Mater. 220-222 (1995) 429.

9. Disruption and Plasma Control

9. 1 Fast current shutdown scenario for major disruption softening in JT-60U [1]

Y. Kawano, R. Yoshino, Y. Neyatani, T. Kondoh, N. Isei, S. Ishida,
K. Tobita, T. Hatae, K. Itami, A. Sakasai, and the JT-60 team

The fast current shutdown scenario using the killer-pellet injection (KPI) has been demonstrated without the generating harmful runaway electrons (REs) [1]. The "burst" like magnetic-fluctuations are enhanced by external helical magnetic-fields. The enhanced magnetic fluctuations can eliminate the relatively low-energy super-thermal electrons created just after the KPI, consequently the quick generation of REs which cause current tail is suppressed. Summaries of the experimental results are as follows;

(1) The current quench rate is raised by the increase in electron density due to the injection of a neon-ice-pellet as a killer pellet.

(2) The "burst" like magnetic fluctuations (n=0) in B_ω/dt signals are enhanced by using external helical fields induced by the four sets of sector coils (the DCW coils).

(3) Super-thermal electrons generated just after KPI can be eliminated by the "burst" like fluctuations, resulting in the avoidance of the current tail caused by REs (see Fig. 1).

(4) Large fluctuation amplitudes of the "n=1" mode can also suppress the REs generation.

(5) The REs generation can not be observed for B_t of <2.5T even without energizing of the DCW coils, and the REs suppression by the DCW coils can not be obtained for B_t of >2.75T, which shows that magnetic fluctuations by the "burst" and the "n=1" mode play an essential role to suppress REs generation.

[1] Y. Kawano, et. al., paper IAEA-CN-64/A3-4 in 16th Fusion Energy Conference, Montreal 1996.

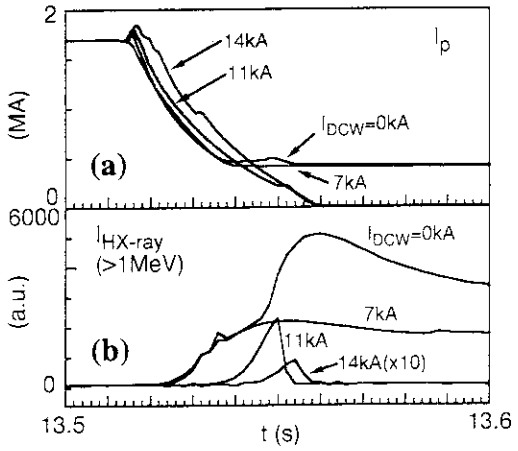

Fig. 1 Suppression of the REs generation by energizing the DCW coils. The DCW coils are energized from 12.9s, and the flat-top coil current (I_{DCW}) is scanned from 0kA to 14kA. (a) The REs tail is suppressed for I_{DCW} =11kA and 14kA, (b) By raising the I_{DCW}, the generation timing of REs is delayed and the intensity of the hard X-ray emission is reduced.

9.2 Plasma-Shape-Control during Slow Plasma-Current-Quench with Avoiding Plasma-Wall Interaction in JT-60U [1)]

R. Yoshino, Y. Nakamura and Y. Neyatani

Vertical Displacement Event (VDE), that is observed for elongated tokamak-plasmas, generates the halo current and intense electromagnetic forces. Fast plasma shutdown caused by the impurity pellet(s) injection is one method to avoid VDE[2)]. On the other hand slow plasma-current-quench (I_p-quench) is considered to be dangerous [3)], because VDE with "full plasma current displacement" is easily generated. However avoidance of VDE at slow I_p-quench has not been thoroughly investigated.

In JT-60U, VDE is caused by error in real-time measurement of the vertical position of the plasma-current center (Z_J) during slow I_p-quench[4)], where real-time measurement of Z_J degrades its accuracy owing to the eddy current. Here Z_J is measured in the real-time from selected magnetic probe signals with using the statistical method derived from the regression analysis, and actual Z_J value is estimated after a plasma discharge from an equilibrium fitting code with long calculation time. The penetration-time of the horizontal magnetic fields into a vacuum vessel is ~8 ms in JT-60U, so the active control of Z_J is possible only for slow I_p-quench with the time constant of > ~20 ms. This VDE has been successfully avoided with minimizing the deviation of the real-time Z_J calculation value from the actual one[1)].

Error in the real-time measurement of the null point height from the divertor plate (X_p) is also observed during I_p-quench with a sudden increase in its positive deviation from the actual X_p, which sometimes reduces the divertor coil current with changing the divertor plasma configuration to the limiter one even when Z_J is controlled well. Causes of this error have not been clarified yet. However proportional control of divertor coil current to the plasma current with improved real-time Z_J measurement have demonstrated the maintenance of the divertor plasma configuration[1)]. Here the horizontal displacement of the geometrical plasma center from the vacuum vessel center has been always controlled around the reference position. This maintenance of gaps has been also demonstrated for ITER-like q_{95} of 2.9.

References

1) Yoshino R., et al., submitted to Nucl. Fusion (1997).
2) Yoshino R., et al., in Plasma Phys. and Control. Fusion **39** (1997) 313.
3) Gruber O., et al., Plasma Phys. Contol. Fusion **35** (1993) B191.
4) Yoshino R., et al., Fusion Technology **30** (1996) 237.

9.3 Vertical Displacement Caused by Giant ELM in JT-60U[1]

Masaya Ohsawa*, Ryuji Yoshino, JT-60 Team, Satoshi Itoh*

In tokamak plasmas, fluctuations of plasma position are frequently observed at various kinds of plasma perturbations, such as giant ELM, β_p-collapse and disruption[2]. These fluctuations will have harmful effects, e.g. the attachment of plasma to the first wall, on tokamak reactors like ITER. Especially, it is very important to study the fluctuations of plasma position caused by giant ELMs, because ITER will operate in ELMy-H mode.

In JT-60U, during ELMy H-mode discharges, some of giant ELMs occur in which plasma position mainly moves in the vertical direction over a maximum distance of ~ 4.7 cm (See Fig. 1). The vertical position of the I_p-center (Z_J) is measured from the midplane of the vacuum vessel, and the horizontal position of that (R_J) is the plasma major radius. The l_i indicates plasma internal inductance and β_p is poloidal β. D_α^{div} indicates D_α emission signal viewing the divertor region. Experimental conditions are an NB heating power of 32 MW, a plasma current of 2.2 MA and a toroidal magnetic field of 4.1 T.

A large vertical displacement (VD) of Z_J occurs at giant ELMs. This phenomenon can be divided into two phases based on plasma movement. In phase I, a small β_p-drop and a small R_J-shift are observed while in phase II, a l_i-drop of ~ 0.25 and a large Z_J-drop of ~ 4.7 cm occur. And this large VD in phase II has been confirmed by the soft X-ray emission. The large VD is always observed with a large decrease in l_i. Intense n = 1 ~ 3 modes are always observed at the giant ELMs accompanied by the large VD, which would explain the sudden l_i-drop. It is nesessary to clarify the mechanism of VD at giant ELMs and work out effective measures to cope with giant ELMs when they occur.

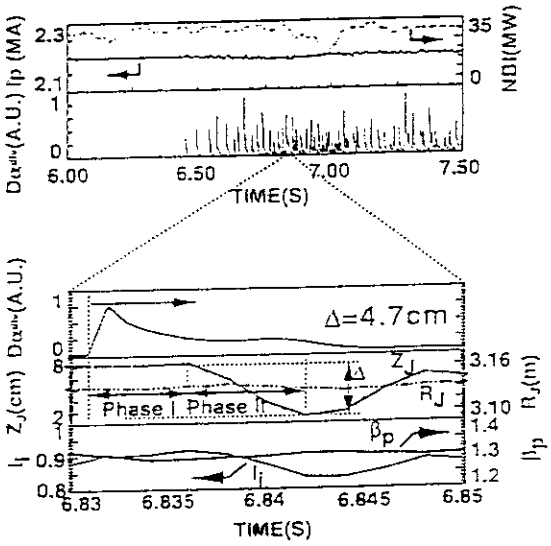

Fig.1 Time evolution of ELMy H-mode discharge with large vertical displacement at giant ELM

Reference

[1] OHSAWA M., et al., ICPP96,12E04

[2] YOSHINO R., OHSAWA M., Fusion Technol. 30 (1996) 159

*Advanced Fusion Research Center, Research Institute for Applied Mechanics, Kyushu University, Kasuga, Fukuoka, 816 Japan

9.4 Improvement of Equilibrium Control Algorithm

K. Kurihara and JT-60 Control Group

1. Introduction

It has been observed that the control accuracy of the JT-60 equilibrium parameters (macroscopic plasma positions) changes with a long time constant (seasonal changes of temperature and/or humidity?), and that the plasma position and PF-coil voltage are irregularly fluctuated. Analysis using JT-60 plasma control model [1] shows that these observation can be completely reproduced, only if the digital computation procedures and error fluctuation of analog-to-digital conversion are strictly taken into account. On the basis of these analyses, a new algorithm has been developed with the numerical simulation made [2], and it was expected to improve the equilibrium control performance to a large extent.

Consequently, the new algorithm was installed in the JT-60 equilibrium control computer (EQCC), and was applied to the actual JT-60 plasma experiment. The improvement of the control performance and the other effects of this algorithm are discussed.

2. New Algorithm

In the JT-60 standard operation, plasma position parameters are the plasma horizontal position Rp, plasma vertical position Zp, and X-point vertical position Xp. Their controls are performed through two levels: the equilibrium control computer (EQCC) for plasma equilibrium

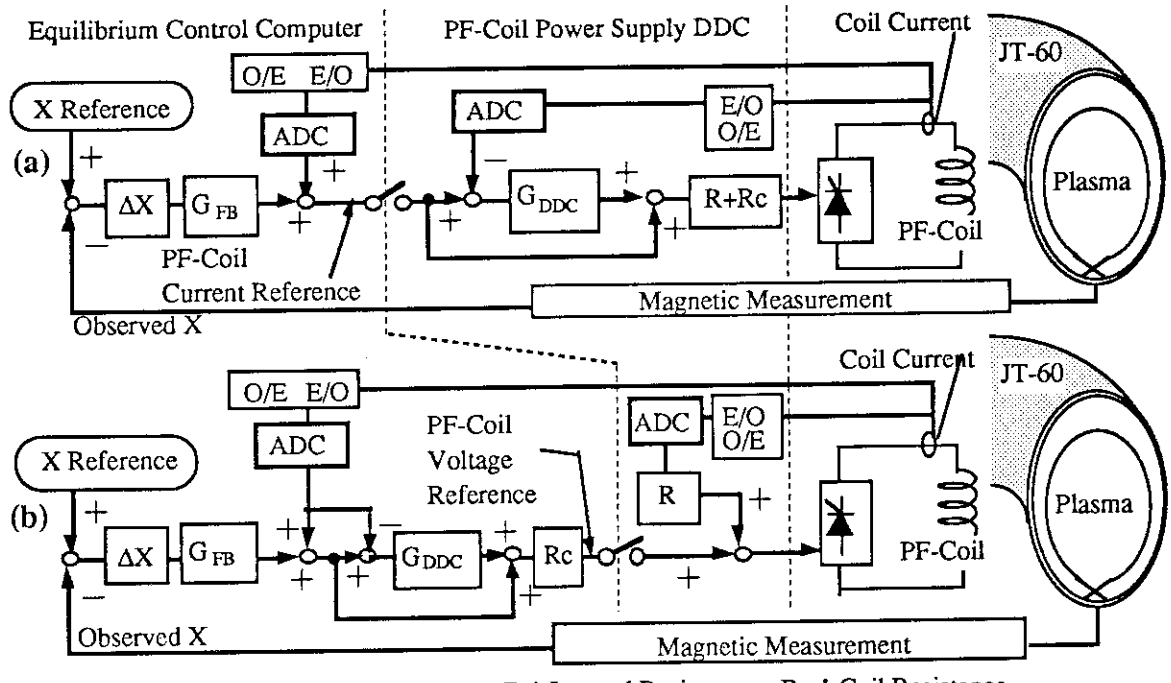

ADC : Analog-to-Digital Converter, R : Internal Resistance, Rc : Coil Resistance
GFB : Feedback Control Gain (Position), GDDC : FB Control Gain (Coil), X= Rp, Zp, Xp

Fig. 1 Block Diagram of the Old and New Control Algorithms ((a): old, (b): new)

control and the PF-coil direct digital controller (DDC) for power supply control.

Since the first plasma of JT-60, an algorithm has been used for plasma experiment, where the EQCC generates the coil current reference value to DDC, and the DDC converts the coil current reference to the coil voltage command according to a feedback control algorithm with voltage-drop compensation (shown in Fig. 1(a)). This algorithm includes two problems that deteriorate control performance: (a) Since the dynamic range of coil current is smaller than that of coil voltage to make control response faster, the digitized error of the coil current reference is more sensitive to the system than that of coil voltage reference with high gain feedback. (b) Since two analog-to-digital converters are used for EQCC and DDC, independently, the conversion error multiplied by the large gain produces the large amount of voltage fluctuations.

To solve the problems, a new algorithm is developed as shown in Fig. 1(b). The features of this algorithm are as follows: (i) Only single ADC is input, and hence no difference of conversion error is produced. (ii) Since the EQCC generates voltage reference, the DDC just realizes the coil voltage using thyrister power supplies.

3. Results

(1) Control accuracy improvement — the Rp, Zp, Xp regulating test (Fig. 2) —

The new control algorithm improved the control accuracy, where the steady-state deviations from the nominal references to less than 5 mm for Rp with the half of the old control gain, 2 mm for Zp, and 6 mm for Xp (2 mm, with an improved gain).

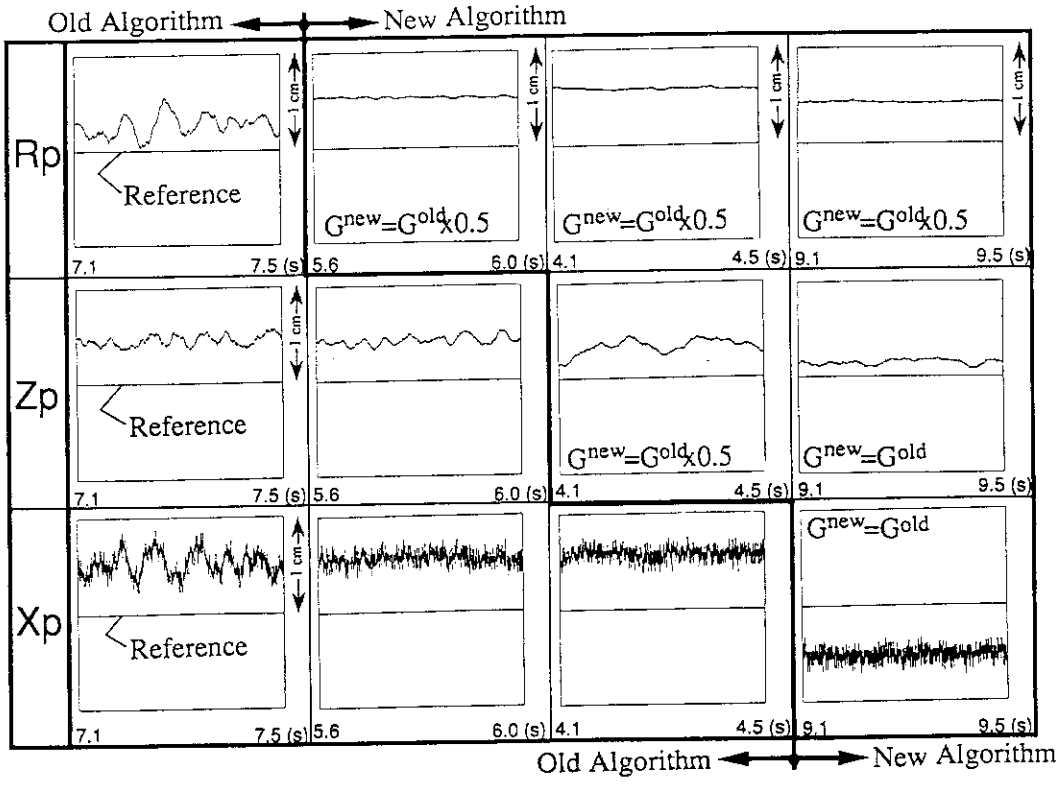

Fig. 2 Control Accuracy by the Old and New Algorithms —Rp, Zp, Xp Regulation Test—

(2) Control accuracy improvement — the Rp, Zp, Xp oscillation/step test (Fig. 3) —

In the Rp-tracking test with the 10-Hz oscillation with 3-cm amplitude, Rp is well controlled by the new algorithm, while the overshooting is observed under the old control algorithm. The control characteristics and coupling effects with other variables are shown in Fig. 3. The figures of the left hand side shows the response to the separately-oscillated reference of Rp, Zp and Xp, and those of the right hand side shows the step response waveforms.

In the oscillation response, the induced error of control is less than 15 kA for Ip, and 1 cm for Xp. In the step response, the error of control is less than 10 kA for Ip, and less than 1 cm for Rp, Zp, or Xp.

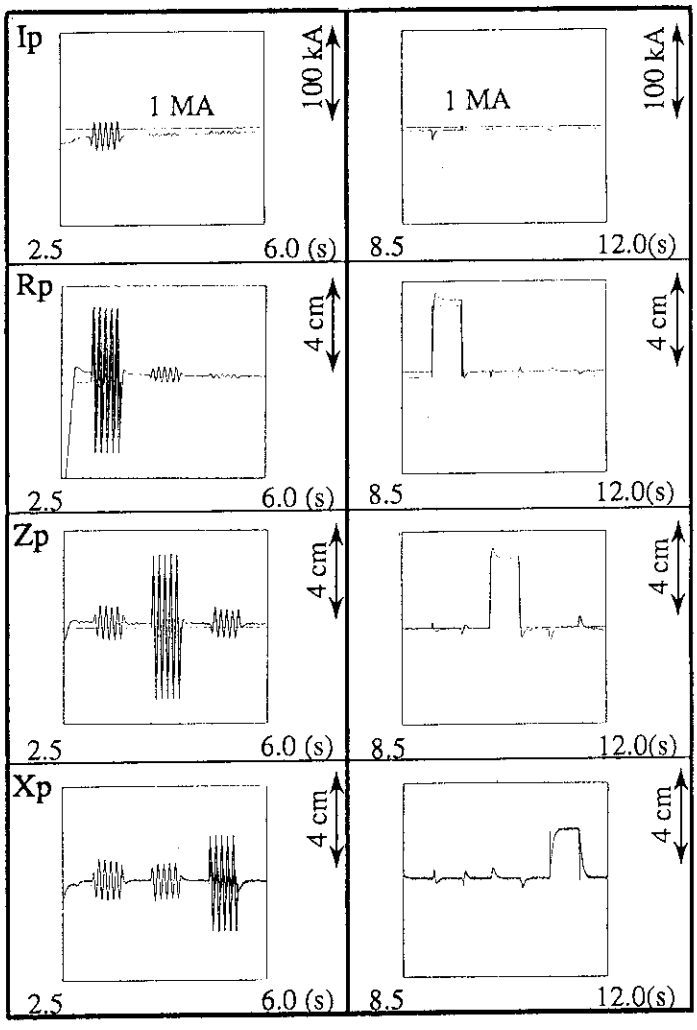

Fig. 3 Coupling Effects of the New Algorithm
—Rp, Zp, Xp Oscillation/Step Test—

(3) Fluctuation suppression

No irregular fluctuation of the position parameters is observed under the control of the new algorithm. In addition, voltage fluctuation observed in the period under the old control is greatly suppressed by the new algorithm. The reduced amount of peak-to-peak voltage are as follows: 1600 V—>300 V (Vertical field coil), 32 V—> 16 V (Divertor coil), but no significant change of the fluctuation for H-coil voltage is observed.

Furthermore, the fluctuation of one-turn voltage difference between inboard and outboard is completely suppressed to 1/10 (3V —> 0.3 V) by the new algorithm, as shown Fig. 4.

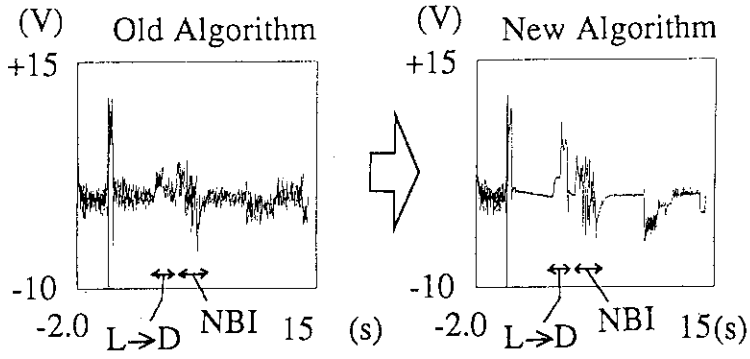

Fig. 4 Suppression of Flux Fluctuation in the Plasma Region

(4) It was checked that plasma current build-up and termination under the new control do not make any problem in comparison with those under the old control.

4. Conclusion

The new algorithm is confirmed effective to improve the performance of equilibrium control accuracy. In addition, this can also suppress the fluctuation of the one-turn voltage, and hence the influence of PF-coil on peripheral plasma characteristics may be expected to change. It is, then, proposed that this new algorithm be applied to all experimental discharge in place of the old one.

References

1) K. Kurihara, Fusion Eng. Des., 19 (1992), 235
2) M. Yoshida and K. Kurihara, JAERI-Tech 95-053 (1995) (in Japanese)

10. Diagnostics

10.1 Corrugated Waveguide Transmission System for ECE Diagnostics in JT-60U

N.Isei, A.Isayama, S.Ishida, M.Sato

1. Introduction

The S-band rectangular waveguides had been used for the transmission line of ECE diagnostics in JT-60U [1]. The total length of the waveguides was about 40m, and the total loss of the transmission line including double Brewster windows, S-band waveguides, 11 bends amounted to about 13dB at 200GHz. The transmission line was shared by power dividers[2] between three systems since February 1996: Fourier transformed spectroscopy system[3] (FTS), grating polychromator system[4] (GPS) and heterodyne radiometer system[5] (HRS). Because of the large transmission loss, it was difficult to get enough time for the absolute calibration of the sytem for FTS, and the signal-to-noise ratio in the observation of the plasma was not more than enough for GPS and HRS. In order to reduce the transmission loss and improve the perfomance of the diagnostic systems, corrugated waveguide[6,7] transmission system was installed in March 1997, in place of the S-band waveguide transmission line.

2. Design of the System

The corrugated waveguide transmission system consists of following components;

(1) windows, polarizer, horn antenna

(2) transition(2pieces), corrugated waveguide(total:24m), miter bend(6pieces)

(3) S-band waveguide(total:14.4m), S-band bend(5pieces)

The block diagram is shown in Fig.1. Some of the S-band waveguides are buried in the wall of Torus hall with shielding materials for neutron radiation, and are difficult to be replaced by corrugated waveguide. Consequently, corrugated waveguides are substituted for S-band waveguides from just after the antenna to just before the wall, as shown in Fig.1. The components in the above items (1) and (3) are not changed from past transmission line. In order to convert transmission mode between TE_{01} in S-band waveguides and HE_{11} in corrugated waveguides, transitions in the above item (2) are used. All corrugated components in the above item (2) are made by General Atomics. The corrugated waveguide has an inside diameter of 63.5mm, with a corrugated period of 0.45mm and depth of 0.3mm, which are designed to get low transmission loss in the bandwidth between 100 and 300GHz.

The total transmission loss (without power dividers) was estimated to be 6.7dB, in which corrugated components contributes 1.1dB and other components contributes 5.6dB. In corrugated components, six miter bends, 24m waveguides and two transitions contribute 0.36dB, 0.005dB and 0.76dB, respectively. The estimated loss shows that the improvement of 6.3dB can be expected against the past transmission line.

3. Obtained Performance

The insertion loss of the corrugated components was measured in General Atomics. The results indicate that two transitions and other components contribute about 1dB and 0.5dB, respectively, for HE_{11} mode propagation at 170GHz.

After the installation of the corrugated components in JT-60U, the total transmission loss was measured by FTS as part of absolute calibration of the system using a low-temperature

blackbody source as shown in Fig.2, where type A and type B were used as the position of a source. The obtained transmittance value, the ratio of emission by type A and type B, is shown in Fig.3. In this measurement, two polarizers were used. One is situated at the antenna, and another is situated at the entrance part in the Michelson interferometer of FTS. The angle of polarizers were set at 0 degree, which corresponds to the selection of extraordinary mode emission from plasma. Fig.3 shows that the transmittance of the corrugated transmission system is almost same level with that of the S-band transmission line, where the transmission loss results in about 13dB at 200GHz for both cases. The measured loss value is larger than the estimated one in the case of corrugated transmission system.

4. Discussion

To understand the unexpected large loss in our corrugated transmission system, first, we tried to investigate the effect of higher order modes, the possibility that the filtering of higher modes at the transition could make large loss. The measurement was performed by type C in Fig.2, without using windows, an antenna and a transition, where a corrugated waveguide was used directly as an antenna, because the S-band horn antenna could generate many higher modes. The measured intensity for the S-band transmission line (where S-band waveguide was directly used as an antenna) and the corrugated transmission system (where corrugated waveguide was used as an antenna) are shown in Fig.4, which indicates no significant difference between two cases, against our expectaions.

Secondly, the effect of polarization was investigated. It is the possibility that the change of polarization, which could arise during transmission from some reason, could make large loss. The measurement was performed by type C in Fig.2, where the angle of polarizer in the Michelson interferometer was changed, although the angle of polarizer at source was fixed at 0 degree. The measured intensity for the S-band transmission line (Fig.5) and the corrugated transmission system (Fig.6) indicates no significant cross polarization, although the intensity of 90° case in corrugated transmission system is higher than that in S-band transmission line.

Thirdly, the insertion loss of a transition was measured by FTS. The measurement was performed by type B in Fig.2, where the transition was inserted at the top of a S-band waveguide just before source. The measured transmittance of a transition in Fig.7 shows about 15% loss at 200GHz, which is a little bit large loss, although it might be come from the no use of corrugated waveguide as an antenna at the top of a transition, where the transition was directly used as an antenna because of the limitation of setup space.

The unexpected large loss in our corrugated transmission system can not be explained by the effect of polarization nor the insertion loss of a transition. But higher order modes which are generated at the antenna could result in large loss for the corrugated transmission system, because modes other than HE_{11} are strongly attenuated in the corrugated waveguide transmission line. Further investigation must be performed.

REFERENCES

[1] Sato M., Ishida S., Isei N., Isayama A., Shirai H., Oyevaar T., Teranishi M., Iwama N. and Uchino K. : to be published in Fusion Engineering and design.
[2] Isayama A. et al., JAERI-Research 96-018, 219 (1996).
[3] Sato M. et al., JAERI-M93057, 359 (1993).
[4] Ishida S. et al., Rev. Sci. Instrum. 61, 2836 (1990).
[5] Isei N. et al., Rev. Sci. Instrum. 66, 413 (1995).
[6] Cavallo A. et al., Rev. Sci. Instrum. 61, 2396 (1990).
[7] Doane J. et al., Infrared Millimeter Waves 13, 123 (1985).

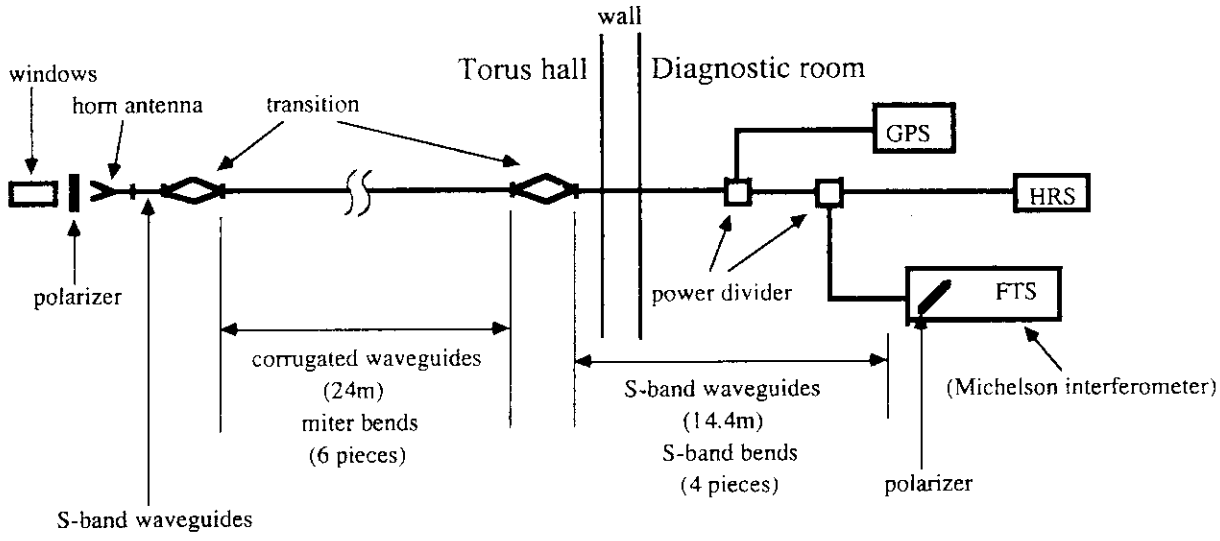

Fig.1: Block diagram of the corrugated waveguide transmission system for ECE diagnostics in JT-60U

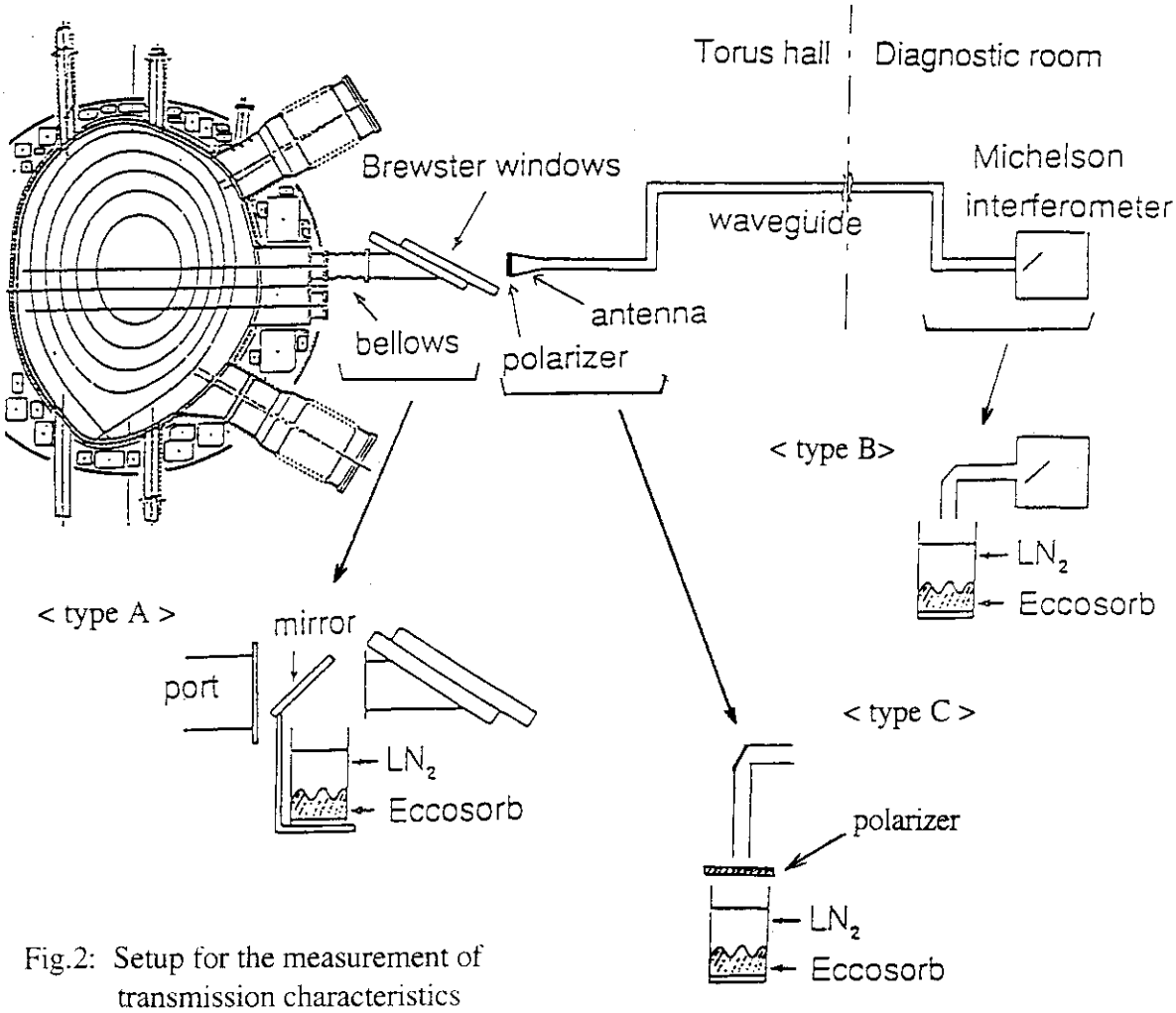

Fig.2: Setup for the measurement of transmission characteristics

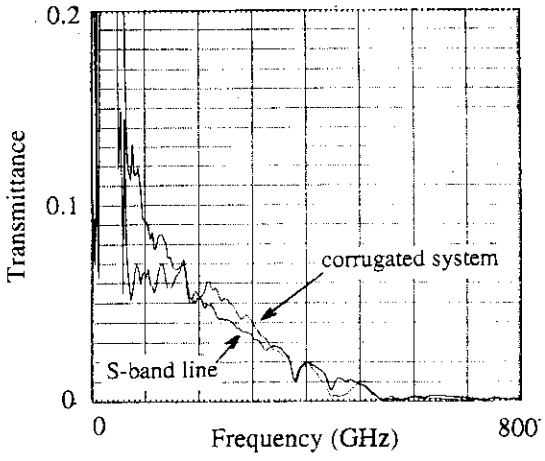

Fig.3: Transmittance of the corrugated transmission system and the S-band transmission line

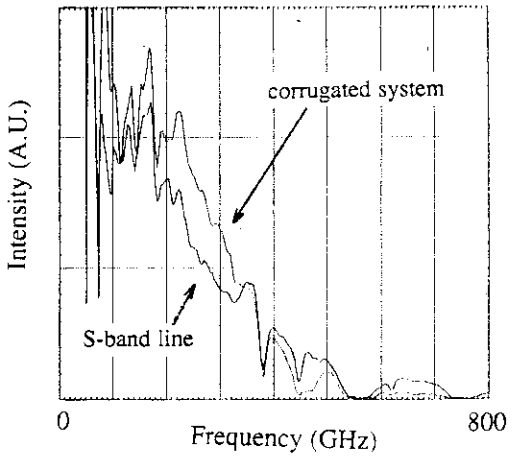

Fig.4: The measured intensity without using windows and horn antenna

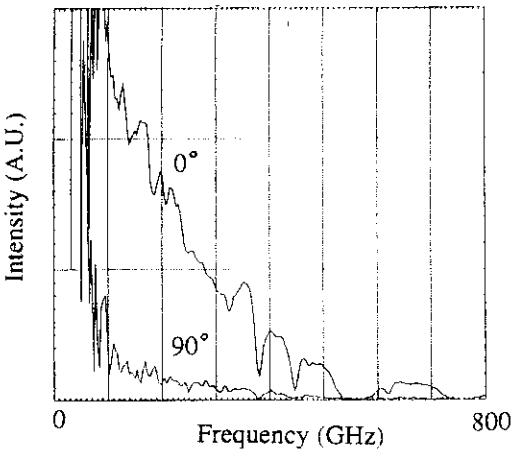

Fig.5: The measured intensity with polarizer angle: 0° , 90° for the S-band transmission line

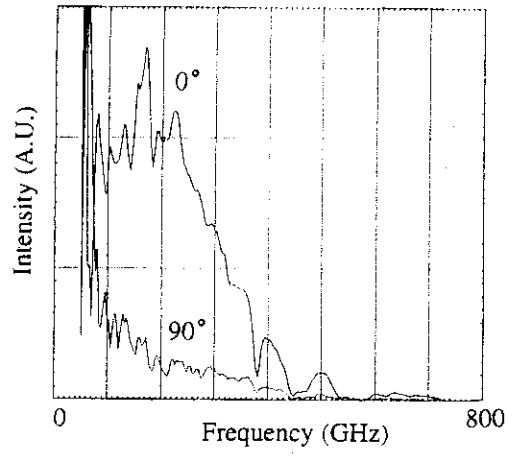

Fig.6: The measured intensity with polarizer angle: 0° , 90° for the corrugated waveguide transmission system

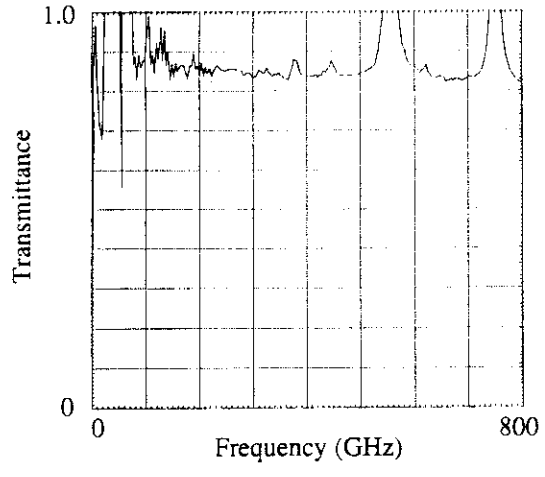

Fig.7: Transmittance of a transition

10.2 Automatic Analysis of Sawtooth Inversion Radius with Adaptive Neural Network

N.Isei, S.Ishida, A.Isayama, M.Sato, Y.Ooi[1], M.Teranishi[2], N.Iwama[1]
Toyama Kenritsu University[1], Nara National College of Technology[2]

The availability of neural network algorithm has been widely noticed in fusion research in recent years, and on the other hand the automatic analysis of experimental data is an important theme for the diagnostics in future reactors. In this paper a neural network algorithm is applied to the ECE data of JT-60U plasma, and sawtooth inversion radius values are automatically acquired to obtain information concerning current profiles.

To detect the time of sawtooth collapse, a method of adaptive signal prediction is applied to the time series of ECE data which were obtained by grating polychromator system[1], and the collapse time is determined[2] from the time when the prediction error is maximized in magnitude, as shown in Fig.1. The prediction is performed by a three-layered perceptron, whose connection weights are changed adaptively so as to reduce the squared prediction error. Inversion radius is calculated from the ECE data using the obtained collapse time.

The method was applied to the NB heated plasma in JT-60U. Figure 2 shows a time evolution of the automatically obtained inversion radius. During a highly heated phase (7.0-9.0sec) all of the existing sawteeth were detected by the neural network, while in the other phases 52% of those were detected.

REFERENCES

[1] Ishida S. et al., Rev. Sci. Instrum. 61, 2836 (1990).
[2] Ooi Y., master thesis 'Nonlinear Adaptive Filter with Neural Network and its Application to Signal Change Detection' (1996).

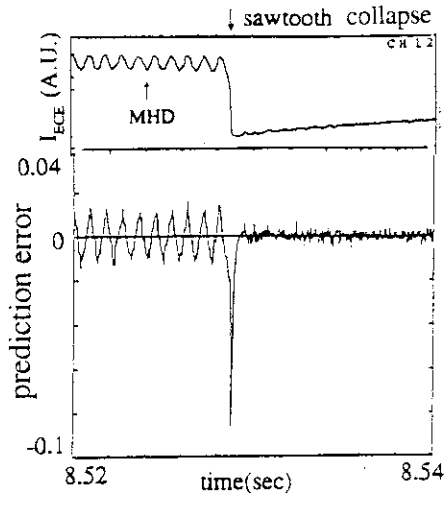

Fig.1: Detection of the time of sawtooth collapse by neural network

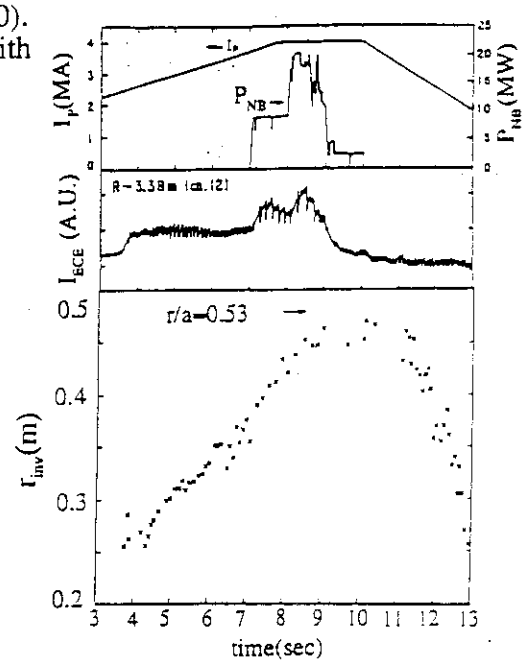

Fig.2: Time evolution of the sawtooth inversion radius

10.3 Elimination of ELM heat pulse from FTS interferogram

A. Isayama, N. Isei, S. Ishida and M. Sato

1. Introduction

Electron temperature measurement by electron cyclotron emission(ECE) diagnostics have long been one of the fundamental diagnostics in many fusion devices. In JT-60U, there are three ECE diagnostics systems[1], which are Fourier-transform spectrometer system(FTS)[2], grating polychromator system(GPS)[3] and heterodyne radiometer system(HRS)[4]. FTS has the advantage of obtaining absolutely calibrated electron temperature profile. The electron temperature profile obtained by GPS and HRS are relatively calibrated using FTS data. Thus FTS is a key diagnostic system for ECE measurement. In ELMy H-mode phase, however, electron temperature measurement by FTS becomes difficult. This is because during a scan interferogram suffers from intense ELM heat pulse which corresponds to non-thermal emission from plasma. In order to establish measurement by FTS during ELMy H-mode phase, the effect of the ELM heat pulse on FTS interferogram is investigated.

2. ECE measurement by FTS during ELMy H-mode phase

The electron temperature profile obtained by FTS is acquired by Fourier-transforming the interferogram. The typical data sampling time is about 20μs and it takes about 50ms for the mirror to go back and forth. Typical FTS interferogram is shown in Fig.1(a). Sharp signal around I=410 corresponds to the position where the difference of optical length becomes zero. The position is referred to as 'zero position', hereafter. Obtained electron temperature profile is shown in Fig.1(b).

Typical time evolution of the output of FTS and GPS during ELMy H-mode phase are shown in Fig.2, where Dα signal is shown in order to refer the behavior of ELMs. The discharge condition shown in this paper is the one with the high triangularity configuration where long ELMy H-mode phase is sustained(See Sec. 3.3). When ELM occurs, the output of FTS becomes meaningless for electron temperature measurement because non-thermal electrons emit intense emission. FTS is subject to the effect of the non-thermal emission since the data are acquired with only one detector. Thus, even if the duration when the interferogram suffers from the heat pulse is short, whole electron temperature profile becomes meaningless. On the other hand, the output of GPS does not suffer from serious effect of the heat pulse since in GPS the output from the detector itself is proportional to electron temperature except for the short time during which the heat pulse enters the detector. In Fig.2, the effect of the ELM heat pulse on GPS is not clear since the data sampling time in Fig.2 is reduced to 20ms.

3. Estimation of the effect of ELM heat pulse

When ELM heat pulses enter, the interferogram is disturbed by two kinds of noises as shown in Fig.3. One is the sharp and intense ELM heat pulse and the other is the slow-decaying noise. The latter is the results of cancellation of the heat pulse in integral circuit. In order to investigate the effect of the heat pulse in the interferogram on electron temperature profile, artificial pulse noise is added to the interferogram which does not suffer from the heat pulse. First, the effect of intensity of the pulse is investigated. The level of the artificial noise is changed at a fixed position, I=700. In Fig.4 and Fig.5, interferogram and the resultant electron temperature profile for the artificial noise level of 400 and 800 are shown. These noise level corresponds to 27% and 53% of the intensity at the zero position, respectively. From these figures, we can see that the effect on electron temperature profile is larger with the intensity of the heat pulse. Secondly, the effect of the position of the pulse is investigated. In Fig.6,

interferogram with the noise level of 800 at I=900 is shown. By comparing Fig.5 with Fig.6, we can see that the effect is larger when the pulse position is located nearer to the zero position. The result is attributed to apodization. In FTS, apodization function is applied in order to reduce aliases caused by the finiteness of the data number of the interferogram. The apodization function has the form of linearly decreasing one with the distance from the zero position.

Note that the artificial noise applied here is much smaller than that observed in experiment. In other words, the ELM heat pulse have a serious effect on FTS interferogram.

4. Correction of interferogram

In order to remove the slow-decaying noise ascribed to the logic in the integral circuit, high-pass filter(HPF) is applied to the interferogram. The filter function we use is expressed by $y=1/\{1+(x/a)^{10}\}$, which is called Butterworth filter. a is constant which is set to be 20 in this paper. We must be careful lest the filter should cut the ECE signal itself. If the constant a is too large, the interferogram around the zero position is smoothed. The high-pass filtering is a first step. In order to remove the ELM pulse, we pay attention to the time evolution of the interferogram. In Fig.7, time evolution of the interferogram at I=415, which locates near the zero position, is shown. It is hard to detect the heat pulse without the HPF as shown in Fig.7(a) because of the slow-decaying noise. By applying the HPF the position of the pulse becomes clear as shown in Fig.7(b). If we pay attention not to MHD events such as sawtooth oscillation but to global evolution of electron temperature, the change of electron temperature can be thought to be small. Thus, if the signal suffers from the ELM heat pulse, it can be replaced by the signal in the previous time step. This is a second step. By using the above two procedures, the interferogram which suffers from the ELM heat pulse is removed successfully as shown in Fig.7(c). Time evolution of electron temperature which is deduced by Fourier-transforming the reconstructed interferogram is shown in Fig.8. Comparing with Fig.3(b), we can see that the constructed signal shows good agreement with the GPS output. The difference between the corrected FTS output and the GPS output is about 10% at most.

5. Summary

The effect of the ELM heat pulse on FTS interferogram is investigated. It is found that the effect of the ELM heat pulse becomes serious if the intensity of the heat pulse is larger and/or the position of the heat pulse is nearer to the zero position. Simple smoothing method is applied in order to remove and reconstruct the interferogram. The electron temperature deduced by Fourier-transforming the reconstructed interferogram showed good agreement with the result of GPS, which means that this procedure is effective for FTS measurement during ELMy H-mode phase. After the optimization of the form of the filter function and the smoothing method, FTS can be a tool for feedback control of electron temperature.

References

[1] Sato M., Ishida S., Isei N., Isayama A., Shirai H., Oyevaar T., Teranishi M., Iwama N. and Uchino K. : to be published in Fusion Engineering and Design.

[2] Sato M., Isei N. and Ishida S. : JAERI-M 93-057, "Development of Fourier Transform Spectrometer System", 359 (1993).

[3] Ishida S., Nagashima A., Sato M., Isei N. and Matoba T. : Rev. Sci. Instrum., 61, 2834 (1990).

[4] Isei N., Sato M., Ishida S., Uchino K., Nagashima A., Matoba T. and Oyevaar T. : Rev. Sci. Instrum. 66, 413 (1995).

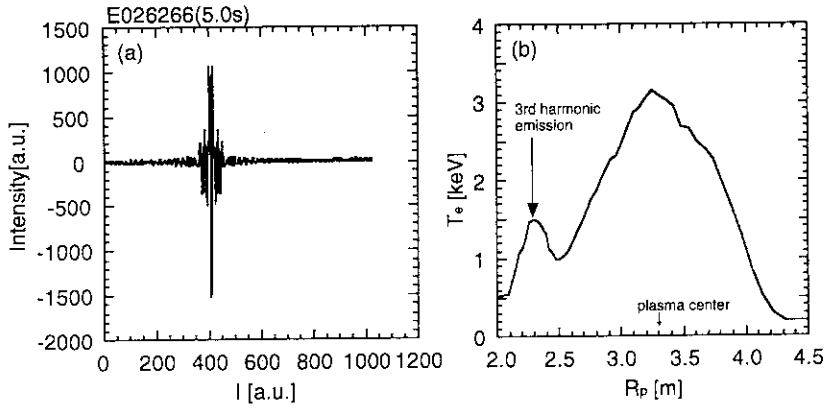

Fig.1: (a)Typical interferogram without ELM heat pulse. The abscissa corresponds to the mirror position. Sharp negative signal around I~410 corresponds to the position where the difference of optical length becomes zero. (b)Typical electron temperature profile, which is obtained by Fourier-transforming the interferogram in Fig.1(a).

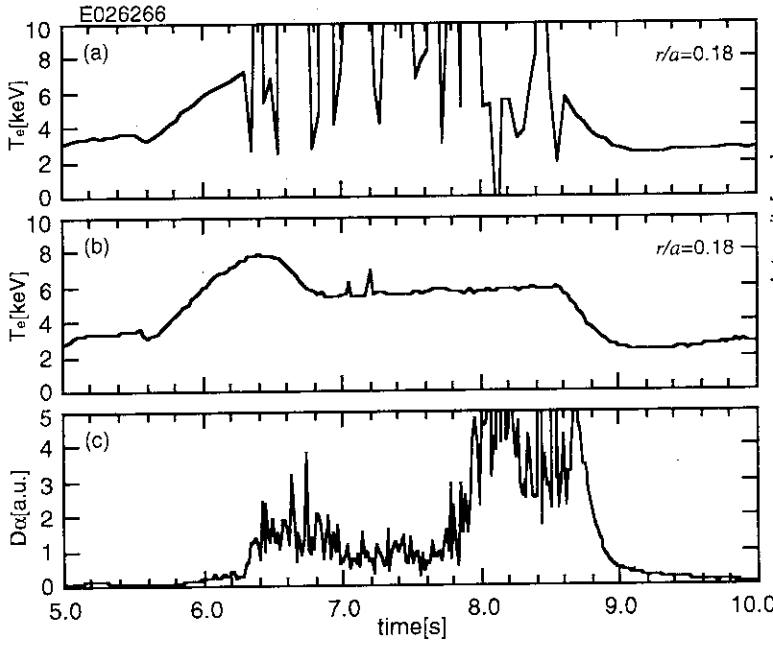

Fig.2: Typical time evolution of (a)electron temperature measured by FTS, (b)electron temperature measured by GPS and (c)intensity of Dα emission.

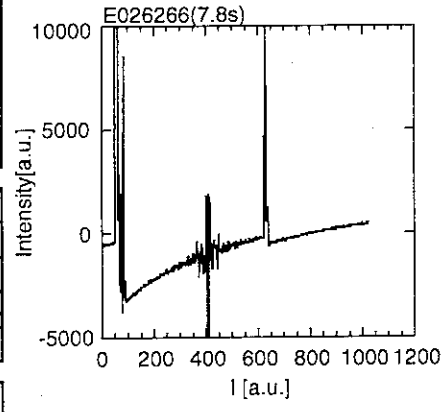

Fig.3: An example of the interferogram which suffers from ELM heat pulses. Sharp heat pulses are found I~50 and 630.

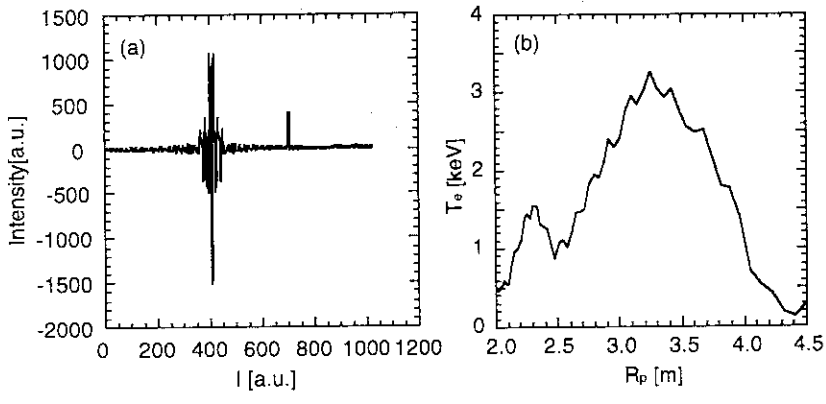

Fig.4: (a)Interferogram which suffers from artificial noise. The original interferogram is the one in Fig.1(a). The position and intensity of the noise are I=700-704 and 400, respectively. (b)Electron temperature which is obtained by Fourier-transforming the interferogram in Fig.4(a).

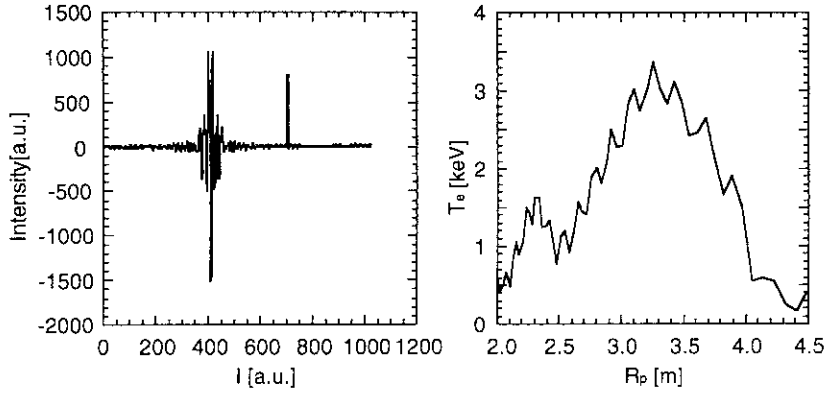

Fig.5: (a)Interferogram which suffers from artificial noise. The original interferogram is the one in Fig.1(a). The position and intensity of the noise are I=700-704 and 800, respectively. (b)Electron temperature which is obtained by Fourier-transforming the interferogram in Fig.5(a).

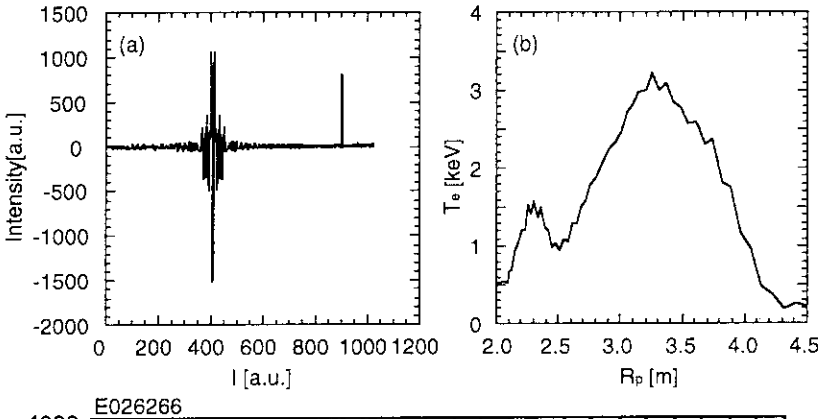

Fig.6: (a)Interferogram which suffers from artificial noise. The original interferogram is the one in Fig.1(a). The position and intensity of the noise are I=900-904 and 800, respectively. (b)Electron temperature which is obtained by Fourier-transforming the interferogram in Fig.6(a).

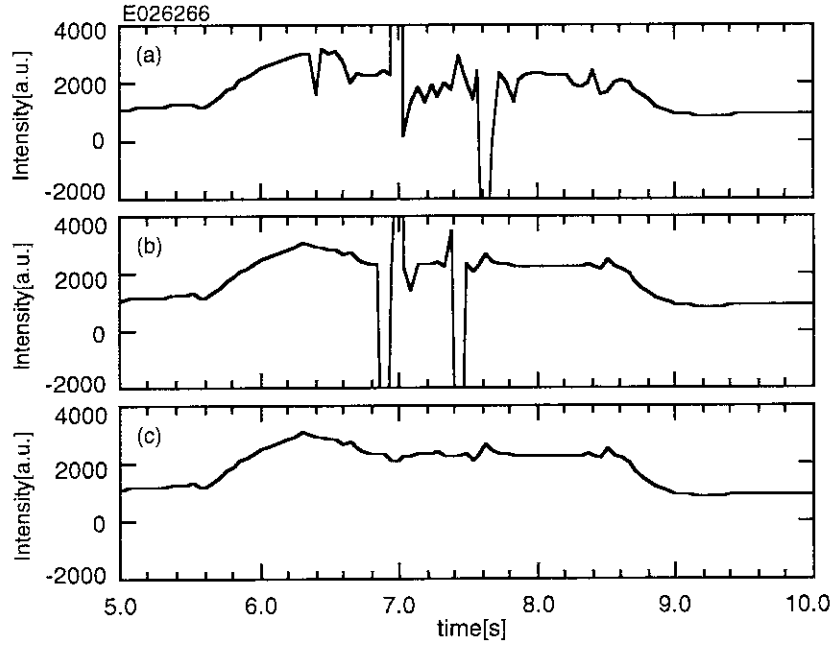

Fig.7: Time evolution of interferogram at I=415: (a)raw data, (b)signal after high pass filter, (c) signal after high pass filter and smoothing.

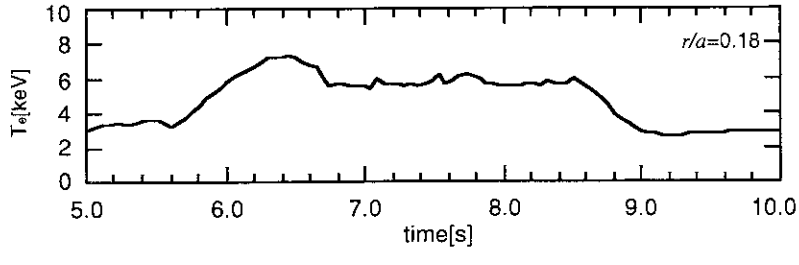

Fig.8: Time evolution of electron temperature acquired by Fourier-transforming the reconstructed interferogram. The shot number is identical with that in Fig.1.

10.4 Determination of Radial Position in the Measurement of Electron Temperature Profiles from Electron Cyclotron Emission[1)]

M. Sato, N. Isei, A. Isayama, S. Ishida and H. Shirai

Plasma confined in a magnetic field radiates electron cyclotron emission (ECE) with a spectrum related to the local electron temperature. In many tokamaks, the measurement of the electron temperature profile ($T_e(r)$) from ECE has been a useful diagnostic tool. The radial position of $T_e(r)$ has been determined by using the radial dependence of non-relativistic second harmonic electron cyclotron (EC) frequency ($2f_{ce}^0$) by taking into account internal magnetic fields: $f_{ce}^0 = (eB/m_e^0)/(2\pi)$, where m_e^0 is rest mass of the electron, and B is the magnetic field. The importance of the relativistic down-shift frequency effect on the determination of $T_e(r)$ in a reactor-grade tokamak has been investigated.[2,3)] Recently the importance of the relativistic effect on the determination of the radial position of $T_e(r)$ at medium electron temperatures was pointed out.[4)] Exclusion of relativistic effects in the determination of the radial position results in a pseudo radial shift (Δr) of the obtained $T_e(r)$. In order to study the dependence of Δr on plasma and machine parameters, $T_e(r)$ has been calculated taking into account relativistic effects for a wide range of parameters.[5,6)] The details of this calculation method are written in ref. 3 or 5. Typical dependence of the shift on τ in the cases of $T_e(0)$ = 2 keV, 5 keV, and 10 keV is shown in Fig. 1. When T_e increases or τ decreases, the shift increases. Although the calculated data are taken in a wide region of n_e and B_t (0.2×10^{19} m$^{-3} \le n_e \le 5 \times 10^{19}$ m^{-3} and 2 T $\le B_t \le$ 4 T), the plotted data seem to be located on a line for fixed T_e. This means that Δr depends on T_e and τ for fixed R, T_e and τ are related to the effects of relativistic down-shift frequency and optical thickness, respectively. The shift depends on only three parameters (T_e , τ, and R). In order to correctly determine the radial position for any tokamak, a scaling of the shift is obtained: Δr=0.0009 R(m) T_e(keV) (1+ 40/(5τ)).[1,6)] This scaling is applicable for $\tau > 5$ where the error is less than 2% of a. Since the radial shift is not negligible compared with the frequency resolution of ECE measurement systems especially for high toroidal magnetic discharges, this effect should be taken into account.

In JT-60U plasmas, $T_e(r)$ from ECE are corrected by taking into account these relativistic and optical thickness effects. The correction is based on the calculated results in ref. 5. Comparison between $T_e(r)$ with and without these effects is shown in Fig. 2. There is a large disagreement between the inside and outside in the case without correction. Although there is a little disagreement between the inside and outside in the case with correction, it has been found that for precise measurement of $T_e(r)$ it is important to correct the shift due to these relativistic and optical thickness effects.

References

1)M. Sato, N. Isei *et al.*, *(Proc. Int. Conf. on Plasma Physics, Nagoya, 1996)* Vol. 2, p1438.
2)V. Mukhovatov *et al.*, *ITER Diagnostics* (IAEA,Vienna,1991) ITER Docum. **33** Chap.4.
3)M. Sato, S.Ishida and N.Isei, J. Phys. Soc Jpn. **62** (1993) 3106.
4)M. Sato, N.Isei and S.Ishida, Jpn. J. Appl. Phys. **34** (1995) L708.
5)M. Sato, N.Isei and S.Ishida, JAERI-Research 95-074 (1995).
6)M. Sato, N.Isei, A. Isayama and S.Ishida, JAERI-Research 97-011(1997).

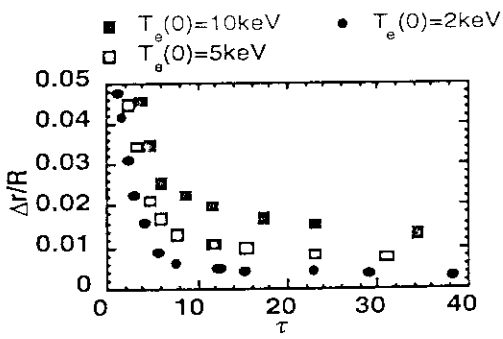

Fig. 1: τ dependence of the radial shift.

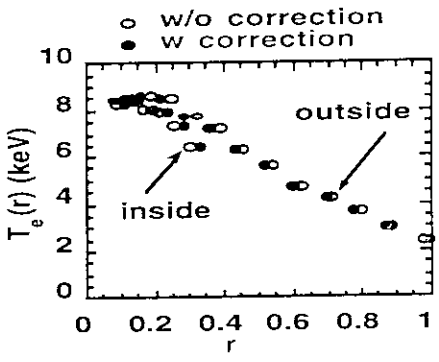

Fig. 2. $T_e(r)$ with and without correction

10.5 Upgrade of MSE diagnostics

T. Fujita, H. Kubo and T. Oikawa

1. Introduction

The five-channel MSE (Motional Stark Effect) diagnostics system in JT-60U was installed in December, 1993 [1]. The polarization angle of σ component of D_α or H_α line from one of the counter-tangential heating neutral beams, called #7B, was measured by a polarimeter which consisted of mirrors, lenses, a pair of PEMs (Photo Elastic Modulators) and a liner polarizer.[2] Its viewing points cover the region of R = 3.04-3.42 m (R is the major radius), which corresponds to a central or high field region of JT-60U plasmas. For plasmas with small R_p (R_p is the plasma major radius), the polarimeter sees the central region and the safety factor (q) only near the axis (r/a < 0.2) is obtained. For plasmas with large R_p, the MSE system sees the region from the axis to the half radius, for example, 0.1<r/a<0.5 in the high field side. Since the neutral beam is injected from the low field side, the attenuation of beam is large for high density or large volume plasmas and the q profile was not available for such conditions. To resolve these problems and to obtain q profiles in the whole region of plasma, a new polarimeter has been installed in December, 1995. Here we describe the modifications in MSE system including the new polarimeter.

2. New polarimeter

The new polarimeter is located at the "P17" section, while the original polarimeter is at the "P13" section (Fig. 1). The new polarimeter has nine viewing points, which cover the range of R = 3.43-4.29 m. By using original and new polarimeters, we can measure the region of R = 3.04-4.29 m with 14 chords, which covers near the axis to near the surface for the standard configuration (Fig. 2). However, since the beam line of #7B is inclined to the equatorial plane, the viewing points diverge from the plasma axis for the configuration with small R_p such as high β_p mode plasmas unless the height of plasma axis is large. Since the angles between sight lines and toroidal direction are smaller for the new polarimeter than for the original polarimeter, the spatial resolution is better for the new polarimeter; dR is 6-8 cm for P17 while it is 15-26 cm for P13, where dR is the radial extent of viewing region for each chord.

The P17 polarimeter is located inside the surface of port box to see the outer region of plasma, while the P13 polarimeter is located outside the port box (Fig. 1). The vacuum widow is located in front of the mirror and the mirror is in the air for the P17 system as well as for the P13 system to prevent the change of mirror properties by surface coating due to the plasma discharges.

A "polarizer shutter" [3] is located in front of the window for the P17 system. With this shutter closed, we can obtain a fixed polarization angle to calibrate the effect of Faraday rotation in the window and the polarimeter.

3. Background light reduction

Substantial background light was observed in the P13 system for high power and high density discharges. A "two-wavelength detector", which measures lights with two different wavelengths by splitting the light with a half-mirror, has been installed for one channel of the P13 system to monitor the background light and has proved to be useful.[1] This two-wavelength detector has been installed for one channel of the P17 system in addition to the P13 system. However, even with two-wavelength detectors, some amount of errors are induced by background light because of the different behavior of background light at different wavelengths. To reduce the error by background light, new type of mirrors have been installed.

Mirrors in the original P13 system were aluminum-coated ones. These mirrors make polarized light from unpolarized light due to the difference in reflectivities for s- and p-polarization (ρ). This polarized light resulted in errors in measurements for high power and high density discharges where large amount of background light is observed. To reduce this error, the multi-layer dielectric mirror has been chosen for the mirror in the P17 system and mirrors in the P13 system have also been changed to multi-layer dielectric ones.

4. Calibration

The change of polarization angle due to the multi-layer dielectric mirrors is large because of large difference in phase for s- and p- polarization (δ) though ρ is nearly unity. The changes have been calibrated using a polarizer after the installation of the system. The value of δ is largest (38 degrees) for the inner most channel of the P17 system whose incident angle at the mirror is large (~71 degrees).

The beam injection into the gas-filled torus was done to calibrate the effect of Faraday rotation due to toroidal magnetic fields. It was found that the difference between measured angles (γ_{mes}) and the calculated angles (γ_{cal}) were not constant for innermost two channels of P17. If we assume that $\gamma_{mes} = a*\gamma_{cal} + b$, a was about 0.6 and 0.8 for the innermost and the 2nd innermost channels, respectively, while a was nearly unity for other channels (including P13). This behavior is supposed to be a result of change of mirror properties. First, the mirror temperature was high due to the baking of the vacuum vessel (~ 280 degC) during the tokamak operation, while the calibration with the polarizer was done at a room temperature. Secondly, the wavelength for the plasma measurement was different from that for the calibration because the calibration with the polarizer was done at a fixed wavelength for all sight lines. These two effects may result in the difference of mirror properties (δ) and the effect is supposed to be larger for channels with larger δ, i.e. inner channels of P17.

The values of a and b obtained by the beam injection into the gas-filled torus were used for the plasma measurements in principle. However, it was found that the measured angles obtained with these values of a and b had some errors by comparing the measured and calculated angles at points where polarization angles were known (for example, at the plasma axis). This implies existence of differences between situations in the beam injection into the gas-filled torus and those in the plasma measurements. To reduce the errors induced by these differences, values of a and b were modified in some cases using tokamak discharges; for example the sawtooth inversion radius from electron cyclotron emission signals was used as the indication of location of $q = 1$ surface.

The whole MSE system has been routinely operated in 1996 and safety-factor profiles have been obtained in various types of discharges including reversed shear experiments, TAE-mode experiments and current drive experiments.

5. Summary

A new polarimeter has been installed and 14 chords which cover $R = 3.04$-4.29 m have become available for safety-factor profile measurements. The effect of background light has been reduced significantly through the use of multi-layer dielectric mirrors in original and new polarimeters.

1) Fujita T. et al., to appear in Fusion Engineering and Design
2) Levinton F.M. et al., Phys. Fluids B 5, 2554 (1993).
3) Rice B.W. et al., Rev. Sci. Instrum. 66, 373(1995).

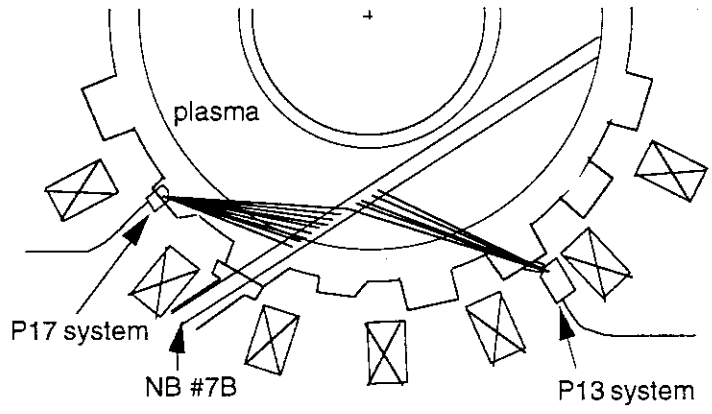

Fig. 1 Plan view of the JT-60U tokamak and MSE (P13 and P17 system).

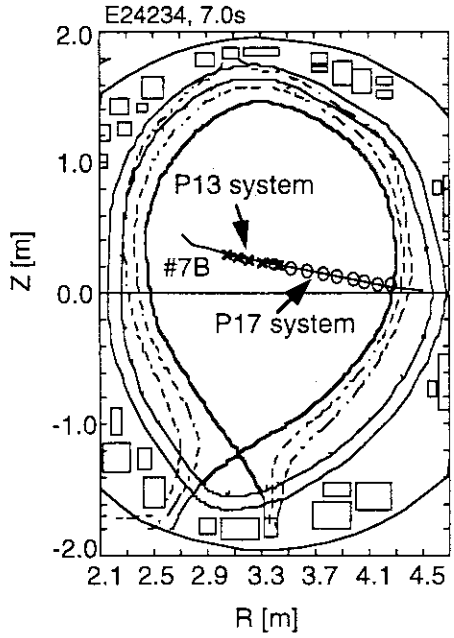

Fig. 2 Viewing points of P13 system (crosses) and of P17 system (circles).

10.6 Charge exchange recombination spectroscopy for fast measurement

J. S. Koog, A. Sakasai

1. Introduction

Charge exchange spectroscopy has been routinely used to measure a ion temperature and a toroidal and poloidal rotation velocities of a tokamak plasma. Recently, fast phenomenon, like a L-H transition, ELMs, and sawtooth, is of special interest, and the improvement of the time resolution of charge exchange spectroscopy has become a more important issue.

2. Apparatus

Three interference filters assembly using charge exchange recombination spectroscopy has been used to measure simultaneously plasma ion temperatures and toroidal rotation velocities of a tokamak plasma, with a sampling time of 160 msec. The C VI 529.2 nm (n=8-7), O VIII 607.0 nm (n=10-9), and He II 468.6 nm (n=4-3) transitions are used conveniently.

An assembly consists of three detection systems. Each system has three interference filters in front of the photomultipliers(Fig. 1).

Each filter has a 0.2 ~ 1 nm bandwidth(FWHM), and the three filters have a slightly different peak wavelength(0.5 ~ 1 nm) to its selected charge exchange recombination line, depending on the ion temperature and rotation velocity at the position measured. As an example, three filters with the peak wavelengths; 528.5 nm, 529.1 nm, and 529.8 nm, are chosen for the measurement of the C VI impurity radiation at a plasma edge.

12 assemblies viewing on and off the neutral beam line are installed on the JT-60U tokamak for a space-resolved ion temperature and toroidal rotation velocity, and the background measurements.

The plasma ion temperature and toroidal rotation velocity are determined using the intensity ratios of three detector signals, after subtracting its simultaneously measured background due to electron impact excitation C VI and charge exchange recombination reactions of C V with thermal background neutrals in the plasma periphery.

3. Discussion

Relative sensitivities of the each detection system included the optics, the filter's characteristics and the photomultiplier were calibrated, which give an effect for the accurate measurement because the ion temperature is derived from the intensity ratios of three signals from the detectors. Total system included a fiber transmission will be corrected soon or later.

Fig. 2 shows the time evolution of the ion temperatures measured with different instruments, one based on charge exchange recombination spectroscopy with CCD detector with a time resolution of 50 msec and the other on filters assembly with 1 msec resolution.

The ion temperature profiles obtained using these interference filter assemblies are compared with those obtained using charge exchange recombination spectroscopy by the visible spectrometers with CCD detector(Fig. 3).

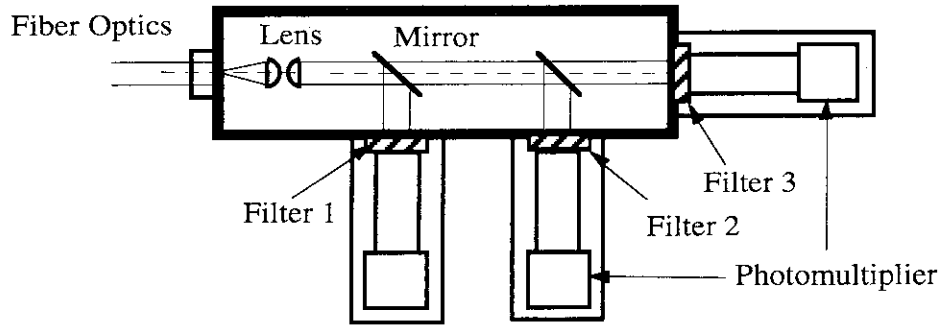

Fig. 1 A filter CXRS assembly. A assembly consists of three detection systems which have interference filters in front of the photomultipliers

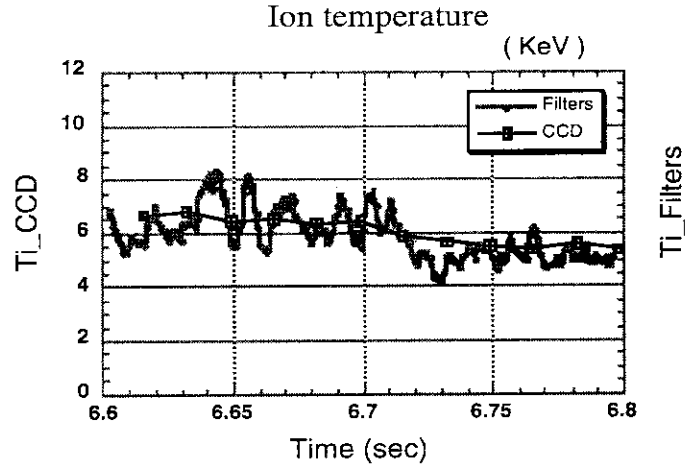

Fig. 2 Time evolution of the ion temperature measured with a spectrometer and filters assembly.

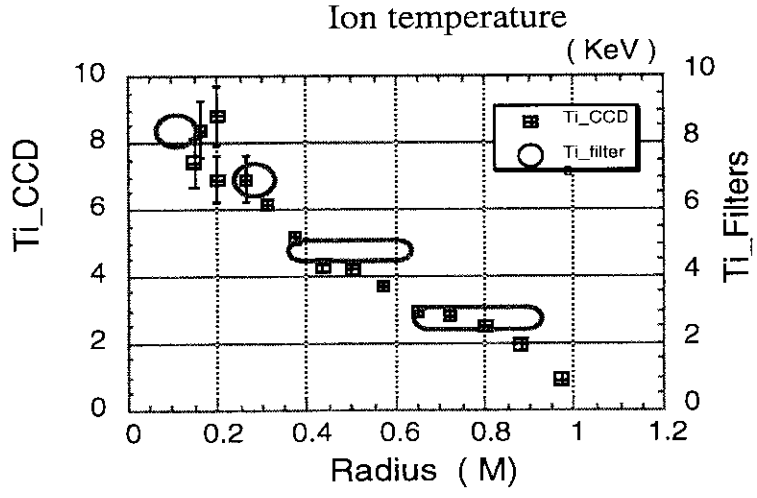

Fig. 3 Ion temperature profiles measured with a spectrometer and filters assembly

10.7 Neutron fluctuation measurement system

A. Morioka, T. Nishitani, T. Kondoh, H. Harano

1. Introduction

In JT-60U, time resolved neutron emission monitor (sampling time: 1ms)[1] and 14MeV neutron detector (sampling time: 10ms)[2] have been installed until now from the start of DD discharge at 1991. By those detectors, it has been confirmed that the neutron measurement is effective to investigate[3]-[8]. However, the time resolution of those detectors is not sufficient MHD-study (e.g. sawtooth, Fishbone instability) of plasmas. Therefore, the neutron detector for good time and spatial resolution was installed in 1993. In this section, the system of neutron fluctuation measurement is reported.

2. Measurement system

The detector consists of a plastic scintillator : NE102A (3×3inchϕ) attached to photomultiplier directry. The detector is used in current mode to get fast response. The gain of detector is controlled by the high voltage power supplying to a photomultiplier. After the signal from detector is converted into the voltage by pre-amplifier, it is transferred to the magnetic shielded room via optical fiber cable through the multiplexer (sampling time $\leqq$100kHz/ch) installed in JT-60U torus hall. There are two systems to collect data of the signal from the detector as shown Fig.1. One is MDR system (sampling time 40μs)[9] which collects the data through TMDS[10] after the output of pre-amplifier is converted into the analog by ADC(TOYO T6700A). The other is CAM system (sampling time 1ms)[9] which collects the data through transient recorder (LeCroy6810). The detector is mounted approximately 2m away from the vacuum vessel surface near midplane. The line of sight of detector is collimated to the central direction of a tokamak with 1cm slit width as shown Fig.2. The spatial resolution is about 15cm at plasma center. The discrimination of neutron and gamma ray or hard X-ray is carried out by putting the lead(9cm) in the detector head.

3. Operational results

In DD discharge experiments, the relative calibration with ^{235}U-fission chamber[1] of the sensitivity calibration-finished was carried out as shown Fig.3. The ratio of DT neutron (14MeV) from the reaction between deutron and triton which is producted by DD discharge is also under about 1% of total neutron emission in discharge variously[11]. Therefore, the effect of 14MeV neutron can be neglected. Still, it was confirmed that the effect of hard X-ray created by runaway electron was included for about 2.5% during plasma disruption.

4. Conclusion

The system of neutron fluctuation measurement was installed in JT-60U. The gain control of detector is done by the high voltage power supplying to a photomultiplier in various discharge. The operational result of this system was reported in the other section[12][13].

References

[1] T. Nishitani, et al.: Rev. Sci. Instrum., **63**, 5270 (1992)
[2] G. A. Wurden, et al.: Rev. Sci, Instrum. **66**, 901 (1995)
[3] K. Tobita, K. Tani, et al.: Nucl. Fusion, **34**, 8, 1097 (1994)
[4] K. Tobita, K. Tani, et al.: Nucl. Fusion, **35**, 12, 1585 (1995)
[5] T. Kondoh, H. Kimura, et al.: J. Plas. Fus. Res., **72**, 12, 1397 (1996) [in Japanese]
[6] M. Isobe, K. Tobita, et al.: JAERI-Research 96-005 (1996)
[7] T. Nishitani, M. Hoek, et al.: Plasma Phys. Cont. Fusion, **38**, 355 (1996)
[8] H. Harano : Ph. D. Thesis, University of Tokyo, Japan (1997)
[9] A. Nagashima, et al : J. Plas. Fus. Res., **59**, sup., 303 (1988) [in Japanese]
[10] T. Aoyagi : J. Plas. Fus. Res., **72**, 12, 1370 (1996) [in Japanese]
[11] M. Hoek, T. Nishitani, et al. : Rev.Sci. Instrum., **66**, 885 (1995)
[12] A. Morioka, K. Tobita: Section 5.7 in this review.
[13] A. Morioka, K. Tobita: Section 6.4 in this review.

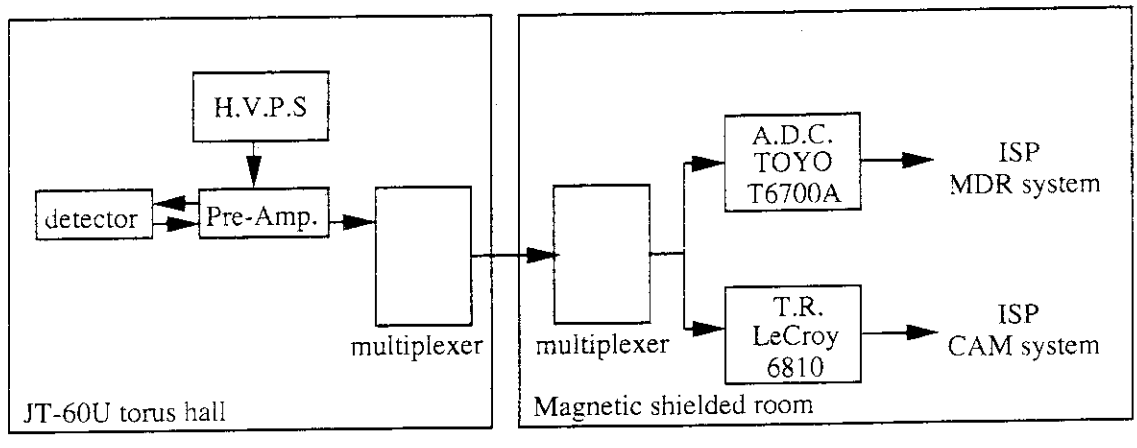

H.V.P.S = High voltage power supply
A.D.C. = Analoge to dagital converter
T.R. = Transient recorder

Fig.1 Neutron fluctuation measurement system in JT-60U

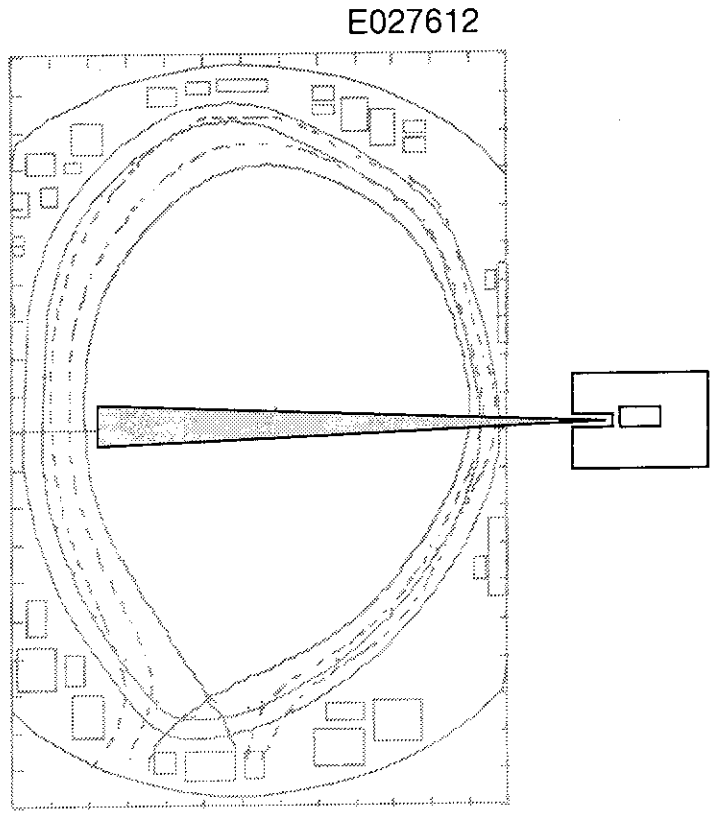

Fig.2 Line of sight of the neutron fluctuation measurement system

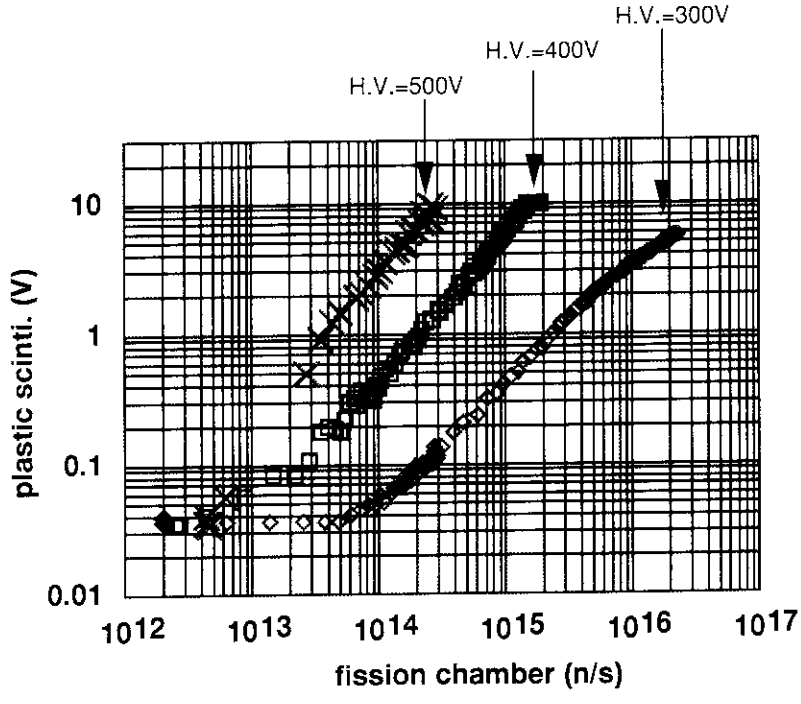

Fig.3 Relative calibration with ^{235}U-fission chamber

Acknowledgments

The authors wish to acknowledge the dedicated efforts of the members of Japan Atomic Energy Research Institute in support of the JT-60U experiments reported here. They also wish to express their gratitude for domestic and international collaborations for the JT-60U program. The contributions of collaborators from many institutions and universities have been critical to the success of these experiments.